

UC Merced

UC Merced Electronic Theses and Dissertations

Title

A Comprehensive Characterization of Surface-Assembled Populations of Giant Liposomes using Novel Confocal Microscopy-Based Methods

Permalink

<https://escholarship.org/uc/item/4v1513rs>

Author

Pazzi, Joseph Edward

Publication Date

2021

Peer reviewed|Thesis/dissertation

UNIVERSITY OF CALIFORNIA, MERCED

A Comprehensive Characterization of Surface-Assembled
Populations of Giant Liposomes using Novel Confocal
Microscopy-Based Methods

A dissertation submitted in partial satisfaction of the requirements
for the degree Doctor of Philosophy

in

Bioengineering

By

Joseph Edward Pazzi III

Committee in charge:

Professor Wei-Chun Chin, Chair

Professor Anand Bala Subramaniam

Professor Andres Martinez

Professor Eva de Alba Bastarrechea

Professor Joel Spencer

2021

The Dissertation of Joseph Edward Pazi III is approved, and it is acceptable in quality and form for publication on microfilm and electronically:

Co-chair (if applicable)

Chair

University of California, Merced
2021

Table of Contents

List of tables	X
List of figures.....	xi
Acknowledgements.....	xv
Curriculum Vita	xviii
Abstract.....	xxiii

Chapter 1: Introduction

1. Motivation and overview of this dissertation.....	1
1.1 Background on the plasma membrane of cells	1
1.2 Liposomes as model systems of the cell membrane	2
1.3 Overview of work completed in this dissertation	2
2. Bibliography.....	4

Chapter 2: Confocal Microscopy Based Method for the Quantification of Populations of Giant Liposomes

1. Introduction	11
1.1 Approach for analysis	12
1.2 Current methods used to characterize GUVs.....	14
1.2.1 Optical microscopy	14
1.2.2 Flow focusing techniques	15
1.2.3 Other techniques	16
1.3 Microscopy of GUVs.....	16
1.3.1 Overview of confocal microscopy	18
1.3.2 Lateral resolution limits of confocal microscope.....	20
1.3.3 Axial resolution limits of confocal microscope	23
2. Materials and methods	27
2.1 Materials	27
2.2 Chemicals.....	27
2.3 Electroformation	27
2.4 PAPYRUS using nanocellulose paper	28
2.5 Custom-made chambers used to collect images of vesicles	28
3. Results	29
3.1 Imaging vesicle buds on the surface	29

3.2 Harvesting the vesicles from the surface	32
3.2.1 Imaging of suspended vesicles.....	33
3.2.2 Sedimentation as a technique to convert 3D imaging to 2D....	34
3.3 Imaging of sedimented vesicles	35
3.3.1 Choice of objectives and pinhole characteristics	35
3.3.2 Choices of field of view and time for imaging	39
3.3.3 Comparison between open-pinhole 10× images and equatorial z-stacks.....	40
3.3.4 Summary of optimal image capture routines	42
3.3.5 Intensity characteristics of GUVs	42
3.4 Large dataset collection	44
3.4.1 Microscope settings used to collect images of vesicles	44
3.4.2 Collection of large datasets using a tilescan imaging routine..	45
4. Image analysis routine and code	46
4.1 Segmentation of fluorescent objects	48
4.1.1 Watershed segmentation on grayscale images.....	48
4.1.2 Histogram analysis.....	49
4.1.3 Watershed segmentation on binary images.....	51
4.1.4 Correcting over segmented large vesicles.....	55
4.2 Selection of GUVs	56
4.2.1 Discrimination based on coefficient of variation to remove poorly segmented objects and MVVs.....	56
4.2.2 Selection of GUVs based on mean intensity.....	60
4.3 Compatibility of code to detect GUVs from different samples	65
4.4 Collecting GUV data into size histograms.....	69
5. Additional controls	70
5.1 Confirmation of identity of small GUVs	70
5.2 Effect of sedimentation time on characterization	71
6. Conclusion.....	73
7. Bibliography.....	74

Chapter 3: A Comprehensive Characterization of Populations of Giant Unilamellar Vesicles Assembled through Surface-Assisted Techniques

1. Introduction	90
1.1 Approach for analysis	90
1.2 Commonly used methods to assemble GUVs.....	91
1.2.1 Gentle hydration.....	91
1.2.2 Electroformation	91
1.2.3 Gel-assisted rehydration.....	91
1.2.4 Solvent-based methods	93
1.3 Novel use of cellulose paper as a substrate to assemble GUVs.....	93

1.4 Molar yield as a standardized metric to compare populations of GUVs assembled from different techniques	94
1.4.1 Definition of molar yield	94
1.4.2 Statistical comparisons of the molar yields	95
1.4.3 Calculation of molar yields reported in the literature	97
2. Materials and methods	105
2.1 Materials	105
2.2 Chemicals.....	105
2.3 Fabrication of the substrates	105
2.3.1 Fabrication of nanocellulose paper	105
2.3.2 Fabrication of nanohybrid paper	106
2.4 Procedures for cleaning the substrates.....	106
2.4.1 Cleaning of the paper substrates	106
2.4.2 Cleaning of the ITO-covered glass slides	106
2.4.3 Cleaning of the regenerated cellulose dialysis membranes ...	106
2.5 Standardized procedures used to assemble GUVs.....	107
2.5.1 Lipid mixture	107
2.5.2 Deposition of lipids.....	107
2.5.3 Hydration of the paper substrates	108
2.5.4 Hydration of the ITO-coated slides followed by electroformation.....	109
2.5.5 One-step modulation of salts	109
2.6 Standardized procedures for harvesting.....	109
2.7 Procedures used to characterize the GUV populations.....	109
2.7.1 Confocal microscopy based methods.....	109
2.7.2 <i>In situ</i> confocal microscopy images of the vesicles on the substrates.....	110
2.7.3 Image processing and data analysis	110
2.8 Comparing size distributions and yields of GUVs across different techniques	110
2.8.1 Plotting size distributions.....	110
2.8.2 Calculation of population size statistics.....	110
2.8.3 Calculation of substrate costs.....	111
2.9 Other methods.....	111
2.9.1 Scanning electron microscopy	111
2.9.2 Hydrophobic modification of the substrates.....	111
2.9.3 Recycling tracing paper for repeated use in GUV formation	112
2.9.4 Scaling up the production of GUVs from tracing paper	112
2.9.5 Fluorescent recovery after photobleaching (FRAP) experiments on GUV buds and harvested GUVs	112
2.9.6 Sodium green assay to evaluate the diffusion of salts inside GUVs	113
3. Results	114
3.1 Effect of cellulose substrate properties on the populations of GUVs.	114

3.1.1	Properties of three cellulose filter papers and one cotton fabric	114
3.1.2	Size distributions of giant liposomes assembled on G41, G1, G42, and cotton fabric Effect of substrate properties on the assembly of GUVs	116
3.2	Lower porosity cellulose substrates produce high yields of GUVs...	119
3.2.1	Comparison of yields from G1, G41, G42 papers and a cotton fabric	119
3.2.2	Assembly of GUVs on hybrid cellulose-nanocellulose papers	120
3.2.3	Sizes and molar yields of GUVs produced from various nanohybrid papers	122
3.2.4	Losses of GUVs in pores of cellulose papers	123
3.3	Reusability of cotton fabric to assemble GUVs.....	125
4.	Effect of substrate properties on the assembly of GUVs.....	127
4.1	Properties of substrates tested.....	127
4.1.1	Tracing paper as potential substrate to assemble GUVs.....	127
4.1.2	Regenerated cellulose membranes and hydrophobic nanocellulose paper as potential substrates to assemble GUVs	129
4.1.3	Characterization of GUV buds on surfaces	131
4.2	Quantitative analysis of populations of GUVs from the selected substrates.....	135
4.2.1	Characterization of populations of GUVs using confocal microscopy based methods	135
4.2.2	Nanocellulose paper and tracing paper produce the highest counts of GUVs.....	137
4.2.3	Nanocellulose paper and tracing paper produce the highest molar yields of GUVs	140
4.3	Insights from the substrate molar yield data	144
4.3.1	Practical advantages of using tracing paper to assemble GUVs	144
4.3.2	GUV buds are attached through membrane connections on the surfaces	148
4.3.3	Assembly of GUV buds occurs through energetically favorable merging	149
4.3.4	Emergence of nanobuds is energetically favorable on substrates composed of nanoscale cylindrical fibers	152
5.	Optimization of assembly of GUVs in physiological conditions	158
5.1	Effect of incubation time on sizes and yields of GUVs.....	158
5.1.1	<i>In situ</i> characterization of bud dynamics reveals bud merging and bud growth	158
5.1.2	Stopped-time technique reveals size distributions broaden with increasing incubation time	162

5.1.3	Highest yields of GUVs reached within one hour for all substrates.....	166
5.1.4	Budding and merging process is diffusion-limited.....	170
5.2	A one-step modulation of the ionic strength results in high yields of GUVs in physiological salt solutions.....	173
5.2.1	Physiological concentrations of salts significantly lower the yields of GUVs from surface-assisted assembly techniques .	173
5.2.2	Assembly of GUVs from PEG-modified membranes and anionic membranes in physiological salts.....	176
5.2.3	Effect of salt concentration on the molar yields of GUVs.....	179
5.2.4	Novel one-step method to modulate the ionic strength of the solution.....	182
5.2.5	One-step modulation of salts experiments.....	186
5.2.6	One-step tracing paper methods to assemble GUVs are general.....	191
6.	Conclusion.....	194
7.	Bibliography.....	195

Appendix

1.	Introduction.....	209
2.	Materials and methods.....	209
2.1	Materials.....	209
2.2	Chemicals.....	209
2.3	Assembly of GUVs from gel-assisted methods.....	209
2.3.1	Fabrication of agarose-coated glass coverslips.....	209
2.3.2	Fabrication of polyvinyl alcohol (PVA) coated glass coverslips.....	210
2.3.3	Fabrication of dextran-tracing paper.....	210
2.3.4	Hydration of agarose-coated glass and PVA-coated glass substrates.....	210
2.4	Pre-hydration with sucrose to obtain GUVs in physiological salts ..	210
2.5	Quantification of immunoprecipitation reactions.....	211
2.5.1	Fabrication of microPADs.....	211
2.5.2	Fabrication of nanoPADs.....	211
2.5.3	Procedure for immunoprecipitation reaction.....	211
2.5.4	Procedure for turbidimetric control.....	211
2.5.5	Procedure for nanoPAD analysis.....	211
2.5.6	Characterization of paper devices.....	212
2.5.7	Pore size distribution analysis.....	212
3.	Effect of osmolytes on the formation of GUVs.....	213
3.1	Molar yield of GUVs obtained from gel-assisted methods in physiological salts.....	213

3.2	Effect of osmotic pressure gradients on the assembly of GUVs in physiological salts.....	214
3.3	Development of a pre-hydration method to assemble GUVs in physiological salts.....	217
4.	Novel uses of cellulosic materials for biosensing applications ...	220
4.1	Development of a clogging-based immunoassay	220
4.2	Semi-quantitative measurements of model immunoprecipitation reaction.....	224
4.3	Templating dense networks of lipid nanotubes with complex compositions on cellulose string.....	225
4.4	Inkjet printing lipids onto cellulose paper	227
5.	Raw code used to process confocal images and analyze GUVs..	229
5.1	Running all of the scripts at once using Run_All.m	229
5.2	Segmentation of GUVs using SegmentObjects.m.....	230
5.3	Selection of GUVs using SelectObjects.m	233
5.4	Visual checking of segmentation using GenerateMontageSegmented.m	236
5.5	Visual checking of selected GUVs using GeneratedMontageSelected.m	238
6.	Bibliography.....	240

List of tables

Table 1: Experimental methods used to obtain GUVs in this chapter.....	13
Table 2: Optical microscopy methods used to characterize GUVs	14
Table 3: Important spatial properties of the available objectives	36
Table 4: Practical limitations of imaging conditions	42
Table 5: Surface-assisted GUV formation methods in the literature.....	99
Table 6: Solvent-based GUV formation methods in literature	102
Table 7: Satisfying ANOVA assumptions.....	142
Table 8: Statistical significance of differences between molar yields of substrates.....	144
Table 9: Material costs of the substrates used to assemble GUVs.	145
Table 10: Parameters for budding and merging model.....	156
Table 11: Counts of red blood cell-sized GUVs.....	172
Table 12: Evaluation of albuminuria test in nanoPADs	224

List of figures

Figure 1: Classifications of liposomes.....	12
Figure 2: Different lipid structures produced from thin film rehydration	17
Figure 3: Appearance of GUVs in images.....	17
Figure 4: Diagram of widefield vs confocal microscope.....	19
Figure 5: Basics of light diffraction	20
Figure 6: Diffraction-limited resolution.....	21
Figure 7: Nyquist oversampling.....	22
Figure 8: Sections through the 3D point spread function	24
Figure 9: Effect of pinhole on the FWHM.....	24
Figure 10: Nonhomogeneous distribution of vesicles on the surface	29
Figure 11: Qualitative analysis of vesicles on the surface.....	30
Figure 12: Manual quantification of vesicle buds on the surface	31
Figure 13: Stratification of vesicles above the surface	31
Figure 14: Preparation of giant vesicles for imaging.....	32
Figure 15: Imaging of suspended vesicles with different pinhole characteristics	33
Figure 16: Effect of sedimentation time	35
Figure 17: Optical slice properties of images collected with different objectives.....	37
Figure 18: Effect of slice thickness on quantification of GUVs.....	38
Figure 19: Lateral dimensions of images collected with different objectives	40
Figure 20: Comparison between the diameters measured in the equatorial plane image and the open pinhole image	41
Figure 21: Effect of GUV size on pixel intensities.....	43
Figure 22: Intensity statistics of gold standard GUVs	44
Figure 23: Images of vesicles after sedimentation.....	45
Figure 24: Flowchart of the image analysis code	46
Figure 25: Steps to obtain watershed transformed image.....	47
Figure 26: Watershed transformation of grayscale images.....	48
Figure 27: Analysis of grayscale images using the Otsu method	50
Figure 28: Watershed segmentation of binary images.....	52
Figure 29: Accuracy of diameter measurements	54
Figure 30: Correction of oversegmentation errors to obtain final segmented image	56
Figure 31: Histograms of the coefficient of variations of objects with diameters consistent with the gold standard vesicles	57
Figure 32: Effect of GUV size on coefficient of variation of intensity histograms.....	58
Figure 33: Pixel properties of 5-6 μm diameter objects	58
Figure 34: Pixel properties of 18-19 μm diameter objects.....	59
Figure 35: Pixel properties of objects $> 30 \mu\text{m}$ in diameter.....	59
Figure 36: Histograms of the normalized mean intensity of objects with diameters consistent with the gold standard vesicles	60

Figure 37: Effect of size on mean intensity of GUVs.....	61
Figure 38: Pixel properties of 5-6 μm diameter GUVs.....	62
Figure 39: Pixel properties of 18-19 μm diameter GUVs.....	63
Figure 40: Pixel properties of GUVs > 30 μm in diameter.....	64
Figure 41: Heatscatter plot shows intensity characteristics of GUVs produced from a pooled nanocellulose paper sample	65
Figure 42: Heatscatter plot shows intensity characteristics of GUVs produced from a typical electroformation sample.....	66
Figure 43: Heatscatter plot shows intensity characteristics of GUVs produced from a typical gentle hydration sample	67
Figure 44: Heatscatter plot shows intensity characteristics of GUVs produced from an electroformation sample where the lipid dye is changed to TFPC	67
Figure 45: Image analysis code accurately selects GUVs from the different test samples	68
Figure 46: Histograms of the distribution of sizes of the GUVs	69
Figure 47: Confirmation of small vesicles.....	70
Figure 48: Effect of sedimentation time on vesicle counts.....	71
Figure 49: Small vesicles in bulk after sedimentation.....	72
Figure 50: Size distribution of 10 μm glass beads	73
Figure 51: Schematic showing an overview of the most common methods used to obtain GUVs	92
Figure 52: Paper-based method to form giant vesicles.....	93
Figure 53: Preparation of substrate.....	108
Figure 54: Hierarchical structure of cellulose.....	114
Figure 55: Microstructure of the cellulose filter papers and cotton fabric	116
Figure 56: GUV buds rest on the fibers of the cellulose paper.....	117
Figure 57: Characterization of populations of GUVs produced from the cellulose substrates.....	118
Figure 58: Yields of GUVs produced from the cellulose substrates	119
Figure 59: Effect of the density of nanocellulose on the assembly of GUVs at the surface	121
Figure 60: Sizes and yields of GUVs assembled on nanohybrid paper.....	122
Figure 61: Characterization of the penetration of lipid into the surface of the various nanohybrid papers.....	123
Figure 62: GUVs remain trapped in the pores of the G1 paper after harvesting.....	124
Figure 63: Cotton fabric supports the assembly of multiple cycles of GUVs	125
Figure 64: Characterization of nanocellulose and tracing paper	128
Figure 65: Characterization on the substrates and the assembled giant vesicle buds.....	130
Figure 66: Supergiant vesicles growing on nanocellulose paper and tracing paper	130
Figure 67: Characterization of the coverage of vesicle buds on the substrates	132
Figure 68: GUV bud coverage on each of the substrates.....	134
Figure 69: Axial distribution of GUVs on surface.....	135

Figure 70: Quantitative analysis of populations of GUVs.....	136
Figure 71: Images of the GUVs harvested from each of the different substrates.....	137
Figure 72: Size distributions of GUVs obtained from the surfaces tested.....	138
Figure 73: Counts and size statistics of GUVs obtained from the substrates tested.....	140
Figure 74: Molar yields of GUVs obtained from the substrates tested.....	142
Figure 75: Comparison of substrate costs.....	145
Figure 76: Characterization of the GUV populations obtained from the reused tracing paper surface.....	147
Figure 77: Scale-up of yields from tracing paper.....	147
Figure 78: GUV buds on the surface are connected.....	148
Figure 79: Appearance of harvested GUVs remains constant over course of 1 hour.....	150
Figure 80: Merging of buds on the surface of tracing paper.....	151
Figure 81: Change in energy associated with forming a spherical bud on the substrates.....	155
Figure 82: Overview of budding and merging model.....	157
Figure 83: Evolution of GUV buds during common surface-assisted hydration techniques.....	15
Figure 84: Decrease in the rate of bud merging at 60 minutes.....	160
Figure 85: Buds increase in size over the course of 60 minutes.....	161
Figure 86: Disappearance of buds over time.....	162
Figure 87: Larger vesicles appear more abundant at later stopping times.....	163
Figure 88: Effect of stopping time on the counts and size properties of the GUVs.....	165
Figure 89: Effect of stopping time on molar yield and coarsening of vesicles.....	169
Figure 90: Diffusion limited budding and merging model.....	171
Figure 91: Molar yields at longer incubation times.....	173
Figure 92: Suppression of formation of GUV buds in physiological concentrations of salts.....	174
Figure 93: Adhesion between zwitterionic GUV buds in 1× PBS.....	175
Figure 94: Significant decrease in molar yields of GUVs during formation in physiological salts.....	176
Figure 95: Adhesion between GUVs minimized using PEGylated lipid.....	178
Figure 96: Formation of GUVs from anionic membranes suppressed in physiological salt conditions.....	179
Figure 97: Effect of salts on molar yields.....	180
Figure 98: Effect of salts on size breakdown of molar yields.....	181
Figure 99: Effect of addition of salts above paper.....	182
Figure 100: One-step methods to modulate the solution ionic strength.....	183
Figure 101: Diffusion of salts through the nanopaper.....	184
Figure 102: Confirmation of sodium inside the GUVs.....	185
Figure 103: Sizes and counts of GUVs obtained from the one-step modulation of salts experiments.....	187

Figure 104: Molar yield of GUVs from one-step modulation of salt experiments.....	188
Figure 105: Molar yield of large GUVs.....	189
Figure 106: Budding and merging model in salts.....	190
Figure 107: One-step modulation of salts method using tracing paper allows for the assembly of GUVs composed from biologically relevant lipid compositions in physiological salts.....	191
Figure 108: Encapsulation of actin inside GUVs	192
Figure 109: Methods developed to assemble GUVs from tracing paper are general to a wide variety of conditions.....	193
Figure 110: Molar yields of GUVs obtained from surface-assisted methods decrease in physiological salts.....	214
Figure 111: Confocal images of GUV buds forming from various surfaces during hydration in physiological salts	215
Figure 112: Effect of osmotic pressure on molar yield of GUVs in physiological salt conditions.....	216
Figure 113: Schematic showing the effect of osmotic gradients	217
Figure 114: Schematic showing the pre-hydration methods used to obtain GUVs in physiological salts.....	218
Figure 115: Appearance of buds assembled from pre-hydration in physiological salts ..	219
Figure 116: Cellulose and nanocellulose paper	220
Figure 117: Development of nanohybrid paper	222
Figure 118: Characterization of nanohybrid paper using electron microscopy	223
Figure 119: Correspondence and ROC plots for albuminuria test.....	225
Figure 120: Phase separation in various lipid structures	226
Figure 121: Inkjet printing lipids onto nanopaper	228

Acknowledgements

Grants:

I would like to acknowledge grants that helped to contribute to the work in this dissertation from the National Science Foundation through NSF CAREER DMR-1848573, NSF CBET-1512686, NSF-CREST: Center for Cellular and Biomolecular Machines, at the University of California, Merced (NSF-HRD-1547848), and the Hellman Fellows Program. The data in this work was also collected, in part, with a confocal microscope acquired through the National Science Foundation MRI Award Number DMR- 1625733, and a scanning electron microscope acquired through NASA Grant NNX15AQ01A.

Funding awards:

I would like to acknowledge funding awards that allowed me to focus on the work in this dissertation including funds from the Graduate Dean's Dissertation Spring 2021 Fellowship, Bioengineering Summer 2020 Fellowship, Bioengineering Summer 2019 Fellowship, Bioengineering and Small-scale Technologies (BEST) Summer 2018 Fellowship, BEST Summer 2017 Fellowship, Merced Nanomaterials Center for Energy and Sensing (MACES) Spring 2017 Fellowship, MACES Fall 2016 Fellowship, and BEST Summer 2016 Fellowship.

Copyrighted material:

I would like to acknowledge the permission of the American Chemical Society (ACS) to reproduce figures from my publications in this dissertation.

Figures were reproduced with permission from Kresse, Kayleigh M.; Xu, Melissa; Pazzi, Joseph; Garcia-Ojeda, Marcos; Subramaniam, Anand B. Novel Application of Cellulose Paper As a Platform for the Macromolecular Self-Assembly of Biomimetic Giant Liposomes. *ACS Appl. Mater. Interfaces* 2016, 8 (47), 32102–32107. © 2016 American Chemical Society.

Figures were reproduced with permission from Pazzi, Joseph; Xu, Melissa; Subramaniam, Anand B. Size Distributions and Yields of Giant Vesicles Assembled on Cellulose Papers and Cotton Fabric. *Langmuir* 2018, 35 (24), 7798–7804. © 2018 American Chemical Society.

Figures were reproduced with permission from Pazzi, Joseph; Subramaniam, Anand B. Nanoscale Curvature Promotes High Yield Spontaneous Formation of Cell-Mimetic Giant Vesicles on Nanocellulose Paper. *ACS Appl. Mater. Interfaces* 2020, 12 (50), 56549–56561. © 2020 American Chemical Society.

Contributions:

Over the course of my Ph.D. studies and 6 years at the University of California, Merced I have received help from countless colleagues, friends, and family members who have provided significant contributions that have allowed me to reach this stage.

Firstly, I would like to acknowledge the contributions of my Ph.D. advisor, Professor Anand Bala Subramaniam, for the countless hours of guidance and for showing me how to conduct excellent scientific research. Thank you for inspiring me to be confident in myself and my ideas. Thank you for all of the intellectual contributions that you added to this dissertation including the conception of the molar yield, the budding and merging model, and the hypothesis for the one-step modulation of ionic strengths to obtain GUVs in physiological buffers.

I would like to acknowledge the contributions provided from my housemates. Adryan Paez thank you for always bringing a smile to my days and putting up with all of the late nights as your roommate when I would finally be getting back from the lab. It is hard believe how much we have grown. Henry Do thank you for all of the joy and energy you brought into my first year of graduate school. I enjoyed all of your knowledge and creativity and the time we spent both inside and outside of lab. Ameer Hashmi thank you for always looking out for me like an older brother, thank you for all of your insightful input in my rehearsals for research presentations, and thank you for those late night dinners you would share with me.

I would like to acknowledge contributions from my past cohort Theresea Stelter, Melissa Xu, and Kayleigh Kresse. Thank you for all of the time we spent together going between lab and classes. Theresea thank you for your continued support and friendship throughout my graduate studies. Melissa and Kayleigh thank you both for all of your contributions related to the development of the method to assemble vesicles from cellulose paper. Thank you all for being bright and dedicated lab partners, I was privileged to have spent time growing and learning to conduct scientific research with you. Thank you for all of your input on my research, and thank you for organizing all of those activity nights with the lab.

I would like to acknowledge contributions of my current cohort in the lab Alexander Li and Vaishnavi Girish. Alex thank you for always bringing your optimism and thoughtfulness to lab everyday. Thank you for all of the help related to the encapsulation of proteins into vesicles and all of your help on the confocal microscope. Vaish thank you for all of your curiosity and sharing your insightful hypotheses related to the assembly of vesicles, and thank you for the help related to obtaining high yields of anionic vesicles. To both of you, thank you for the countless times you have helped me with experiments, thank you for always listening to my research ideas and hypotheses, thank you for all of your input, and thank you for sharing all of those late night dinners and drives together. I am excited to see where our careers take us.

I would like to acknowledge contributions from my best friend Chistopher Aboujaoude. Thank you for the countless trips up to Merced. Thank you for the late night phone calls and total confidence that I would get through any rough patches that might

come my way during graduate school. Thank you for listening to all of the specifics of my research even when I would talk about the technical details and try to work ideas out of my head. Thank you for putting up with all the times I would still be working in my head while we were talking and most of all thank you for always being a brother to me.

I would like to acknowledge contributions from my Dad, Joe Pazzi, my Mom, Ann Pazzi, and my sister, Alyssa Pazzi. Dad thank you for sharing your undeniable work ethic. Mom thank you for sharing your curiosity and untapped passion for science. Thank you both for the courage you have shown to me everyday. Thank you both for your regular visits to the campus (with and without Chelsea). I will forever cherish the time we were able to spend together during these years. Alyssa thank you for the extra meals and for all of the visits to Merced. Thank you all for supporting me in my journey and the patience you have shown me over the last 6 years.

Above all, I would like to acknowledge the contributions from my wife Ana Paula Menezes Simões Pazzi. Ana, thank you for standing by me through the challenges of the last couple of years. Thank you for your unwavering support and for the endless patience you have had with me while I spend long hours working. Thank you for the late nights you have stayed up with me to help me through work. Thank you for your encouragement and your help with the completion of this dissertation, and thank you for helping me work ideas out of my head and for providing crucial feedback to keep me on track. You know the struggles I have faced better than anyone, and your love has gotten me through them. I owe you everything.

Joseph Edward Pazzi III

Education

- Ph.D.** **2021** Bioengineering, University of California, Merced. GPA: 3.83
Advisor: Anand Subramaniam, Ph.D.
- B.S.** **2014** Biomedical Engineering, University of California, Irvine.

Positions and Employment

- 06/2021 – 08/2021 *Lecturer*
Computing for Bioengineers (BIOE 021)
UC Merced
- 08/2015 – 08/2021 *Ph.D. Student*
Bioengineering, School of Engineering
UC Merced (Advisor: Anand Subramaniam, Ph.D.)
- 08/2014 – 08/2015 *Research Associate I*
Antigen Discovery Inc. | The Proteome Company
Irvine, CA
- 02/2014 – 10/2014 *Undergraduate Student Researcher*
Center for Functional Onco-Imaging, School of Engineering
UC Irvine (Advisor: Gultekin Gulsen, Ph.D.)

Awards and Honors

- Graduate Dean's Dissertation Spring 2021 Fellowship
- Bioengineering Summer 2020 Fellowship
- Bioengineering Summer 2019 Fellowship
- BEST Summer 2018 Fellowship
- BEST Summer 2017 Fellowship
- MACES Spring 2017 Fellowship
- MACES Fall 2016 Fellowship
- BEST Summer 2016 Fellowship

Peer Reviewed Publications

6. **Pazzi, J.**; Subramaniam, A.B. Nanoscale curvature promotes high yield spontaneous formation of cell-mimetic giant vesicles on nanocellulose paper. *ACS Applied Materials & Interfaces*. 12 (50), 56549-56561 (2020).
5. Girish, V.; **Pazzi, J.**; Li, A.; Subramaniam, A.B. Fabrics of diverse chemistry promote the formation of giant vesicles from phospholipids and amphiphilic block copolymers. *Langmuir* 35 (28), 9264-9273 (2019).
4. **Pazzi, J.**; Xu, M.; Subramaniam, A.B. Size distribution and yields of giant vesicles assembled on cellulose paper and cotton fabric. *Langmuir* 35 (24), 7798-7804 (2019).

Highlights: Cover article for Issue 24.

3. Li, A.*; **Pazzi, J.***; Xu, M.; Subramaniam A.B. Cellulose abetted assembly and temporally-decoupled loading of cargo into vesicles synthesized from functionally diverse lamellar phase forming amphiphiles. *Biomacromolecules*. 19, 849-859 (2018). (*equal contribution)
2. *Kresse, K.M.; * Xu, M.; **Pazzi, J.**; García-Ojeda; M.; Subramaniam, A.B. Novel Application of Cellulose Paper as a Platform for the Macromolecular Self-Assembly of Biomimetic Giant Liposomes. *ACS Applied Materials & Interfaces*. 8 (47), 32102-2107 (2016). (*equal contribution)

Highlights: Cover article for Issue 48 and highlighted in UC Merced Panorama News.

1. Silva, J. C.; Co, E.; Mccracken, C.; Usmani-brown, S.; Dwivedi, A.; Ifeonu, O. O.; Crabtree, J.; Gotia, H. T.; Virji, A. Z.; Reynes, C.; Colinge, J.; Kumar, V.; Lawres, L.; **Pazzi, J.**; Pablo, J. V; Hung, C.; Brancato, J.; Kumari, P.; Orvis, J.; Tretina, K.; Chibucos, M.; Ott, S.; Sadzewic, L.; Sengamalay, N.; Shetty, A. C.; Su, Q.; Tallon, L.; Fraser, C. M.; Frutos, R.; Molina, D. M.; Krause, P. J.; Mamoun, C. Ben. Genome-Wide Diversity and Gene Expression Profiling of Babesia Microti Isolates Identify Polymorphic Genes That Mediate Host-Pathogen Interactions. *Scientific Reports*. 6, 35284 (2016).

Intellectual Property

1. **Pazzi, J.**; Girish, V; Subramaniam, A.B. U.S. Application for International Patent. Vesicle-coated fibers and methods of making and using. 2021.

Presentations

1. **Pazzi, J;** Subramaniam, A.B. Nanoscale curvature of nanocellulose paper promotes high yield spontaneous formation of giant vesicles. *65th Annual Biophysical Society Meeting*. Virtual Symposia, February 22, 2021.
2. **Pazzi, J;** Subramaniam, A.B. Modulation of ionic strength to obtain high yields of cell-like giant vesicles in physiological conditions. *UC Merced Bioengineering Seminar Series*. Merced, CA, October 23, 2020.
3. **Pazzi, J;** Xu, M ;Subramaniam, A.B. High yield growth of GUVs assembled on cellulose paper and cotton fabrics. *20th UC Systemwide Bioengineering Symposium*. Merced, CA, June 27-29, 2019.
4. **Pazzi, J;** Xu, M; Subramaniam A.B. Sizes and yields of giant unilamellar vesicles on cellulose paper and cotton fabrics. *257th American Chemical Society Annual Meeting*. Orlando Fl. March 31-April4, 2019.
5. **Pazzi, J;** Xu, M ;Subramaniam, A.B. High yield growth of GUVs assembled on cellulose paper and cotton fabrics. *64th Biophysical Society Annual Meeting*. Baltimore, Md. February 15-19, 2019.
6. **Pazzi, J;** Xu, M.; Subramaniam, A.B. Using cellulose paper to assemble and load cargo into polymerosomes. *19th UC Systemwide Bioengineering Symposium*. Riverside, CA, June 21-24, 2018.
7. **Pazzi, J;** Xu, M.; Subramaniam, A.B. Formation of tethered lipid nanotubes on cellulose paper. *255th ACS National Meeting*. New Orleans, CA, March 18-22, 2018.
8. **Pazzi, J;** Xu, M.; Subramaniam, A.B. Label-free detection and quantification of specific proteins in complex biological fluids through clogging in cellulose paper. *253rd ACS National Meeting*. San Francisco, CA, April 2-6, 2017.

Teaching

1. **Computing for Bioengineers (BIOE 021)**
Lecturer (Summer 2021) – Designed 8 week introductory Python course adapting material from *A Primer on Scientific Programming with Python* textbook. Prepared and taught weekly 2 hour lectures, prepared and graded 12 lab assignments, 8 quizzes, and 1 final. Covered important Python concepts with an emphasis on bioengineering including basics of programming using Anaconda and Spyder, loops, lists, functions, modules, and dictionaries.

2. **Biotransport Phenomena (BIOE 104)**
Teaching assistant (Fall 2019 and Fall 2020) – Teaching assistant for 2, 1 hour undergraduate discussions and held 2 office hours per week that go over fundamental concepts important for quantifying mass transport in living systems.
3. **Electron Microscopy Lab (ENGR 170L/270L)**
Teaching assistant (Fall 2017) – Teaching assistant for 4, 4 hour undergraduate and graduate level lab sections on fundamental techniques and practical applications of using an electron microscope each week. Conducted sample preparations, ensured proper working conditions and experimental conditions of the microscope, prepared notes and questions, and graded lab reports before each week. Taught students necessary fundamentals as well as practical skills required to collect images of different sample types, such as hard metals or soft biological materials, using the electron microscope. Gained experience working with field emission SEM, Environmental SEM, Energy dispersive X-ray spectroscopy, and TEM imaging.
4. **Introduction to Materials Science (ENGR 45)**
Teaching assistant (Spring 2016) – Teaching assistant for 2, 4 hour lab undergraduate level sections where we covered topics including atomic bonding, crystal structure, material defects, thermodynamics, and kinetics related to materials at an introductory level.

Mentorship

- **Calvin Hu** – CCBM C-SIP fellow (Summer 2019). Studied chemical biology at UC Berkeley.
- **Kurtis Brent** – CCBM undergraduate fellow (Fall 2018 – Fall 2019). Studied bioengineering at UC Berkeley.
- **Jared Tse** – CCBM undergraduate fellow (Fall 2017 – Fall 2019). Studied bioengineering at UC Merced.
- **Maycy Lee** – ACS SEED Student (Summer 2018). Studied math at UC Merced.
- **Ramces Gonzalez** – MACES undergraduate fellow (Fall 2016 – Spring 2017). Studied Computer Engineering at UC Davis.
- **Jacob Orosco** – C-SIP Fellow (Summer 2017). Studied biomedical engineering at UC Irvine.
- **William Cheung** – Undergraduate student researcher (Fall 2016 – Spring 2017). Works as an engineer at The Wine Group.
- **Luis Garcia** – ACS SEED Student II (Summer 2016). Studied computer science at Cal Poly San Louis Obispo.

Outreach and Diversity

- **Cañada Community College** – Co-hosted tour of the Subramaniam lab for 15 students from Cañada College through the ASPIRES program. Specifically carried out an experiment with lipids and paper that demonstrated proper technique and typical lab equipment we use in a biomaterials lab such as fume hood, plasma cleaner, and confocal microscope (2019).
- **Livingston High School students** – Taught module to 30 Livingston High School students using an indigestion treatment Alka Seltzer tablet. The module taught the students the importance of surface area to volume ratio on the rate of a reaction by measuring the time it took for a whole tablet to dissolve versus a tablet that was broken into pieces. The module helped to increase interest in STEM research (2017).
- **El Capitan High School**– High school teacher Mr. Maril Soomalan spent one week in lab. Specifically I exposed him to my research, where he learned new potential uses of paper for bioengineering applications as well as basics of confocal microscopy, expectations of undergraduate and graduate research, and a paper-making experiment that he plans to implement in his science course (2017).
- **CCBM undergraduate fellowship students** – Led a tour of the Subramaniam lab for a group of 10 undergraduate CCBM summer fellowship students. The tour focused on teaching the students about characterization techniques available including two confocal microscopes and a field emission scanning electron microscope (2017).

Programming Languages

- **Python** – Was instructor of record for 1 undergraduate course that taught the basics of Python at UC Merced, Computing for Bioengineers (BIOE 021). Took 4 undergraduate courses on Python at UC Irvine including Introduction to Python (ICS 31), Software Libraries (ICS 32), Intermediate Programming (ICS 33), and Introduction to Computer Organization (ICS 51).
- **MATLAB** – Took 1 undergraduate course on MATLAB at UC Irvine and used MATLAB extensively during my Ph.D. developing novel image analysis technique (Publications 4, 6).
- **R** – Learned to use R programming language to collect and analyze large datasets while working at startup Antigen Discovery Inc.

Abstract

Title: A Comprehensive Characterization of Surface-Assembled Populations of Giant Liposomes using Novel Confocal Microscopy-based Methods

Name: Joseph Edward Pazzi III

Degree: Bioengineering

University/Year: University of California, Merced. 2021.

Committee Chair: Professor Wei-Chun Chin

Giant liposomes, or giant unilamellar vesicles (GUVs), are thin, semi-permeable, man-made compartments that often serve as models of the cell plasma membrane due to their sizes (1–100 μm) and molecular composition (composed of lipids). GUVs have proven useful for understanding a variety of different biophysical phenomena such as lipid membrane organization, membrane protein function, and cytoskeletal mechanics. A variety of different formation methods have been developed to try to optimize the populations of GUVs produced. However, information that allows for the direct comparison of the sizes and yields of the GUVs obtained from the different methods is lacking. In my dissertation, I describe my work on the development of a novel confocal microscopy-based technique that allows for the characterization of the populations of GUVs produced from the most commonly employed surface-assisted assembly methods. Through the development and standardization of careful protocols that allow for the quantification of $O(100,000)$ vesicles per sample, I characterize the surface-assembled populations of GUVs in comprehensive sets of experiments. From this work, I show novel discoveries including i) the use of nanocellulose paper as a surface to obtain GUVs, ii) the effect of substrate properties on the formation of GUVs, iii) the modulations of ionic strength technique to allow high yields of GUVs to be obtained using physiological salts, and iv) the effect of osmolytes on the formation of GUVs. The results from these quantitative experiments has led to the development of the budding and merging thermodynamic model which describes the mechanism of GUV formation. Overall, the discoveries pave the way for the large-scale production of GUVs for biophysical studies as well as towards more practical applications of GUVs such as for compartments for targeted drug delivery or synthetic cells.

Chapter 1: Introduction

1. Motivation and overview of this dissertation

1.1 Background on the plasma membrane of cells

Biological membranes serve a vital role as containers for all living organisms and have long been a fascinating subject of research¹⁻³. One of the most important biological membranes for living organisms, the plasma membrane of the cell, is a selectively permeable barrier that provides a protective encasing for all of the components inside the cell while also controlling complex tasks such as allowing the transport of important nutrients and signals in either direction across the membrane of the cell³. Solving the structure of the cell plasma membrane has been an intriguing problem ever since the initial discovery of cells in 1665 by Hooke⁴, and it was not until 1972 when Singer and Nicolson presented a fluid mosaic model¹, that a proposed structure of the plasma membrane was supported by conclusive data². Although detailed information on the organization of the cell plasma membrane is still lacking and new information is continually being discovered^{5,6}, the basic proposal of the fluid mosaic model, which states the cell membrane is formed from a collection of lipid and protein molecules that are constantly moving as fluids¹, is still relevant as a starting point for research today².

Lipid molecules are fundamental to the structure of the plasma membrane of cells⁷. Each lipid molecule is amphiphilic which means that one side of the lipid molecule is hydrophilic (prefers to be near water) and the other side is hydrophobic (prefers to be away from water)⁸. In aqueous environments, these amphiphilic lipid molecules will self-assemble and can form bilayer structures to ensure the hydrophobic portions of the lipid are not exposed to water⁹. These bilayer structures are composed of two leaflets of lipids where the hydrophobic parts of each leaflet are facing each other and are away from the water and the hydrophilic parts of each leaflet are facing outwards and are exposed to the water¹⁰. Lateral interactions within the leaflets are considered fluid as lipids are free to move through diffusion within their leaflet¹¹.

The composition of the cell plasma membrane is complex and is comprised of various different types of molecules¹². Even only considering lipids, more than 100 different species of lipids can be found present with different concentrations across the two leaflets of the bilayer membrane in natural plasma membranes¹². In eukaryotic cells to name a few, the outer leaflet is often composed of a higher amount of phosphatidylcholine (PC) and sphingomyelin (SM) lipids whereas the inner leaflet is often composed of a higher amount of phosphatidylserine (PS) and phosphatidylethanolamine (PE) lipids¹³. Along with lipids, a complex collection of other molecules can be contained within the lipid bilayer including cholesterol, glycolipids (lipids with sugars attached to them), and proteins¹⁴. Due to the complexity of the composition of the cell plasma membrane, advances in the understanding of the interactions and processes controlled by the membrane have typically relied on the use of more simple, man-made, model membrane systems where specific membrane-related phenomena can be controllably tested using less complex membrane compositions¹⁵⁻¹⁸.

1.2 Liposomes as model systems of the cell membrane

Model membranes are simplified systems that mimic the cell membrane and typically contain only a few molecular species so that specific interactions can be controllably probed^{19,20}. Commonly used model membrane systems include lipid monolayers²¹, solid-supported planar lipid bilayers²², and liposomes²³. Of these three systems, liposomes, which are spherical vesicles composed from a lipid bilayer²⁴, are of particular interest due their spherical shape, which mimics the basic compartmental properties of natural cell membranes²⁵, as well as the large range of sizes that can be obtained, with diameters ranging from around 20 nm up to 100 μm ²⁶. Liposomes can be classified into a variety of different categories that are based on their size and their lamellarity (number of lipid bilayers they contain)²⁶. For use as model systems of the plasma membrane of the cell, liposomes that are both unilamellar (a single bilayer) and that have diameters greater than 1 μm , are of particular interest since they mimic both the size and basic structural properties of the plasma membrane²⁶. These liposomes are termed giant unilamellar vesicles (GUVs) and have proven to be extremely useful for experimental interrogation²⁷⁻²⁹ and are the primary focus of the research conducted in this dissertation. Their large sizes allow for the straightforward probing of membrane properties through optical and fluorescence microscopy³⁰⁻³², that has lead to important discoveries such as membrane phase separation³³⁻³⁶, membrane protein function³⁷⁻⁴⁴, membrane protein interactions⁴⁵⁻⁴⁷, membrane fusion⁴⁸⁻⁵³, cytoskeletal mechanics⁵⁴, and membrane transport^{55,56}. Advances in the understanding of the properties of the cell membrane may also lead to the improvement of the design of GUVs for use in practical applications such as drug delivery⁵⁷⁻⁶² and synthetic cells⁶³⁻⁷⁰.

1.3 Overview of work completed in this dissertation

Although GUVs have proven to be instrumental models of the cell membrane, the most common methods used to assemble GUVs in the field are still limited^{26,27,71}. These limitations, which include issues such as low yields of GUVs in physiological salt conditions⁷² or the inefficient protein reconstitution inside GUVs⁷³, are exacerbated due to the lack of quantitative data that is available on the populations of GUVs that can be obtained from the different assembly methods⁷⁴. This lack of quantitative data makes it difficult to rationally optimize methods, or even develop new methods, that can begin to address the current limitations associated with the assembly of GUVs in the field.

In Chapter 2 of this dissertation, I develop novel confocal microscopy-based methods that enable for the first time quantitative data to be obtained from populations of GUVs assembled using the most common methods. The chapter includes a review of the previous methods used to characterize populations of GUVs, a review of the physics and optics of confocal microscopy, and a description of the methods used to obtain the GUVs for the confocal microscopy experiments. In the remaining sections, I include the experiments conducted to both standardize the assembly of GUVs across different techniques as well as to optimize the imaging of the GUVs using the confocal microscope. I conclude by reporting the development of an automated image analysis routine that allows for the rapid quantification of $O(100,000)$ vesicles from each population of GUVs. The work I conduct in this chapter has resulted in my contributions in 2 publications^{75,76}.

In Chapter 3, I begin with a review of the most commonly used methods to obtain GUVs and describe a newly developed concept termed the molar yield⁷⁷, that allows fair comparisons of the populations of GUVs obtained between the techniques. Using the novel confocal microscopy-based methods developed in Chapter 2, I conduct a comprehensive series of experiments that provide crucial quantitative data on the populations of GUVs assembled through the most commonly used techniques. The results of the data lead to a wealth of information including highlights such as the novel discovery of the use of surfaces composed of nanoscale cylindrical fibers to assemble high yields of GUVs and the development of a one-step method that uses the commercially available cellulose surface, tracing paper, to overcome current challenges associated with obtaining high yields of GUVs in physiological salt conditions. The work I conduct in this chapter has resulted in my contribution in 3 publications⁷⁷⁻⁷⁹.

Lastly, in the appendix I include additional experiments related to the effect of osmolytes on the assembly of GUVs as well as experiments that demonstrate novel uses of cellulose materials for prospective biosensing applications.

2. Bibliography

- (1) Singer, S. J. J.; Nicolson, G. L. L. The Fluid Mosaic Model of the Structure of Cell Membranes. *Science* (80). **1972**, *175* (4023), 720–731. <https://doi.org/10.1126/science.175.4023.720>.
- (2) Nicolson, G. L. The Fluid - Mosaic Model of Membrane Structure: Still Relevant to Understanding the Structure, Function and Dynamics of Biological Membranes after More than 40 Years. *Biochim. Biophys. Acta - Biomembr.* **2014**, *1838* (6), 1451–1466. <https://doi.org/10.1016/j.bbamem.2013.10.019>.
- (3) Lombard, J. Once upon a Time the Cell Membranes: 175 Years of Cell Boundary Research. *Biol. Direct* **2014**, *9* (1), 1–35. <https://doi.org/10.1186/s13062-014-0032-7>.
- (4) Xu, C.; Hu, S.; Chen, X. Artificial Cells: From Basic Science to Applications. *Mater. Today* **2016**, *19* (9), 516–532. <https://doi.org/10.1016/j.mattod.2016.02.020>.
- (5) Munro, S. Lipid Rafts: Elusive or Illusive? *Cell* **2003**, *115* (4), 377–388. [https://doi.org/10.1016/S0092-8674\(03\)00882-1](https://doi.org/10.1016/S0092-8674(03)00882-1).
- (6) Engelman, D. M. Membranes Are More Mosaic than Fluid. *Nature* **2005**, *438* (7068), 578–580. <https://doi.org/10.1038/nature04394>.
- (7) Vance, D.E.; Vance, J. E. *Biochemistry of Lipids; Lipoproteins; and Membranes*; Elsevier B.V., 2008.
- (8) Seifert, U. *Configurations of Fluid Membranes and Vesicles*; 1997; Vol. 46. <https://doi.org/10.1080/00018739700101488>.
- (9) Israelachvili, J. N.; Mitchell, D. J.; Ninham, B. W. Theory of Self-Assembly of Lipid Bilayers and Vesicles. *BBA - Biomembr.* **1977**, *470* (2), 185–201. [https://doi.org/10.1016/0005-2736\(77\)90099-2](https://doi.org/10.1016/0005-2736(77)90099-2).
- (10) Nagle, J. F.; Tristram-Nagle, S. Structure of Lipid Bilayers. *Biochim. Biophys. Acta.* **2000**, *1469*.
- (11) Macháň, R.; Hof, M. Lipid Diffusion in Planar Membranes Investigated by Fluorescence Correlation Spectroscopy. *Biochim. Biophys. Acta - Biomembr.* **2010**, *1798* (7), 1377–1391. <https://doi.org/10.1016/j.bbamem.2010.02.014>.
- (12) Simons, K.; Gerl, M. J. Revitalizing Membrane Rafts: New Tools and Insights. *Nat. Rev. Mol. Cell Biol.* **2010**, *11* (10), 688–699. <https://doi.org/10.1038/nrm2977>.
- (13) Ikeda, M.; Kihara, A.; Igarashi, Y. Lipid Asymmetry of the Eukaryotic Plasma Membrane: Functions and Related Enzymes. *Biol. Pharm. Bull.* **2006**, *29* (8), 1542–1546. <https://doi.org/10.1248/bpb.29.1542>.
- (14) Galbiati, F.; Razani, B.; Lisanti, M. P. Emerging Themes in Lipid Rafts and

- Caveolae. *Cell* **2001**, *106*, 403–411. [https://doi.org/10.1016/S0092-8674\(01\)00472](https://doi.org/10.1016/S0092-8674(01)00472).
- (15) Ottova-Leitmannova, A.; Ti Tien, H. Bilayer Lipid Membranes: An Experimental System for Biomolecular Electronic Devices Development. *Prog. Surf. Sci.* **1992**, *41* (4), 337–445. [https://doi.org/10.1016/0079-6816\(92\)90012-7](https://doi.org/10.1016/0079-6816(92)90012-7).
- (16) Kam, L. C. Capturing the Nanoscale Complexity of Cellular Membranes in Supported Lipid Bilayers. *J. Struct. Biol.* **2009**, *168* (1), 3–10. <https://doi.org/10.1016/j.jsb.2009.05.006>.
- (17) Castellana, E.; Cremer, P. Solid Supported Lipid Bilayers: From Biophysical Studies to Sensor Design. *Surf. Sci. Rep.* **2006**, *61* (10), 429–444. <https://doi.org/10.1016/j.surfrep.2006.06.001>.
- (18) Dimova, R.; Aranda, S.; Bezlyepkina, N.; Nikolov, V.; Riske, K. a; Lipowsky, R. A Practical Guide to Giant Vesicles. Probing the Membrane Nanoregime via Optical Microscopy. *J. Phys. Condens. Matter* **2006**, *18* (28), S1151–S1176. <https://doi.org/10.1088/0953-8984/18/28/S04>.
- (19) Shen, H. H.; Lithgow, T.; Martin, L. L. Reconstitution of Membrane Proteins into Model Membranes: Seeking Better Ways to Retain Protein Activities. *Int. J. Mol. Sci.* **2013**, *14* (1), 1589–1607. <https://doi.org/10.3390/ijms14011589>.
- (20) Eeman, M.; Deleu, M. From Biological Membranes to Biomimetic Model Membranes. *Biotechnol. Agron. Soc. Environ.* **2010**, *14* (4), 719–736.
- (21) Kühner, M.; Tampé, R.; Sackmann, E. Lipid Mono- and Bilayer Supported on Polymer Films: Composite Polymer-Lipid Films on Solid Substrates. *Biophys. J.* **1994**, *67* (1), 217–226. [https://doi.org/10.1016/S0006-3495\(94\)80472-2](https://doi.org/10.1016/S0006-3495(94)80472-2).
- (22) Domanov, Y. Supported Lipid Bilayers. *Biointerphases* **2008**, *3*, FA108-FA116. <https://doi.org/10.1116/1.2948313>.
- (23) Saliba, A.-E.; Vonkova, I.; Gavin, A.-C. The Systematic Analysis of Protein–Lipid Interactions Comes of Age. *Nat. Rev. Mol. Cell Biol.* **2015**, *16* (12), 753–761. <https://doi.org/10.1038/nrm4080>.
- (24) Woodle, M. C.; Papahadjopoulos, D. Liposome Preparation and Size Characterization. *Methods Enzymol.* **1989**, *171* (C), 193–217. [https://doi.org/10.1016/S0076-6879\(89\)71012-0](https://doi.org/10.1016/S0076-6879(89)71012-0).
- (25) Sercombe, L.; Veerati, T.; Moheimani, F.; Wu, S. Y.; Sood, A. K.; Hua, S. Advances and Challenges of Liposome Assisted Drug Delivery. *Front. Pharmacol.* **2015**, *6* (DEC), 1–13. <https://doi.org/10.3389/fphar.2015.00286>.
- (26) Has, C.; Sunthar, P. A Comprehensive Review on Recent Preparation Techniques of Liposomes A Comprehensive Review on Recent Preparation Techniques of Liposomes. *J. Liposome Res.* **2019**, *0* (0), 1–30. <https://doi.org/10.1080/08982104.2019.1668010>.

- (27) Wesolowska, O.; Michalak, K.; Maniewska, J.; Hendrich, A. B. Giant Unilamellar Vesicles - a Perfect Tool to Visualize Phase Separation and Lipid Rafts in Model Systems. *Acta Biochim. Pol.* **2009**, *56* (1), 33–39. <https://doi.org/20091772>.
- (28) Morales-pennington, N. F.; Wu, J.; Farkas, E. R.; Lin, S.; Konyakhina, T. M.; Zheng, J. Y.; Webb, W. W.; Feigenson, G. W. Biochimica et Biophysica Acta GUV Preparation and Imaging : Minimizing Artifacts. *BBA - Biomembr.* **2010**, *1798* (7), 1324–1332. <https://doi.org/10.1016/j.bbamem.2010.03.011>.
- (29) Collins, M. D.; Gordon, S. E. Giant Liposome Preparation for Imaging and Patch-Clamp Electrophysiology. *J. Vis. Exp.* **2013**, No. 76, 1–9. <https://doi.org/10.3791/50227>.
- (30) Paper, O. Fluorescent Quantification of Size and Lamellarity of Membrane Nanotubes. *Eur. Biophys. J.* **2014**, 595–602. <https://doi.org/10.1007/s00249-014-0989-2>.
- (31) Bagatolli, L. A.; Parasassi, T.; Gratton, E. Giant Phospholipid Vesicles: Comparison among the Whole Lipid Sample Characteristics Using Different Preparation Methods - A Two Photon Fluorescence Microscopy Study. *Chem. Phys. Lipids* **2000**, *105* (2), 135–147. [https://doi.org/10.1016/S0009-3084\(00\)00118-3](https://doi.org/10.1016/S0009-3084(00)00118-3).
- (32) Baumgart, T.; Hunt, G.; Farkas, E. R.; Webb, W. W.; Feigenson, G. W. Fluorescence Probe Partitioning between Lo/Ld Phases in Lipid Membranes. *Biochim. Biophys. Acta - Biomembr.* **2007**, *1768* (9), 2182–2194. <https://doi.org/10.1016/j.bbamem.2007.05.012>.
- (33) The, C.; Rittig, M.; Meda-, D.; Pozzi, G.; Amigorena, S.; Ricciardi-, P. Characterization of Lipid Bilayer Phases by Confocal Microscopy. *Proc. of Nat. Aca. USA.* **1999**, *96* (13), 7563–7568.
- (34) Marsh, D. Cholesterol-Induced Fluid Membrane Domains: A Compendium of Lipid-Raft Ternary Phase Diagrams. *Biochim. Biophys. Acta - Biomembr.* **2009**, *1788* (10), 2114–2123. <https://doi.org/10.1016/j.bbamem.2009.08.004>.
- (35) Dietrich, C.; Bagatolli, L. a; Volovyk, Z. N.; Thompson, N. L.; Levi, M.; Jacobson, K.; Gratton, E. Lipid Rafts Reconstituted in Model Membranes. *Biophys. J.* **2001**, *80* (3), 1417–1428. [https://doi.org/10.1016/S0006-3495\(01\)76114-0](https://doi.org/10.1016/S0006-3495(01)76114-0).
- (36) Veatch, S. L.; Keller, S. L. Separation of Liquid Phases in Giant Vesicles of Ternary Mixtures of Phospholipids and Cholesterol. *Biophys. J.* **2003**, *85* (5), 3074–3083. [https://doi.org/10.1016/S0006-3495\(03\)74726-2](https://doi.org/10.1016/S0006-3495(03)74726-2).
- (37) Goldenberg, N. M.; Steinberg, B. E. Surface Charge : A Key Determinant of Protein Localization and Function. *Cancer Res.* **2010**, No. 10, 1277–1281. <https://doi.org/10.1158/0008-5472.CAN-09-2905>.
- (38) Gutierrez, M. G.; Jalali-yazdi, F.; Peruzzi, J.; Riche, C. T.; Roberts, R. W.;

- Malmstadt, N. G Protein-Coupled Receptors Incorporated into Rehydrated Diblock Copolymer Vesicles Retain Functionality. *Small*. **2016**, No. 38, 5256–5260. <https://doi.org/10.1002/smll.201601540>.
- (39) Geertsma, E. R.; Mahmood, N. A. B. N.; Schuurman-wolters, G. K.; Poolman, B. Membrane Reconstitution of ABC Transporters and Assays of Translocator Function. *Nature Protocols*. **2008**, 3, 256–266.
- (40) Horger, K. S.; Liu, H.; Rao, D. K.; Shukla, S.; Sept, D.; Ambudkar, S. V.; Mayer, M. Hydrogel-Assisted Functional Reconstitution of Human P-Glycoprotein (ABCB1) in Giant Liposomes. *Biochim. Biophys. Acta - Biomembr.* **2015**, 1848 (2), 643–653. <https://doi.org/10.1016/j.bbmem.2014.10.023>.
- (41) Hovijitra, N. T.; Wu, J. J.; Peaker, B.; Swartz, J. R. Cell-Free Synthesis of Functional Aquaporin Z in Synthetic Liposomes. *Biotechnol Bioeng* **2009**, 104 (1), 40–49. <https://doi.org/10.1002/bit.22385>.
- (42) Gutierrez, M. G.; Mansfield, K. S.; Malmstadt, N. The Functional Activity of the Human Serotonin 5-HT1A Receptor Is Controlled by Lipid Bilayer Composition. *Biophys. J.* **2016**, 110 (11), 2486–2495. <https://doi.org/10.1016/j.bpj.2016.04.042>.
- (43) Quemeneur, F.; Sigurdsson, J. K.; Renner, M.; Atzberger, P. J.; Bassereau, P. Shape Matters in Protein Mobility within Membranes. *Proc. Natl. Acad. Sci. USA*. **2014**, Apr 8; 111(14):5083-7. <https://doi.org/10.1073/pnas.1321054111>.
- (44) Salafsky, J.; Groves, J. T.; Boxer, S. G. Architecture and Function of Membrane Proteins in Planar-Supported Bilayers: A Study with Photosynthetic Reaction Centers. *Biochemistry* **1996**, 35 (96), 14773–14781. <https://doi.org/10.1021/bi961432i>.
- (45) Louise, I.; Gerdi, J.; Kemmer, C.; Günther, T. Membrane Protein Reconstitution into Giant Unilamellar Vesicles : A Review on Current Techniques. *Eur. Biophys. J.* **2016**, Mar;46(2):103-119. <https://doi.org/10.1007/s00249-016-1155-9>.
- (46) Hansen, J. S.; Thompson, J. R.; Hélix-Nielsen, C.; Malmstadt, N. Lipid Directed Intrinsic Membrane Protein Segregation. *J. Am. Chem. Soc.* **2013**, 135 (46), 17294–17297. <https://doi.org/10.1021/ja409708e>.
- (47) Shaklee, P. M.; Semrau, S.; Malkus, M.; Kubick, S.; Dogterom, M. Protein Incorporation in Giant Lipid Vesicles under Physiological Conditions. *Eur. Chem.* **2010**, 175–179. <https://doi.org/10.1002/cbic.200900669>.
- (48) Zan, G. H.; Tan, C.; Deserno, M.; Lanni, F.; Lösche, M. Hemifusion of Giant Unilamellar Vesicles with Planar Hydrophobic Surfaces: A Fluorescence Microscopy Study. *Soft Matter* **2012**, 8 (42), 10877. <https://doi.org/10.1039/c2sm25702e>.
- (49) Kalb, E.; Frey, S.; Tamm, L. K. Formation of Supported Planar Bilayers by Fusion of Vesicles to Supported Phospholipid Monolayers. *Biochim. Biophys. Acta - Biomembr.* **1992**, 1103 (2), 307–316. <https://doi.org/10.1016/0005->

2736(92)90101-Q.

- (50) Micheletto, Y. M. S.; Marques, C. M.; Silveira, N. P. Da; Schroder, A. P. Electroformation of Giant Unilamellar Vesicles: Investigating Vesicle Fusion versus Bulge Merging. *Langmuir* **2016**, *32* (32), 8123–8130. <https://doi.org/10.1021/acs.langmuir.6b01679>.
- (51) Nussbaum, O.; Rott, R.; Loyter, A. Fusion of Influenza Virus Particles with Liposomes : Requirement for Cholesterol and Virus Receptors to Allow Fusion with and Lysis of Neutral but Not of Negatively Charged Liposomes. *J. Gen Virol.* **2018**, No. 1992, 2831–2837.
- (52) Estes, D. J.; Lopez, S. R.; Fuller, A. O.; Mayer, M. Triggering and Visualizing the Aggregation and Fusion of Lipid Membranes in Microfluidic Chambers. *Biophys. J.* **2006**, *91* (July), 233–243. <https://doi.org/10.1529/biophysj.105.076398>.
- (53) Terasawa, H.; Nishimura, K.; Suzuki, H.; Matsuura, T.; Yomo, T. Coupling of the Fusion and Budding of Giant Phospholipid Vesicles Containing Macromolecules. *Proc. Natl. Acad. Sci. U. S. A.* April 17, 2012 *109* (16) 5942–5947.
- (54) Tsai, F. C.; Stuhmann, B.; Koenderink, G. H. Encapsulation of Active Cytoskeletal Protein Networks in Cell-Sized Liposomes. *Langmuir* **2011**, *27* (16), 10061–10071. <https://doi.org/10.1021/la201604z>.
- (55) Muraoka, T.; Umetsu, K.; Tabata, K. V.; Hamada, T.; Noji, H. .; Yamashita, T.; Kinbara, K. Mechano-Sensitive Synthetic Ion Channels. *J. Am. Chem. Soc.* **2017**, No. 139, 18016–18023.
- (56) Garten, M.; Mosgaard, L. D.; Bassereau, P.; Toombes, G. E. S. . Whole-GUV Patch Clamping. *Proc. Natl. Acad. Sci. U. S. A.* **2017**, No. 114, 328–333.
- (57) Vemuri, S.; Rhodes, C. T. Preparation and Characterization of Liposomes as Therapeutic Systems : A Review. *Pharm. Acta. Helv.* **1995**, *70*, 95–111.
- (58) Dm, P.; Rh, J.; Cn, P. Ufasomes : A Vesicular Drug Delivery. *Sys. Rev. Pharm.* **2011**, *2* (2), 72–78. <https://doi.org/10.4103/0975-8453.86290>.
- (59) Čejková, J.; Štěpánek, F. Compartmentalized and Internally Structured Particles for Drug Delivery - A Review. *Curr. Pharm. Des.* **2013**, *19* (35), 6298–6314. <https://doi.org/10.2174/1381612811319350007>.
- (60) Mantripragada, S. Sustained Release Drug Delivery. *Pharmaceutics.* **2002**, *41*, 392–406.
- (61) Jullient, L.; Megliot, J. D. I. Drug Delivery : Piercing Vesicles by Their Adsorption Onto a Porous Medium. *Proceedings of the National Academy of Sciences of the United States of America.* **2018**, *92* (21), 9590–9592.
- (62) Republic, C. Compartmentalized and Internally Structured Particles for Drug Delivery - A Review. *Curr. Pharm. Des.* **2013**, 6298–6314.

- (63) Long, M. S.; Jones, C. D.; Helfrich, M. R.; Mangeney-Slavin, L. K.; Keating, C. D. Dynamic Microcompartmentation in Synthetic Cells. *Proc. Natl. Acad. Sci.* **2005**, *102* (17), 5920–5925. <https://doi.org/10.1073/pnas.0409333102>.
- (64) Weiss, M.; Frohnmayer, J. P.; Benk, L. T.; Haller, B.; Janiesch, J.; Heitkamp, T.; Börsch, M.; Lira, R. B.; Dimova, R.; Lipowsky, R.; Bodenschatz, E.; Baret, J.; Vidakovic-koch, T.; Sundmacher, K.; Platzman, I.; Spatz, J. P. Sequential Bottom-up Assembly of Mechanically Stabilized Synthetic Cells by Microfluidics. *Nature Mat.* **2018**, *17* (January). <https://doi.org/10.1038/NMAT5005>.
- (65) Hest, J. C. M. Van. Synthetic Cells and Organelles : Compartmentalization Strategies. *Bioessays.* **2009**, 1299–1308. <https://doi.org/10.1002/bies.200900106>.
- (66) Blain, J. C.; Szostak, J. W. Progress Toward Synthetic Cells. *Annu. Rev. Biochem.* **2014**, *83* (1), 615–640. <https://doi.org/10.1146/annurev-biochem-080411-124036>.
- (67) Maeda, Y. T.; Nakadai, T.; Shin, J.; Uryu, K.; Noireaux, V.; Libchaber, A. Assembly of MreB Filaments on Liposome Membranes: A Synthetic Biology Approach. *ACS Synth. Biol.* **2012**, *1* (2), 53–59. <https://doi.org/10.1021/sb200003v>.
- (68) York-Duran, M. J.; Godoy-Gallardo, M.; Labay, C.; Urquhart, A. J.; Andresen, T. L.; Hosta-Rigau, L. Recent Advances in Compartmentalized Synthetic Architectures as Drug Carriers, Cell Mimics and Artificial Organelles. *Colloids Surfaces B Biointerfaces* **2017**, *152*, 199–213.
- (69) Göpflich, K.; Platzman, I.; Spatz, J. P. Mastering Complexity : Towards Bottom-up Construction of Multifunctional Eukaryotic Synthetic Cells. *Trends Biotechnol.* **2018**, 1–14. <https://doi.org/10.1016/j.tibtech.2018.03.008>.
- (70) Walde, P. Building Artificial Cells and Protocell Models: Experimental Approaches with Lipid Vesicles. *BioEssays* **2010**, *32* (4), 296–303. <https://doi.org/10.1002/bies.200900141>.
- (71) Stein, H.; Spindler, S.; Bonakdar, N.; Wang, C.; Sandoghdar, V. Production of Isolated Giant Unilamellar Vesicles under High Salt Concentrations. *Front. Physiol.* **2017**, *8* (FEB), 1–16. <https://doi.org/10.3389/fphys.2017.00063>.
- (72) Stein, H.; Spindler, S.; Bonakdar, N.; Wang, C. Production of Isolated Giant Unilamellar Vesicles under High Salt Concentrations. *Front. Physiol.* **2017**, *8* (February), 1–16. <https://doi.org/10.3389/fphys.2017.00063>.
- (73) Litschel, T.; Schwille, P. Protein Reconstitution Inside Giant Unilamellar Vesicles. *Annu. Rev. Biophys.* **2021**, *50*, 525–548. <https://doi.org/10.1146/annurev-biophys-100620-114132>.
- (74) Has, C.; Sunthar, P. A Comprehensive Review on Recent Preparation Techniques of Liposomes. *J. Liposome Res.* **2019**, No. 0, 1–30. <https://doi.org/10.1080/08982104.2019.1668010>.

- (75) Kresse, Kayleigh M.; Xu, Melissa; Pazzi, Joseph; Garcia-Ojeda, Marcos; Subramaniam, Anand B. Novel Application of Cellulose Paper As a Platform for the Macromolecular Self-Assembly of Biomimetic Giant Liposomes. *ACS Appl. Mater. Int.* **2016**, 8 (47), 32102–32107..
- (76) Li, A*.; Pazzi, J*.; Xu, M.; Subramaniam, A. B. Cellulose Abetted Assembly and Temporally-Decoupled Loading of Cargo into Vesicles Synthesized from Functionally Diverse Lamellar Phase Forming Amphiphiles. *Biomacromolecules* **2018**, 19, 3, 849–859. *equal contribution
- (77) Pazzi, J.; Subramaniam, A. B. Nanoscale Curvature Promotes High Yield Spontaneous Formation of Cell-Mimetic Giant Vesicles on Nanocellulose Paper. *ACS Appl. Mater. Interfaces* **2020**, 12 (50), 56549–56561. <https://doi.org/10.1021/acsami.0c14485>.
- (78) Pazzi, J.; Xu, M.; Subramaniam, A. B. Size Distributions and Yields of Giant Vesicles Assembled on Cellulose Papers and Cotton Fabric. *Langmuir* **2018**, 35 (24), 7798–7804. <https://doi.org/10.1021/acs.langmuir.8b03076>.
- (79) Girish, V.; Pazzi, J.; Li, A.; Subramaniam, A. B. Fabrics of Diverse Chemistries Promote the Formation of Giant Vesicles from Phospholipids and Amphiphilic Block Copolymers. *Langmuir* **2019**, 35, 9264–9273. <https://doi.org/10.1021/acs.langmuir.9b01621>.

Chapter 2 : Confocal Microscopy Based Method for the Quantification of Populations of Giant Liposomes

1. Introduction

Biological membranes serve a vital role as boundaries for all living organisms and have long been a fascinating subject of research¹⁻³. Due to their complexity, advances in the understanding of biological membranes have typically relied on the use of more simple, man-made, model membrane systems where specific membrane-related phenomena can be controllably tested⁴⁻⁸. Liposomes, which are one of the most commonly employed model membranes systems, are man-made spherical vesicles (sacs) bounded by at least one lipid bilayer⁹. In contrast to the complex composition of biological membranes which often contain a variety of different lipids^{2,10-18}, proteins^{12,16,19-25}, and compartmentalized substructures²⁶⁻³⁰, liposomes are commonly prepared from only a few types of membrane molecules^{5,31-36} and encapsulant molecules³⁷⁻⁴³ (though more complex liposomal systems can be obtained if desired⁴⁴⁻⁴⁷) which allows for the fabrication of membrane systems with more simple and predictable behavior^{2,13,48,49}. Since interactions within biological systems are complex, liposomes are particularly useful for experimental studies on membrane interactions in model membrane systems where experimental variables can be tested one at a time^{13,48,50-55} as well as for practical applications as simple compartments in drug delivery systems with reproducible properties⁵⁵⁻⁶⁴.

Overall, liposomes can be categorized into two main groups i) based on their lamellarity (number of bilayers) and ii) based on their size^{5,65,66}. Figure 1 shows a schematical representation of the different lamellarity classifications of liposomes including i) unilamellar vesicles, which contain only a single lipid bilayer, ii) multilamellar vesicles, which contain 2 or more bilayers, and iii) multivesicular vesicles, which contain at least one other concentric vesicle within a larger vesicle. Amongst the lamellarity classifications, the unilamellar liposome structures occupy a majority of the focus of liposome preparation protocols due to their usefulness as models for various membrane studies such as phase separation⁶⁷⁻⁷¹, membrane fusion⁷²⁻⁷⁷, protein function⁷⁸⁻⁸⁵ and as compartments for use in practical applications such as drug delivery^{65,86-90} and synthetic cells^{27,44,46,91-96}. Unilamellar liposomes can be further classified into three groups based on their size including i) small unilamellar vesicles (SUVs) which range from 20 – 100 nm in diameter, ii) large unilamellar vesicles (LUVs) which range from 100 – 1000 nm diameter, and iii) giant unilamellar vesicles (GUVs) which range from 1 – 200 μm in diameter (Figure 1). Of these three size groupings, GUVs are of particular interest for research on biological membranes⁵ due to their size and compositional resemblance to the membranes of mammalian cells ($\sim 5 - 100 \mu\text{m}$)⁹⁷⁻¹⁰⁰, plant cells ($\sim 10 - 100 \mu\text{m}$), bacteria cells ($\sim 1 - 5 \mu\text{m}$)^{101,102} and other cell organelles with membranes such as the cell nucleus ($\sim 6 \mu\text{m}$)¹⁰³ and mitochondria ($\sim 2 \mu\text{m}$)¹⁰³.

Due to their larger sizes ($> 1 \mu\text{m}$) the interrogation of GUVs is relatively straightforward using optical techniques such as light¹⁰⁴, fluorescence¹⁰⁵, or confocal

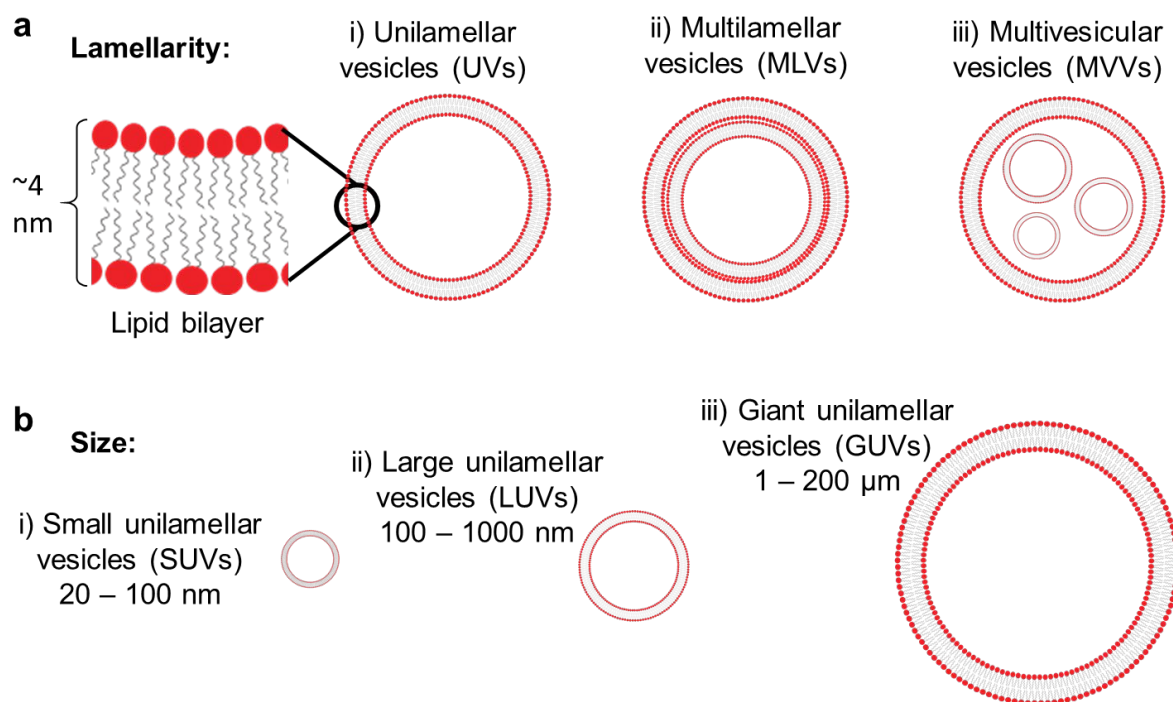


Figure 1: Classifications of liposomes. Schematical representation of lipid vesicles (liposomes) with **a** different lamellarities including i) unilamellar vesicles (UVs), ii) multilamellar vesicles (MLVs) and multivesicular vesicles (MVVs). The typical structure of a lipid bilayer is shown to the left with the lipid molecules, composed of a hydrophilic head group (red) and two hydrophobic tails (black lines), arranged in a bilayer configuration. **b** Size classifications of unilamellar vesicles including i) small unilamellar vesicles (SUVs), ii) large unilamellar vesicles (LUVs), and iii) giant unilamellar vesicles (GUVs). Note vesicles are only depictions and not drawn to exact scale.

microscopy¹⁰⁶. The size of the smallest GUVs that can be observed depends primarily on the optical resolution, or the minimum distance between two points on a specimen that can be distinguished¹⁰⁷. Since the limit in the lateral resolution of optical techniques is typically around 0.2 μm due to the diffraction of light¹⁰⁷, observing the GUVs using optical microscopy techniques is straightforward.

1.1 Approach for analysis

The goal of my dissertation is to characterize the different populations of GUVs that can be obtained from the most commonly used methods to assemble them. Current methods to characterize the distribution of sizes and yields of GUVs are inadequate to achieve this goal. In this chapter, I report the work I conducted to develop a method of characterization that allows meaningful comparisons of the GUVs assembled from different techniques. The method involves the standardization of the conditions used to assemble the GUVs, to harvest the GUVs, to collect images of the GUVs, and to analyze the sizes and yields of

the GUVs. I use two thin film hydration techniques, POPYRUS¹⁰⁶ (Paper-Abetted liPid hYdRation in aqUeous Solutions) on nanocellulose paper and electroformation to obtain GUVs for the results in the chapter. I review the details of the preparation conditions briefly in this chapter. A full description of the yields and effects of various conditions are provided in Chapter 3. All the experiments were performed using an upright confocal laser scanning microscope (Zeiss Upright Confocal Laser Scanning Microscope (LSM) 880 with Airyscan). For all images, I used a 488 nm laser to excite the fluorescent lipid probe in the GUVs and a GaAsP-PMT detector to collect the emitted photons. Typical image settings, unless specified in the sections are a 10× objective with the pinhole fully open, a laser power of 4, a gain of 500, a zoom magnification of 1.0, an image size of $850.19 \mu\text{m} \times 850.19 \mu\text{m}$, and a scanning field size of 3208 pixels \times 3208 pixels.

This chapter is organized as follows. I begin by reviewing methods that have been used to characterize GUVs in the literature. I review the physics and optics of confocal microscopy in section 1.3. In section 2, I go over the materials and methods used to obtain the populations of GUVs used in this work. In section 3.1, I report the results of imaging and manually counting GUVs directly on the surface. In section 3.2, I report results of attempting to quantify GUVs suspended in solution from z-stacks. I then report results from sedimentation and collection of gold-standard images for understanding the effects of choice of objectives and imaging settings. In section 4, I report the process and results of the automated image analysis code, and in section 5, I report the results from additional control experiments. The methods used to obtain the GUVs used for various figures in this chapter are shown in Table 1.

Figure/Table	Formation method
Fig. 2: Lipid structures (pg. 17)	Nanocellulose paper
Fig. 10: Bud distribution (pg. 29)	Glass slides
Fig. 11: Whole tilescan (pg. 30)	Nanocellulose paper
Fig. 12: Manual quantification (pg. 31)	Nanocellulose paper
Fig. 13: Stratification of buds (pg. 31)	Nanocellulose paper
Fig. 15: Suspended vesicles (pg. 33)	Electroformation
Fig. 18: Slice thickness (pg. 38)	Electroformation
Fig. 20: Diameter size comparison (pg. 41)	Nanocellulose paper
Fig. 21: GUV pixel intensities (pg. 43)	Nanocellulose paper
Fig. 23: Whole tilescan (pg. 45)	Nanocellulose paper
Fig. 26: Grayscale watershed (pg 48)	Nanocellulose paper, Electroformation
Fig. 27: Otsu thresholding (pg. 50)	Nanocellulose paper, Electroformation
Fig. 28: Watershed binary (pg 52)	Nanocellulose paper, Electroformation
Fig. 29: Size accuracy (pg. 54)	Nanocellulose paper
Fig. 30: Oversegmentation (pg 56)	Electroformation
Fig. 31-36: Image analysis code (pg.57-60)	Nanocellulose paper

Fig. 45: Selected GUV images (pg. 68)	Nanocellulose paper, electroformation, glass slides
Fig. 46: Size histograms (pg. 69)	Nanocellulose paper, electroformation, glass slides
Fig. 47: Small vesicles (pg. 70)	Electroformation
Fig. 48: Sedimentation (pg. 71)	Electroformation
Fig. 49: Small GUVs in bulk (pg. 72)	Electroformation

Table 1: Experimental methods used to obtain GUVs in this chapter. The title of the figure in the chapter along with the page number is in the left column with the formation method used to obtain the GUVs in the right column.

1.2. Current methods used to characterize GUVs

1.2.1 Optical microscopy

Optical microscopy is by far the most common technique used to characterize GUVs. Table 2 shows a collection of the various optical microscopy techniques used previously to characterize populations of GUVs and the different limitations of each technique. The columns of the table from left to right show the first author and date the literature was published, the method of characterization, whether the GUVs were harvested, whether an automated image analysis routine was used, and the limitations associated with each method. Since there are many reports that use repetitive methods, I include, to the best of my knowledge, the literature with the most quantitative results from each different characterization method.

For optical microscopy techniques, typically, the GUVs are imaged using phase contrast or using differential interference contrast (DIC), or the GUVs are fluorescently labeled and imaged with fluorescence widefield or confocal microscopy. Most characterization is done in a qualitative or semi-quantitative fashion, by manual counting of the GUVs and their diameters measured from a limited number of images¹⁰⁸⁻¹¹⁰. To date, GUVs are most commonly analyzed in images through manual selection using image analysis programs such as ImageJ where one can draw the contour of the GUV and determine an equivalent diameter^{31,35,83,111,112}. However, manual counting is tedious and could potentially introduce measurement errors, particularly for vesicles with smaller sizes that are more difficult to distinguish, making it difficult to realistically measure much more than a hundred of GUVs an hour. The consequent characterization of the population relies heavily on extrapolation from what is most likely to be a statistically insignificant portion of the population. There has been some interest in an automated methods to quantify GUVs from images including image analysis routines that use watershed segmentation¹¹³, a flood fill and erosion sedimentation technique¹¹⁴, and different Hough transform methods employed for the detection of vesicles¹¹⁵ as well as bubbles¹¹⁶. However, none of these methods were directly applicable to the images of harvested GUVs since the confocal objective and pinhole parameters that were optimized in this work provide higher lateral and axial resolution images than previously analyzed.

Literature	Characterization method	Harvested GUVs	Automated analysis	Limitations
Reeves, 1969 ¹¹⁷	Phase contrast microscopy	No	None	Yields are unclear since very few (around 100) vesicles analyzed. Sizes are unclear since images have low resolution and vesicles are attached to surface making boundaries unclear.
Akashi, 1996 ¹¹⁸	Phase contrast microscopy	Yes	None	Yields are unclear since only 10 vesicles are counted for each harvested chamber analyzed. Size distributions are unclear since images have low resolution and low counts.
Montes, 2006 ¹¹⁹	Fluorescence microscopy	Yes	None	Yields are unclear since very few (around 50) vesicles analyzed. Sizes are more accurate since vesicles are fluorescently labeled, but distribution is unclear with low counts.
Politano, 2006 ¹¹³	Fluorescence microscopy	No	Custom segmentation routine	Method assumes all detected objects are GUVs. Yields are unclear since the vesicles are not harvested.
Zupanac, 2014 ¹²⁰	Phase contrast (video) microscopy	Yes	Custom segmentation routine	Method assumes all detected objects are GUVs and the resolution of phase contrast microscopy is more limited than confocal.
Mora, 2014 ¹²¹	Confocal fluorescence microscopy	Yes	None	Sample size is limited to around 2,000 since vesicles due to manual

				counting. Yields are unclear since the volume of the solutions are not considered.
Li, 2016 ¹²²	Fluorescence microscopy	No	None	Yields and sizes are unclear since the vesicles are not harvested and are counted manually.
Fayolle, 2018 ¹²³	Confocal fluorescence microscopy	Yes	None	Sample size is limited to around 500 due to manual counting.

Table 2: Optical microscopy methods used to characterize GUVs. The author and the date of the relevant publication is shown in the first column. The optical microscopy method used to characterize GUVs is shown in the second column. Whether the GUVs analyzed were harvested or analyzed using an automated detection routine is shown in the third and fourth columns. The limitations of the characterization method are written in the final column.

1.2.2 Flow focusing techniques

Flow focusing techniques have also been investigated to quantify GUVs such as flow cytometry^{124–131} and Coulter counting^{66,132,133}. In flow cytometry, fluorescently labeled GUVs are counted in a flow cytometer instrument. The sizes of the vesicles are determined by focusing the GUVs in a single file line, passing the GUVs through a laser light source, and measuring the amount of fluorescence emitted and laser light scattered by the GUVs. In Coulter counting, the GUVs are similarly focused in a single file line but passed instead through a detector that measures electrical impedance¹³⁴. The detector determines the sizes and counts of the GUVs by measuring the amount of electrical impedance that occurs when a GUV passes through the detector¹³⁴.

The flow focusing techniques allow for the more rapid counting of a large numbers of objects^{134–136} but do not allow for direct visualization of all of the objects being detected. Thus, the methods can be highly inaccurate since it is difficult to differentiate whether objects are GUVs, MLVs or other debris¹³⁰. In addition, unanticipated technical challenges often arise when using these techniques due to the large range in sizes, 1 – 150 μm amongst a typical GUV population. Both flow cytometry and Coulter counting are best suited for more narrow ranges of sizes (around 5 – 30 μm ^{66,124,125}) and due to their reliance on flow, issues with multiple liposomes passing a detector¹³⁴ at the same time and the effects of the breakage of liposomes from the shear flow¹³⁷ can further complicate analysis.

1.2.3 Other techniques

Other characterization techniques such as electron microscopy^{132,138} or atomic force microscopy¹³⁹, which although allow for visualization with a higher resolution, require

removal of the GUVs from their native aqueous environments. These removal processes can result in alteration in the structure of the vesicles and lead to significant losses in vesicle yields and are thus only used to characterize small numbers of GUVs or used to examine lamellarity of the GUVs and are not used for population analyses.

1.3. Microscopy of GUVs

Currently the most common methods employed to assemble GUVs (thin film rehydration techniques) also result in the assembly of a variety of other lipid bilayer structures including MLVs, MVVs, lipid nanotubes (LNTs), as well as other lipid debris (Figure 2). The accurate characterization of a population of GUVs therefore depends on the ability of the characterization method to be able to select out any of the non-GUV structures. Since there are a variety of different lipid structures with sizes that can range more than 4 orders of magnitude (LNT diameters can be as small as 20 nm¹⁴⁰ and the largest GUV diameters can be up to 200 μm ¹⁴¹) and lipid concentrations that can range more than 5 orders of magnitude (a 1 μm MLV could contain 5 bilayers in a 0.5 μm^3 volume¹⁴² compared to a 100 μm GUV which contains 1 bilayer in a $5 \times 10^5 \mu\text{m}^3$ volume), distinguishing GUVs from non-GUV structures is most easily accomplished through direct visualization using fluorescence microscopy.

In fluorescent microscopy images, GUVs appear as a circular bright ring with a dim interior^{105,138,143} (Figure 2c). This appearance is due to the two-dimensional nature of the focal plane, or plane the microscope is focused on, which is typically thin and illuminates the equator of the GUVs more brightly than the caps (Figure 3). The contrast between the

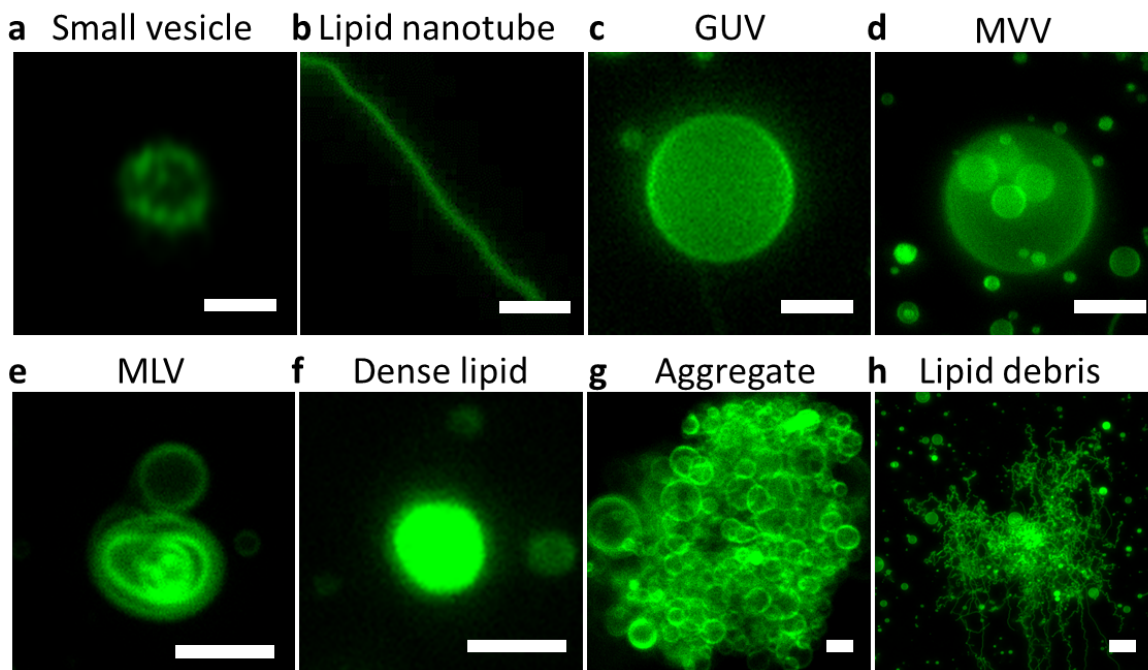


Figure 2: Different lipid structures produced from thin film rehydration. Confocal images showing various lipid structures produced from thin film rehydration including **a**

vesicle smaller than $1\ \mu\text{m}$ **b** lipid nanotube, **c** GUV, **d** MVV, **e** MLV, **f** dense lipid structure, **g** vesicle aggregate, and **h** lipid debris. Scale bars: **a,b** $1\ \mu\text{m}$ **c-h** $5\ \mu\text{m}$.

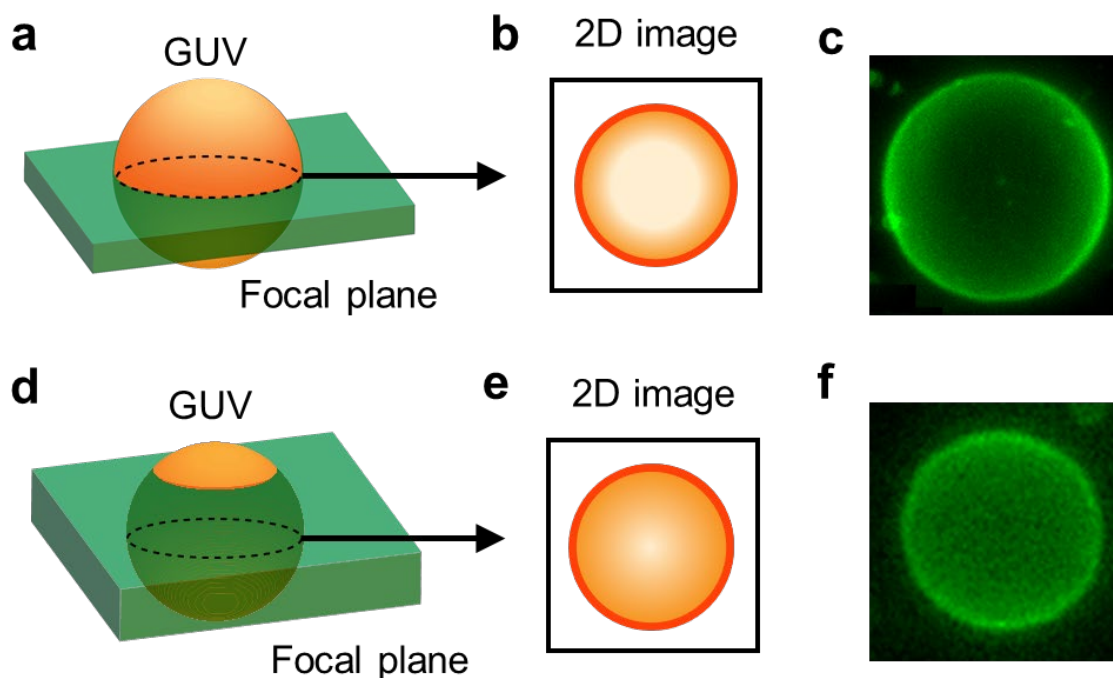


Figure 3: Appearance of GUVs in images. **a** Cartoon representation showing the effect of the focal plane (green) on the **b** appearance of a GUV in an image. Since the GUV is a hollow three-dimensional object and the focal plane essentially only collects a two-dimensional slice through the center of the GUV, the GUV in the 2D image appears as a bright ring and dim interior. A typical example of a GUV in a confocal image is shown in **c**. **d** Cartoon representation showing the effect of the relative sizes of the focal plane and GUV on the **e** appearance of the GUV in the image. Since the GUV is similar to the size of the focal plane there is less contrast between the bright ring and dim interior. A typical example of a smaller GUV in a confocal image is shown in **f**.

intensity of the bright ring and the dim interior thus depends on the relationship between the size of the GUV and the thickness of the focal plane. As the size of the GUVs become comparable to the thickness of the focal plane (Figure 3d-f), either through increasing the thickness of the focal plane or by imaging smaller sized GUVs, the interior of the GUVs in the images will be less dim since more of the fluorescence from the caps of the GUVs will be captured. For the experiments conducted in this work the GUVs $\leq 3\ \mu\text{m}$ typically do not have enough contrast to distinguish the bright ring and dim interior and instead appear as a completely bright circle in the image.

1.3.1 Overview of confocal microscopy

Fluorescence microscopy is one of the most common techniques used to study biological samples due to the ease with which one can probe and identify specific molecular targets^{144,145}. Briefly, the technique relies on the physical phenomena of fluorescence that occurs when a molecule that has been excited to a higher energy state falls to a lower energy state and emits a photon¹⁴⁶. The basic approach to collect images using a fluorescence microscope is to excite molecules related to the specimen of interest using a specific wavelength of light and then to collect the consequent photons that are emitted from the excited molecules using a detector¹⁴⁶.

A confocal microscope differs in a few ways from a widefield microscope setup (Figure 4). Starting with the sample irradiation, the confocal microscope uses lasers instead of light sources such as lamps or LEDs that are used in conventional widefield microscopy¹⁴⁷. The use of a laser allows the user to select points on the sample to expose light but requires a scanning mechanism to collect an entire image¹⁴⁶. This scanning mechanism is in contrast to the widefield where the entire image area is exposed to light all at once¹⁴⁶. To collect the light, both microscopes require the use of an objective, the lens responsible for the primary collection and magnification of the light used to form an image¹⁴⁸. The objective lens, depending on the specific field of view or resolution requirements of a sample, can be switched out to allow optimization of the imaging parameters between different samples.

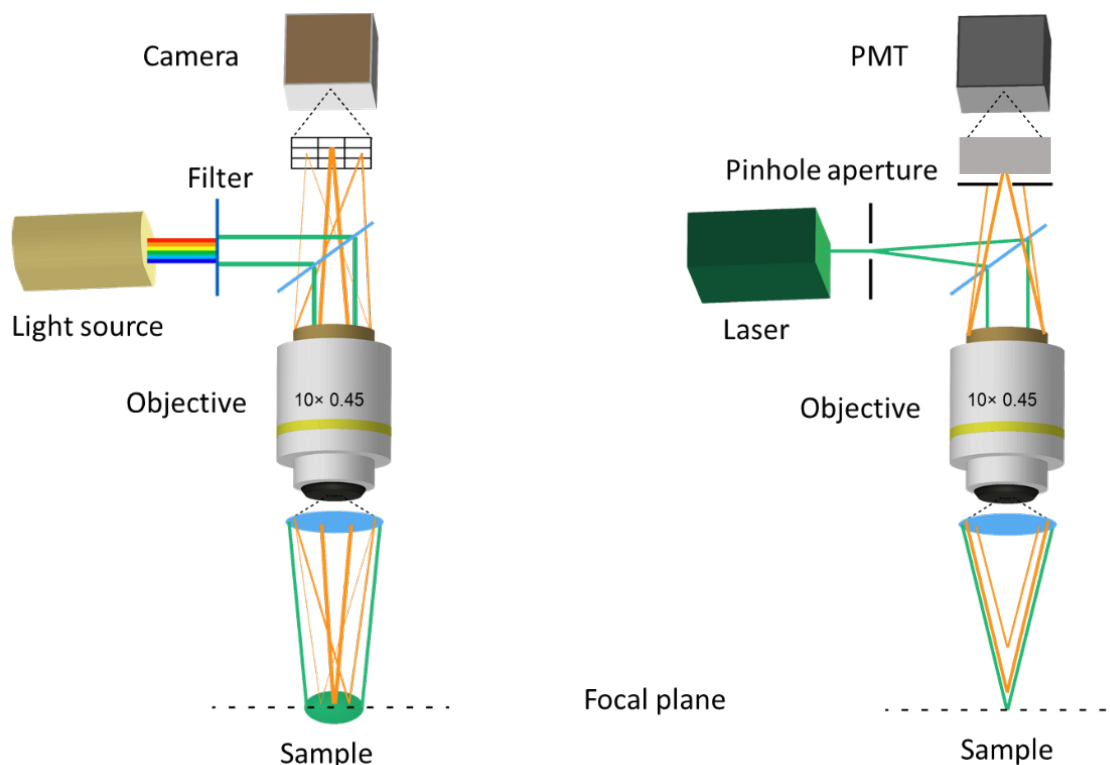


Figure 4: Diagram of widefield vs confocal microscope. Schematic showing the typical components and differences between a fluorescence widefield microscope and a confocal

microscope. The green lines show the path of the light from the source to the sample focal plane (dashed line) and the orange lines show the path of the light emitted due to fluorescence from the sample back through the microscope into the detectors.

Before the light reaches the detector, the confocal also crucially has an additional pinhole, or small aperture, in contrast to the widefield, which allows for the exclusion of out of focus light from above and below the focal plane¹⁴⁷. This decrease in the amount of out of focus light allows for the collection of thin slices through a specimen of interest without significant effects from the background¹⁴⁷. The pinhole size can be adjusted depending on the optimal amount of light or slice thickness that is desired. To detect the amount of light collected from the sample, a confocal microscope requires a photon multiplier tube (PMT) which allows for the fast acquisition of a low amounts of light on a single detector¹⁴⁷. A widefield microscope can use more conventional cameras based on photodiodes, such as charged coupled devices (CCDs) or complementary metal oxide semiconductors (CMOS) that collect light from the entire field of view of the sample at once using an array of detectors¹⁴⁸.

Overall the confocal microscope critically improves the resolution compared to conventional widefield through the reduction of background signal at the expense of requiring more costly laser-scanning components¹⁴⁶. Due to the reduced background, one major advantage of the confocal over the widefield is the ability to perform optical sectioning, or the collection of many thin z-slices, over the height of a specimen of interest¹⁴⁶. These stacks of z-slices, also known as “z-stacks”, can be recombined to obtain 3D projections of a specimen with high axial resolution¹⁴⁶. Together the advantages in the lateral and axial resolution make the confocal microscope an ideal instrument to collect data on the populations of GUVs.

1.3.2 Lateral resolution limits of the confocal microscope

For all optical microscopy techniques, the microscope resolution is limited by the diffraction limit of light¹⁴⁶, which is a physical phenomena that results when a light wave travels through an aperture¹⁴⁶ (Figure 5). The size of the diffraction limited spot can be related to the wavelength of light and numerical aperture of the objective lens through Abbe’s formula¹⁴⁷ which for fluorescence microscopy techniques such as widefield or confocal results in a typical limit in the lateral resolution of down to around $0.2 \mu\text{m}$ ¹⁰⁷. More specifically, according to the Rayleigh criterion, which refines the Abbe equation to consider the resolvable distance between two adjacent fluorophores by considering their principle diffraction maximums, or Airy disk¹⁴⁷ (Figure 6), the lateral resolution is given by¹⁴⁷

$$r_{lateral} = \frac{0.61\lambda}{NA_o} \quad (1)$$

where r is the lateral resolution limit according to Rayleigh, λ is the wavelength of light and NA_o is the numerical aperture of the objective. Thus, a microscope with a wavelength

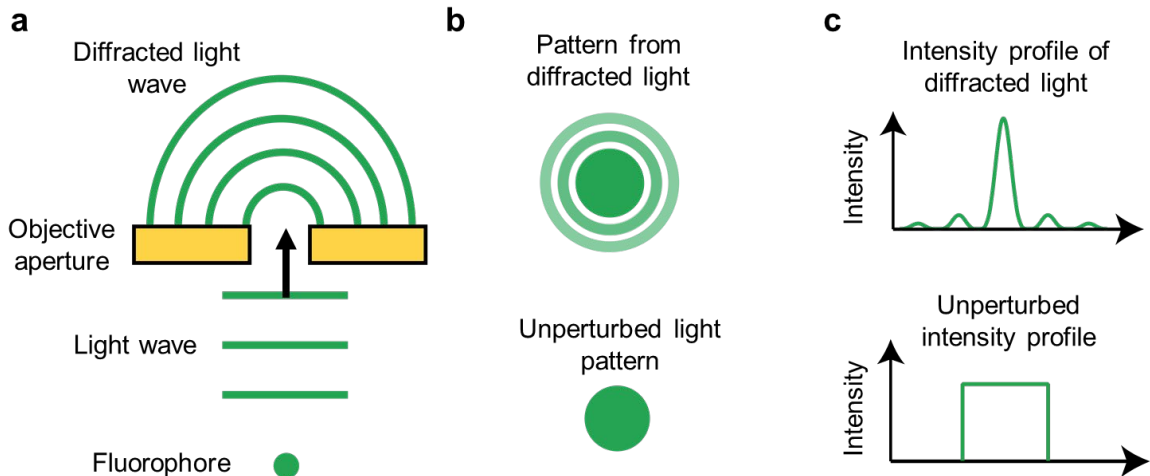


Figure 5: Basics of light diffraction. **a** Schematic showing the fluorescence light waves from a fluorophore (bottom) passing through an objective aperture. The light wave (bottom) is diffracted (top) proportionally to the size of the aperture. **b** Characteristic diffraction pattern (bullseye) showing the distribution of light from diffraction (top) and unperturbed light (bottom). **c** Intensity profile (point spread function) of the radial distribution of the light waves from the diffracted light (top) and the unperturbed light (bottom).

of 488 nm and an objective with a numerical aperture of 0.45 would have a microscope resolution limit according to Rayleigh criteria of 0.66 μm . A 1 μm diameter GUV thus would appear as a 2 pixel \times 2 pixel bright object.

The optical resolution is also dependent on the detection capabilities of the camera system¹⁰⁷. The resolving power of the camera system is dependent on the scanning field size (number of pixels) of the detector and the magnification settings of the objective. To fully ensure the camera resolution does not limit the overall optical resolution, the Nyquist sampling criteria is typically applied to determine an optimal zoom and pixel size corresponding to the scanning field of the detector¹⁴⁷. Specifically, the pixel size according to the Nyquist 2-fold oversampling criteria should be 2.5 times the diffraction-limited resolution to ensure that two points can be optimally resolved from one another^{147,148}. This is because to resolve two points according to Rayleigh criteria there still needs to be a change in intensity (contrast) in the middle between them. If the detector resolution is set equal to the diffraction-limited resolution, even though the drop in fluorescence intensity in the area where the outer portions of the diffraction profile overlap could be detected, the detector will not be able to pick up this drop in intensity making the two points indistinguishable (Figure 7). Thus, a value of around 2.5 times the pixel size from the diffraction-limited resolution can be used to distinguish the points. Combining with Equation 1, the Nyquist 2-fold oversampling criteria gives

$$Nyquist = \frac{0.61\lambda}{2.5NA_o} \quad (2)$$

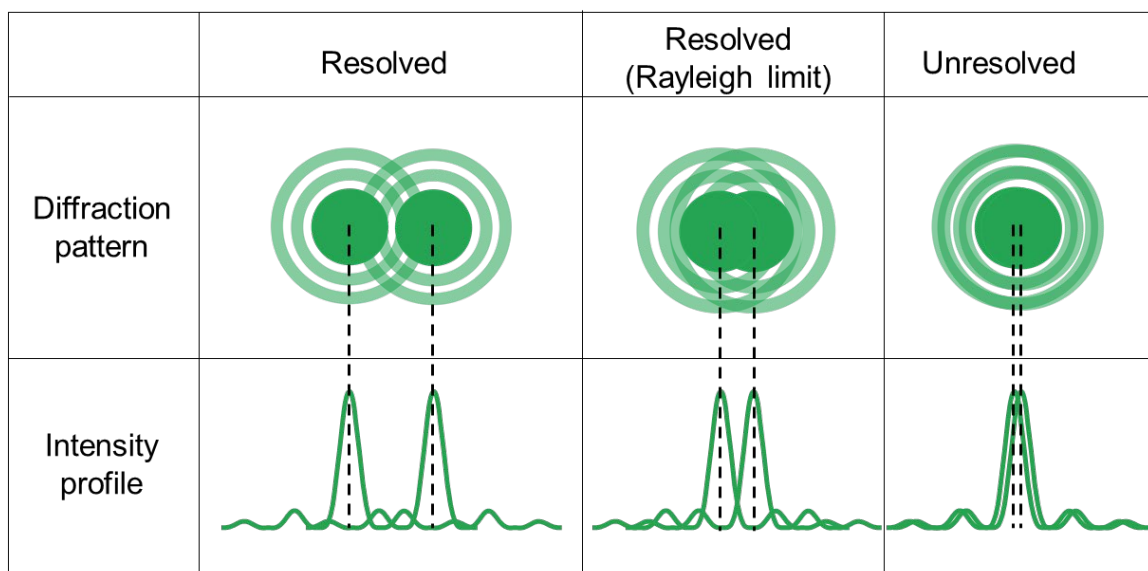


Figure 6: Diffraction-limited resolution. Schematic showing as an example, the relative resolution distances between the point spread function (intensity) curves (top) and diffraction patterns (bottom) of two points according to the Abbe resolution limit (left), the Rayleigh criteria (middle) and an unresolvable distance (right).

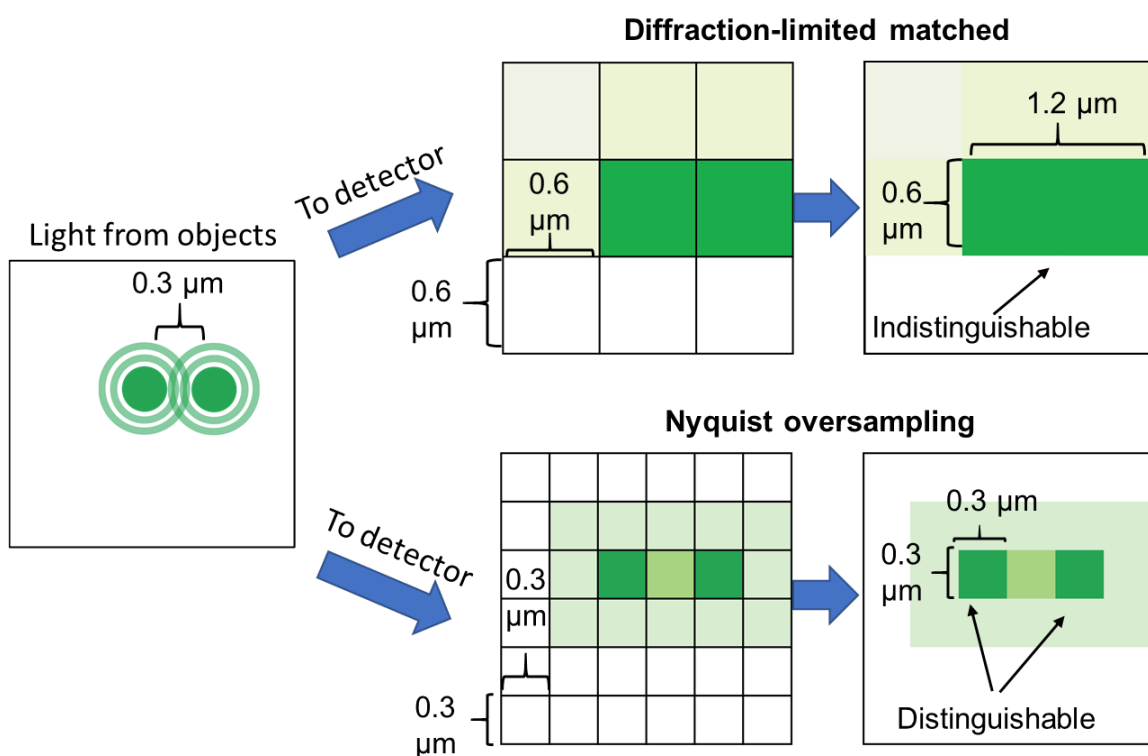


Figure 7: Nyquist oversampling. Intensity of objects separated by small distances (left). Setting the pixel size to match the diffraction limit (top) the entire fluorescence signal from

each diffraction pattern is detected in neighboring pixels making the objects indistinguishable from one another. Setting the pixel size to the Nyquist oversampling limit (bottom) the small drop in fluorescence intensity, in the area where the outer portions of the diffraction profiles overlap, is detected making the objects distinguishable.

where the lateral size of each pixel is a factor of 2.5 times smaller than the diffraction-limited resolution. Using a 10x 0.45 NA objective and a light wavelength of 488 nm, the camera pixel resolution would be approximately 265 nm. Assuming the detector has a typical scanning field size of least 3208 pixels \times 3208 pixels the maximum field of view that could be imaged without loss of resolution would be around 850 μm \times 850 μm .

Following the Nyquist 2-fold oversampling criteria, the smallest features that could be distinguished in a typical fluorescence microscopy setup are around 265 nm. In comparison to the sizes of the GUVs, a lateral pixel size of 265 nm would be enough to obtain at least 3 pixels along the diameter of a 1 μm GUV and closer to 9 pixels across both lateral dimensions of the GUV. Assuming the molar percentage of fluorescent lipid to be present in a single GUV to be 0.5 mol %, a 1 μm GUV should contain at least 40,000 fluorophores and each pixel of the GUV should contain at least 4,000 fluorophores. The overall signal that is detected is a function of the fluorescence signal that reaches the objective lens and the quantum efficiency of the detector¹⁴⁷. Performing an example calculation using a 10 \times 0.45 NA objective along with a high sensitivity gallium arsenide phosphide photomultiplier tube (GaAsP-PMT) detector, approximately 30% of the photons emitted are expected to reach the objective¹⁴⁷ and 30%, based on the quantum efficiency of GaAsP detector¹⁴⁷, of those collected are expected to be measured by the detector, in total resulting in around 9% of the photons emitted being measured. Simplifying the photon flux of the fluorophore to a very low 1 photon/ μs (typical fluorophore such as fluorescein is actually much higher closer to 100 photons/ μs ¹⁴⁷) and the pixel dwell time to just 1 μs /pixel (typical pixel dwell time in CLSM¹⁴⁹), approximately 360 photons (9%) are expected to be detected at each point, significantly higher than the minimum amount necessary to be above noise of around 10 photons¹⁴⁷. Compared to the shot noise, most sources of noise including dark noise, electronic noise, and background noise are expected to have negligible contributions to the total noise in confocal fluorescence microscopy due to the short sampling times and lower background fluorescence signal inherent to the confocal microscope¹⁴⁷. Since the main expected source of noise in the measurement is from the shot noise of the detector, which follows a Poisson distribution and can be calculated as the square-root of number of photons detected, $\sqrt{n_p}$ ¹⁴⁷, the signal-to-noise ratio (S/N) can be calculated using $\sqrt{n_p}$. Considering the signal from a 1 μm GUV was estimated to be made up from at least 360 photons, the resulting signal-to-noise ratio in this case would be high at around 19. This result confirms that discrimination of even the smallest GUVs should be straightforward with respect to the lateral optical limits of the confocal. If necessary, the effects from noise can be further minimized by decreasing the scanning speed and increasing the pixel dwell time at each spot, or by rescanning each spot multiple times and calculating the average of the signal from the scans.

1.3.3 Axial resolution limits of confocal microscope

Along with the lateral resolution, the axial resolution and thickness of the optical section (slice thickness) also have an important effect on the microscopy of the GUVs. In the confocal microscope, the axial resolution and the slice thickness can be related to the diameter of the pinhole aperture¹⁴⁷. To evaluate the effect of the pinhole on the optical performance and determine an optimal pinhole diameter, the axial (xz) projection of the point spread function (Figure 8) is typically analyzed^{146–151}. The axial projection of the point spread function (PSF_{total}) can be split into two components i) the PSF from the illuminating beam path (PSF_{ill}) which is used to determine the axial resolution and ii) the PSF from the detection beam path (PSF_{det}) which is used to determine the slice thickness. More specifically, both the axial resolution and slice thickness are typically estimated by calculating the length in the z -direction corresponding to number of pixels with intensities of no less than 50% of the peak of the PSF, also known as the full width at half maximum (FWHM) of the PSF.

Figure 9 shows the corresponding location of the FWHM (marked in red) of the axial projection of the PSF along with the effect of the pinhole on the size of the size of the FWHM. The first size range, corresponding to more open pinhole diameters (greater than around 3 AU), shows the large difference in the FWHM of the PSF_{det} compared to the PSF_{ill} as a result of the limitation in the depth discrimination properties of geometric optics¹⁵⁰. In this pinhole range, the axial resolution can be estimated as function of the FWHM of the PSF_{ill} using¹⁵⁰

$$FWHM_{ill,axial} = \frac{1.77n\lambda}{NA_o^2} \quad (3)$$

where axial resolution is equal to the FWHM of the PSF_{ill} which is a function of the index of refraction of the objective immersion liquid, n , the wavelength of light, λ , and the objective numerical aperture NA_o . Thus, for a $10\times$ 0.45 NA objective with a refractive index of air of 1.0 and light wavelength of 488 nm, the axial resolution would be approximately $4.3 \mu\text{m}/\text{pixel}$.

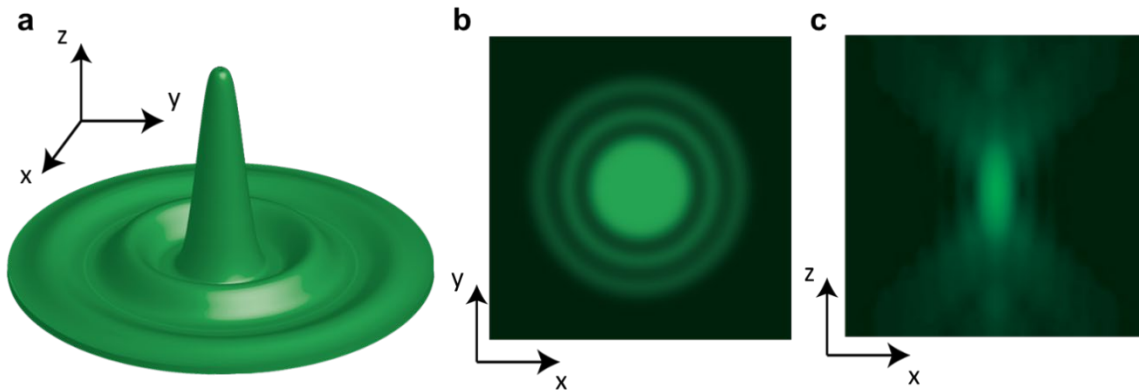


Figure 8: Sections through the 3D point spread function. a A 3-dimensional depiction of the point spread function corresponding to the intensity profile of a diffraction-limited

fluorescent object. **b,c** Two dimensional projections of the point spread function **b** through the x - y plane where the central circular maximum (bright circle in middle) corresponds to one Airy disk unit (AU) and **c** through the x - z plane where the central ellipsoidal maximum (bright ellipse in middle) corresponds to one AU.

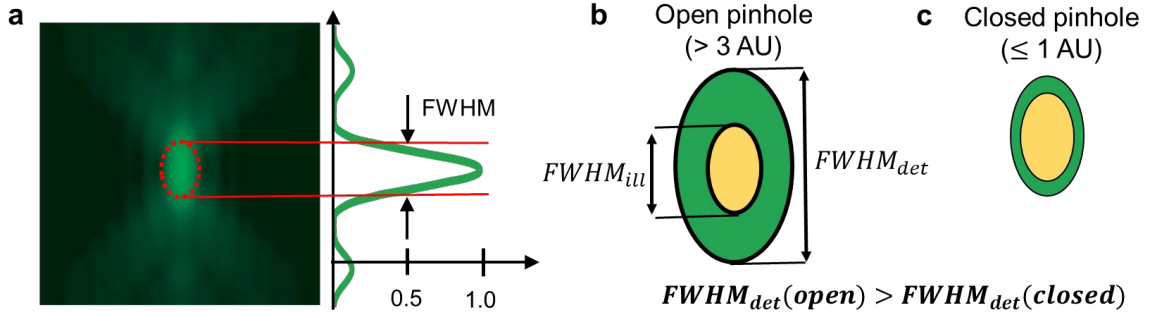


Figure 9: Effect of pinhole on the FWHM. **a** Axial projection of point spread function with the location of the pixels with intensities corresponding to the FWHM of the PSF marked in red. **b** When the pinhole is large in size (at least 3 AU) the length of the FWHM of the PSF of the detector becomes larger than the FWHM of the illuminated PSF point. **c** As the size of the pinhole decreases towards 1 AU, the FWHM of the PSF of the detector becomes smaller and begins to approach the size of the FWHM of the illuminated PSF point.

Furthermore, the slice thickness, or amount of light in the z -plane that is not rejected by the pinhole¹⁴⁷, is a function of the pinhole diameter and can be estimated from the FWHM of the PSF_{det} using¹⁵⁰

$$FWHM_{det,slice} = \sqrt{\left(\frac{0.88\lambda}{n - \sqrt{n^2 - NA_o^2}}\right)^2 + \left(\frac{\sqrt{2}nPH_{\mu m}}{NA_o}\right)^2} \quad (4)$$

where the slice thickness is equal to the FWHM of the PSF_{det} which is a function of the wavelength of light, λ , the immersion liquid, n , the objective numerical aperture NA_o , and the pinhole diameter in μm , $PH_{\mu m}$. The relationship to convert the pinhole diameter in AU into a physical pinhole size in μm is given by¹⁴⁷

$$PH_{\mu m} = \left(\frac{1.22\lambda_{\mu m}}{NA_o}\right) PH_{AU} M_o M_{sys} \quad (5)$$

where the prefactor (2 times Rayleigh criteria) is the definition of 1 Airy unit, PH_{AU} is the pinhole size in number of Airy units, M_o is the objective magnification, and M_{sys} is the

total system magnification of the microscope. Using a confocal LSM 880 microscope setup with a total system magnification of 2.8, a 10×0.45 NA objective, a wavelength of light of 488 nm, and a pinhole set to 15.64 AU, the physical pinhole diameter would be approximately $37 \mu\text{m}$. Plugging these values into Equation 4 along with a refraction index of 1.3, results in a slice thickness of approximately $5.5 \mu\text{m/slice}$. For larger pinhole diameters (> 3 AU) the relationship between the slice thickness and pinhole size is linear¹⁵⁰ and can vary slightly between microscopes and objectives with the relationship for the same LSM 880 setup given by¹⁵²

$$FWHM_{det,slice} = 0.132PH_{\mu\text{m}} + 0.23 \quad (6)$$

Plugging in the maximum physical pinhole size of approximately $599 \mu\text{m}$, results in a maximum slice thickness of approximately $79.3 \mu\text{m/slice}$. Notably, along with the axial resolution and slice thickness, any use of the confocal pinhole below around 6 AU also improves the lateral resolution calculated using the Rayleigh criteria by a factor of approximately 0.8^{148} .

When the pinhole diameter is approximately equal to or less than 1 AU, the difference between the PSF_{det} and PSF_{ill} is less significant and the axial resolution is improved. Overall the axial resolution when the pinhole is smaller than 1 AU can be calculated as function of the FWHM of the PSF_{ill} using¹⁵⁰

$$FWHM_{ill,axial} = \frac{1.28n\lambda}{NA_o^2} \quad (7)$$

and the slice thickness can be calculated using¹⁵⁰

$$FWHM_{det,slice} = \frac{0.64\lambda}{n - \sqrt{n - NA_o^2}} \quad (8)$$

Again using the same values for the confocal LSM 880 and 10×0.45 objective, with the exception of a smaller pinhole diameter of 0.25 AU, the axial resolution improves slightly to $4.1 \mu\text{m/pixel}$, and the slice thickness falls to $1.2 \mu\text{m/slice}$.

Although decreasing the pinhole size does result in a slight improvement in axial and lateral resolution, it comes at the cost of the amount of signal that reaches the detector. If the amount of signal is too low, the signal-to-noise ratio will decrease resulting in a decrease in the resolution. To overcome issues with low signal-to-noise ratio while maintaining a small pinhole diameter, pseudo-super resolution techniques can be employed, such as employing the use of an Airyscan detector which collects the light using an array of detectors to increase the signal while maintaining a small pinhole diameter¹⁴⁶. Overall since the pinhole is easily adjustable, the standard confocal microscopy setup offers the significant advantage of being able to easily tune and optimize a wide variety of different resolution and signal requirements depending on the imaging conditions necessary for different samples.

2. Materials and methods

In this section, I briefly lay out the materials and methods necessary to obtain the GUVs used to optimize the confocal microscopy parameters for the characterization of populations of GUVs. Further details on the different GUV formation methods and the insights gained from the standardization methods developed in this chapter can be found in Chapters 2 and 3.

2.1 Materials

To assemble the vesicles used in this chapter, I required indium tin oxide (ITO) coated-glass slides (25×25 mm squares, surface resistivity of 8-12 Ω /sq) which were purchased from Sigma-Aldrich (St. Louis, MO). A 3 wt % aqueous slurry of nanofibrillated cellulose was purchased from the University of Maine Process Development Center. I purchased circular hole punches (EK Tools Circle Punch, 3/8 in.), square hollow punch cutters (Amon Tech), a Paasche Gravity Feed Airbrush Kit (Model TG-3W) and Paasche Compressor system (Model D3000R) from Amazon Inc. (Seattle, WA). Fisherbrand Regenerated Cellulose Dialysis Tubing (MWCO-12,000-14,000), glass coverslips (Gold Seal™, 22 mm x 22 mm), premium plain glass microscope slides (75 mm x 25 mm), and glass Petri dishes (Pyrex™, 150 mm diameter) were purchased from Thermo Fisher Scientific (Waltham, MA).

2.2 Chemicals

Sucrose (BioXtra grade, purity $\geq 99.5\%$), glucose (BioXtra grade, purity $\geq 99.5\%$), and casein from bovine milk (BioReagent grade) were purchased from Sigma-Aldrich (St. Louis, MO). I purchased chloroform (ACS grade, purity $\geq 99.8\%$, with 0.75% ethanol as preservative) from Thermo Fisher Scientific (Waltham, MA). A silicone elastomer kit (184 Sylgard) with gel and curing agent was purchased from Dow Inc. (Midland, MI) to make polydimethylsiloxane (PDMS). I obtained 18.2 M Ω ultrapure water from an ELGA Purelab Ultra water purification system (Woodridge, IL). I purchased 1,2-dioleoyl-sn-glycero-3-phosphocholine (18:1 (Δ^9 -cis) PC (DOPC)), 1-palmitoyl-2-(dipyrrometheneboron difluoride)undecanoyl-sn-glycero-3-phosphocholine (TopFluor-PC), and 23-(dipyrrometheneboron difluoride)-24-norcholesterol (TopFluor-Chol) from Avanti Polar Lipids, Inc. (Alabaster, AL).

2.3 Electroformation

To date, the most commonly employed method to assemble large amounts of GUVs has been the electroformation method^{110,141,153,154}. Following previously optimized methods¹⁴¹, I start by depositing a 10 μ L solution lipids dissolved in chloroform onto a conductive ITO-coated glass slide. In this work the standard lipid mixture unless otherwise specified is a 1 mg/mL solution of 99.5:0.5 mol % DOPC:TFC. The lipids are spread over a circular area on the slide with a diameter of 9.5 mm. The lipid-coated slide is then placed in vacuum to allow any excess chloroform to evaporate. After 1 hour the lipid-coated slide is removed from vacuum and is connected to a function generator using conductive tape and electronic leads. The tape is carefully placed on one corner of the conductive side of the glass slide. A circular PDMS gasket (5/8 inch inner diameter) is placed around the dried lipid film. I

fill the PDMS gasket with 150 μL of 100 mM sucrose solution and then place a second ITO-coated glass slide with conductive tape in the corner onto the PDMS gasket to form a sandwich and seal the filled chamber. I ensure the conductive tape of the second top ITO slide is facing down and is opposite to the corner the tape is placed on the bottom slide. I set the function generator to a voltage of 1.5 V and a frequency of 10 Hz and allow the vesicles to grow for 1 hour.

2.4 PAPYRUS using nanocellulose paper

In my recent work¹⁵⁵, I show the ability of nanocellulose paper as a novel substrate to obtain large amounts of GUVs. I prepare flat sheets of nanocellulose paper in lab using solution casting^{156,157} (more detailed procedures on the fabrication process can be found in Chapter 3). Adapting standard GUV formation methods, I cut out a 9.5 mm diameter circular piece of nanopaper using a hole punch and carefully deposit 10 μL of lipid onto the paper. I place the lipid-coated paper into vacuum for 1 hour and then move it to a 48 well plate. I then hydrate the lipid-coated paper with 150 μL of 100 mM sucrose solution and allow the vesicles to grow for 1 hour. No external equipment or extra steps are necessary to obtain GUVs using the PAPYRUS method.

2.5 Custom-made chambers used to collect images of vesicles

Due to a number of factors including the percentage of the GUV population that ideally needed to be imaged, the maximum density limits of GUVs in an image (too many GUVs near each other make it difficult to accurately measure sizes), the effect of sedimentation time, and the objective working distance, the dimensions of the imaging chambers needed to be consistent across the different experiments. To control the dimensions of the imaging chambers I carefully weigh 6 grams of a PDMS mixture (9:1 ratio of PDMS and PDMS curing agent) in a 100 mm diameter Petri Dish. I place the Petri dish in vacuum chamber for 1 hour to remove any air bubbles and then moved the PDMS to a (completely flat) hot plate set at 65 $^{\circ}\text{C}$ to cure for at least 2 hours. From the cured PDMS, I punch out circular disks using a 5/8 inch (15.875 mm) diameter circular metal punch, and then punch out a square area within the disk using a 6 mm \times 6 mm (length \times width) metal square punch. The final dimensions of the PDMS gaskets that form the walls of the imaging chambers should have dimensions of 6 mm \times 6 mm \times 1 mm (width \times length \times height). To attach the PDMS gaskets to glass slides, I clean the PDMS in a sonication bath using 20 minute cycles of acetone, isopropanol, and ultrapure water and then moved the PDMS into a 65 $^{\circ}\text{C}$ oven for 1 hour to dry. Once dry, I place the PDMS gasket in contact with a clean glass slide. To prevent the GUVs from spontaneously rupturing onto the bare glass slides^{158,159}, which could have a significant effect on the yield, I passivate the chamber with a solution of 1 mg/mL casein in 1X PBS for 1 hour. Once passivated, I wash any unbound casein gently with ultrapure water and dry the imaging chamber using a nitrogen gun. To add the vesicles, I fill the imaging chamber with 58 μL of a 100 mM solution of glucose, gently mix in a 2 μL aliquot of the harvested GUV solution, and then seal the chamber with a glass coverslip. The GUVs are then allowed to sediment for 3 hours.

3. Results

3.1 Imaging vesicle buds on the surface

Observation of the surfaces during assembly reveal dense stratified layers of vesicle buds ranging from 1 – 150 μm in diameter on the surface (Figure 10). The lateral coverage of the buds is nonhomogeneous across the lipid-coated surface. The bud density can vary significantly depending on distribution of the lipid on the surface with some regions in a typical field of view of 200 μm \times 200 μm having only 50 to 100 sparsely packed small vesicle buds and other regions having more than thousands of vesicle buds both large and small in size. Figure 11 shows qualitatively the vesicle coverage across a 5 mm \times 5 mm surface of the nanocellulose paper after 1 hour of assembly. Since the vesicle buds are typically packed tightly together on the surface, determining definite boundaries of the buds through thresholding is difficult (Figure 11b). Thus, the most reliable method to obtain quantitative information of the vesicle buds while on the surface is to manually select the vesicle buds and analyze their sizes using image analysis software.

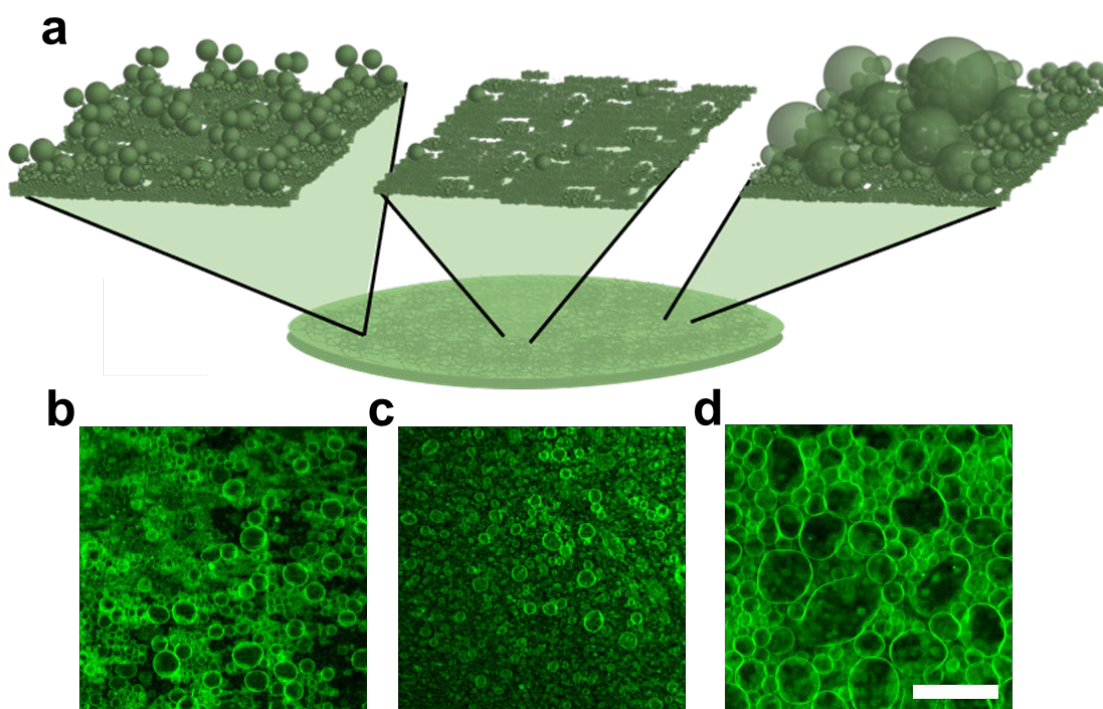


Figure 10: Nonhomogeneous distribution of vesicles on the surface. **a** Cross-sectional schematic showing the large local differences in bud sizes and bud density on a substrate. The schematic was based on the experimental images of vesicle buds assembled on glass in regions with **b** medium **c** low and **d** high density of buds. Scale bar 50 μm . Images were published¹⁶⁰ and reproduced here with permission from the American Chemical Society.

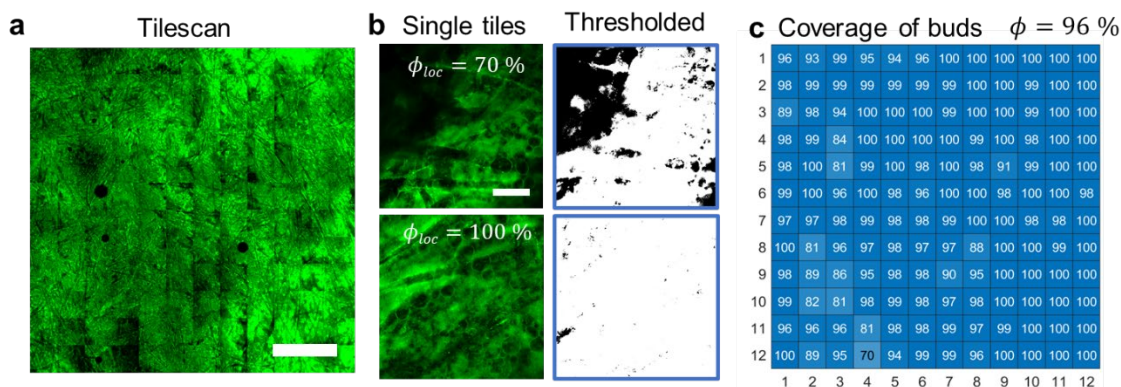


Figure 11: Qualitative analysis of vesicles on the surface. **a** Confocal tilescan images stitched together showing the variation in fluorescence intensity across the surface of nanocellulose paper after hydration. **b** Example of two single tiles with an estimated surface coverage (ϕ_{loc}) based on the fluorescence threshold of the vesicles buds in the image (right). **c** Heatmap showing the qualitative percent of the surface covered by vesicle buds based on the thresholded images. Scale bars **a** 1 mm **b** 100 μm .

Figure 12 shows the distribution of sizes of the vesicle buds that I manually analyzed using ImageJ. The buds are analyzed from a single 200 $\mu\text{m} \times 200 \mu\text{m}$ summed projection z-stack image of a region representative of the typical coverage of vesicle buds on the surface of nanocellulose paper. I carefully counted and measured the sizes of all of the vesicles visible in the image over the course of more than 3 hours. Analysis of the 987 vesicle buds counted in the image reveal a broad distribution that falls sharply from 3 μm with 910 of the vesicles having sizes less than 10 μm in diameter, 75 vesicles having sizes between 10 μm and 50 μm in diameter and 2 vesicles having sizes above 50 μm in diameter. The rarity of the largest sized buds highlights the importance of collecting large amounts of data to obtain an unbiased picture of the population. However, the manual quantification process is not only tedious, but it is further complicated by the stratification of the vesicle buds based on size where smaller vesicle buds that tend to be closer to the surface are more difficult to observe making them more likely to be miscounted.

To confirm the stratification of the vesicle buds based on size, I collect z-stack images of the buds on the surface. Figure 13 shows a depth coded maximum intensity projection along with an orthogonal projection (corresponding to the white dashed line of the depth coded image) of the vesicles above a typical region on the surface of nanocellulose paper. Vesicle buds with diameters between 25 – 50 μm can be observed more than 100 μm above the surface (brighter colors), while buds smaller than 25 μm in diameter tend to be much closer within 0 – 50 μm above the surface (darker colors). The layered packing obscures the buds on lowest planes making it particularly difficult to characterize the smallest buds closest to the surface with sizes between 1 – 10 μm in diameter. It is likely that previous reports that use analysis of images of GUVs on surfaces^{117,161–164} also underestimate the abundance of smaller vesicles.

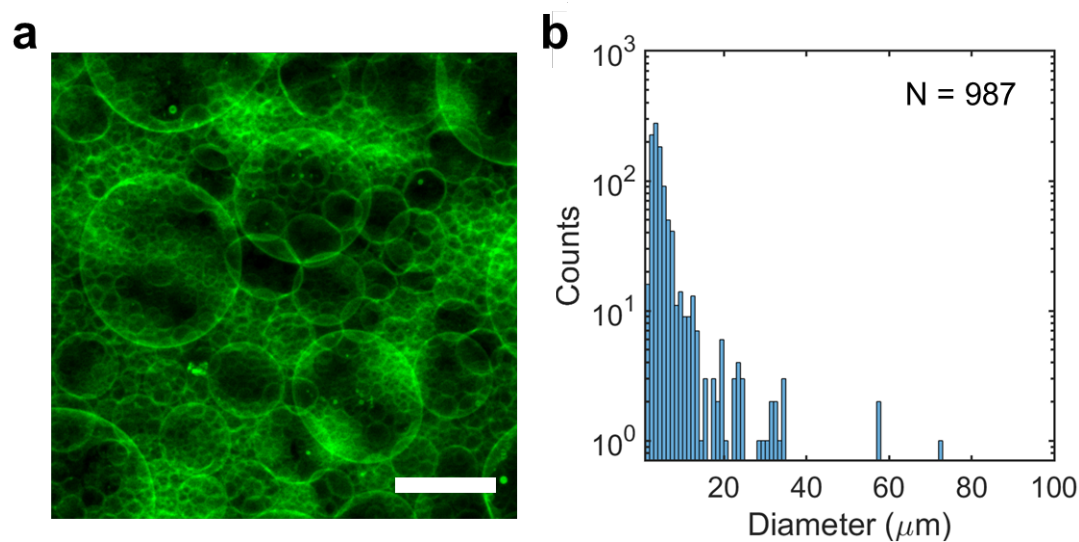


Figure 12: Manual quantification of vesicle buds on the surface. **a** Confocal image showing the typical appearance of vesicle buds assembled on nanocellulose paper. **b** Histogram showing the distribution of sizes of the vesicles analyzed manually using ImageJ. Note the logarithmic scaling of the y-axis. Scale bar **a** 50 μm .

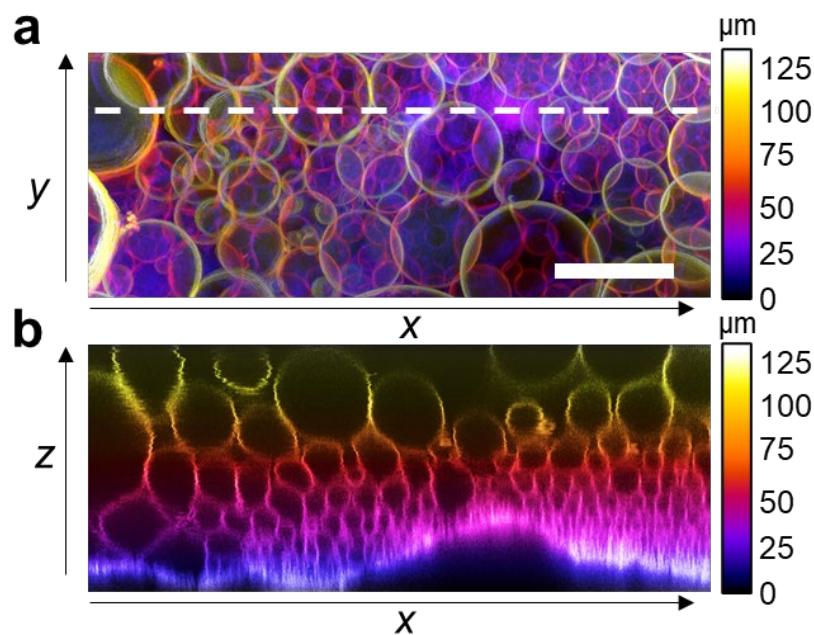


Figure 13: Stratification of vesicles above the surface. **a** Depth-coded projection of vesicle buds on the surface (x - y) of nanocellulose paper. **b** Orthogonal projection (x - z) of the region signified with a white dashed line in **a**. Smaller vesicle buds are located closer to the surface and larger vesicle buds are located further away from the surface. Color bars show the z -height of the vesicle buds. Scale bar is 50 μm .

3.2 Harvesting the vesicles from the surface

Multiple technical challenges prevent accurate quantification of buds on surfaces even with manual steps. The challenges include vesicles being densely packed, stratified on different planes, and being laterally nonhomogeneous. I thus designed a procedure that involves harvesting and diluting the vesicles for quantification. Furthermore, most experimental or practical applications that use GUVs require them to be isolated, cell-sized compartments suspended in solution^{5,8,165}. Thus, quantifying harvested populations is representative of the intended applications of GUVs.

To detach the vesicles from the surface, I manually apply gentle shear flow over the surface using a pipette. This application of shear flow at the surface creates a scission between the buds and their connections to the membrane harvesting the vesicles into solution (Figure 14a). I harvest each sample the same way each time aspirating and expelling 100 μL of solution 6 times to cover the surface and then aspirating all 150 μL on the final aspiration. I collect and store each sample of harvested vesicles in an Eppendorf tube until moving an aliquot of the sample into an imaging chamber for quantification (Figure 14b,c).

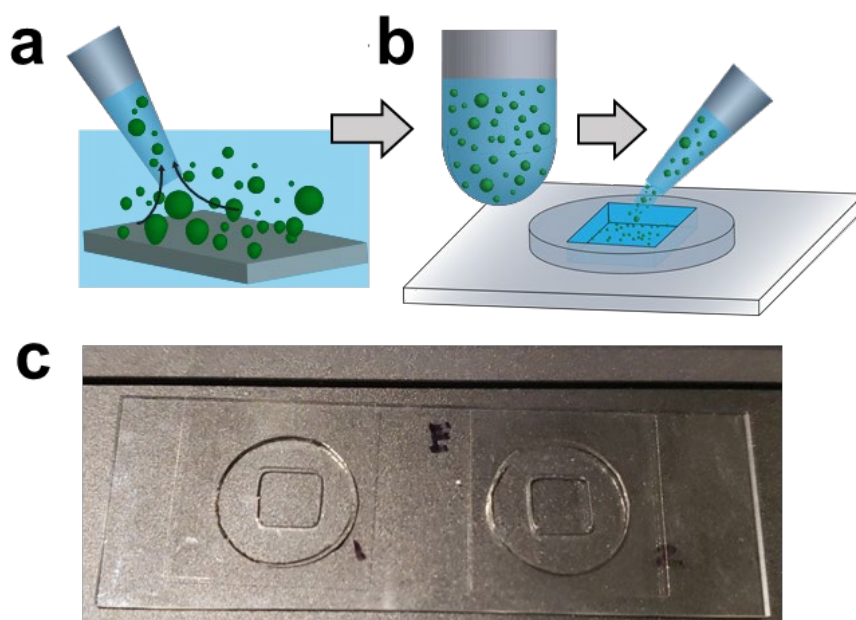


Figure 14: Preparation of giant vesicles for imaging. After **a** harvesting the GUVs from the surface, the solution is moved into **b** an Eppendorf tube for storage. A small portion of the harvested solution is then added into an imaging chamber for quantification. **c** A photograph showing an example of two imaging chambers after addition of the vesicles.

3.2.1 Imaging of suspended vesicles

I first attempted to image suspended vesicles immediately after harvesting without any dilution by taking tilescans at a few different z-heights. In these sets of experiments, I use the 10 \times objective and collect images in 10 μm steps from the surface of the glass to 200 μm above the surface of the glass. Figure 15 shows the images from one of the tile locations at three different z-heights. Obtaining the equatorial diameter of the objects is challenging because the vesicles are suspended at multiple different z-heights. Although, in principle a projected image should be able to capture the equatorial diameter, thermal drift which occurs during the long acquisition time results in a poorly defined blurry projection. Furthermore, the high fluorescence of lipid-dense objects such as MVVs (white arrows) bleeds across multiple slices. I estimate that taking a single z-stack at a single position of the imaging chamber would take about 8 minutes. Since each tilescan covers 64 tiles, the entire imaging time would require more than 8 hours. However even if this were accomplished, the vesicles translate due to Brownian motion and some bulk convection making determining vesicle position and size difficult.

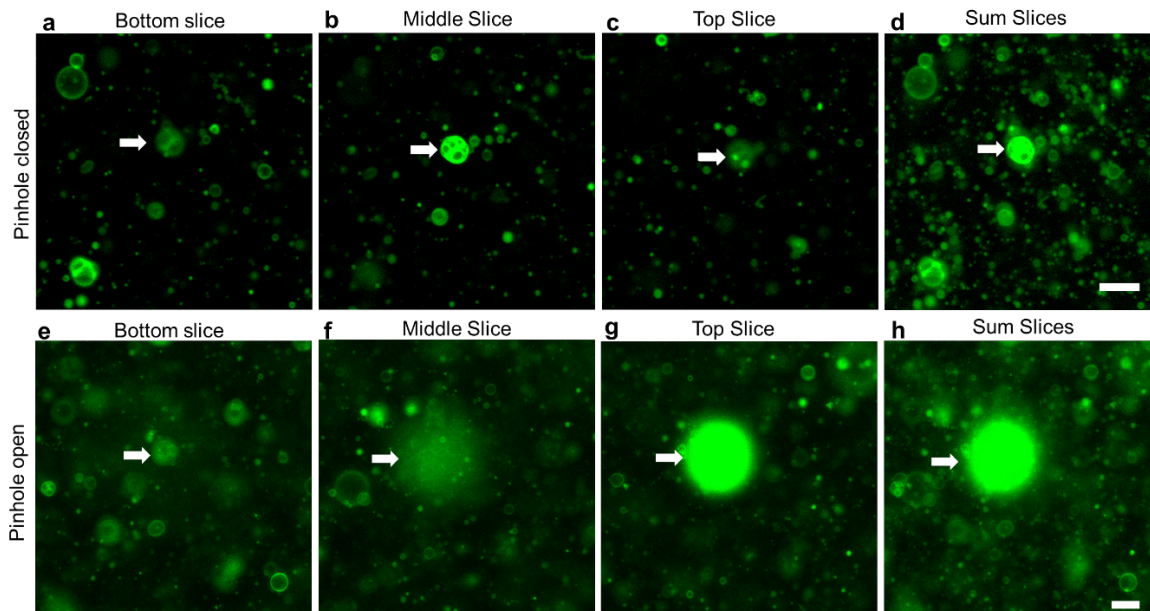


Figure 15: Imaging of suspended vesicles with different pinhole characteristics. **a-c** Confocal z-slices of the same x - y region of vesicles suspended in solution collected with the pinhole is closed to 1 AU. **d** The summed intensity projection of the three slices is shown on the right. **e-g** Confocal z-slices of the same x - y region of vesicles suspended in solution collected with the pinhole is fully open. The sum intensity projection of the slices is shown in **h**. The white arrows indicate the effect of the focal plane on the appearance of the MVVs in the image. Scale bars are 25 μm .

3.2.2 Sedimentation as a technique to convert 3D imaging to 2D

Since the imaging of suspended vesicles is difficult due to the dependence on the fluorescence intensity of the object on the z-height as well as the drift of the vesicles during the image collection, I sediment the vesicles to a single plane at the bottom of the imaging chamber¹⁶⁶⁻¹⁷⁰. I establish a density gradient across the interior and exterior of the vesicles using sugar molecules that are impermeable to the membranes to collect the vesicles on a single plane. For data collection, I assemble the vesicles in 100 mM sucrose and move the vesicles into a less dense solution of 95 mM glucose to initiate the sedimentation processes. I use a slightly lower concentration of osmolytes on the exterior of the GUV to ensure there is a modest osmotic pressure gradient. Without the modest gradient, some of the GUVs occasionally appear flaccid and deform into slightly oblate spheres instead of the perfect spheres that are ideal for imaging on the glass surface. I evenly mix the vesicles into the glucose solution so the vesicles should initially be equally distributed, and I seal the top of the imaging chamber to minimize effects of convection.

Neglecting the effects from diffusion, I can estimate the velocity of the vesicles during sedimentation using¹⁶⁶

$$u_t = \frac{2(\rho_v - \rho_s)gR^2}{9\mu} \quad (9)$$

where u_t , is the terminal velocity of the vesicle, ρ_v is the density of the vesicle, ρ_s is the density of the solution, g is the gravitational constant, R is the radius of the particle, and μ is the viscosity of the solution. I can then estimate the time it should take the vesicles furthest from the bottom of the imaging chamber to sediment based on size using¹⁶⁶

$$t_{max} = h/u_t = \frac{9}{2} \frac{\mu h}{(\rho_v - \rho_s)gR^2} \quad (10)$$

where t_{max} is the maximum sedimentation time and h , is the height of the chamber.

Using Equation 10, I calculate the expected maximum sedimentation time of the vesicles according to size (Figure 16). Corresponding to the typical sedimentation conditions, I set ρ_v equal to 1034 kg m^{-3} , ρ_s equal to 1019 kg m^{-3} , and g equal to 9.8 m s^{-2} , and following the expected viscosity of the glucose solution¹⁷¹, I set μ equal to $0.001 \text{ kg m}^{-1} \text{ s}^{-1}$. Figure 16b shows the results of the calculations for various vesicle diameters. The plot shows that within 3 hours (dashed red line) all of the vesicles with diameters of $4 \mu\text{m}$ and larger, are expected to have reached the bottom of the chamber when effects from diffusion are neglected. The maximum sedimentation time expected for vesicles with diameters, for example, of $5 \mu\text{m}$ is 82 minutes, $10 \mu\text{m}$ is 20 minutes, and $50 \mu\text{m}$ is 1 minute. Vesicles smaller than $4 \mu\text{m}$ are expected to take significantly longer. Specifically, the calculated maximum sedimentation times expected for vesicles with diameters of $1 \mu\text{m}$ is 34 hours, $2 \mu\text{m}$ is 9 hours and $3 \mu\text{m}$ is 4 hours.

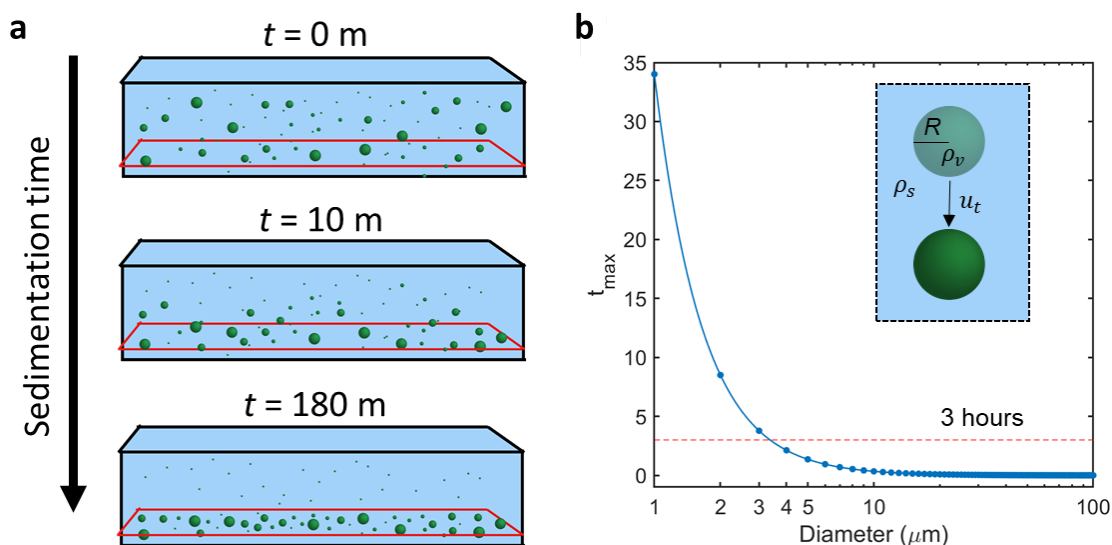


Figure 16: Effect of sedimentation time. **a** Schematic showing collection of vesicles at bottom of the imaging chamber over the course of 180 minutes (3 hours). **b** Plot of maximum sedimentation time of vesicles of different sizes calculated using Equation 9. The dashed red line marks the typical sedimentation time used for experiments of 3 hours. Note the log scaling of the x-axis.

3.3 Imaging of sedimented vesicles

3.3.1 Choice of objectives and pinhole characteristics

The confocal microscope setup allows for a wide range of changeable components including various lenses, apertures, mirrors, lasers, detectors, and light filters. The objective is a crucial component to any microscope setup since it is the first lens to collect the light from the sample¹⁴⁷. In confocal microscopy, the objective controls the magnification, resolution, and slice thickness of each image. The pinhole, a circular aperture at the conjugate focal plane, is a crucial component that separates the confocal setup from the wide field setup¹⁴⁷. The diameter of the pinhole aperture can be adjusted to manually change the slice thickness of each image and generally control the amount of light from above and below the focal plane of interest that is excluded¹⁴⁷. Exclusion of the light above and below the focal plane of interest helps to lower the background and improves the axial resolution¹⁴⁷. Overall, the characterization of the vesicles which range over three orders of magnitude between 1 – 150 μm in diameter, will depend on the optimization of the objective lens and pinhole diameter.

In previous work, high magnification objectives with large numerical apertures are often used^{5,37,172}. Furthermore, for techniques using confocal microscopy, the pinhole is typically closed so as to obtain a thin imaging slice. I show that for the purposes of measuring the size histogram and yield, a lower powered objective with a NA of 0.45 and

Objective	NA	Field of view at zoom of 1.0	Max lateral resolution	Slice thickness at 1 AU	Maximum slice thickness
10×	0.45	850.19 $\mu\text{m} \times$ 850.19 μm	0.265 $\mu\text{m}/\text{pixel}$	5.8 μm (37 μm)	79.3 μm (599 μm)
20×	1.0	425.10 $\mu\text{m} \times$ 425.10 μm	0.119 $\mu\text{m}/\text{pixel}$	1.5 μm (34 μm)	23.8 μm (599 μm)
40×	1.2	212.55 $\mu\text{m} \times$ 212.55 μm	0.099 $\mu\text{m}/\text{pixel}$	1.1 μm (56 μm)	10.7 μm (599 μm)
63×	1.4	134.95 $\mu\text{m} \times$ 134.95 μm	0.085 $\mu\text{m}/\text{pixel}$	0.8 μm (75 μm)	6.1 μm (599 μm)

Table 3: Important spatial properties of the available objectives. Objectives available on the LSM 880 are listed in the first column. Along the row of each objective the corresponding numerical aperture (NA) is shown in the second column, max lateral resolution is shown in the third column, the optimal slice thickness at 1 AU is shown in the fourth column, and the maximum slice thickness attainable is shown in the fifth column. The values in brackets indicate the physical size of the pinhole aperture at the various objective and slice thickness selected.

open pinhole configuration offers significant advantages. I compare images acquired using a Plan-Apochromat 10× 0.45 NA air objective and a Plan-Apochromat 20× 1.0 NA water immersion objective with various confocal pinhole sizes.

Following the Nyquist 2-fold oversampling criteria (Equation 2), the 10× 0.45 NA objective can be used to obtain a lateral resolution of 0.265 μm per pixel. With the pinhole closed at this resolution, the dark lumen of GUVs $< 3 \mu\text{m}$ cannot be resolved. For the 20× 1.0 NA the lateral resolution is 0.119 μm per pixel. With the pinhole closed at this resolution, the dark lumen in GUVs $< 1 \mu\text{m}$ in diameter cannot be resolved. Table 3 provides a list some of the other important spatial properties of the objectives including the optimal slice thickness at 1 AU and the maximum slice thickness. Using the objective with a NA of 0.45, the 1 μm diameter GUV appears as an object of about 12 pixels in size in the image; using the objective with a NA of 1.0, the 1 μm diameter GUV appears as an object of about 56 pixels in size in the image. Since the PMT is fully adjustable to account for the change in resolution, unlike camera based acquisition, the magnification of the objective does not factor into imaging. In principle, use of objectives with higher numerical aperture will increase the confidence of detecting the GUVs since the object will be mapped onto a larger number of pixels of smaller size. The higher image resolution could also improve the sharpness of the image and allow better discernment of objects that are close together. However, the improved resolution from using the higher numerical aperture objective comes at the expense of decreasing both the total field of view and maximum slice thickness that can be captured in each image. The limitations in the field of view can be overcome by taking large area tilescans. In principle, the limitations of the slice thickness can be addressed by taking z-stacks.

Figure 17 show the differences in the slice thickness between the objectives when the pinhole is fully opened and when the pinhole is closed to 1 AU respectively. With the 10× objective, when the pinhole completely open (15.64 AU) the slice thickness is 79.3 μm, and when the pinhole is closed to 1 AU the slice thickness falls to 5.8 μm. Since the majority of the light that is outside the slice thickness is excluded by the pinhole, if a vesicle is outside of the slice it will likely not be captured. Furthermore, if the equatorial plane of a vesicle is outside the slice, the actual size of the vesicle will be underestimated. Thus, the only way to accurately capture the size of the vesicle is to collect the fluorescence from the equatorial plane. Compared to the 10× objective, the 20× objective with the pinhole completely open to 17.38 AU results in a significantly lower slice thickness of 23.8 μm. Thus, vesicles larger than 50 μm will be more likely to be underestimated. With the pinhole closed to 1 AU the slice thickness shrinks down to 1.5 μm, resulting in the significant exclusion of fluorescence of vesicles larger than around 5 μm in diameter.

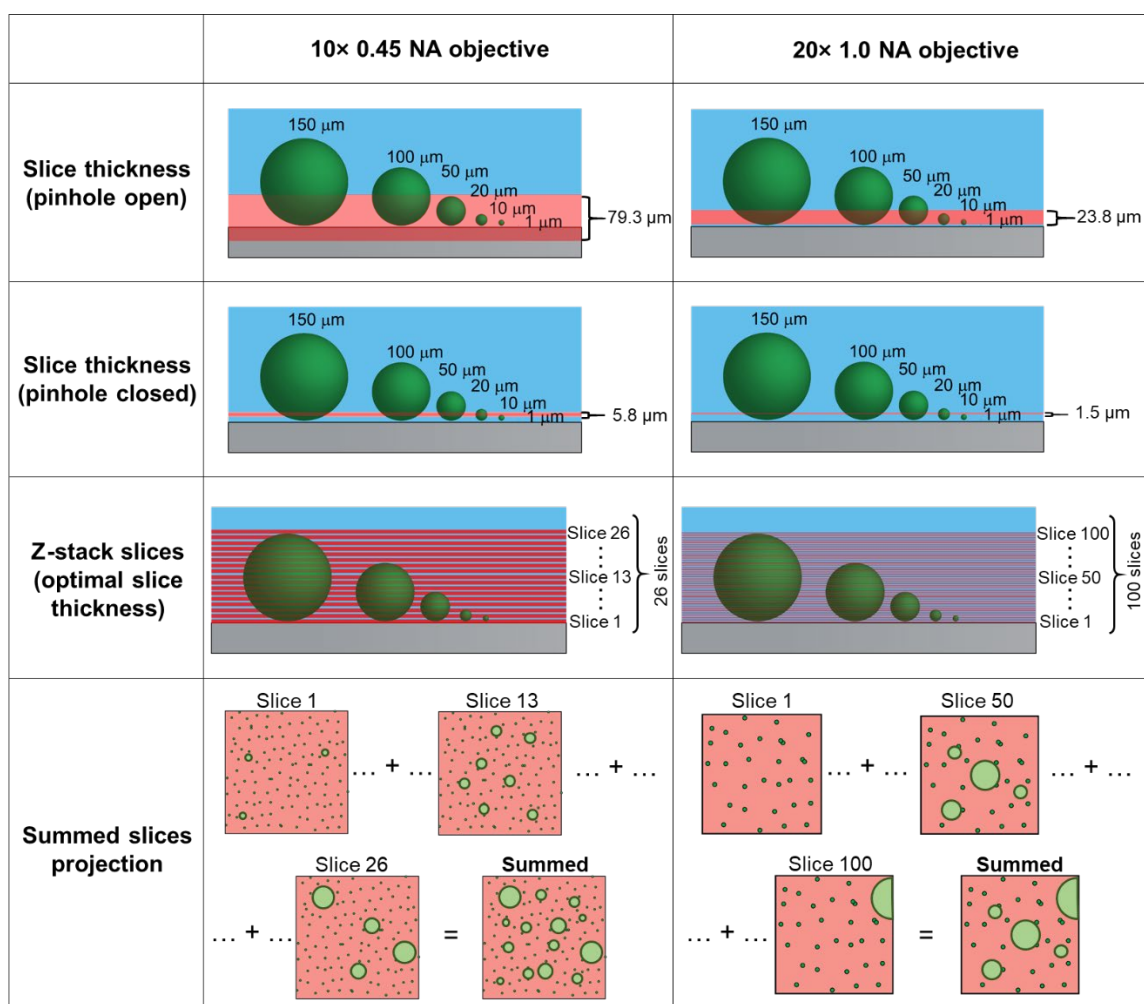


Figure 17: Optical slice properties of images collected with different objectives. Schematic showing the properties of the optical slice using the 10× 0.45 NA objective in the left column and the 20× 1.0 NA objective in the right column. The first row shows the axial slice thickness captured with the pinhole open. The second row shows the axial slice

thickness captured with the pinhole closed. The third row shows the number of z-stack slices necessary to image an entire sample. The fourth row illustrates the concept of summing the slices of a z-stack to obtain a single image. This process compresses the entire z-stack into a single image by summing the pixels in the same x and y location in every z-slice. Thus, as long as there are no vesicles suspended on top of each other, the summed intensity projection holds the fluorescence information of the entire object.

To test the effect of slice thickness on the quantification of GUVs, I collect images from the same region of harvested vesicles using different imaging settings (Figure 18). The slice thickness is expected to vary from $1.5\ \mu\text{m}$ for the $20\times$ pinhole closed, $5.8\ \mu\text{m}$ for the $10\times$ pinhole closed, $23.8\ \mu\text{m}$ for the $20\times$ pinhole open, and $79.3\ \mu\text{m}$ for the $10\times$ pinhole open. A summed intensity projection with an equivalent slice thickness of $93.2\ \mu\text{m}$ was also collected using the $20\times$ objective to provide a baseline to compare the effect of the slice thickness on the size of the GUVs in the images. Due to the exclusion of most of the fluorescent information that is located above or below the optical slice, I expect the equatorial plane of the vesicles with diameters larger than the size of the optical slice (with a $5\ \mu\text{m}$ buffer due to the location of the optical slice above the glass) to not be fully captured. Comparing the largest correctly captured vesicle in the $1.5\ \mu\text{m}$ slice (Figure 18f,k) with the baseline image (Figure 18j,o), to approximate the slice thickness

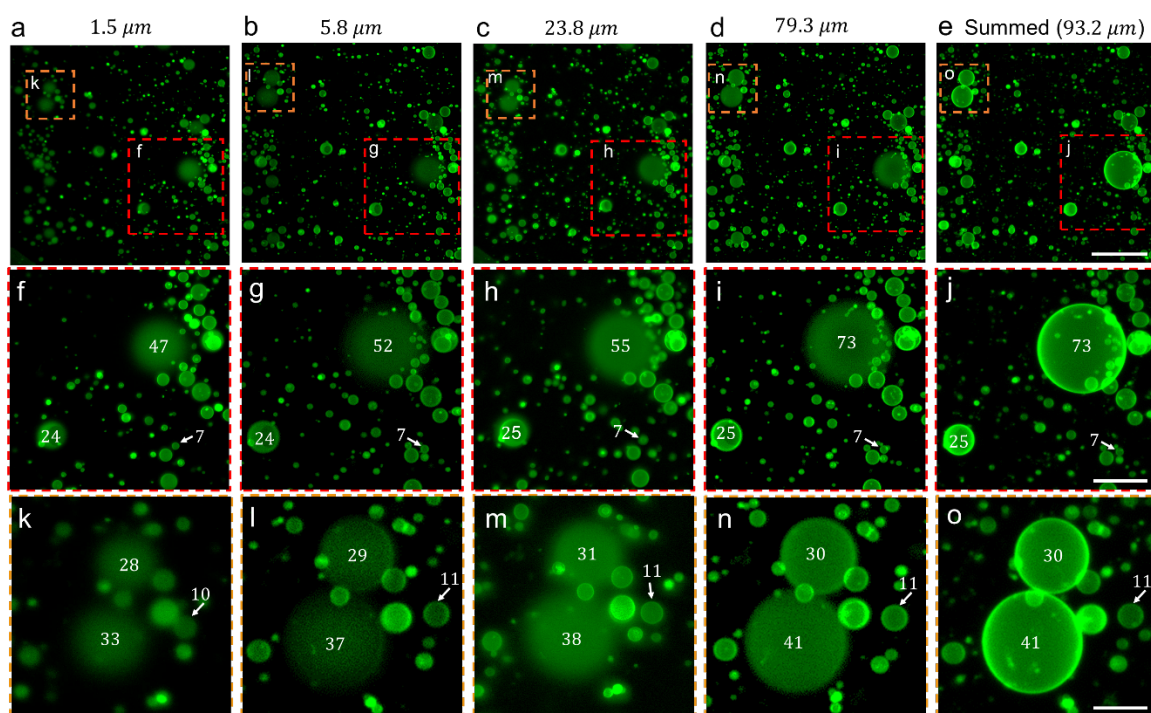


Figure 18: Effect of slice thickness on quantification of GUVs. a-e Images of the same region of vesicles collected with various slice thicknesses. The regions marked with red dashed lines are shown in f-j and orange dashed lines are shown in k-o. The numbers indicate the equivalent diameters of the vesicles measured manually in image j in micrometers. Scale bars are a-e $100\ \mu\text{m}$, f-j $50\ \mu\text{m}$, k-o $25\ \mu\text{m}$.

empirically, the 1.5 μm slice accurately captures vesicles with sizes up to 7 μm in diameter resulting in an effective slice thickness of at least 2 μm . The 5.8 μm , 23.8 μm , and 79.3 μm slices accurately capture the vesicles with sizes up at least up to 11 μm , 25 μm , and 73 μm respectively, resulting in an effective slice thickness of 6 μm , 20 μm , and 68 μm respectively. These effective slice thickness measurements correspond well with the minimum slice thicknesses that are expected and confirm that the 79.3 μm slice which uses the 10 \times pinhole open imaging settings accurately captures the largest range of vesicle sizes.

3.3.2 Choice of field of view and time for imaging

The choice of objective also affects the field of view that can be obtained. Figure 19 shows a schematical representation of the differences between the lateral dimensions of the images collected from the objectives. The absolute maximum field of view usable for imaging the GUVs depends on the “zoom” magnification of the objective and the pixel area of the detector. The zoom feature of the objective allows the user to manually adjust the magnification of the image¹⁴⁸. In the context of characterizing GUVs, the zoom capabilities for each objective are limited by the effects of the flatness of field¹⁴⁸, where the edges of the image appear less bright than the center when the zoom is too low. This gradient in the image brightness could cause potential challenges down the line during the intensity analysis of the GUVs and thus should be minimized. Although the effects of flatness of field are an unavoidable consequence of all optical imaging techniques which focus light through a curved lens resulting in the curved image plane¹⁴⁸, the objectives chosen here are both “plan-” corrected objectives which can significantly correct for the effects of flatness of the field at the edges¹⁰⁷. The first row in Figure 19 shows the maximum image sizes without significant effects from the flatness of field which are 850.19 $\mu\text{m} \times 850.19 \mu\text{m}$ for the 10 \times objective and 429.4 $\mu\text{m} \times 429.4 \mu\text{m}$ for the 20 \times objective. Since the GUVs analyzed are typically dispersed over an area of approximately 6 mm \times 6 mm, the 10 \times objective requires a tilescan with 8 tiles \times 8 tiles or 64 tiles. This tile total is significantly fewer than the 16 tiles \times 16 tiles or 256 total tiles required using the 20 \times objective.

The second row of Figure 19 shows the equivalent pixel area of the detector needed to obtain images following the Nyquist 2-fold oversampling criteria for each objective. The maximum pixel area available with the GaAsP detector is 8192 pixels \times 8192 pixels. Thus, even for the largest field of view with the highest NA objective (3604 pixels \times 3604 pixels), the GaAsP detector has more than 5 times enough pixels to collect the oversampled images, ensuring the maximum field of view is not limited by the detector. Considering the total number of pixels (spots) being scanned in each tile, the dwell time at each pixel, approximately 1 μs /pixel, and that each pixel is scanned 4 times to calculate an average, the 10 \times and 20 \times objectives are expected to collect an image in approximately 41 seconds

	10× 0.45 NA objective	20× 1.0 NA objective
Maximum field of view	<p>Single tile: 850.19 μm Whole tilescan: 8 tiles</p>	<p>Single tile: 429.4 μm Whole tilescan: 16 tiles</p>
Pixel size (Nyquist)	<p>Image: 3208 pixels by 3208 pixels Single pixel: 0.265 μm</p>	<p>Image: 3604 pixels by 3604 pixels Single pixel: 0.119 μm</p>

Figure 19: Lateral dimensions of images collected with different objectives. Schematic showing the lateral properties of the 10× 0.45 NA objective in the left column and the 20× 1.0 NA objective in the right column. The first row shows the top down view of the field of view (red) that can be collected in one image without effects from flatness of field. The second row shows the number of pixels needed to obtain images with a pixel size equal to the Nyquist 2-fold oversampling criteria.

52 seconds respectively. Excluding the time the microscope takes to move to the correct position of each tile, in this example a tilescan using the 10× objective could be completed in approximately 44 minutes, significantly shorter than a tilescan using the 20× objective which can be completed in approximately 222 minutes.

3.3.3 Comparison between open-pinhole 10× images and equatorial z-stacks

Since the 10× open pinhole configuration has clear benefits in terms of image acquisition time and minimizing the effects of vesicle drift, I perform control experiments to determine if it is possible to obtain an accurate measurement of the GUV diameters. I collect confocal z-stacks of GUVs with diameters that span from 1 to 150 μm using a 20× 1.0 NA objective. Since the z-stack captures sections of the vesicles, including the equatorial plane, I can select for the image slice that captures the equatorial diameter of the vesicles. I then imaged the same GUVs with a 10× 0.45 NA objective with the pinhole open. I show representative images in Figure 20. I measured the diameters of the GUVs from the equatorial slice manually using ImageJ. I observe that since the pinhole is closed and the slice thickness is small, the membranes of the GUVs are sharply delineated, particularly for the GUVs > 10 μm in diameter. I observe for the open pinhole images with a larger slice thickness, a greater fraction of the GUV membrane is imaged which causes the pixel intensity of the

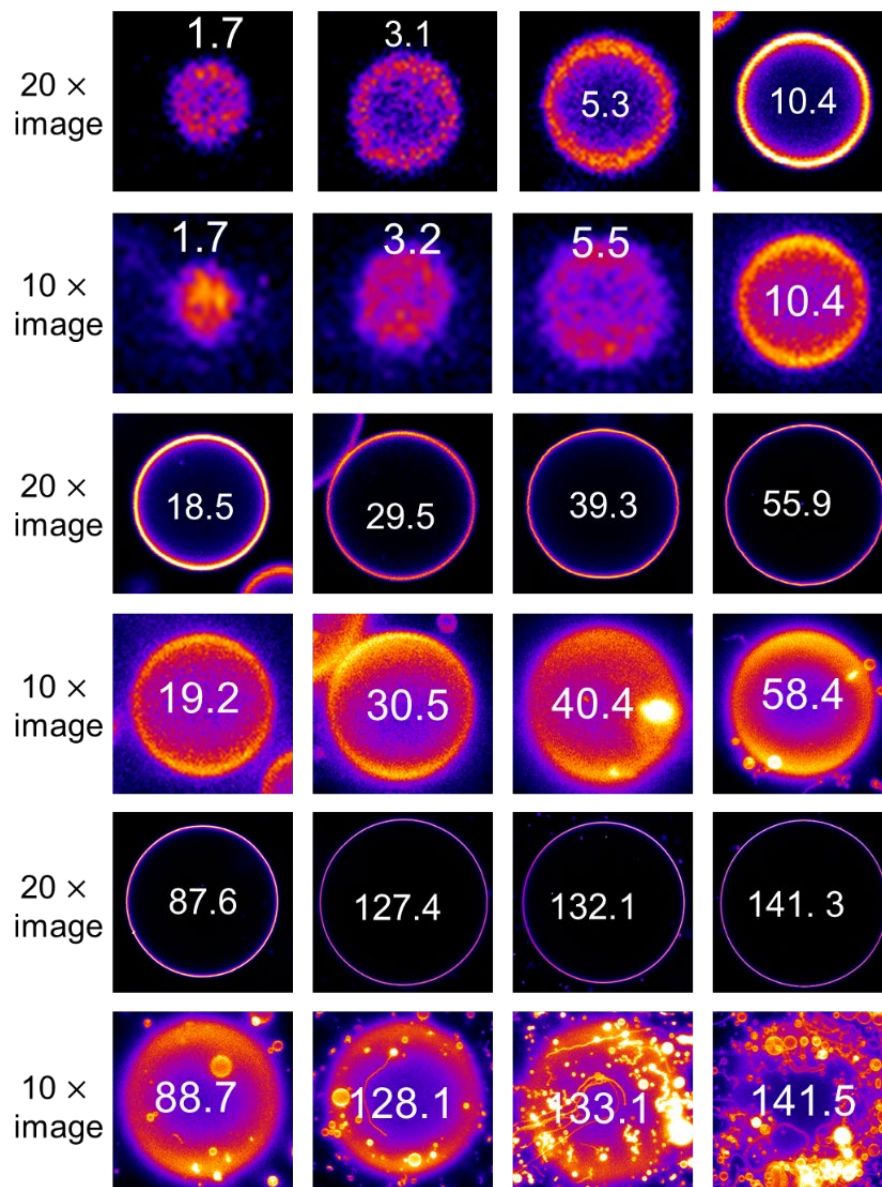


Figure 20: Comparison between the diameters measured in the equatorial plane image and the open pinhole image. Manual measurements in ImageJ (white numbers in μm) confirm the size of the GUVs are accurately depicted in the open pinhole images.

the interior of the GUVs to increase. However, I find the true edges of the GUVs in the open pinhole images are clearly identifiable since the brightest pixels that form a ring around the dimmer interior correlate well with the edges. When these outside edges of the brightest pixels are used to define the edges of the GUVs in the open pinhole images, the diameters measured in ImageJ match within 5% to the diameters previously measured in the closed pinhole images.

3.3.4 Summary of optimal image capture routines

Table 4 shows the number of z-slices required to image a $79.3 \mu\text{m}$ optical section, the number of tiles required to image a $6 \text{ mm} \times 6 \text{ mm}$ area, and the time required to capture an entire tilescan for each of the objective and pinhole settings that were investigated. Clearly the use of the $10\times$ objective with an open pinhole allows for the fastest analysis of the largest number of vesicles and is the most practical configuration to implement to analyze a large dataset of GUVs. Specifically the $10\times$ open pinhole imaging configuration only requires 64 images and 44 minutes to collect data on the population of vesicles, whereas the remaining methods would be impractical requiring between 896 – 13,568 images and 612 – 11,759 minutes to collect data on the same population of vesicles.

Imaging conditions	Number of z-slices	Number of images in tilescan	Total capture time (minutes)
10× pinhole open	1	64	44
10× pinhole closed	14	896	612
20× pinhole open	4	1,024	888
20× pinhole closed	53	13,568	11,759

Table 4: Practical limitations of imaging conditions. The number of z-slices required to image a $79.3 \mu\text{m}$ optical section, the number of tiles required to image a $6 \text{ mm} \times 6 \text{ mm}$ area, and the time required to collect all of the images in a single experiment are shown in the columns of the table for the various imaging conditions investigated.

3.3.5 Intensity characteristics of GUVs

Next, I analyze the fluorescence properties of the open-pinhole fluorescent GUVs. Figure 21 shows the line profiles of the gold standard vesicles along with the various statistics on the pixel intensities of each vesicle. From the line profiles, it is clear that the properties of the GUVs depend significantly on size. The larger vesicles typically have higher overall mean intensity as well as a higher coefficient of variation in intensity. Figure 22 shows a plot of the mean intensity and coefficient of variation in intensity determined by both the line profile (red) and the code (blue) for the gold standard vesicles. Overall the GUVs have mean intensities that fall over a broad range of values from 35 – 93 arb. units. However, separating the GUVs by size class, it is clear the range in mean intensities narrows where the smaller GUVs ($<10 \mu\text{m}$) have mean intensities that range from 35 – 49 arb. units, larger GUVs with sizes between $10 - 60 \mu\text{m}$ in diameter have intensities that range from 61-93 arb. units and very large GUVs ($> 60 \mu\text{m}$) have mean intensities that range from 40 – 43 arb. units. This dependence on the mean intensity of the vesicle according to size is expected due to differences between the location of the equatorial plane of the GUV and the imaging focal plane. For example, GUVs smaller than $10 \mu\text{m}$ are expected to have equatorial planes that fall below the focal plane set at $5 \mu\text{m}$ above the surface of the glass, while very large GUVs will have equatorial planes much further above the focal plane. In contrast to mean intensity, the coefficient of variation of intensity steadily rises from around 0.2 for small GUVs to 0.6 for large GUVs. This steady rise is likely due to both the bright ring that emerges in the image for GUVs $\geq 10 \mu\text{m}$ as well as the presence of other vesicles trapped beneath the larger vesicles after sedimentation.

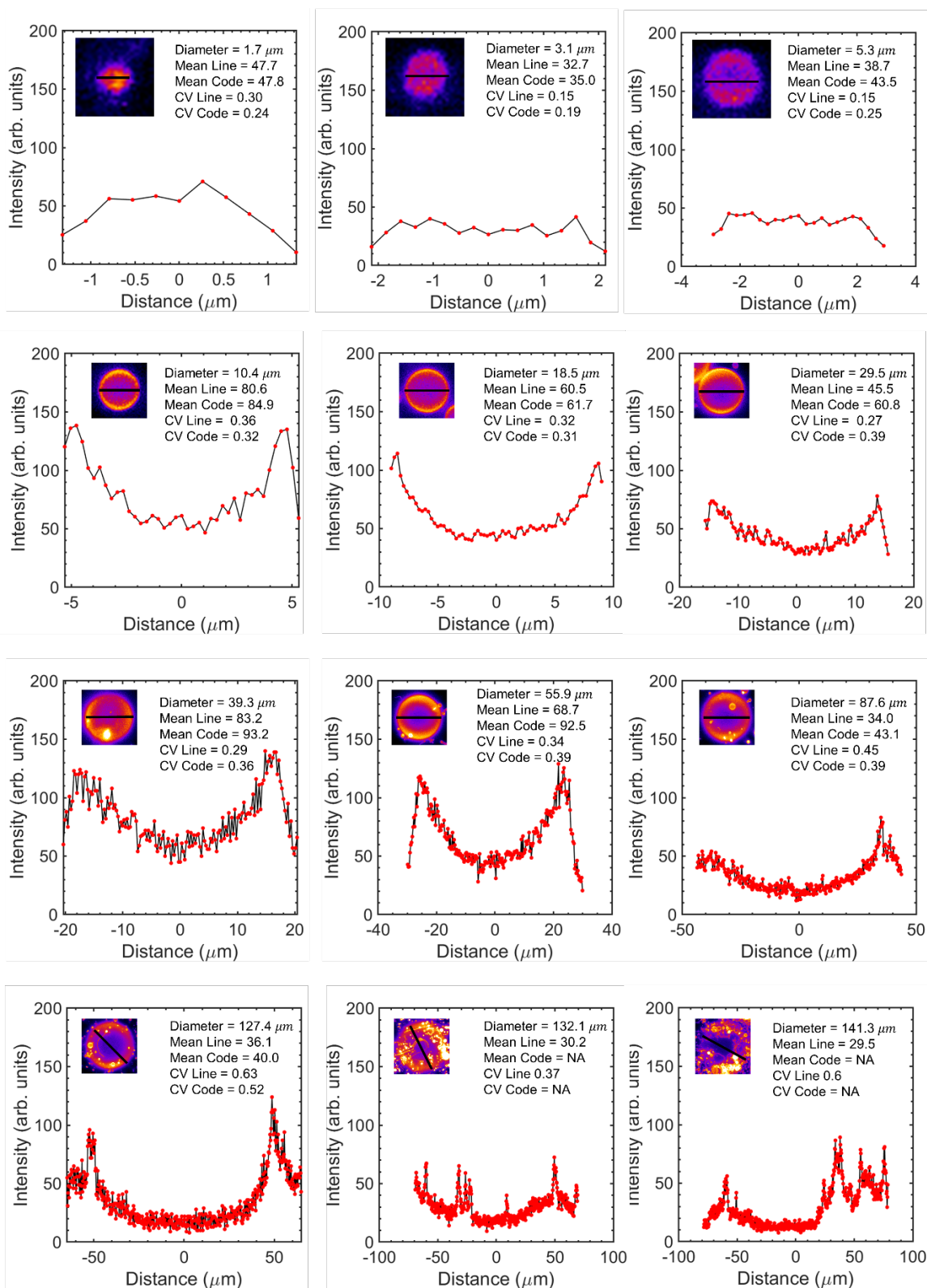


Figure 21: Effect of GUV size on pixel intensities. Line profiles of various gold standard GUVs with different sizes. The inset shows the region along each GUV where the line profile was taken (black line). The mean intensity and coefficient of variation in intensity of the pixels values from the line profile and the code were obtained and written into each plot. These variations in imaging characteristics will be useful for quantifying the GUVs using image analysis.

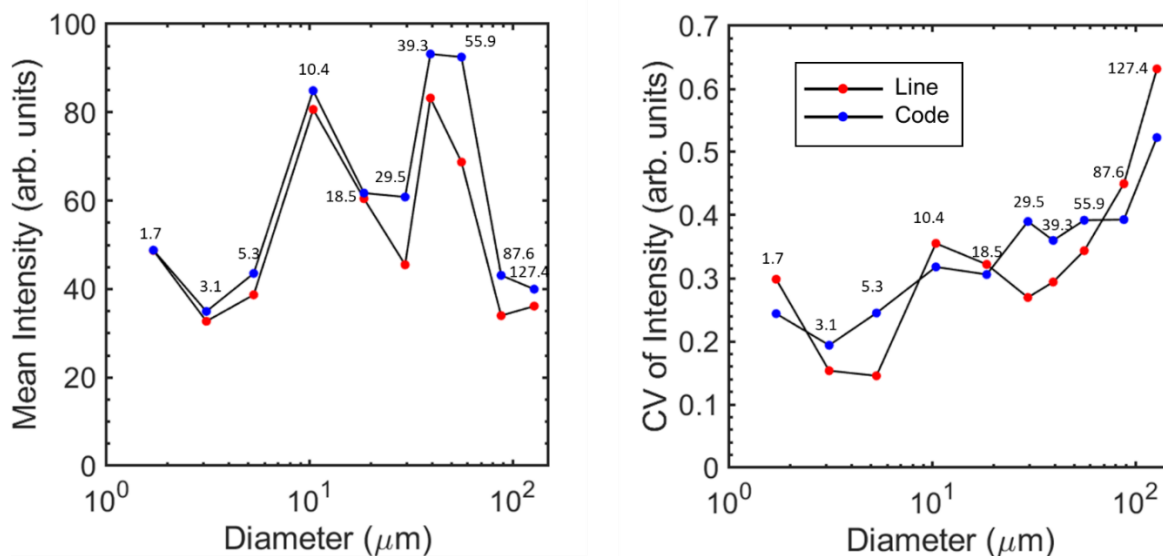


Figure 22: Intensity statistics of gold standard GUVs. Gold standard GUVs show the mean intensity of the GUV depends on the size of the GUV, and CV of intensity increases with increasing size. The smaller GUVs (<10 micrometers) have mean intensities that range from 35 – 49 arb. units while the larger GUVs (10-60 micrometers) have intensities that range from 61 – 93 because the smaller GUVs fall below the focal plane. Very large GUVs (>60 micrometers) also have lower mean intensities that range from 40 – 43 arb. units since the top of the GUVs fall above the focal plane. In contrast, the coefficient of variation of the intensity increases steadily from small GUVs to large GUVs due to the emergence of much brighter rings that emerge for GUVs with sizes above 10 micrometers due to the sedimentation of smaller vesicles beneath these larger GUVs. The red dots signify the results from the line profile and the blue dots signify the results from the code.

3.4 Large dataset collection

Using the 10 \times objective and open pinhole configuration to collect images on populations of vesicles, in this section I standardize the image collection process for large datasets.

3.4.1 Microscope settings used to collect images of vesicles

To visualize the vesicles, excitation of the TopFluor[®] dye was performed using a 488 nm argon laser and emission was collected using a GaAsP detector with a main beam splitter (MBS) for the visible laser light line of 488/561/633 and a detector wavelength range from

489 – 700 nm. The laser power was set at 4.0 % (max power 25 mW) and the detector gain was set at 500. The confocal pinhole size was set to max which was 15.16 Airy Units or 79.3 μm . Using the LSM 880 confocal setup and a 10X/0.45 NA plan-apochromat objective a zoom of 1.0 provided a field of view of 850.19 $\mu\text{m} \times 850.19 \mu\text{m}$. Following the Nyquist resolution criteria (twofold oversampling), the optimal frame size was 3212 pixels \times 3212 pixels with a pixel size of 0.26 μm . I acquired the images with an 8 bit pixel depth from an average of 4 scans per line. The scan time of each image was approximately 24 seconds. As a quality control due to any potential issues with dye fluorescence concentration or laser strength, I check between experiments to confirm that the mean intensity of GUVs with sizes of approximately 10 μm in diameter is around 70 ± 10 arb. units. If the GUVs are clearly much brighter or darker than normal, I adjust the laser power until the 10 μm diameter GUVs have mean intensities between 70 ± 10 arb. units.

3.4.2 Collection of large datasets using a tilescan imaging routine

Typically following sedimentation there is a nonhomogeneous distribution of vesicles throughout the entirety of the chamber (Figure 23). To collect data on a statistically significant portion of the GUV population while ensuring the data is not biased due to gradients in the density of the vesicles at the different locations imaged inside the chamber, I developed a tilescan protocol to collect images of the entirety of the imaging chamber. The tilescan imaging protocol consists of a total of 64 images in a square layout with dimensions of 8 images \times 8 images (with 0% overlap) covering a total area of approximately 6802 $\mu\text{m} \times 6802 \mu\text{m}$. Due to the non-flatness of the stage, I used an autofocus routine to optimally focus the GUVs in each image. A typical example of a harvested vesicle image can be seen in in the zoomed in panels (red) of Figure 23.

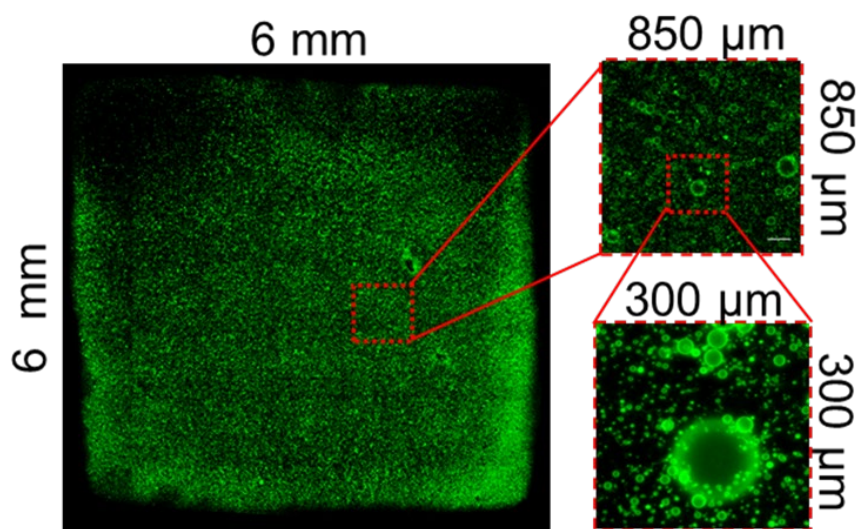


Figure 23: Images of vesicles after sedimentation. An example of a stitched image collected from the typical confocal tilescan routine can be seen on the left. The entire 6 mm \times 6 mm area of the chamber is imaged to account for nonhomogeneous distribution of the vesicles (dark and bright regions). The top right shows a zoom in of a single image from the whole tilescan and the bottom right shows a further zoom in of the typical vesicles assembled from nanocellulose paper.

4. Image analysis routine and code

I next developed an automated image analysis routine that can accurately select GUVs from the confocal images. An overall processes diagram of the custom code developed in Matlab to analyze the images in this work is shown in Figure 24. The main structure of the code can be broken up into two subscripts i) *SegmentObjects.m* which segments all of the foreground objects in the image and ii) *SelectObjects.m* which selects the objects with a coefficient of variance that is characteristic of GUVs. The segmentation portion determines the location of all pixels in the image that contain lipids and segments touching groups of pixels together into individual objects. The selection portion determines from the segmented groups which objects are GUVs and which objects are not GUVs. To ease the readability, usability, and any maintenance of the code, a few additional subscripts are also used which include iii) *GenerateMontageSegmented.m*, a script to produce an image with an overlay of the segmented objects chosen to contain lipids, iv) *GenerateMontageSelected.m*, a script to produce an image with an overlay of the objects selected as GUVs, and vi) *Run_All.m*, a script to run all of the scripts at once.

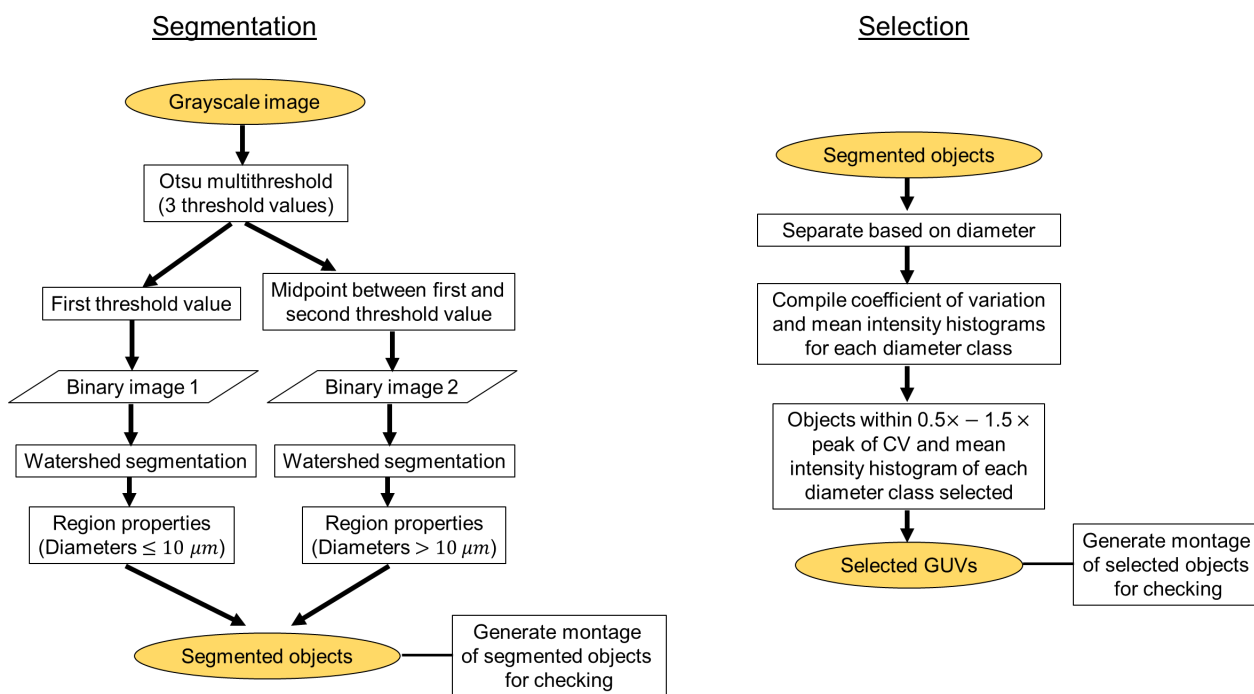


Figure 24: Flowchart of the image analysis code. Flowchart showing the step by step process of the image analysis routine. The yellow circles (terminator symbols) indicate the starting and ending point of i) the segmentation process and ii) the selection process. The rectangles (process symbols) indicate the processes performed on the data. Additional information such as specific settings typically used in each process are extended in the rectangles to the right of each process. The trapezoids (data symbol) represent the data obtained after each process.

To enable automated measurements, the vesicles must first be well defined from each other and distinguished from the background. This process, known as segmentation, can be performed using a variety of different techniques depending on the properties of the image and the features of interest¹⁷³. In this work, I focus on the segmentation of any bright, non-background, lipid object present in the images produced by the confocal. The confocal, which uses a PMT detector that counts and normalizes the photons emitted to a particular bit depth, produces monochromatic grayscale images. These grayscale images consist of pixels that have intensity values corresponding to their brightness¹⁷³, which in this case is the relative number of photons collected at each pixel. Some of the most common segmentation methods employed on grayscale images include thresholding techniques with various post processing operations such as erosion, dilation, and closing and Euclidean distance map techniques such as the watershed transformation, Hough transformation, and skeletonization¹⁷³. In this section, I show the optimal segmentation of the bright, non-background lipid objects in the images can be obtained automatically through a combination of thresholding, watershed, and post process closing techniques.

I design the tilescan experiments to maximize the statistical sampling of the vesicles mixed in solution while minimizing the overcrowding of vesicles during imaging. Although minimizing overcrowding simplifies the automated segmentation process, there are still many instances over the area of the tilescan where the fluorescent signal of the circular vesicles overlap. Among the various image segmentation methods, the preferred technique employed to separate touching, convex features is the watershed transformation^{173,174}, which has been used previously for the segmentation of other fluorescent objects in images including GUVs¹¹³, closely touching cells¹⁷⁵, and the cell nucleus¹⁷⁶. The process can operate directly on the grayscale images collected by the confocal. Briefly, the watershed algorithm uses a distance transform on the image to calculate the linear distance of each pixel to an edge^{173,174}. Replacing each pixel in the original image with the vector associated with the linear distance to the edge results in the distance transform image (Figure 25). The watershed algorithm then uses the resulting peaks, valleys, and saddles (pixels between neighboring peaks) in the distance transform image to obtain the segmented, watershed transformed image^{173,174} (Figure 25c).

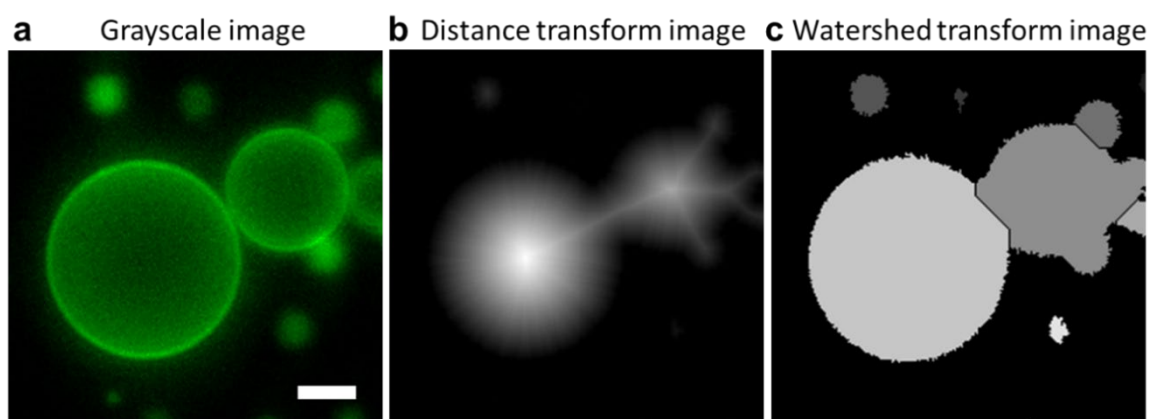


Figure 25: Steps to obtain watershed transformed image. Applying the watershed algorithm on **a** typical confocal image of neighboring GUVs results in the **b** computed

distance transform of the image and the **c** watershed transformed image where the dark lines show the contours of the now divided GUVs. Scale bar **a-c** 10 μm .

4.1 Segmentation of fluorescent objects

4.1.1 Watershed segmentation on grayscale images

To evaluate the ability of the watershed method to segment the grayscale images directly obtained from the confocal, I run the algorithm on three representative tilescan images. I select these images to test the ability of the method to segment images with i) smaller and less densely packed vesicles (Figure 26a), ii) larger and more densely packed vesicles (Figure 26b), and iii) many aggregates and highly densely packed vesicles (Figure 26c). An overlay of the objects segmented by the watershed algorithm is shown below each image with the different colors being added to help distinguish the segmented objects (Figure 26d-f). The segmentation is poor. Firstly, the segmented regions are significantly larger than the size of the objects in the grayscale image, especially for vesicles larger than approximately 10 μm . Secondly, visually distinct isolated vesicles appear to be segmented as a single connected object. Thirdly, larger vesicles appear to be oversegmented that is the single vesicles is detected as different split objects. Oversegmentation appears common for vesicles larger than approximately 20 μm .

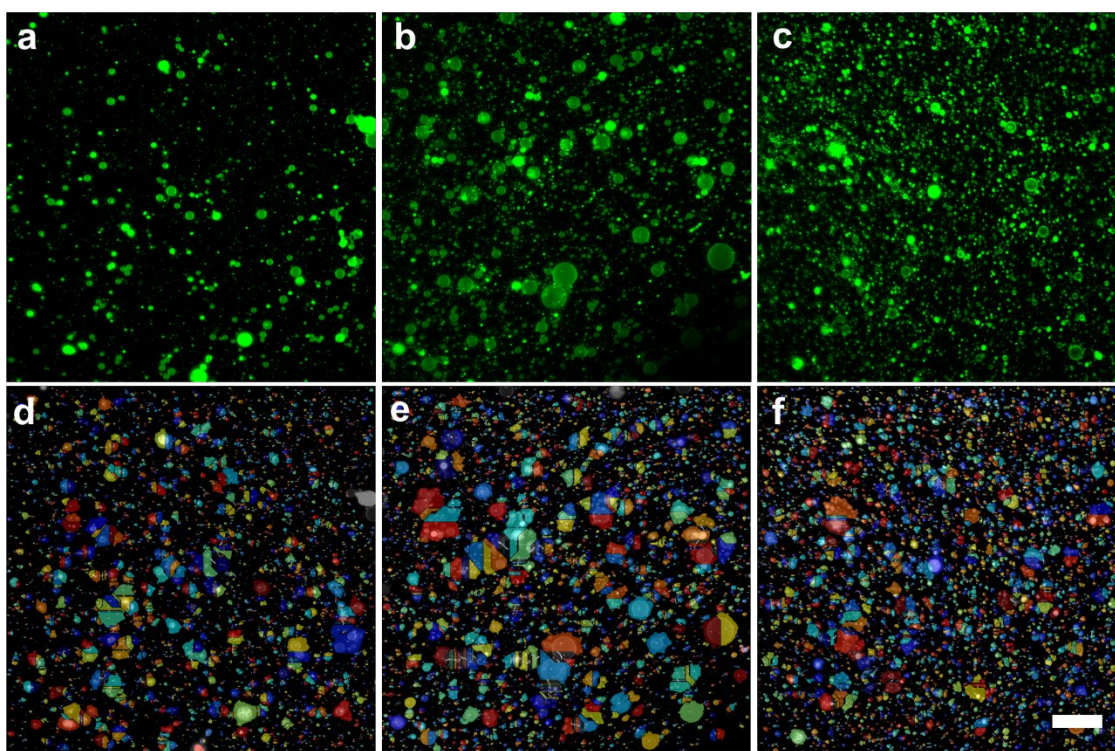


Figure 26: Watershed transformation of grayscale images. **a-c** Grayscale images used to test the effects of image processing on images with a sparsely distributed and smaller

vesicles, **b** densely packed and larger vesicles, and **c** densely packed vesicles with many aggregates. **d-f** Overlay of the watershed transformation from the grayscale images with **d** sparsely distributed and smaller vesicles, **e** densely packed and larger vesicles, and **f** densely packed vesicles with many aggregates. The different colors show the regions segmented as individual objects using the watershed transformation. Scale bar **a-f** 100 μm .

4.1.2 Histogram analysis

Through observation of multiple images, I hypothesized that the open pinhole results in a halo of out of focus light which affects image analysis. To test this hypothesis, I analyze the intensity histograms from representative images shown in Figure 26. Figure 27a-c shows the three representative images from a tilescan routine with the corresponding histograms on a semilog-y plot below. The first two histograms (Figure 27d,e) have 3 different peaks where the first peak in the histogram is at 2 AU, the second peak is around 50 AU, and the third peak is at 255 AU. The last histogram (Figure 27f) has 2 peaks at the same locations as the first and third peaks in the previous histograms but does not have a clear peak in the middle since any potential bump is indistinguishable from the downward slope of the first peak. Generally, the bins that fall under each of the peaks can be placed into three categories. The first bump in the intensity histograms is mostly from the background noise and is the largest bump in the histogram since the experiment is designed to ensure the vesicles are not overly crowded and that there is plenty of dark pixels between each vesicle. The second bump is mostly from the intensity of the GUVs in the image, and the location of this bump in the histogram depends on a number of factors such as the fluorescent dye concentration, pinhole size, or laser power, as well as experimental variables such as the number and size of the GUVs from each different sample. Since the imaging factors are always kept the same for quantification experiments, the location of the bump mostly depends on the number and size of the GUVs in the image and becomes an important location to define in the analysis of the images. The last spike in the histogram is from the MLVs, MVVs, and aggregates present in the sample and is located in the highest intensity bin since these structures have such high concentrations of fluorescent lipid. Given the imaging factors are held constant and designed to focus on the GUVs, only the size of this spike changes between samples and is dependent on the number and size of MLVs, MVVs, or aggregates present in a sample.

To define quantitative boundaries within the intensity histogram, I use an Otsu thresholding method that is useful in the analysis of multimodal histograms^{173,177,178}. The Otsu method analyzes the intensity histogram by iterating over each possible pixel value from left to right, setting an intensity boundary, and calculating the intra-class variance between the pixels from each group¹⁷⁹. After the iteration is complete, the boundary values that lead to the lowest variance are selected as the Otsu values¹⁷⁹. Otsu thresholding could be used to calculate an optimal boundary value for histograms containing multiple groups¹⁷⁸. Empirically I find that three boundary values separate the image pixels into useful categories for analysis.

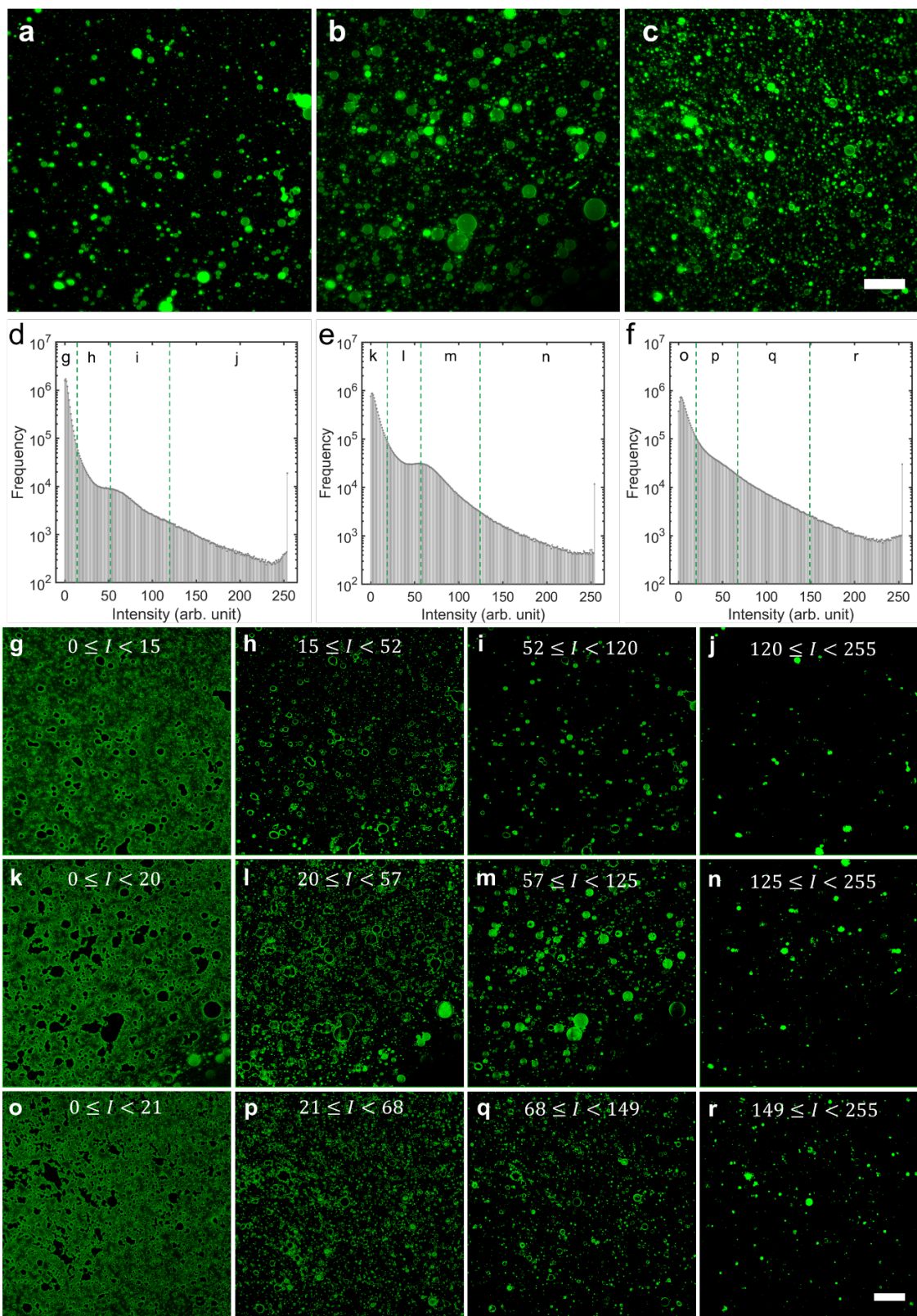


Figure 27: Analysis of grayscale images using the Otsu method. **a-c** Grayscale images used to test segmentation (same as in Figure 26). **d-f** Histograms showing the distribution of the intensities of all of the pixels in **d** image **a**, **e** image **b**, and **f** image **c**. The location of the three threshold values calculated using the Otsu method in each histogram are shown as green dashed lines. **g-f** Partially thresholded images corresponding only the pixel intensities of the bins alphabetically marked (letters between the green dashed lines) in the histograms. The exact intensity bins (I) calculated by the Otsu method are written in each image. Scale bars **a-c** 100 μm , **g-r** 100 μm .

Figure 27g-r show the resulting images calculated using the Otsu threshold to determine the three boundary values (marked as green dashed lines in the histograms). The first group of bins in each of the histograms contains the fluorescence intensity of the background noise, most of the diffuse light from the halo that surrounds the vesicles, and some of the light from the smaller vesicles (Figure 27g,k,o). The second group of bins mostly contains the fluorescence intensity of smaller GUVs and some dimmer diffuse light from the larger vesicles (Figure 27h,l,p). The remaining fluorescence information contained above this threshold value includes the third group of bins which contain the remaining fluorescence signal from the larger GUVs (Figure 27i, j, q), and the final group of bins which contain only the fluorescence signal of the MLVs, MVVs and aggregates (Figure 27j, n, r). Amongst the three different test images with different intensity histograms, the final thresholds determined by the Otsu threshold method split the image into the same four groups. These groups are i) the background noise and diffuse light, ii) diffuse light information contained above this threshold value includes the third group of bins which contain the remaining fluorescence signal from the larger GUVs (Figure 27i, j, q), and the final group of bins which contain only the fluorescence signal of the MLVs, MVVs and aggregates (Figure 27j,n,r). Amongst the three different test images with different intensity histograms, the final boundary determined by the Otsu threshold method split the image into the same four groups. These groups are i) the background noise and diffuse light, ii) diffuse light and smaller GUVs, iii) larger GUVs, and iv) MLVs, MVVs, and aggregates. This analysis appears consistent with my hypothesis that the background noise and diffuse light around the vesicles interferes with segmentation. A potential solution to address this is to threshold out the noise and diffuse light and convert the image to binary.

4.1.3 Watershed segmentation on binary images

To separate the background noise and diffuse light from the pixels associated with lipid objects in the image, I convert the grayscale image into a binary image where the value of each pixel is thresholded to either a 0 (background) or 1 (foreground)¹⁷³. I use the first boundary value determined using the Otsu thresholding method to threshold the representative images of the vesicles (Figure 28a-c) into binary images (Figure 28d-f). Figure 28g-q shows the results after applying the watershed segmentation on the binary images. For the smaller vesicles (GUVs $< 10 \mu\text{m}$) the watershed method is able to better

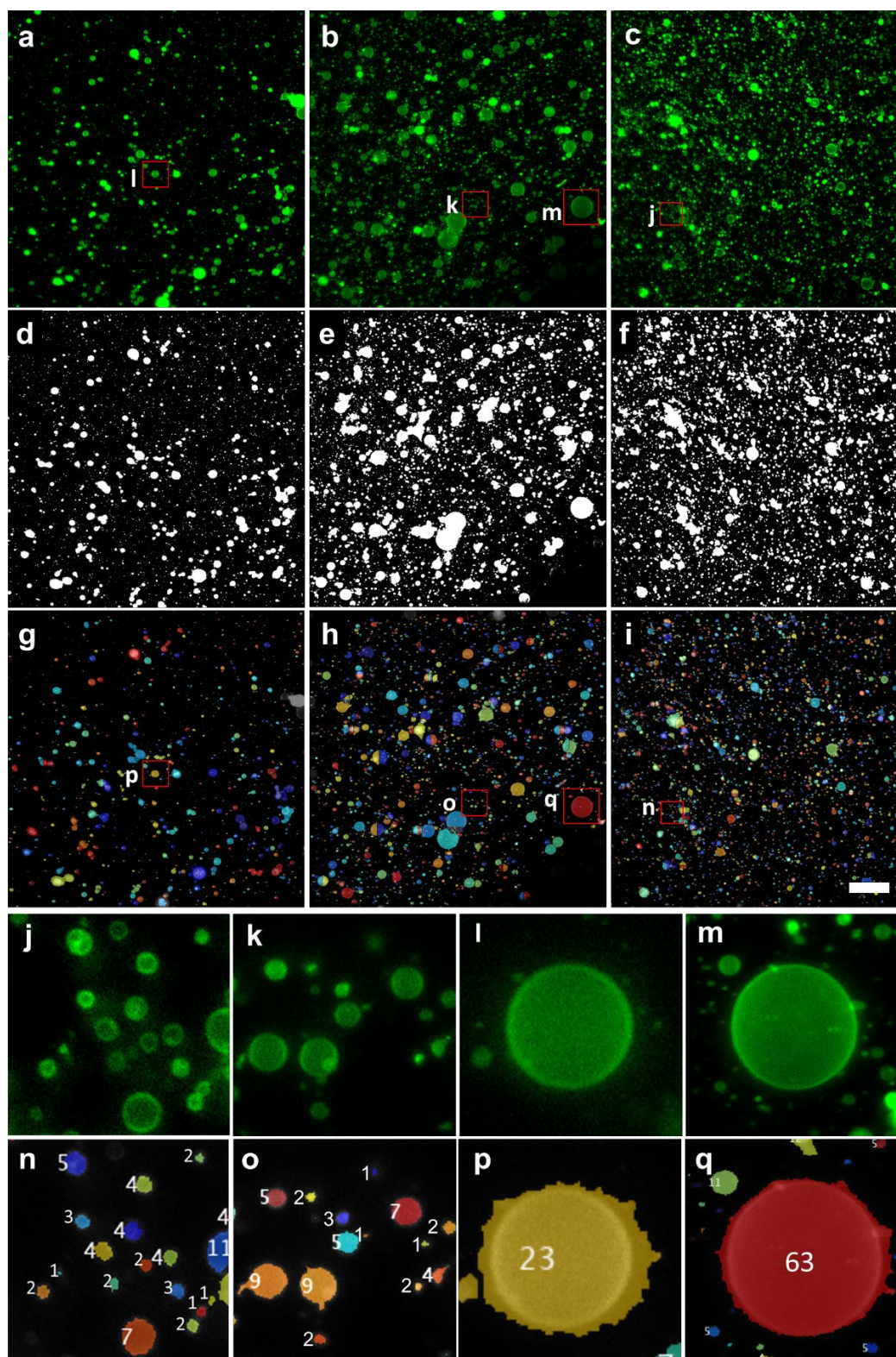


Figure 28: Watershed segmentation of binary images. **a-c** Grayscale images used to test segmentation (same as in Figures 26). **d-f** Binary images of **d** image **a**, **e** image **b**, and **f** image **c** thresholded using the lowest threshold value calculated by the Otsu method. **g-i** Overlay of the watershed transformation from the binary images of **g** image **d**, **h** image **e**, and **i** image **f**. The different colors show the regions segmented as individual objects using the watershed transformation. **j-q** Zoomed in view corresponding to the regions marked alphabetically in **a-i**. Scale bar **a-i** 100 μm .

segment the binary images and now accurately captures the morphology of the vesicles. For the larger vesicles (GUVs $\geq 10 \mu\text{m}$), however, the method appears to overestimate the size of the vesicles (Figure 28p,q). The larger vesicles appear to be overestimated since they typically have brighter diffuse halos surrounding them than the smaller vesicles. The diffuse halos of the larger vesicles typically have intensities that fall above the first Otsu threshold value and are included in the binary image.

From the histogram analysis the diffuse area of the larger vesicles appears to have a similar intensity as the vesicles smaller than $10 \mu\text{m}$ in diameter. One potential solution is to threshold at a higher intensity value before applying the watershed segmentation. However, the higher intensity value will threshold out the smaller GUVs as well. To address this issue, I threshold the images into two different binary images. The first binary image I obtain using the first Otsu threshold value the same as before. However the second binary image I obtain using a higher threshold value specifically for GUVs $\geq 10 \mu\text{m}$ in diameter. Since some of the diffuse light of the larger vesicles is captured between the first and second Otsu threshold values (Figure 28h,l,p), I use the midpoint between the first and second Otsu threshold values to threshold the grayscale image into a second binary image. Figure 29 shows the results of this analysis on vesicles ranging in size from 1 to $150 \mu\text{m}$ in diameter. To create a gold standard, the diameters of the vesicles were also measured manually from images collected at the equatorial plane of the vesicles using the $20\times$ objective with the pinhole closed. Regardless of size, all of the vesicles are accurately segmented within 5% of gold standard using this routine.

A limitation of this automated analysis is in the detection of GUVs $\geq 130 \mu\text{m}$ in diameter (last 2 rows of Figure 29). The equatorial plane of a GUV in this size class is far enough outside the slice thickness that the fluorescence signal is extremely close to the background signal. In addition, these vesicles, due to the large area they occupy, typically have more than 10 – 100 fluorescent objects that sediment underneath them, further complicating the segmentation process. As a check after the automatic thresholding routine, I manually inspect the images and add any GUVs $\geq 130 \mu\text{m}$ to the dataset.

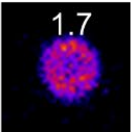
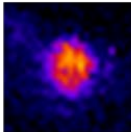
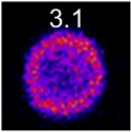
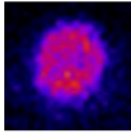
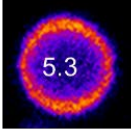
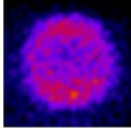
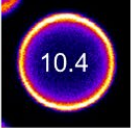
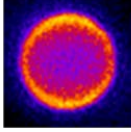
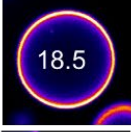
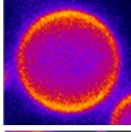
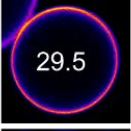
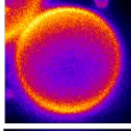
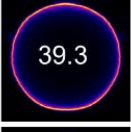
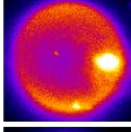
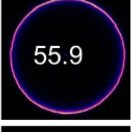
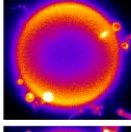
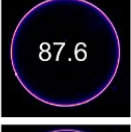
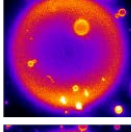

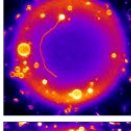
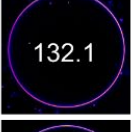
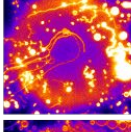

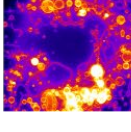
20 × image	10 × image	Code	True Diameter (μm)	Measured Diameter (μm)	$\frac{\text{Measured}}{\text{True}}$	Error (%)
		1.7	1.7	1.7	1.00	0.0
		3.2	3.1	3.2	1.03	-3.2
		5.5	5.3	5.5	1.04	-3.8
		10.4	10.4	10.4	1.0	0.0
		19.2	18.5	19.2	1.04	-3.8
		30.5	29.5	30.5	1.03	-3.4
		40.4	39.3	40.4	1.03	-2.8
		58.4	55.9	58.4	1.04	-4.5
		88.7	87.6	88.7	1.01	-1.3
		128.1	127.4	128.1	1.01	-0.5
		Not detected	132.05	NA	NA	NA
		Not detected	141.3	NA	NA	NA

Figure 29: Accuracy of diameter measurements. The first column shows high resolution images of vesicles of various sizes that were captured using a 20× objective with the confocal pinhole completely closed. The equivalent diameters measured in ImageJ are written in each image in μm . The second column shows images of the same vesicles that were captured with the typical tilescan settings that use a 10× objective with the confocal pinhole completely open. The third column shows the sizes of the vesicles determined by image analysis routine. The fourth column shows the diameter closest to the true diameter of the vesicle from the 20× image. The fifth column shows the diameter measured using the 10× image and image analysis routine. The sixth and seventh columns show respectively the ratio and percent error between the measured and true diameter of the vesicles.

4.1.4 Correcting over segmented large vesicles

The gold standard images shown in Figure 29 show that there is a gradient in intensity towards the center of the vesicles. The lower intensity at the center occasionally causes GUVs $\geq 20 \mu\text{m}$ to be oversegmented (segmented into multiple parts) during the watershed segmentation of the binary image (Figure 30a,b). To correct the errors with oversegmentation, I perform a post-process closing method to resegment any potentially oversegmented object. To select the objects that are potentially oversegmented, I call the native *regionprops* function¹⁸⁰ on the now watershed transformed image to measure the eccentricity, deviation of an object from a perfect circle, and collect the pixel locations of all of the objects in the image. The *regionprops* function organizes all of the objects in the image and orders them in a list collects various useful properties of the objects¹⁸⁰. Using the ‘*Eccentricity*’ command, I calculate the ratio between the major and minor axis lengths of all of the objects in the image. A perfect circle will have an eccentricity value of 0 while a line segment will have an eccentricity value of 1. Since I expect the oversegmented objects to deviate further from the circular shape of the vesicles, I treat any objects that have an eccentricity value higher than 0.6 as potentially oversegmented. Using the ‘*PixelIdxList*’ command, I create a list of the location of all of the objects in the image. Since the *regionprops* function organizes the lists by object, I can specifically select the locations of the pixels that correspond to objects that meet the eccentricity criteria for being potentially oversegmented. These pixels are then mapped onto a new binary image that contains only these potentially oversegmented objects to be processed. To correct oversegmentation, I use a closing operation to close gaps between neighboring objects^{173,180}, specifically dark gaps of only 1 pixel. I recombine the morphologically closed binary image with the watershed transformed binary image and show the results of the final segmented image in Figure 30c. The correction significantly improves the segmentation of the larger GUV objects that were previously oversegmented (marked with white arrows). On this final segmented image, I call the native *regionprops* function to collect various properties such as the pixel locations, the pixel values, the total areas, the equivalent diameters, and the mean intensities, of the objects that will be used for GUV analysis.

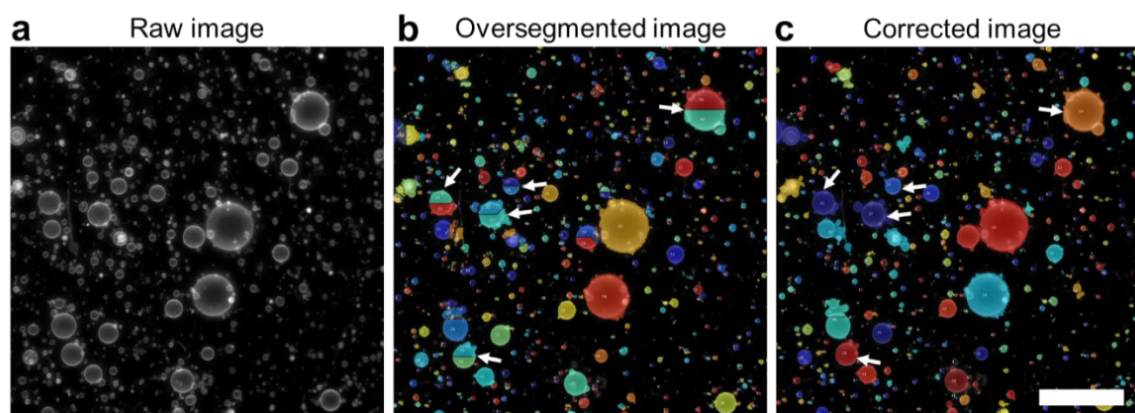


Figure 30: Correction of oversegmentation errors to obtain final segmented image. a Typical image of larger vesicles that are more prone to oversegmentation errors. **b** Objects segmented from the binary image. **c** Objects segmented after correcting the image in **b** using a closing process. Scale bar **a-c** 100 μm .

4.2 Selection of GUVs

4.2.1 Discrimination based on coefficient of variation to remove poorly segmented objects and MVVs

Even with the double thresholding, there are still some objects that are poorly segmented. I first remove any poorly segmented objects by performing a selection based on the coefficient of variation of the objects. A signature of a poorly segmented object is an object that has a high variation in the values of its pixels and can be quantified using the coefficient of variation. The coefficient of variation or CV is simply the standard deviation over the mean of the pixel values. I find that poorly segmented objects typically have a high CV because many of the incorrectly segmented pixels that are included in the object are background pixels with very low intensities that increase the standard deviation. To determine a criteria that could be used to remove poorly segmented objects, I analyze the CV histograms of a typical sample of vesicles based on size.

To obtain the histograms I pool together the data from 5 aliquots from the same sample of vesicles produced using nanocellulose paper. I split up the histograms based on objects that are within 1 μm steps in size of each other starting with diameters (D) of $1 \leq D < 2$ and then move up. For size classes greater than 30 μm in diameter, which do not have enough data to obtain a histogram, I pool the objects from 30 – 120 μm in diameter together to obtain a histogram and make conclusions about the shape of the histogram. Figure 31 shows the CV histograms of size classes corresponding to the gold standard vesicles. The histograms mostly have a single peak and a long, right-skewed tail. Figure 32 shows various statistics from the CV histograms including the mean, median, and peak location values based on size. Similar to the gold standard vesicles, the CV of intensity of the pooled samples also changes with size, with the first peak location in the CV histograms

matching closely with the gold standard vesicles moving from around 0.2 for 1 μm diameter objects to around 0.4 for 30 μm diameter objects. This close relationship between the location of the peak in the CV histogram and the CV of the gold standard GUVs suggests that most of the data from the tilescan is from GUVs.

To determine a range of CV values that fall outside of the typical range of a GUV, I collect representative images of vesicles from the pooled sample that fall within various ranges around the peak of the CV histogram. Figure 33 shows the typical appearance of 5–6 μm diameter objects that fall i) below $0.5\times$, ii) between $0.5\times - 1.5\times$, and iii) above $1.5\times$ the first peak location in the CV histograms. Using the same CV criteria ranges, the typical appearance of 18–19 μm and $\geq 30 \mu\text{m}$ diameter objects are shown in Figure 34 and Figure 35 respectively. The right and left tail of the CV histograms mostly consist of either poorly segmented objects or MVVs and lipid nanotubes. Objects closer to the peak location of the CV histogram, between $0.5\times - 1.5\times$ the peak location, however are mostly GUVs and some MLVs. Thus, I only use objects that have CVs between $0.5\times - 1.5\times$ the first peak in the CV histogram for the next step in the analysis.

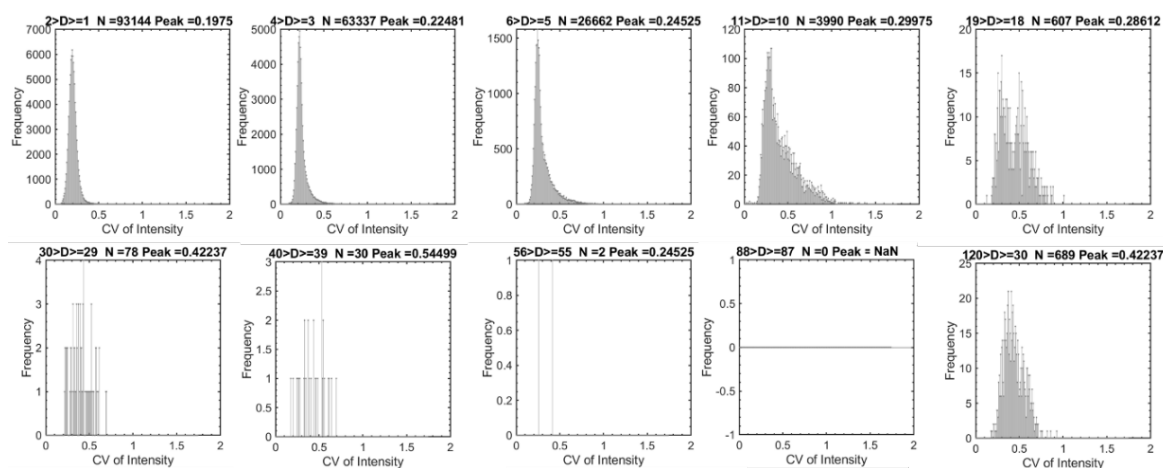


Figure 31: Histograms of the coefficient of variations of objects with diameters consistent with the gold standard vesicles. For the objects with sufficient samples the CV histograms are peaked. The histograms are asymmetric with a longer right tail than the left tail. For vesicles larger than 30 micrometers the number of objects in each size class is small and conclusions about the shape of the histogram cannot be made. Instead grouping the bins for vesicles larger than 30 micrometers can increase the number of objects and allow for conclusions about the shape of the histogram.

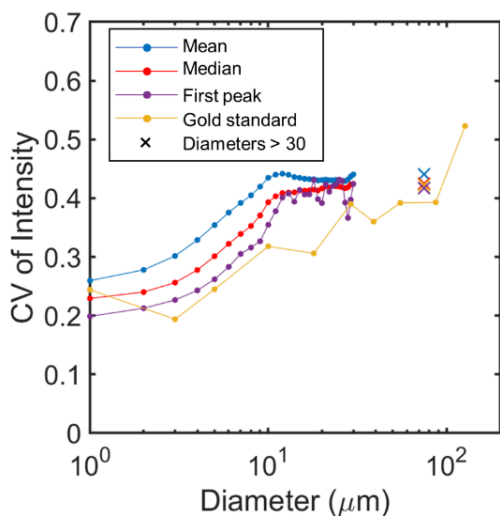


Figure 32: Effect of GUV size on coefficient of variation of intensity histograms. Plot of the mean, median, and peak of the CV histograms from the pooled sample. Note the log scale in the x-axis. Each of the diameter bins from 1 to 30 μm have enough counts to calculate statistics from the shape of the histogram (circles). Diameter bins greater than 30 μm are pooled together (crosses) to obtain histograms. For comparison the values obtained by the code on the gold standard vesicles are also plotted (yellow).

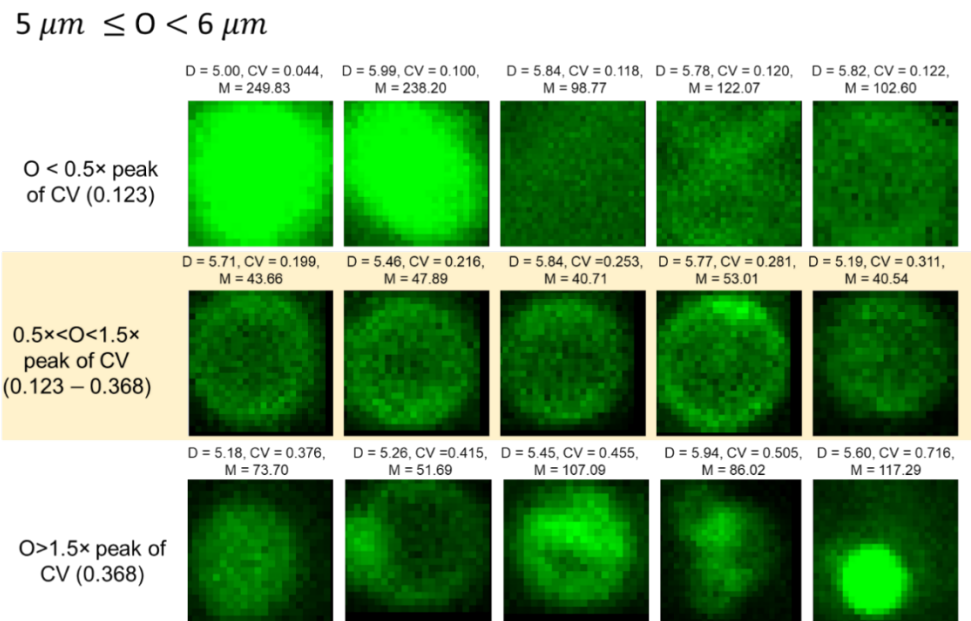


Figure 33: Pixel properties of 5 – 6 μm diameter objects. Representative images of objects between 5 and 6 μm in diameter with coefficient of variation values of less than $0.5 \times$, between $0.5 \times$ – $1.5 \times$, and above $1.5 \times$ the first peak location in the CV histograms.

$18 \mu m \leq O < 19 \mu m$

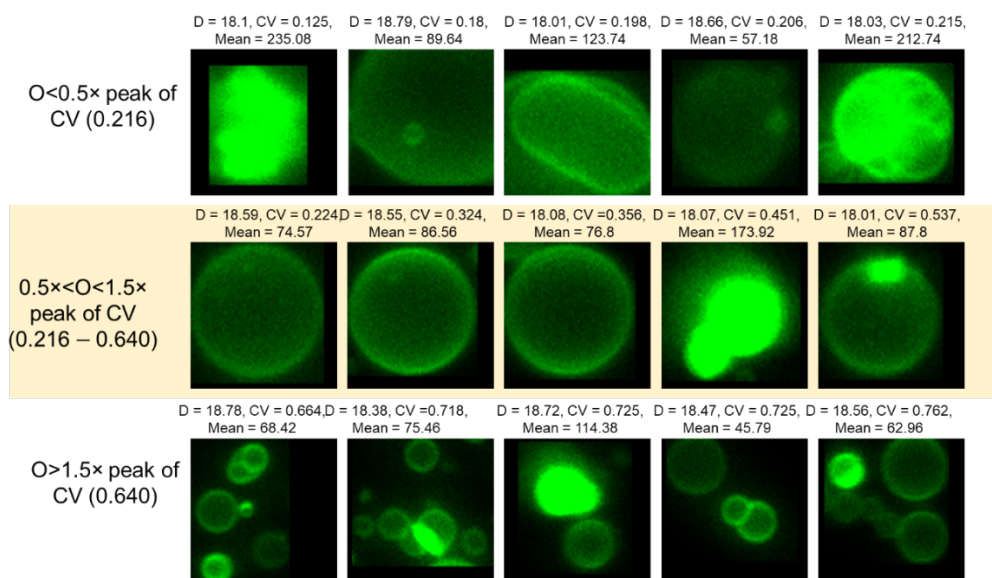


Figure 34: Pixel properties of 18 – 19 μm diameter objects. Representative images of objects between 18 and 19 μm in diameter with coefficient of variation values of less than 0.5×, between 0.5× – 1.5×, and above 1.5× the first peak location in the CV histograms.

$O > 30 \mu m$

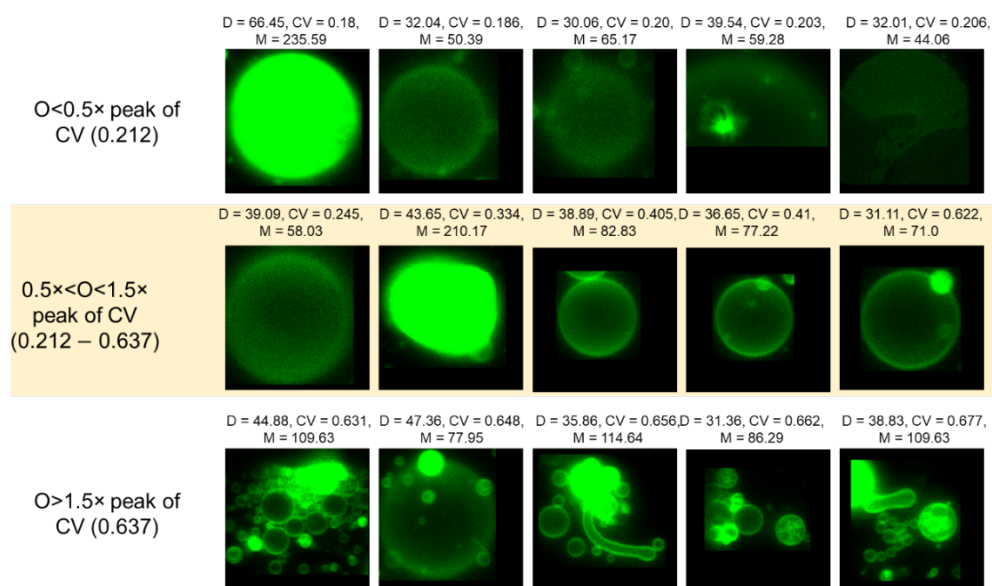


Figure 35: Pixel properties of objects > 30 μm in diameter. Representative images of objects greater than 30 μm in diameter with coefficient of variation values of less than 0.5×, between 0.5× – 1.5×, and above 1.5× the first peak location in the CV histograms.

4.2.2 Selection of GUVs based on mean intensity

To select GUVs from the objects remaining after the CV analysis, I analyze the mean intensity histograms based on size to select for GUVs (Figure 36). In idealized conditions, I expect that MLVs will have intensities that are integer multiples of the GUV intensity. Thus, an MLV with two bilayers is expected to have $2\times$ the mean intensity of a GUV with a single bilayer. In practice however, differences in where the GUVs are located within the image and differences in the background intensity causes there to be some variation of intensities around the mean. The mean intensity histograms show well defined peaks with a right-skewed tail. Figure 37 shows a plot of the change in the location of the peak of the mean intensity histogram with size. The plot matches closely with the change in the mean intensity of the gold standard GUVs confirming that the location around the first peak is indeed composed of GUVs as expected.

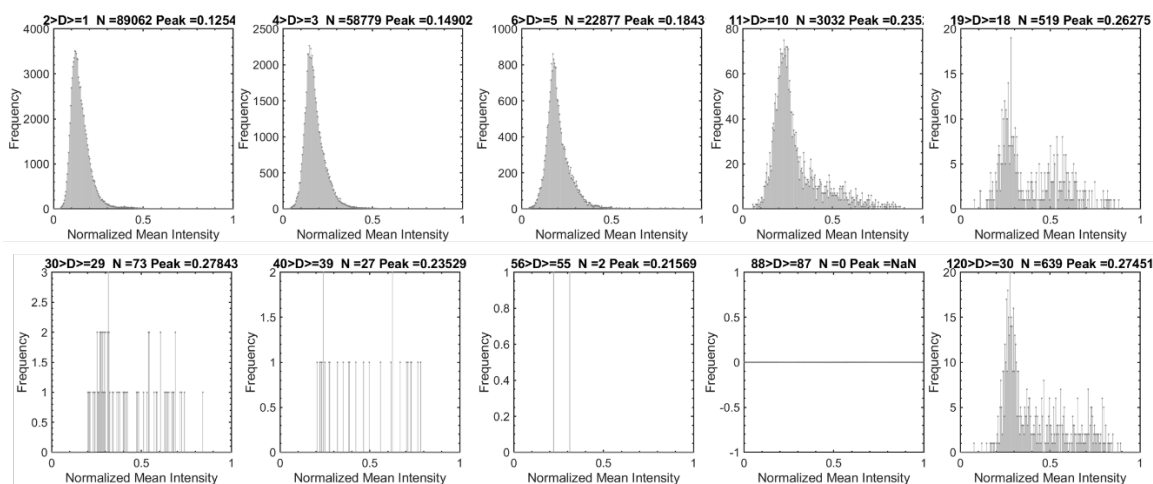


Figure 36: Histograms of the normalized mean intensity of objects with diameters consistent with the gold standard vesicles. For the objects with sufficient samples the normalized mean intensity histograms have a single peak with a longer right tail than left tail. For vesicles larger than $30\ \mu\text{m}$ since the number of objects in each size class is small, the size classes are grouped together to form a histogram.

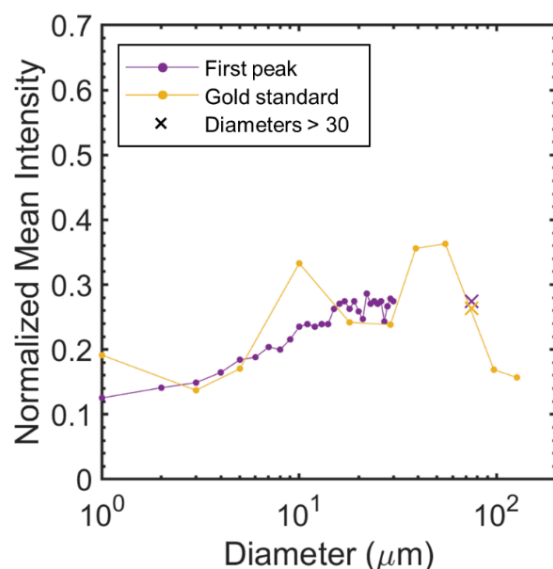


Figure 37: Effect of size on mean intensity of GUVs. Plot of the peak location of the mean intensity histogram from the pooled sample. Note the log scale in the x-axis. For comparison the gold standard values obtained from the code (yellow) are reproduced. The average values match well with the gold standard vesicles demonstrating that most of the objects are consistent with GUVs.

Using a selection criteria of excluding vesicles that are $> 2\times$ the left most peak in intensity resulted in too many vesicles being included that visually did not appear to conform to GUVs. Thus, I empirically determined a more stringent criteria for selection. To determine the range of mean intensity values that correspond to the GUVs, I collect representative images of vesicles from the pooled sample that fall within various ranges. Figure 38 shows the appearance of $5\text{--}6\ \mu\text{m}$ diameter objects that fall i) below $0.5\times$, ii) between $0.5\times - 1.5\times$, and iii) above $1.5\times$ the first peak location in the mean intensity histograms. The appearance of the $18\text{--}19\ \mu\text{m}$ diameter objects and $\geq 30\ \mu\text{m}$ diameter objects are shown in Figures 39 and 40 respectively.

For all of the size classifications, it is clear that the objects above $1.5\times$ the location of the peak of the mean intensity histogram are mostly MLVs and MVVs, and the objects between $0.5\times - 1.5\times$ the peak of the mean intensity histogram are mostly GUVs. Objects below $0.5\times$ are much less common (around 1 per 1000) for each of the size classifications and are typically out-of-focus or poorly segmented objects that were not excluded in the CV criteria analysis. Objects that were previously included in the accepted CV range for GUVs that were clearly non-GUV lipid structures (row 2 and column 4 of Figure 34 and row 2 and column 2 of Figure 35) are now correctly excluded from being characterized as GUVs after additional mean intensity analysis (row 5 and column 3 of Figure 37 and row 5 and column 5 of Figure 38). Thus for the data presented in this work, I define the GUVs as objects within $0.5\times - 1.5\times$ the peak of the CV and mean intensity histogram for each diameter class.

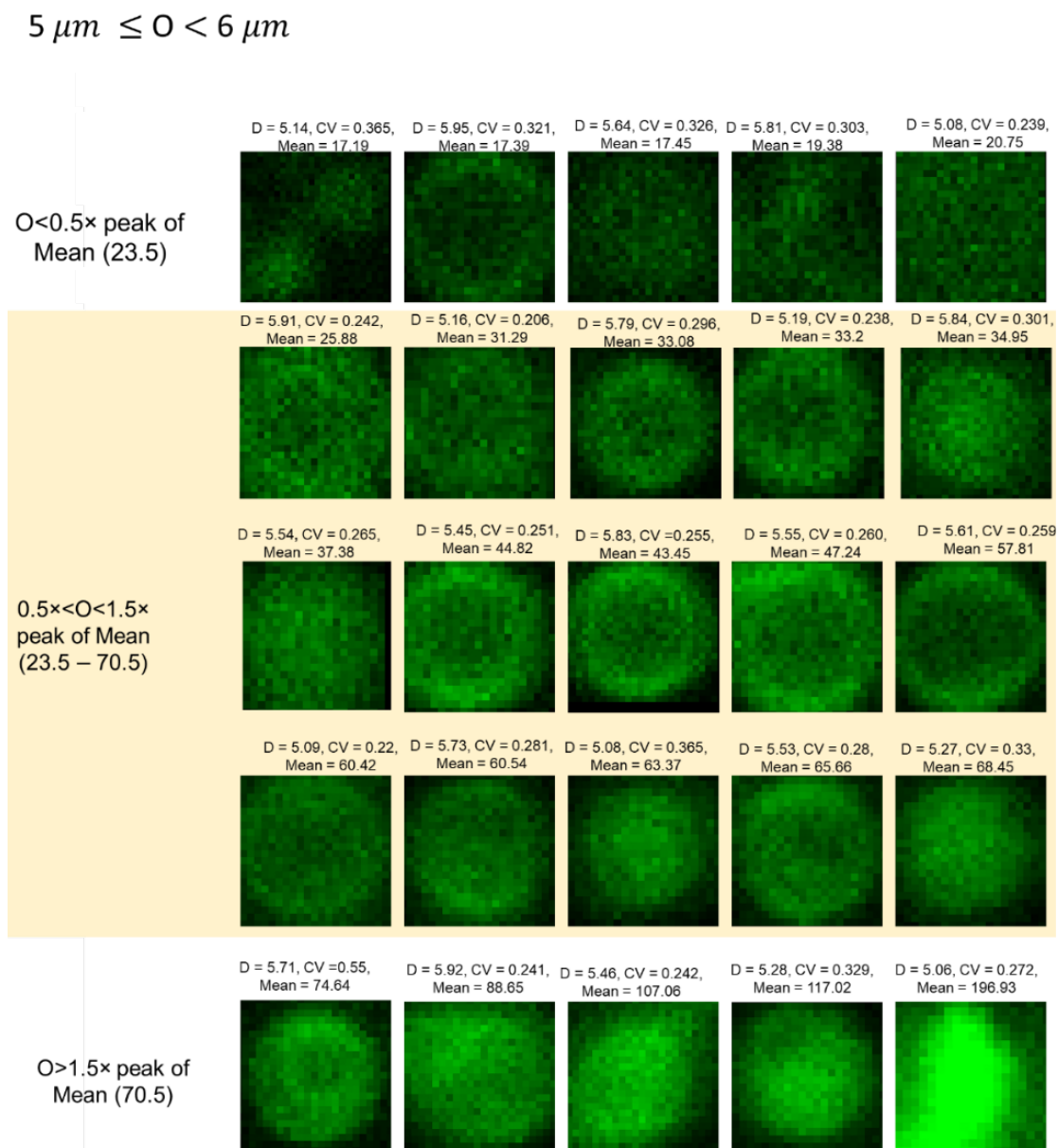


Figure 38: Pixel properties of 5 – 6 μm diameter GUVs. Representative images of objects between 5 and 6 μm in diameter with mean intensity values of less than 0.5 \times , between 0.5 \times – 1.5 \times , and above 1.5 \times the first peak location in the mean intensity histograms.

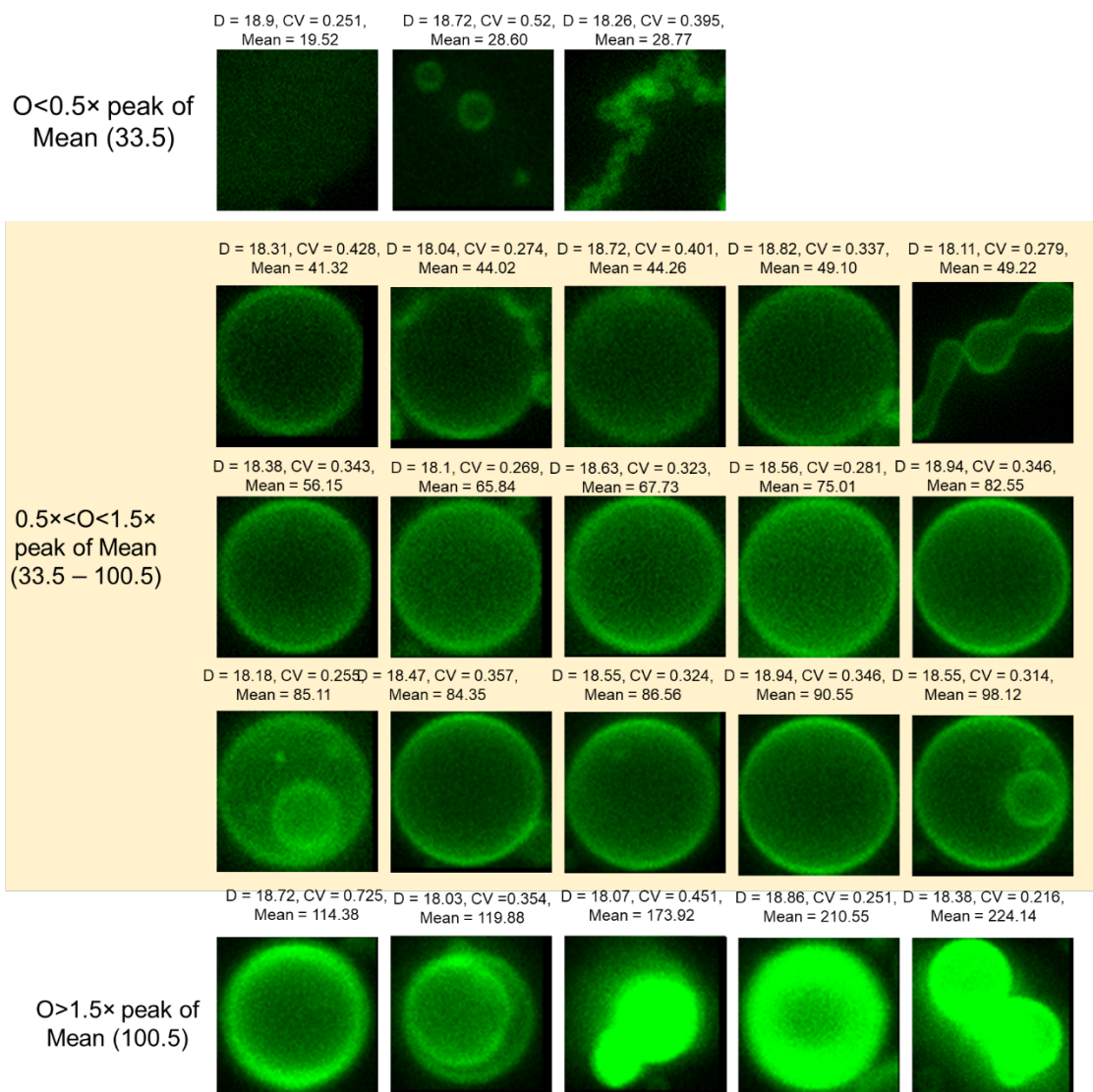
$18 \mu\text{m} \leq O < 19 \mu\text{m}$


Figure 39: Pixel properties of 18 – 19 μm diameter GUVs. Representative images of objects between 18 and 19 μm in diameter with mean intensity values of less than $0.5 \times$, between $0.5 \times - 1.5 \times$, and above $1.5 \times$ the first peak location in the mean intensity histograms.

$O > 30 \mu m$

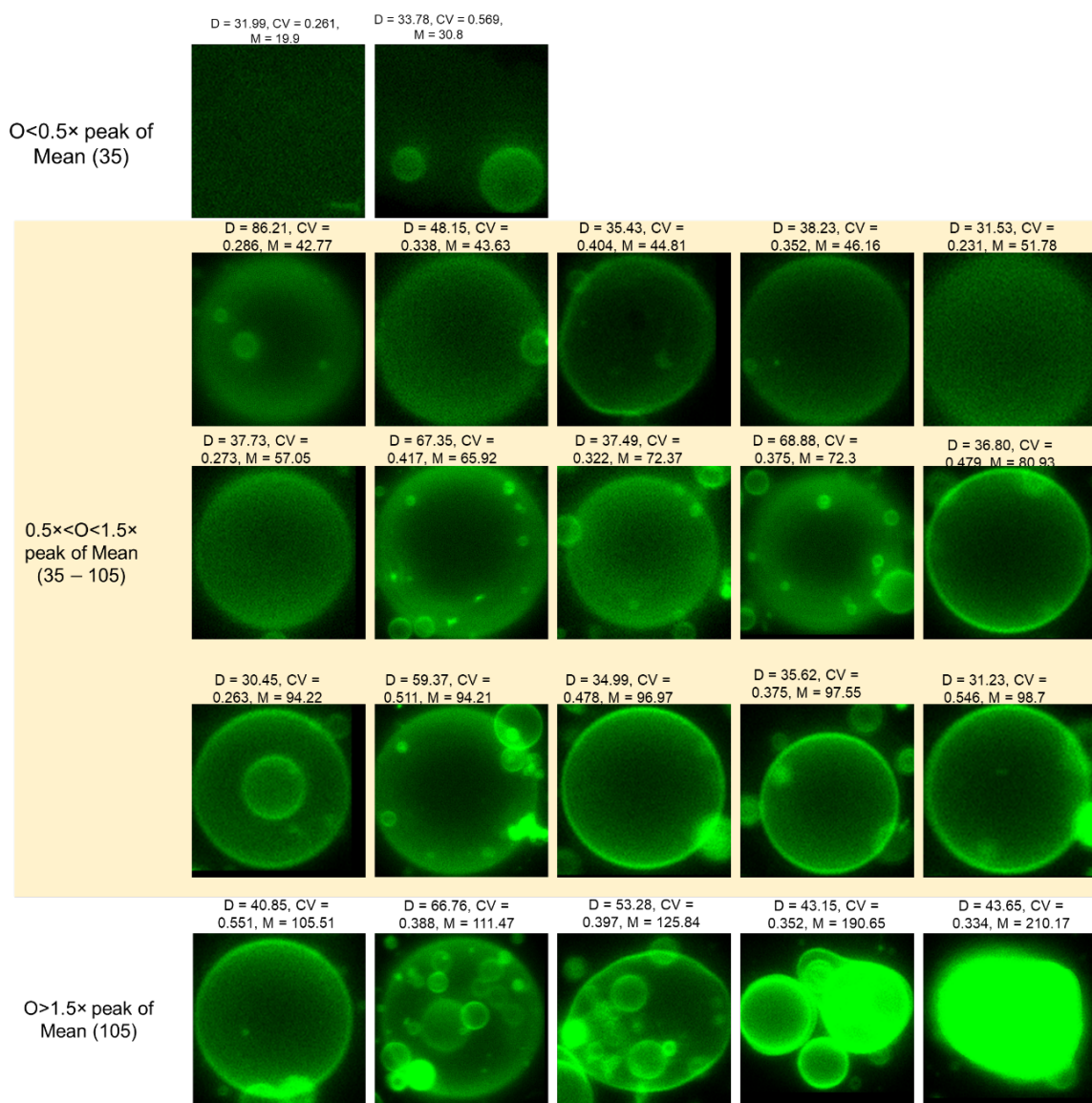


Figure 40: Pixel properties of GUVs $> 30 \mu m$ in diameter. Representative images of objects greater than $30 \mu m$ in diameter with mean intensity values of less than $0.5 \times$, between $0.5 \times - 1.5 \times$, and above $1.5 \times$ the first peak location in the mean intensity histograms.

4.3 Compatibility of code to detect GUVs from different samples

To evaluate the number of objects that are selected as GUVs by the code, I show the CV and mean intensity distribution of the segmented objects by size using heatscatter plots. Figure 41 shows the heatscatter plots of vesicles obtained using the data from a large sample size of 5 aliquots from a single sample of nanocellulose paper. Since most of the objects are GUVs, the objects concentrate towards a single cluster (yellow/light blue region) that is contained within the mean intensity and CV criteria of a GUV (dashed red lines) for each size class. As the location of the cluster increases with increasing object size, the bounds of the intensity criteria of a GUV also increase confirming the ability of the code to correctly adjust the intensity criteria based on the effects of size.

For diameter bins greater $29 \mu\text{m}$ (bottom row of Figure 43), the amount of points on the scatter plot falls below 100. For samples with lower yields, this decrease in counts can make it difficult to obtain CV and normalized mean intensity histograms with definitive peaks. Combining the bins from $20 \mu\text{m} - 120 \mu\text{m}$ into a single plot (row 2 and column 5 of Figure 41) ensures that there will be enough counts to determine a peak from the intensity histograms. Combining these sizes is reasonable since the effect of size on the intensity of the GUVs is minimal from $20 \mu\text{m}$ to $120 \mu\text{m}$. In addition, objects larger than $20 \mu\text{m}$ are easily detectable manually and are checked after processing to ensure there are no significant issues with their automated detection.

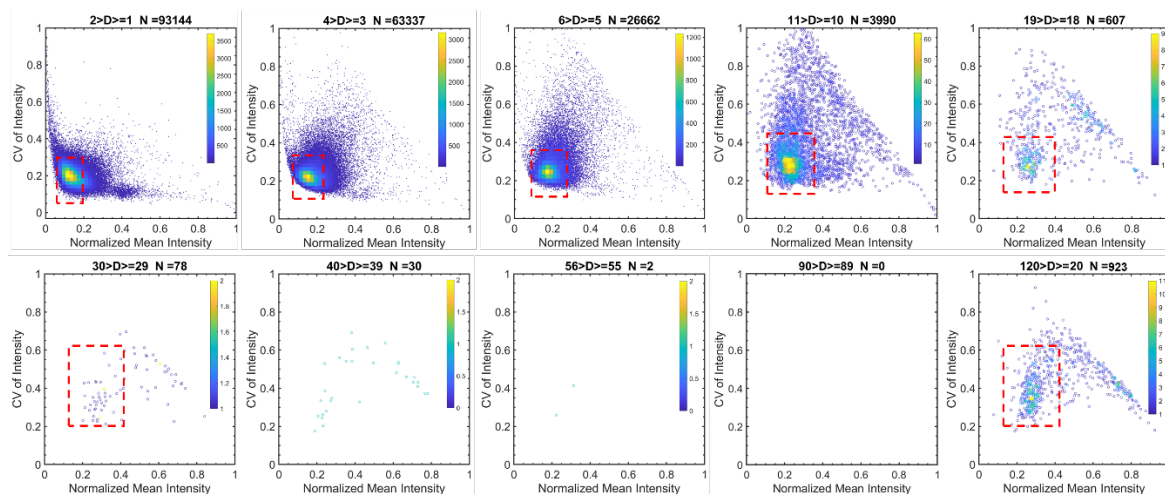


Figure 41: Heatscatter plot shows intensity characteristics of GUVs produced from a pooled nanocellulose paper sample. All objects that are segmented in each size class are plotted on a heatscatter plot of coefficient of variation in intensity versus normalized mean intensity. The region of the heatscatter plot that contains the objects that are selected as GUVs is contained within the dotted red box. The color bar in each plot shows the density of the counts.

To confirm that the intensity characteristics of populations of GUVs prepared from different types of samples are similar to the nanocellulose paper sample, I also plot the CV and normalized mean intensity data of the objects from one electroformation sample (Figure 42), one gentle hydration sample (Figure 43), and one sample where a different lipid dye is used (Figure 44). The heatscatter plots from all three types of samples appear similar to the nanocellulose paper sample with 5 aliquots. Generally, the location of the concentrated regions of the heatscatter plots containing the GUVs (yellow/light blue regions) shifts similarly up and to the right with increasing size bin until around $20\ \mu\text{m}$ for all four samples. These results confirm that the code should be compatible to three additional types of samples. First, the agreement in the shapes of the nanocellulose paper heatscatter plots to the shapes of the electroformation and gentle hydration heatscatter plots, confirms that the intensity statistics do not depend on the growth technique. Second, the ability of the code to determine peaks for the larger diameter bins obtained using specifically the gentle hydration sample confirms that code is compatible for populations obtained from even for the lowest yielding method used in this work. Lastly, the agreement between the heaterscatter plots of the populations doped with a TFC dye to the population doped with a TFPC dye confirms that the code is compatible to different dyes as well.

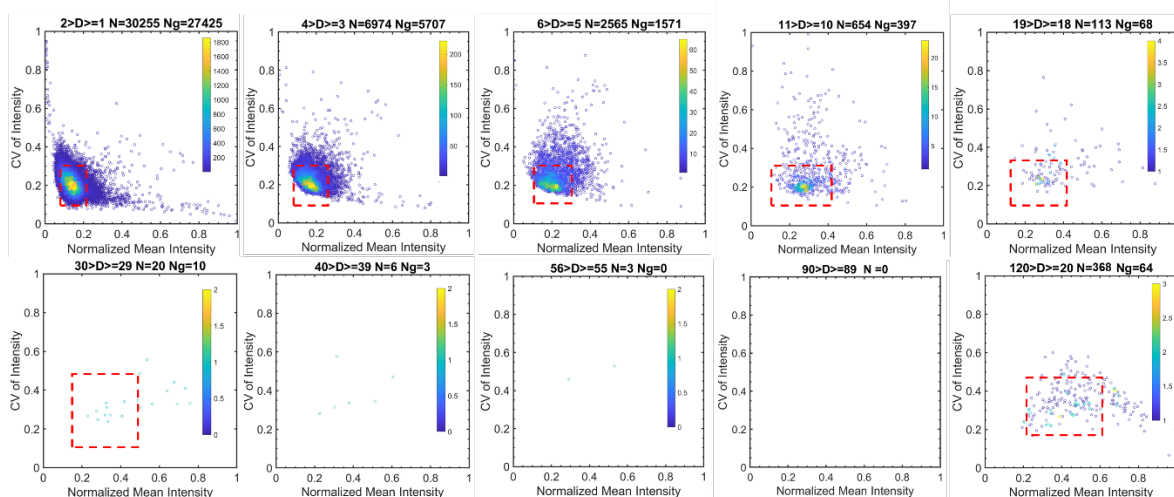


Figure 42: Heatscatter plot shows intensity characteristics of GUVs produced from a typical electroformation sample. All objects that are segmented in each size class are plotted on a heatscatter plot of coefficient of variation in intensity versus normalized mean intensity. The region of the heatscatter plot that contains the objects that are selected as GUVs is contained within the dotted red box. The color bar in each plot shows the density of the counts.

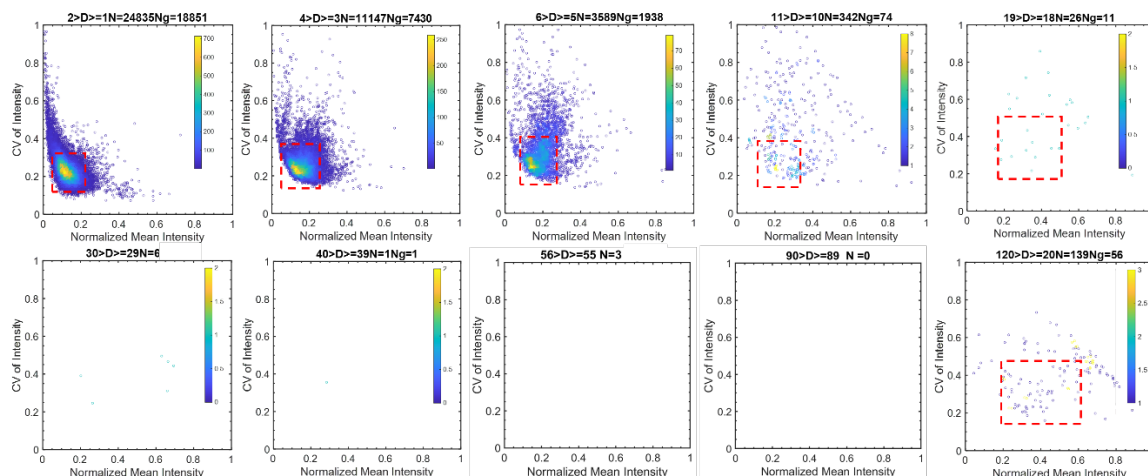


Figure 43: Heatscatter plot shows intensity characteristics of GUVs produced from a typical gentle hydration sample. All objects that are segmented in each size class are plotted on a heatscatter plot of coefficient of variation in intensity versus normalized mean intensity. The region of the heatscatter plot that contains the objects that are selected as GUVs is contained within the dotted red box. The color bar in each plot shows the density of the counts.

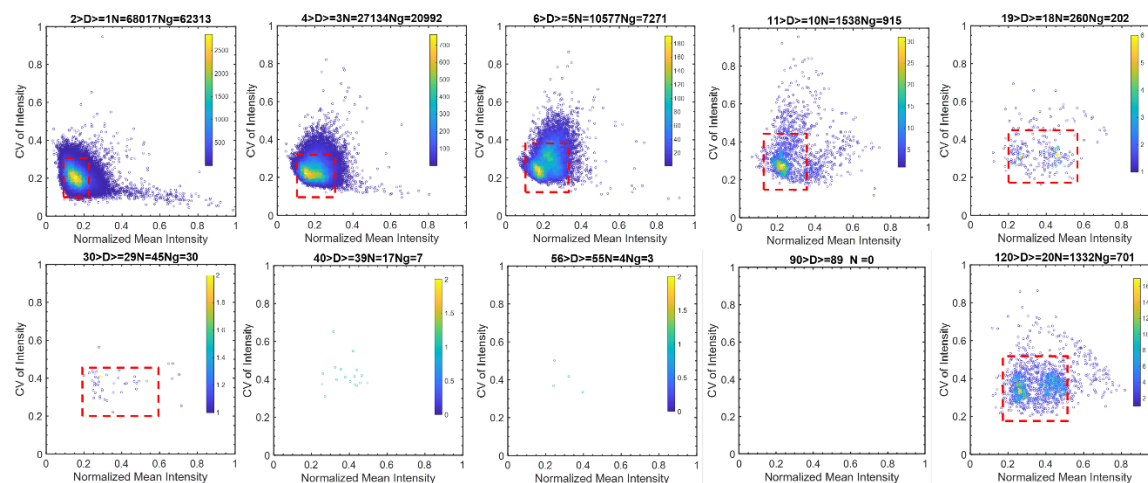


Figure 44: Heatscatter plot shows intensity characteristics of GUVs produced from an electroformation sample where the lipid dye is changed to TFPC. All objects that are segmented in each size class are plotted on a heatscatter plot of coefficient of variation in intensity versus normalized mean intensity. The region of the heatscatter plot that contains the objects that are selected as GUVs is contained within the dotted red box. The color bar in each plot shows the density of the counts.

The final results of the objects selected by the code as GUVs for each of the samples used to test the compatibility are shown in Figure 45. The original grayscale images are shown in the top row and the final processed images are in the bottom row. In the processed images, the objects marked in gray show the objects that were segmented but not selected as GUVs, and the objects marked in red show the objects that were both segmented and selected as GUVs. The images confirm that the code does an excellent job both segmenting the correct size of the objects and selecting only the objects that are defined as GUVs for each of the different types of samples. Combining the histograms from the largest GUVs also does not appear to result in any significant issues with their detection. However, since these larger vesicles are easy to observe and so few in number, I still manually go back through the montages to make sure there are no significant issues with the largest GUVs. This manual checking, which most often results in the addition of no more than 1 or 2 larger GUVs to the population, can be completed as the *GenerateMontageSelected.m* code runs through the images and prints the montages and adds minimal extra time to the processing.

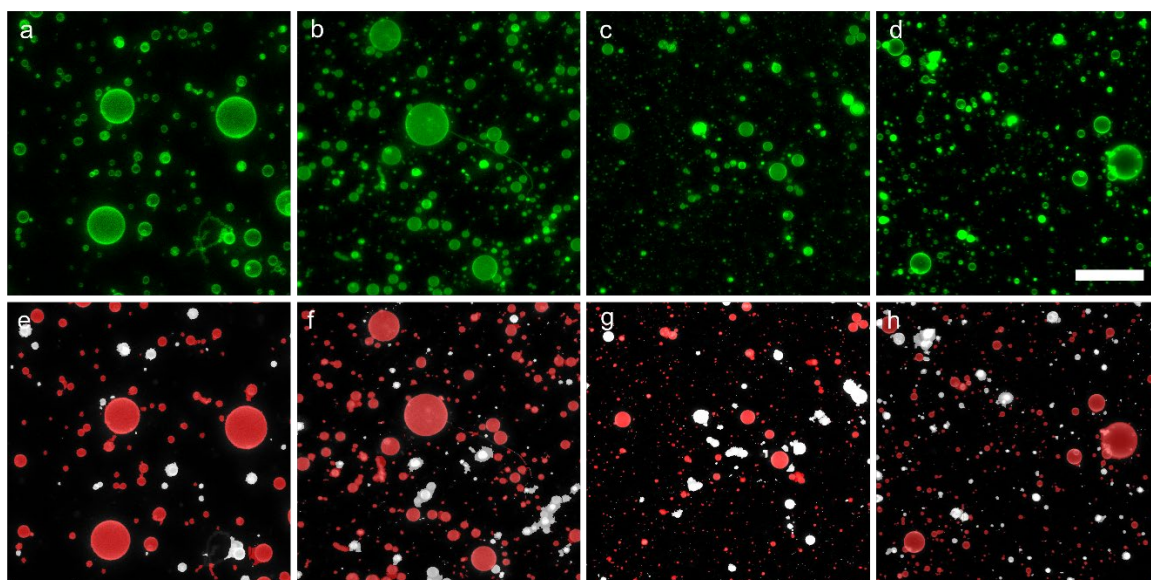


Figure 45: Image analysis code accurately selects GUVs from the different test samples. a-d Grayscale images of GUVs from populations obtained using **a** nanocellulose paper, **b** electroformation, **c** gentle hydration, and **d** electroformation (TFPC dye used). **e-h** Final results showing the objects selected as GUVs (red) from the images above after processing the data with the automated image analysis routine. Scale bars **a-h** 50 μm

4.4 Collecting GUV data into size histograms

Once the objects that meet the intensity criteria of a GUV have been selected from the images of a tilescan, I save the equivalent diameters of only the GUVs which were stored previously using the *regionprops* function. I then plot the diameters of all of the GUVs and produce a histogram of the distribution of the sizes of the entire GUV population. I use the built-in *histcounts* function to bin each GUV into 1 μm sized bins ranging 1 – 150 μm in diameter. I then can multiply the height of each bin by the ratio between the total volume of GUVs harvested over the total volume of GUVs analyzed (typically 75) and then divide by the total amount of lipid initially deposited (typically 10 μg). To obtain a final size histogram, I repeat the entire GUV assembly process with 2 to 4 more independent replicate samples and then plot the mean of the counts in each bin from all samples.

Figure 46 shows the resulting size histograms from the nanocellulose, electroformation, and gentle hydration samples used to test the compatibility of the code. Clearly the distributions appear overall similar with a single peak at 1 μm and a long tail. The distributions also reveal that the nanocellulose and electroformation methods appear to have many more GUVs larger than 10 μm in diameter compared to the gentle hydration method. From the size distribution data other summary statistics, such as mean, median, and mode diameters can be obtained as well as new metric termed the molar yield which will be the primary metric I use to gain insights into optimizing the growth protocols, quantifying and comparing the yield from different techniques and understanding the different mechanisms involved in GUV growth in Chapter 3.

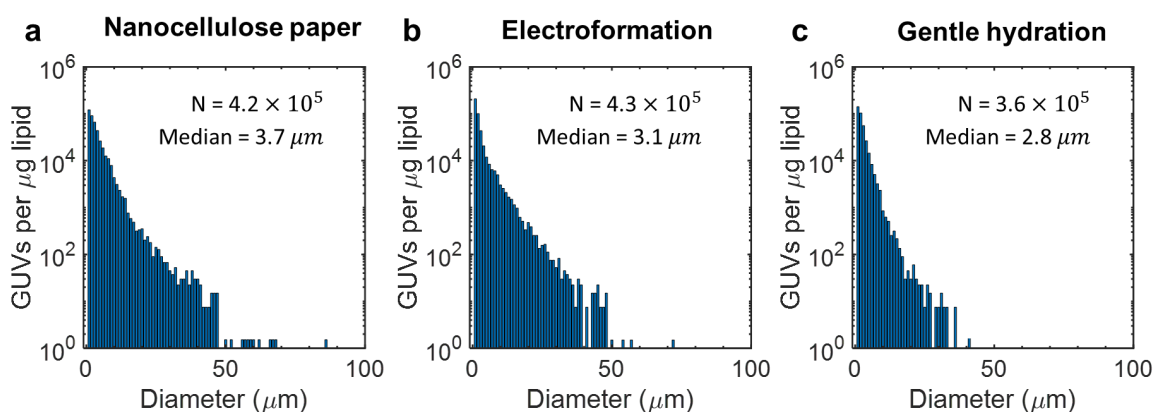


Figure 46: Histograms of the distribution of sizes of the GUVs. The GUV diameter data obtained from the automated code is compiled, normalized per μg of lipid, and plotted into a histogram that shows the distribution of sizes of the GUVs. Each GUV analyzed is placed into 1 μm sized bins. The bins are normalized by the percentage of the harvested solution analyzed by the code as well as the amount of lipid originally deposited onto the surface. Note the logarithmic scaling of the y-axes. The inset of the histograms show the number of GUVs analyzed (N) and median diameter of the GUVs.

5. Additional controls

5.1 Confirmation of identity of small GUVs

Since GUVs with sizes of around $1\ \mu\text{m}$ in diameter are only 4 pixels in length I conduct additional tests to confirm that the measurement of the smallest GUVs with sizes of around $1\ \mu\text{m}$ in diameter is accurate and should be included in the data analysis. I collect regular tilescan images as well as pseudo super-resolution images using the $20\times$ 1.0 NA objective of various small $1\ \mu\text{m}$ sized objects. Figure 47 shows the typical tilescan image, the selected GUV image, and the pseudo super-resolution images of these small vesicles. In all cases where the code detected a $1\ \mu\text{m}$ sized GUV from the typical tilescan image, the pseudo-super resolution image revealed the object to have a single bright ring and a dark interior confirming that most of these small objects appear to be GUVs and should be included in collection of the data.

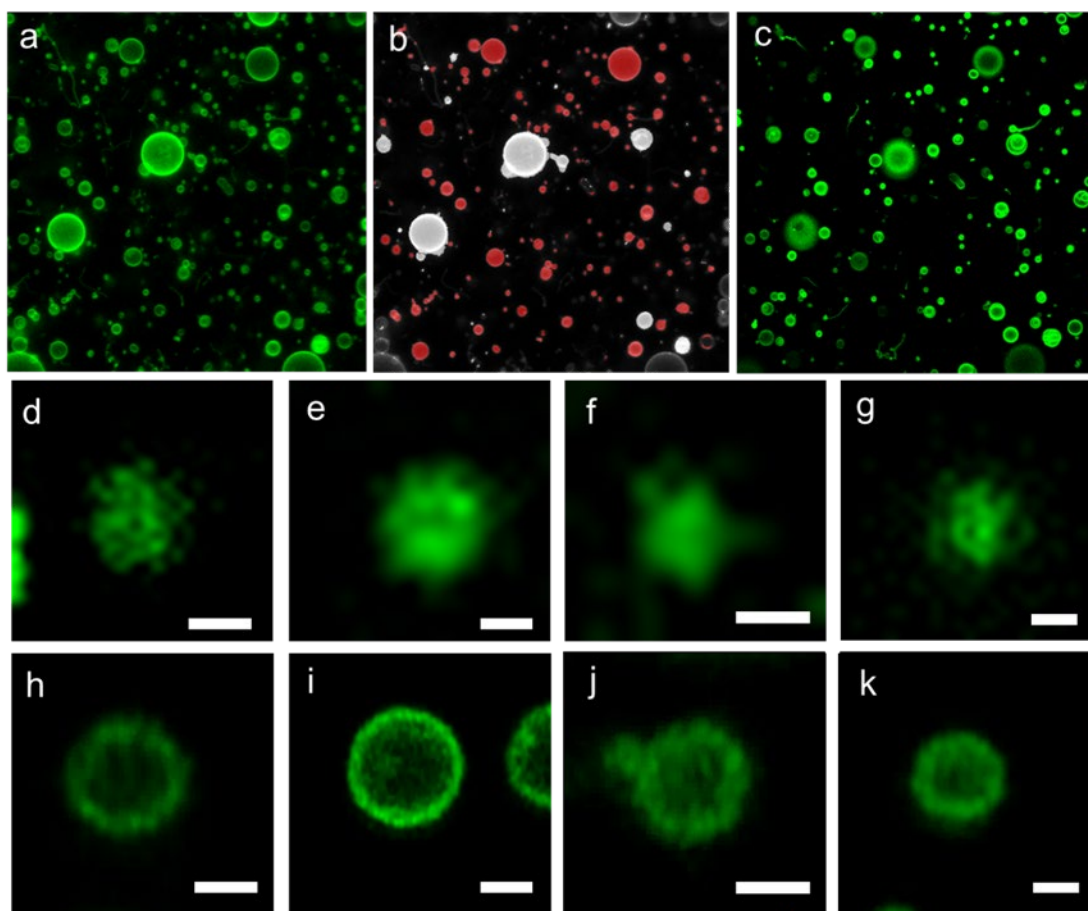


Figure 47: Confirmation of small vesicles. **a)** Typical $10\times$ tilescan image. **b)** Objects from **a)** selected by image analysis routine. **c)** Pseudo super-resolution image of the same region in **a)** collected using the $20\times$ objective and Airyscan detector. **d-f)** Objects detected as $1\ \mu\text{m}$ sized GUVs in the $10\times$ image. **g-j)** Higher resolution images of the objects detected as $1\ \mu\text{m}$ sized GUVs in **d-f)**. Scale bars **a-c)** $20\ \mu\text{m}$, **d-j)** $1\ \mu\text{m}$.

5.2 Effect of sedimentation time on characterization

To determine the effect of the sedimentation time on number of vesicles quantified using the confocal tilescan procedure, I prepare GUVs using the electroformation method. I collect tilescans continuously over the course of 3 hours. Figure 48 shows the plots of the change in the normalized counts of vesicles with sedimentation time. The vesicles GUVs $\geq 10 \mu\text{m}$ have mostly all sedimented approximately 5 minutes of sedimentation. However, the GUVs $< 10 \mu\text{m}$ appear to take around 1.5 to 2 hours to reach a plateau in vesicle counts including the vesicles which are expected to continue to sediment after 3 hours (sizes between $1 \mu\text{m}$ and $3 \mu\text{m}$ in diameter). A z-stack of the solution, reveals that there are still small GUVs present in the bulk after 15 hours (Figure 49). These GUVs do not appear to sediment, likely because their sizes are small enough that convection and Brownian motion prevents their sedimentation.

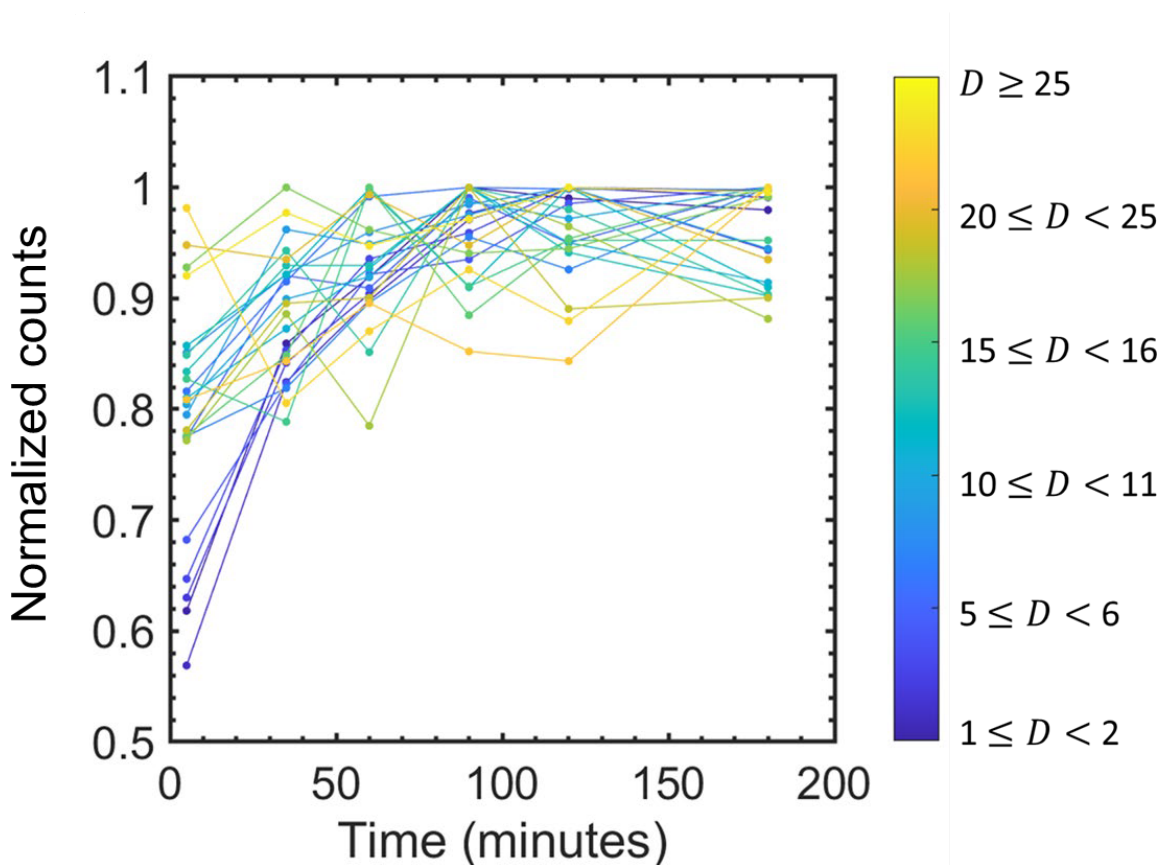


Figure 48: Effect of sedimentation time on vesicle counts. Scatter plots showing the change in the normalized counts of vesicles of various size classes with sedimentation time. The color bar shows indicates color of the data associated with each different size class of vesicles.

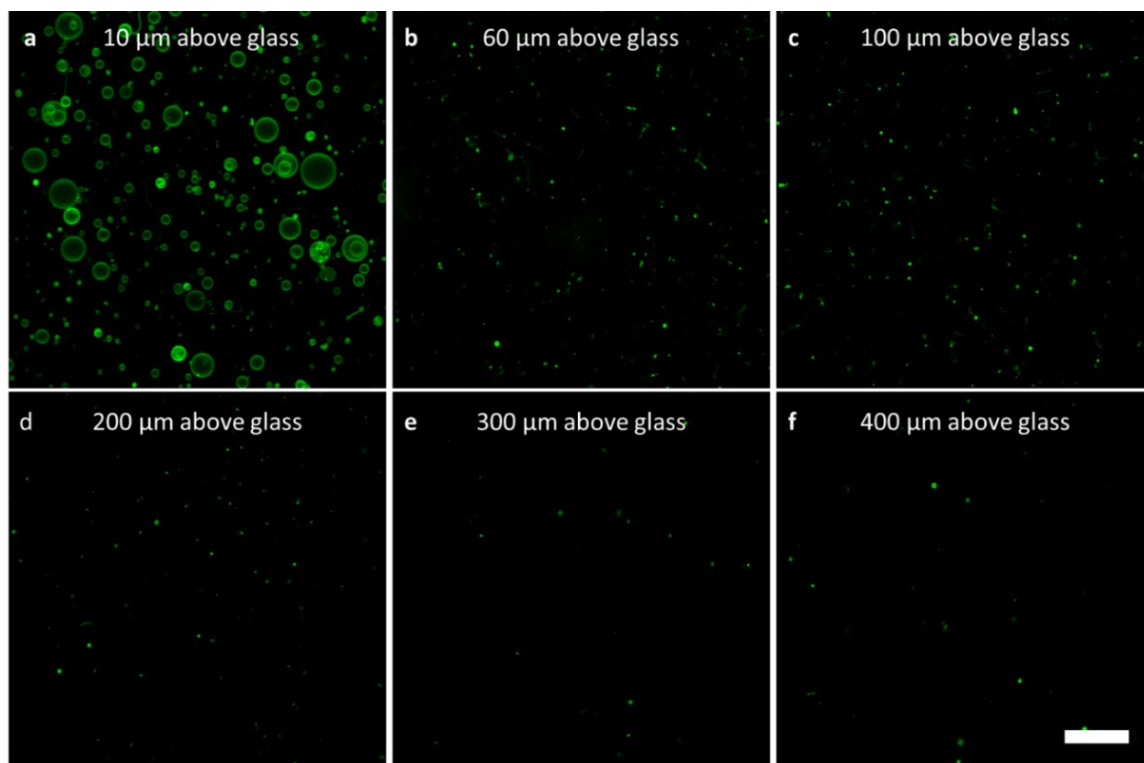


Figure 49: Small vesicles in bulk after sedimentation. Confocal images showing the distributions of vesicles after 15 hours of sedimentation **a** 10 μm, **b** 60 μm, **c** 100 μm, **d** 200 μm, **e** 300 μm, and **f** 400 μm above the bottom glass surface. Scale bar 50 μm.

6. Conclusion

In this chapter, I construct comprehensive methods to accurately quantify populations of GUVs using novel confocal microscopy-based methods. I develop a confocal tilescan imaging routine to collect large datasets on a statistically significant percentage of the GUV population. I developed a custom image analysis routine to analyze the more than 100,000 GUVs present in a single tilescan which allows for the rapid quantification of the GUVs from the images. The routine is able to distinguish GUVs from MLVs, MVVs, and aggregates. The comprehensive routine is better than current alternate methods such as flow cytometry¹³¹ or coulter counting¹³² which are unable to distinguish MLVs, MVVs and aggregates from GUVs. In addition, the routine addresses challenges with current fluorescence microscopy methods which include the careful standardization and control of the GUV growth conditions as well the analysis of a statistically large portion of the GUV population.

The limitations of the protocol is that, similar to other protocols, it likely underestimates the number of GUVs with diameters $\leq 3 \mu m$ due to a combination of challenges with sedimentation due to Brownian motion and imaging due to the dimmer intensities of vesicles with smaller sizes. The method also requires access to a sophisticated confocal microscope for imaging. It is possible that a similar imaging routine can be performed using a motorized widefield microscope with tilescan capabilities since I do not use the pinhole/confocal characteristics of the confocal microscope. I expect that the standardization procedures and image analysis routines to be applicable to widefield images. Widefield microscopes are more widely accessible. Furthermore, the comprehensive methods I developed in this chapter provide a framework to address the questions previously unanswered in the field related to the growth mechanism and optimization of GUV yields which are covered in the remaining chapters.

7. Bibliography

- (1) Singer, S. J. J.; Nicolson, G. L. L. The Fluid Mosaic Model of the Structure of Cell Membranes. *Science* (80). **1972**, *175* (4023), 720–731. <https://doi.org/10.1126/science.175.4023.720>.
- (2) Nicolson, G. L. The Fluid - Mosaic Model of Membrane Structure: Still Relevant to Understanding the Structure, Function and Dynamics of Biological Membranes after More than 40 Years. *Biochim. Biophys. Acta - Biomembr.* **2014**, *1838* (6), 1451–1466. <https://doi.org/10.1016/j.bbamem.2013.10.019>.
- (3) Lombard, J. Once upon a Time the Cell Membranes: 175 Years of Cell Boundary Research. *Biol. Direct* **2014**, *9* (1), 1–35. <https://doi.org/10.1186/s13062-014-0032-7>.
- (4) Ottova-Leitmannova, A.; Ti Tien, H. Bilayer Lipid Membranes: An Experimental System for Biomolecular Electronic Devices Development. *Prog. Surf. Sci.* **1992**, *41* (4), 337–445. [https://doi.org/10.1016/0079-6816\(92\)90012-7](https://doi.org/10.1016/0079-6816(92)90012-7).
- (5) Wesolowska, O.; Michalak, K.; Maniewska, J.; Hendrich, A. B. Giant Unilamellar Vesicles - a Perfect Tool to Visualize Phase Separation and Lipid Rafts in Model Systems. *Acta Biochim. Pol.* **2009**, *56* (1), 33–39. <https://doi.org/20091772> [pii].
- (6) Kam, L. C. Capturing the Nanoscale Complexity of Cellular Membranes in Supported Lipid Bilayers. *J. Struct. Biol.* **2009**, *168* (1), 3–10. <https://doi.org/10.1016/j.jsb.2009.05.006>.
- (7) Castellana, E.; Cremer, P. Solid Supported Lipid Bilayers: From Biophysical Studies to Sensor Design. *Surf. Sci. Rep.* **2006**, *61* (10), 429–444. <https://doi.org/10.1016/j.surfrep.2006.06.001>.
- (8) Dimova, R.; Aranda, S.; Bezlyepkina, N.; Nikolov, V.; Riske, K. a; Lipowsky, R. A Practical Guide to Giant Vesicles. Probing the Membrane Nanoregime via Optical Microscopy. *J. Phys. Condens. Matter* **2006**, *18* (28), S1151–S1176. <https://doi.org/10.1088/0953-8984/18/28/S04>.
- (9) Bangham, A. D.; Standish, M. M.; Watkins, J. C. Diffusion of Univalent Ions across the Lamellae of Swollen Phospholipids. *J. Mol. Biol.* **1965**, *13* (1), 238–252, IN26–IN27. [https://doi.org/10.1016/S0022-2836\(65\)80093-6](https://doi.org/10.1016/S0022-2836(65)80093-6).
- (10) McIntosh, T. J.; Carolina, N.; Simqn, S. A. Hydration and Steric Pressures Between Phospholipid Bilayers. *Ann. Rev. Biophys. Biomol. Struct.* **1994**, 27–51.
- (11) Elson, E. L.; Genin, G. M.; Fried, E.; Dolbow, J. E.; Genin, G. M. Phase Separation in Biological Membranes: Integration of Theory and Experiment. *Annu. Rev. Biophys.* **2010**, *39*, 207–226. <https://doi.org/10.1146/annurev.biophys.093008.131238.Phase>.
- (12) Nicolson, G. L. The Fluid - Mosaic Model of Membrane Structure: Still Relevant to Understanding the Structure, Function and Dynamics of Biological Membranes

- after More than 40 Years. *Biochim. Biophys. Acta - Biomembr.* **2014**, 1838 (6), 1451–1466. <https://doi.org/10.1016/j.bbamem.2013.10.019>.
- (13) Eeman, M.; Deleu, M. From Biological Membranes to Biomimetic Model Membranes. *Biotechnol. Agron. Soc. Environ.* **2010**, 14 (4), 719–736.
- (14) Engelman, D. M. Membranes Are More Mosaic than Fluid. *Nature* **2005**, 438 (7068), 578–580. <https://doi.org/10.1038/nature04394>.
- (15) Parthasarathy, R.; Groves, J. T. Curvature and Spatial Organization in Biological Membranes. *Soft Matter* **2007**, 3 (1), 24. <https://doi.org/10.1039/b608631d>.
- (16) Benga, G.; Holmes, R. P. Interactions between Components in Biological Membranes and Their Implications for Membrane Function. *Prog. Biophys. Mol. Biol.* **1984**, 43 (3), 195–257. [https://doi.org/10.1016/0079-6107\(84\)90014-2](https://doi.org/10.1016/0079-6107(84)90014-2).
- (17) Gordesky, S. E. Phospholipid Asymmetry in the Human Erythrocyte Membrane. *Trends Biochem. Sci.* **1976**, 1 (9), 208–211. [https://doi.org/10.1016/0968-0004\(76\)90389-3](https://doi.org/10.1016/0968-0004(76)90389-3).
- (18) Op den Kamp, J. A. F. Lipid Asymmetry in Membranes. *Annu. Rev. Biochem.* **1979**, 48 (1), 47–71. <https://doi.org/10.1146/annurev.bi.48.070179.000403>.
- (19) Parthasarathy, R.; Rabuka, D.; Bertozzi, C. R.; Groves, J. T. Molecular Orientation of Membrane-Anchored Mucin Glycoprotein Mimics. *J. Phys. Chem. B* **2007**, 111 (42), 12133–12135. <https://doi.org/10.1021/jp072136q>.
- (20) Saliba, A.; Vonkova, I.; Gavin, A. The Systematic Analysis of Protein–Lipid Interactions Comes of Age. *Nat. Publ. Gr.* **2015**, 16 (12), 753–761. <https://doi.org/10.1038/nrm4080>.
- (21) Bentz, Joe; Ellens, Harma. Membrane Fusion: Kinetics and Mechanisms. *Colloids and Surfaces* **1988**, 30, 65-112.
- (22) Seddon, A. M.; Curnow, P.; Booth, P. J. Membrane Proteins , Lipids and Detergents : Not Just a Soap Opera. *Biochimica et Biophysica Acta* **2004**, 1666, 105–117. <https://doi.org/10.1016/j.bbamem.2004.04.011>.
- (23) Knowles, T. J.; Finka, R.; Smith, C.; Lin, Y. P.; Dafforn, T.; Overduin, M. Membrane Proteins Solubilized Intact in Lipid Containing Nanoparticles Bounded by Styrene Maleic Acid Copolymer. *J. Am. Chem. Soc.* **2009**, 131 (22), 7484–7485. <https://doi.org/10.1021/ja810046q>.
- (24) Smirnova, I. A.; Ädelroth, P.; Brzezinski, P. Extraction and Liposome Reconstitution of Membrane Proteins with Their Native Lipids without the Use of Detergents. *Sci. Rep.* **2018**, 8 (1), 1–6. <https://doi.org/10.1038/s41598-018-33208-1>.
- (25) Martiniere, A.; Lavagi, I.; Nageswaran, G.; Rolfe, D. J.; Maneta-Peyret, L.; Luu, D.-T.; Botchway, S. W.; Webb, S. E. D.; Mongrand, S.; Maurel, C.; Martin-Fernandez, M. L.; Kleine-Vehn, J.; Friml, J.; Moreau, P.; Runions, J. Cell Wall

- Constrains Lateral Diffusion of Plant Plasma-Membrane Proteins. *Proc. Natl. Acad. Sci.* **2012**, *109* (31), 12805–12810.
<https://doi.org/10.1073/pnas.1202040109>.
- (26) Marguet, M.; Bonduelle, C.; Lecommandoux, S. Multicompartmentalized Polymeric Systems: Towards Biomimetic Cellular Structure and Function. *Chem. Soc. Rev.* **2013**, *42* (2), 512–529. <https://doi.org/10.1039/C2CS35312A>.
- (27) Hest, J. C. M. Van. Synthetic Cells and Organelles : Compartmentalization Strategies. *Bioessays*. **2009**, 1299–1308. <https://doi.org/10.1002/bies.200900106>.
- (28) Osumi, M. The Ultrastructure of Yeast: Cell Wall Structure and Formation. *Micron* **1998**, *29* (2–3), 207–233. [https://doi.org/10.1016/S0968-4328\(97\)00072-3](https://doi.org/10.1016/S0968-4328(97)00072-3).
- (29) Schoonen, L.; Hest, J. C. M. Van. Compartmentalization Approaches in Soft Matter Science : From Nanoreactor Development to Organelle Mimics. *Adv. Mat.* **2016**, 1109–1128. <https://doi.org/10.1002/adma.201502389>.
- (30) Roodbeen, R.; Van Hest, J. C. M. Synthetic Cells and Organelles: Compartmentalization Strategies. *BioEssays* **2009**, *31* (12), 1299–1308. <https://doi.org/10.1002/bies.200900106>.
- (31) Juhasz, J.; Sharom, F. J.; Davis, J. H. Quantitative Characterization of Coexisting Phases in DOPC/DPPC/Cholesterol Mixtures: Comparing Confocal Fluorescence Microscopy and Deuterium Nuclear Magnetic Resonance. *Biochim. Biophys. Acta - Biomembr.* **2009**, *1788* (12), 2541–2552.
<https://doi.org/10.1016/j.bbamem.2009.10.006>.
- (32) Wang, L.; Malmstadt, N. Interactions between Charged Nanoparticles and Giant Vesicles Fabricated from Inverted-Headgroup Lipids. *J. Phys. D. Appl. Phys.* **2017**, *50* (41). <https://doi.org/10.1088/1361-6463/aa86e6>.
- (33) Claessens, M. M. A. E.; Oort, B. F. Van; Leermakers, F. A. M.; Hoekstra, F. A.; Stuart, M. A. C. Charged Lipid Vesicles : Effects of Salts on Bending Rigidity , Stability , and Size. *Biophys. J.* **2004**, *87* (6), 3882–3893.
<https://doi.org/10.1529/biophysj.103.036772>.
- (34) Schöps, R.; Amado, E.; Müller, S. S.; Frey, H.; Kressler, J. Block Copolymers in Giant Unilamellar Vesicles with Proteins or with Phospholipids. *Faraday Discuss.* **2013**, *166*, 303. <https://doi.org/10.1039/c3fd00062a>.
- (35) Carvalho, K.; Ramos, L.; Roy, C.; Picart, C. Giant Unilamellar Vesicles Containing Phosphatidylinositol(4,5)Bisphosphate: Characterization and Functionality. *Biophys. J.* **2008**, *95* (9), 4348–4360.
<https://doi.org/10.1529/biophysj.107.126912>.
- (36) Bezlyepkina, N.; Gracià, R. S.; Shchelokovskyy, P.; Lipowsky, R.; Dimova, R. Phase Diagram and Tie-Line Determination for the Ternary Mixture DOPC/ESM/Cholesterol. *Biophys. J.* **2013**, *104* (7), 1456–1464.
<https://doi.org/10.1016/j.bpj.2013.02.024>.

- (37) Tsai, F. C.; Stuhrmann, B.; Koenderink, G. H. Encapsulation of Active Cytoskeletal Protein Networks in Cell-Sized Liposomes. *Langmuir* **2011**, *27* (16), 10061–10071. <https://doi.org/10.1021/la201604z>.
- (38) Singla, S.; Harjai, K.; Raza, K.; Wadhwa, S.; Katare, O. P.; Chhibber, S. Phospholipid Vesicles Encapsulated Bacteriophage: A Novel Approach to Enhance Phage Biodistribution. *J. Virol. Methods* **2016**, *236*, 68–76. <https://doi.org/10.1016/j.jviromet.2016.07.002>.
- (39) Colletier, J.-P.; Chaize, B.; Winterhalter, M.; Fournier, D. Protein Encapsulation in Liposomes: Efficiency Depends on Interactions between Protein and Phospholipid Bilayer. *BMC Biotechnol.* **2002**, *2*, 9. <https://doi.org/10.1186/1472-6750-2-9>.
- (40) Eloy, J. O.; Claro de Souza, M.; Petrilli, R.; Barcellos, J. P. A.; Lee, R. J.; Marchetti, J. M. Liposomes as Carriers of Hydrophilic Small Molecule Drugs: Strategies to Enhance Encapsulation and Delivery. *Colloids Surfaces B Biointerfaces* **2014**, *123*, 345–363. <https://doi.org/10.1016/j.colsurfb.2014.09.029>.
- (41) Sercombe, L.; Veerati, T.; Moheimani, F.; Wu, S. Y.; Sood, A. K.; Hua, S. Advances and Challenges of Liposome Assisted Drug Delivery. *Front. Pharmacol.* **2015**, *6* (DEC), 1–13. <https://doi.org/10.3389/fphar.2015.00286>.
- (42) Vázquez-gonzález, M. L.; Calpena, A. C.; Domènech, Ò.; Montero, M. T.; Borrell, J. H. Colloids and Surfaces B : Biointerfaces Enhanced Topical Delivery of Hyaluronic Acid Encapsulated in Liposomes : A Surface-Dependent Phenomenon. *Colloids Surfaces B Biointerfaces* **2015**, *134*, 31–39. <https://doi.org/10.1016/j.colsurfb.2015.06.029>.
- (43) Litschel, T.; Ramm, B.; Maas, R.; Heymann, M.; Schwille, P. Beating Vesicles : Encapsulated Protein Oscillations Cause Dynamic Membrane Deformations. *Angew. Chem. Int. Ed.* **2018**, 16286–16290. <https://doi.org/10.1002/anie.201808750>.
- (44) Walde, P. Building Artificial Cells and Protocell Models: Experimental Approaches with Lipid Vesicles. *BioEssays* **2010**, *32* (4), 296–303. <https://doi.org/10.1002/bies.200900141>.
- (45) Marquardt, D.; Geier, B.; Pabst, G. Asymmetric Lipid Membranes: Towards More Realistic Model Systems. *Membranes (Basel)*. **2015**, *5* (2), 180–196. <https://doi.org/10.3390/membranes5020180>.
- (46) Blain, J. C.; Szostak, J. W. Progress Toward Synthetic Cells. *Annu. Rev. Biochem.* **2014**, *83* (1), 615–640. <https://doi.org/10.1146/annurev-biochem-080411-124036>.
- (47) Veatch, S. L.; Keller, S. L. Separation of Liquid Phases in Giant Vesicles of Ternary Mixtures of Phospholipids and Cholesterol. *Biophys. J.* **2003**, *85* (5), 3074–3083. [https://doi.org/10.1016/S0006-3495\(03\)74726-2](https://doi.org/10.1016/S0006-3495(03)74726-2).
- (48) Bourgaux, C.; Couvreur, P. Interactions of Anticancer Drugs with Biomembranes: What Can We Learn from Model Membranes? *J. Control. Release* **2014**, *190*,

- 127–138. <https://doi.org/10.1016/j.jconrel.2014.05.012>.
- (49) Peetla, C.; Stine, A.; Labhasetwar, V. Biophysical Interactions with Model Lipid Membranes: Applications in Drug Discovery and Drug Delivery. *Mol. Pharm.* **2009**, *6* (5), 1264–1276. <https://doi.org/10.1021/mp9000662>.
- (50) Scherfeld, D.; Kahya, N.; Schwille, P. Lipid Dynamics and Domain Formation in Model Membranes Composed of Ternary Mixtures of Unsaturated and Saturated Phosphatidylcholines and Cholesterol. *Biophys. J.* **2003**, *85* (6), 3758–3768. [https://doi.org/10.1016/S0006-3495\(03\)74791-2](https://doi.org/10.1016/S0006-3495(03)74791-2).
- (51) Bhatia, T.; Husen, P.; Brewer, J.; Bagatolli, L. A.; Hansen, P. L.; Ipsen, J. H.; Mouritsen, O. G. Biochimica et Biophysica Acta Preparing Giant Unilamellar Vesicles (GUVs) of Complex Lipid Mixtures on Demand : Mixing Small Unilamellar Vesicles of Compositionally Heterogeneous Mixtures. *BBA - Biomembr.* **2015**, *1848* (12), 3175–3180. <https://doi.org/10.1016/j.bbamem.2015.09.020>.
- (52) Crane, J. M.; Tamm, L. K. Role of Cholesterol in the Formation and Nature of Lipid Rafts in Planar and Spherical Model Membranes. *Biophys. J.* **2004**, *86* (5), 2965–2979. [https://doi.org/10.1016/S0006-3495\(04\)74347-7](https://doi.org/10.1016/S0006-3495(04)74347-7).
- (53) Shen, H. H.; Lithgow, T.; Martin, L. L. Reconstitution of Membrane Proteins into Model Membranes: Seeking Better Ways to Retain Protein Activities. *Int. J. Mol. Sci.* **2013**, *14* (1), 1589–1607. <https://doi.org/10.3390/ijms14011589>.
- (54) Buboltz, J. T. A More Efficient Device for Preparing Model-Membrane Liposomes by the Rapid Solvent Exchange Method. *Rev. Sci. Instr.* **2015**, *124301* (2009). <https://doi.org/10.1063/1.3264073>.
- (55) Szoka, F. Comparative Properties Preparation of Lipid Vesicles (Liposomes). *Ann. Rev. Biophys. Bioeng.* **1980**, 467–508.
- (56) Dhand, C.; Prabhakaran, M. P.; Beuerman, R. W.; Lakshminarayanan, R.; Dwivedi, N.; Ramakrishna, S. Role of Size of Drug Delivery Carriers for Pulmonary and Intravenous Administration with Emphasis on Cancer Therapeutics and Lung-Targeted Drug Delivery. *RSC Adv.* **2014**, *4* (62), 32673–32689. <https://doi.org/10.1039/c4ra02861a>.
- (57) Edwards, K. A.; Baeumner, A. J. Liposomes in Analyses. *Talanta.* **2006**, *68*, 1421–1431. <https://doi.org/10.1016/j.talanta.2005.08.044>.
- (58) Deng, N.; Yelleswarapu, M.; Huck, W. T. S. Monodisperse Uni- and Multicompartment Liposomes. *Jour. Amer. Chem. Soc.* **2016**, *138*, 7584-7591. <https://doi.org/10.1021/jacs.6b02107>.
- (59) Cells, R. B. Oxygen Carriers (“ Blood Substitutes ”). *Chem. Rev.* **2001**, *101* 2797-2919. <https://doi.org/10.1021/cr970143c>.
- (60) Nagayasu, A.; Uchiyama, K.; Kiwada, H. The Size of Liposomes: A Factor Which

- Affects Their Targeting Efficiency to Tumors and Therapeutic Activity of Liposomal Antitumor Drugs. *Adv. Drug Deliv. Rev.* **1999**, *40* (1–2), 75–87. [https://doi.org/10.1016/S0169-409X\(99\)00041-1](https://doi.org/10.1016/S0169-409X(99)00041-1).
- (61) Liu, Q.; Boyd, B. J. Liposomes in Biosensors. *Analyst* **2013**, *138* (2), 391–409. <https://doi.org/10.1039/c2an36140j>.
- (62) Allen, T. M.; Cullis, P. R. Liposomal Drug Delivery Systems: From Concept to Clinical Applications. *Adv. Drug Deliv. Rev.* **2013**, *65* (1), 36–48. <https://doi.org/10.1016/j.addr.2012.09.037>.
- (63) Maruyama, K.; Yuda, T.; Okamoto, A.; Kojima, S.; Suginaka, A.; Iwatsuru, M. Prolonged Circulation Time in Vivo of Large Unilamellar Liposomes Composed of Distearoyl Phosphatidylcholine and Cholesterol Containing Amphipathic Poly(Ethylene Glycol). *Biochim. Biophys. Acta (BBA)/Lipids Lipid Metab.* **1992**, *1128* (1), 44–49. [https://doi.org/10.1016/0005-2760\(92\)90255-T](https://doi.org/10.1016/0005-2760(92)90255-T).
- (64) Schwendener, R. A. Liposomes as Vaccine Delivery Systems : A Review of the Recent Advances. **2014**, 159–182. <https://doi.org/10.1177/2051013614541440>.
- (65) Vemuri, S.; Rhodes, C. T. Preparation and Characterization of Liposomes as Therapeutic Systems : A Review. *Pharm. Acta Helv.* **1995**, *70*, 95–111.
- (66) Patil, Y. P.; Jadhav, S. Novel Methods for Liposome Preparation. *Chem. Phys. Lipids* **2014**, *177*, 8–18. <https://doi.org/10.1016/j.chemphyslip.2013.10.011>.
- (67) Dao, T. P. T.; Fernandes, F.; Er-Rafik, M.; Salva, R.; Schmutz, M.; Brûlet, A.; Prieto, M.; Sandre, O.; Le Meins, J. F. Phase Separation and Nanodomain Formation in Hybrid Polymer/Lipid Vesicles. *ACS Macro Lett.* **2015**, *4* (2), 182–186. <https://doi.org/10.1021/mz500748f>.
- (68) Juhasz, J.; Sharom, F. J.; Davis, J. H. Quantitative Characterization of Coexisting Phases in DOPC/DPPC/Cholesterol Mixtures: Comparing Confocal Fluorescence Microscopy and Deuterium Nuclear Magnetic Resonance. *Biochim. Biophys. Acta - Biomembr.* **2009**, *1788* (12), 2541–2552. <https://doi.org/10.1016/j.bbamem.2009.10.006>.
- (69) Kubsch, B.; Robinson, T.; Steinkühler, J.; Dimova, R. Phase Behavior of Charged Vesicles Under Symmetric and Asymmetric Solution Conditions Monitored with Fluorescence Microscopy. *J. Vis. Exp.* **2017**, No. 128, 1–17. <https://doi.org/10.3791/56034>.
- (70) Sarmiento, M. J.; Prieto, M.; Fernandes, F. Biochimica et Biophysica Acta Reorganization of Lipid Domain Distribution in Giant Unilamellar Vesicles upon Immobilization with Different Membrane Tethers. *BBA - Biomembr.* **2012**, *1818* (11), 2605–2615. <https://doi.org/10.1016/j.bbamem.2012.05.028>.
- (71) Ariola, F. S.; Li, Z.; Cornejo, C.; Bittman, R.; Heikal, A. A. Membrane Fluidity and Lipid Order in Ternary Giant Unilamellar Vesicles Using a New Bodipy-Cholesterol Derivative. *Biophysj* **2009**, *96* (7), 2696–2708.

<https://doi.org/10.1016/j.bpj.2008.12.3922>.

- (72) Zan, G. H.; Tan, C.; Deserno, M.; Lanni, F.; Lösche, M. Hemifusion of Giant Unilamellar Vesicles with Planar Hydrophobic Surfaces: A Fluorescence Microscopy Study. *Soft Matter* **2012**, *8* (42), 10877. <https://doi.org/10.1039/c2sm25702e>.
- (73) Kalb, E.; Frey, S.; Tamm, L. K. Formation of Supported Planar Bilayers by Fusion of Vesicles to Supported Phospholipid Monolayers. *Biochim. Biophys. Acta - Biomembr.* **1992**, *1103* (2), 307–316. [https://doi.org/10.1016/0005-2736\(92\)90101-Q](https://doi.org/10.1016/0005-2736(92)90101-Q).
- (74) Micheletto, Y. M. S.; Marques, C. M.; Silveira, N. P. Da; Schroder, A. P. Electroformation of Giant Unilamellar Vesicles: Investigating Vesicle Fusion versus Bulge Merging. *Langmuir* **2016**, *32* (32), 8123–8130. <https://doi.org/10.1021/acs.langmuir.6b01679>.
- (75) Nussbaum, O.; Rott, R.; Loyter, A. Fusion of Influenza Virus Particles with Liposomes : Requirement for Cholesterol and Virus Receptors to Allow Fusion with and Lysis of Neutral but Not of Negatively Charged Liposomes. *Jorn. of Gen. Virol.* **2018**, No. 1992, 2831–2837.
- (76) Estes, D. J.; Lopez, S. R.; Fuller, A. O.; Mayer, M. Triggering and Visualizing the Aggregation and Fusion of Lipid Membranes in Microfluidic Chambers. *Biophys. Journ.* **2006**, *91* (July), 233–243. <https://doi.org/10.1529/biophysj.105.076398>.
- (77) Terasawa, H.; Nishimura, K.; Suzuki, H.; Matsuura, T.; Yomo, T. Coupling of the Fusion and Budding of Giant Phospholipid Vesicles Containing Macromolecules. *P.N.A.S.* **2012**, *109*, 5942-5947. <https://doi.org/10.1073/pnas.1120327109/-/DCSupplemental.www.pnas.org/cgi/doi/10.1073/pnas.1120327109>.
- (78) Goldenberg, N. M.; Steinberg, B. E. Surface Charge : A Key Determinant of Protein Localization and Function. *Amer. Assoc. for Canc. Res.* **2010**, No. 10, 1277–1281. <https://doi.org/10.1158/0008-5472.CAN-09-2905>.
- (79) Gutierrez, M. G.; Jalali-yazdi, F.; Peruzzi, J.; Riche, C. T.; Roberts, R. W.; Malmstadt, N. G Protein-Coupled Receptors Incorporated into Rehydrated Diblock Copolymer Vesicles Retain Functionality. *Small.* **2016**, No. 38, 5256–5260. <https://doi.org/10.1002/smll.201601540>.
- (80) Geertsma, E. R.; Mahmood, N. A. B. N.; Schuurman-wolters, G. K.; Poolman, B. Membrane Reconstitution of ABC Transporters and Assays of Translocator Function. *Nature Protocols.* **2008**. <https://doi.org/10.1038/nprot.2007.519>.
- (81) Horger, K. S.; Liu, H.; Rao, D. K.; Shukla, S.; Sept, D.; Ambudkar, S. V.; Mayer, M. Hydrogel-Assisted Functional Reconstitution of Human P-Glycoprotein (ABCB1) in Giant Liposomes. *Biochim. Biophys. Acta - Biomembr.* **2015**, *1848* (2), 643–653. <https://doi.org/10.1016/j.bbamem.2014.10.023>.
- (82) Hovijitra, N. T.; Wu, J. J.; Peaker, B.; Swartz, J. R. Cell-Free Synthesis of

- Functional Aquaporin Z in Synthetic Liposomes. *Biotechnol Bioeng* **2009**, *104* (1), 40–49. <https://doi.org/10.1002/bit.22385>.
- (83) Gutierrez, M. G.; Mansfield, K. S.; Malmstadt, N. The Functional Activity of the Human Serotonin 5-HT_{1A} Receptor Is Controlled by Lipid Bilayer Composition. *Biophys. J.* **2016**, *110* (11), 2486–2495. <https://doi.org/10.1016/j.bpj.2016.04.042>.
- (84) Quemeneur, F.; Sigurdsson, J. K.; Renner, M.; Atzberger, P. J.; Bassereau, P. Shape Matters in Protein Mobility within Membranes. *P.N.A.S.* **2014**, *111*, 5083–5087. <https://doi.org/10.1073/pnas.1321054111>.
- (85) Salafsky, J.; Groves, J. T.; Boxer, S. G. Architecture and Function of Membrane Proteins in Planar-Supported Bilayers: A Study with Photosynthetic Reaction Centers. *Biochemistry* **1996**, *35* (96), 14773–14781. <https://doi.org/10.1021/bi961432i>.
- (86) Gebiki, JM; Hicks, M. Ufasomes : A Vesicular Drug Delivery. *Nature.* **2011**, *2* (2), 72–78. <https://doi.org/10.4103/0975-8453.86290>.
- (87) Čejková, J.; Štěpánek, F. Compartmentalized and Internally Structured Particles for Drug Delivery - A Review. *Curr. Pharm. Des.* **2013**, *19* (35), 6298–6314. <https://doi.org/10.2174/1381612811319350007>.
- (88) Mantripragada, S. A Lipid Based Depot (DepoFoam technology) for Sustained Release Drug Delivery. *Prog. Lipid Res.* **2002**, *41*, 392–406.
- (89) Jullient, L.; Megliot, J. D. I. Drug Delivery : Piercing Vesicles by Their Adsorption Onto a Porous Medium. *Proceedings of the National Academy of Sciences of the United States of America.* **2018**, *92* (21), 9590–9592.
- (90) Republic, C. Compartmentalized and Internally Structured Particles for Drug Delivery - A Review. *Current Pharm. Design.* **2013**, 6298–6314.
- (91) Xu, C.; Hu, S.; Chen, X. Artificial Cells: From Basic Science to Applications. *Mater. Today* **2016**, *19* (9), 516–532. <https://doi.org/10.1016/j.mattod.2016.02.020>.
- (92) Long, M. S.; Jones, C. D.; Helfrich, M. R.; Mangeney-Slavin, L. K.; Keating, C. D. Dynamic Microcompartmentation in Synthetic Cells. *Proc. Natl. Acad. Sci.* **2005**, *102* (17), 5920–5925. <https://doi.org/10.1073/pnas.0409333102>.
- (93) Weiss, M.; Frohnmayer, J. P.; Benk, L. T.; Haller, B.; Janiesch, J.; Heitkamp, T.; Börsch, M.; Lira, R. B.; Dimova, R.; Lipowsky, R.; Bodenschatz, E.; Baret, J.; Vidakovic-koch, T.; Sundmacher, K.; Platzman, I.; Spatz, J. P. Sequential Bottom-up Assembly of Mechanically Stabilized Synthetic Cells by Microfluidics. *Nature Materials.* **2018**, *17* (January). <https://doi.org/10.1038/NMAT5005>.
- (94) Maeda, Y. T.; Nakadai, T.; Shin, J.; Uryu, K.; Noireaux, V.; Libchaber, A. Assembly of MreB Filaments on Liposome Membranes: A Synthetic Biology Approach. *ACS Synth. Biol.* **2012**, *1* (2), 53–59.

<https://doi.org/10.1021/sb200003v>.

- (95) York-Duran, M. J.; Godoy-Gallardo, M.; Labay, C.; Urquhart, A. J.; Andresen, T. L.; Hosta-Rigau, L. Recent Advances in Compartmentalized Synthetic Architectures as Drug Carriers, Cell Mimics and Artificial Organelles. *Colloids Surfaces B Biointerfaces* **2017**, *152*, 199–213. <https://doi.org/10.1016/j.colsurfb.2017.01.014>.
- (96) Göpfrich, K.; Platzman, I.; Spatz, J. P. Mastering Complexity : Towards Bottom-up Construction of Multifunctional Eukaryotic Synthetic Cells. *Trends Biotechnol.* **2018**, *xx*, 1–14. <https://doi.org/10.1016/j.tibtech.2018.03.008>.
- (97) Krombach, F.; Münzing, S.; Allmeling, A. M.; Gerlach, J. T.; Behr, J.; Dörger, M. Cell Size of Alveolar Macrophages: An Interspecies Comparison. *Environ. Health Perspect.* **1997**, *105 Suppl* (September), 1261–1263. <https://doi.org/10.1289/ehp.97105s51261>.
- (98) Child, J. A.; King, J.; Newman, T. H.; Waterfield, R. L. A Diffraction Method for Measuring the Average Volumes and Shapes of Red Blood Cells. *Br. J. Haematol.* **1967**, *13* (3), 364–375. <https://doi.org/10.1111/j.1365-2141.1967.tb08751.x>.
- (99) Fujioka, A.; Terai, K.; Itoh, R. E.; Aoki, K.; Nakamura, T.; Kuroda, S.; Nishida, E.; Matsuda, M. Dynamics of the Ras/ERK MAPK Cascade as Monitored by Fluorescent Probes. *J. Biol. Chem.* **2006**, *281* (13), 8917–8926. <https://doi.org/10.1074/jbc.M509344200>.
- (100) Leith, K. M. Dxl 600 and Dxl 800. *Immunoass. Handb.* **2013**, 597–601. <https://doi.org/10.1016/B978-0-08-097037-0.00049-X>.
- (101) Nelson, D. E.; Young, K. D. Penicillin Binding Protein 5 Affects Cell Diameter, Contour, and Morphology of Escherichia Coli. *J. Bacteriol.* **2000**, *182* (6), 1714–1721. <https://doi.org/10.1128/JB.182.6.1714-1721.2000>.
- (102) Grossman, N.; Ron, E. A.; Woldringh, C. L. Changes in Cell Dimensions during Amino Acid Starvation of Escherichia Coli. *J. Bacteriol.* **1982**, *152* (1), 35–41.
- (103) Bruce Alberts, Alexander Johnson, Julian Lewis, Martin Raff, Keith Roberts, and P. W. *Molecular Biology of the Cell*, 4th ed.; Garland Science, 2002.
- (104) Akashi, K.; Miyata, H.; Itoh, H.; Kinoshita, K. Preparation of Giant Liposomes in Physiological Conditions and Their Characterization under an Optical Microscope. *Biophys. J.* **1996**, *71* (6), 3242–3250. [https://doi.org/10.1016/S0006-3495\(96\)79517-6](https://doi.org/10.1016/S0006-3495(96)79517-6).
- (105) Rodriguez, N.; Cribier, S. Giant Vesicles Formed by Gentle Hydration and Electroformation : A Comparison by Fluorescence Microscopy. *Colloids and Surfaces.* **2005**, *42*, 125–130. <https://doi.org/10.1016/j.colsurfb.2005.01.010>.
- (106) Kresse, K. M.; Xu, M.; Pazzi, J.; García-ojeda, M.; Subramaniam A.B. Novel Application of Cellulose Paper as a Platform for the Macromolecular Self-

- Assembly of Biomimetic Giant Liposomes. *ACS Appl. Mater. Interfaces* **2016**, *8*, 47, 32102–32107.
- (107) Pawley, J. B. Fundamental and Practical Limits in Confocal Light Microscopy. *Scanning* **1991**, *13* (2), 184–198. <https://doi.org/10.1002/sca.4950130205>.
- (108) Greene, A. C.; Sasaki, D. Y.; Bachand, G. D. Forming Giant-Sized Polymersomes Using Gel-Assisted Rehydration. **2016**, No. May, 3–9. <https://doi.org/10.3791/54051>.
- (109) Li, Q.; Wang, X.; Ma, S.; Zhang, Y.; Han, X. Electroformation of Giant Unilamellar Vesicles in Saline Solution. *Colloids Surfaces B Biointerfaces* **2016**, *147*, 368–375. <https://doi.org/10.1016/j.colsurfb.2016.08.018>.
- (110) Pott, T.; Bouvrais, H.; Méléard, P. Giant Unilamellar Vesicle Formation under Physiologically Relevant Conditions. *Chem. Phys. Lipids* **2008**, *154* (2), 115–119. <https://doi.org/10.1016/j.chemphyslip.2008.03.008>.
- (111) Sankaranarayanan, K.; Hakkim, V.; Nair, B. U.; Dhathathreyan, A. Colloids and Surfaces A : Physicochemical and Engineering Aspects Nanoclusters of Nickel Oxide Using Giant Vesicles. *Colloids Surfaces A Physicochem. Eng. Asp.* **2012**, *407*, 150–158. <https://doi.org/10.1016/j.colsurfa.2012.05.023>.
- (112) Hadorn, M.; Boenzli, E.; Hotz, P. E. A Quantitative Analytical Method to Test for Salt Effects on Giant Unilamellar Vesicles. *Biophys. Chem.* **2011**, 1–8. <https://doi.org/10.1038/srep00168>.
- (113) Politano, T. J.; Froude, V. E.; Jing, B.; Zhu, Y. AC-Electric Field Dependent Electroformation of Giant Lipid Vesicles. *Colloids Surfaces B Biointerfaces* **2010**, *79* (1), 75–82. <https://doi.org/10.1016/j.colsurfb.2010.03.032>.
- (114) Blanken, D.; Van Nies, P.; Danelon, C. Quantitative Imaging of Gene-Expressing Liposomes Reveals Rare Favorable Phenotypes. *Phys. Biol.* **2019**, *16* (4). <https://doi.org/10.1088/1478-3975/ab0c62>.
- (115) Hermann, E.; Bleicken, S.; Subburaj, Y.; García-Sáez, A. J. Automated Analysis of Giant Unilamellar Vesicles Using Circular Hough Transformation. *Bioinformatics* **2014**, *30* (12), 1747–1754. <https://doi.org/10.1093/bioinformatics/btu102>.
- (116) Zabulis, X.; Papara, M.; Chatziargyriou, A.; Karapantsios, T. D. Detection of Densely Dispersed Spherical Bubbles in Digital Images Based on a Template Matching Technique. Application to Wet Foams. *Colloids Surfaces A Physicochem. Eng. Asp.* **2007**, *309* (1–3), 96–106. <https://doi.org/10.1016/j.colsurfa.2007.01.007>.
- (117) Reeves, J. P.; Dowben, R. M. Formation and Properties of Thin-Walled Phospholipid Vesicles. *J. Cell. Physiol.* **1969**, *73* (1), 49–60. <https://doi.org/10.1002/jcp.1040730108>.

- (118) Akashi, K.; Miyata, H.; Itoh, H.; Kinoshita, K. Preparation of Giant Liposomes in Physiological Conditions and Their Characterization under an Optical Microscope. *Biophys. Journ.* **1996**, *71* (December), 3242–3250.
- (119) Montes, L.-R.; Alonso, A.; Goñi, F. M.; Bagatolli, L. a. Giant Unilamellar Vesicles Electroformed from Native Membranes and Organic Lipid Mixtures under Physiological Conditions. *Biophys. J.* **2007**, *93* (10), 3548–3554. <https://doi.org/10.1529/biophysj.107.116228>.
- (120) Zupanc, J.; Dras, B.; Boljete, S.; Kralj-iglic, V.; Erdogmus, D.; Drobne, D. Lipid Vesicle Shape Analysis from Populations Using Light Video Microscopy and Computer Vision. *PLOS One.* **2014**, 1–14. <https://doi.org/10.1371/journal.pone.0113405>.
- (121) López Mora, N.; Hansen, J. S.; Gao, Y.; Ronald, A. a; Kieltyka, R.; Malmstadt, N.; Kros, A. Preparation of Size Tunable Giant Vesicles from Cross-Linked Dextran(Ethylene Glycol) Hydrogels. *Chem. Commun. (Camb).* **2014**, *50* (16), 1953–1955. <https://doi.org/10.1039/c3cc49144g>.
- (122) Li, W.; Wang, Q.; Yang, Z.; Wang, W.; Cao, Y.; Hu, N.; Luo, H.; Liao, Y.; Yang, J. Impacts of Electrical Parameters on the Electroformation of Giant Vesicles on ITO Glass Chips. *Colloids Surfaces B Biointerfaces* **2016**, *140*, 560–566. <https://doi.org/10.1016/j.colsurfb.2015.11.020>.
- (123) Fayolle, D.; Fiore, M.; Stano, P.; Strazewski, P. Rapid Purification of Giant Lipid Vesicles by Microfiltration. **2018**, 1–16.
- (124) Shohda, K.; Takahashi, K.; Suyama, A. A Method of Gentle Hydration to Prepare Oil-Free Giant Unilamellar Vesicles That Can Confine Enzymatic Reactions. *Biochem. Biophys. Reports* **2015**, *3*, 76–82. <https://doi.org/10.1016/j.bbrep.2015.07.005>.
- (125) Nishimura, K.; Matsuura, T.; Nishimura, K.; Sunami, T.; Suzuki, H.; Yomo, T. Cell-Free Protein Synthesis inside Giant Unilamellar Vesicles Analyzed by Flow Cytometry. *Langmuir.* **2012**, *28*, 8426-8432.
- (126) Nishimura, K.; Hosoi, T.; Sunami, T.; Toyota, T.; Fujinami, M.; Oguma, K.; Matsuura, T.; Suzuki, H.; Yomo, T. Population Analysis of Structural Properties of Giant Liposomes by Flow Cytometry. *Langmuir.* **2009**, *25* (10), 11443–11447. <https://doi.org/10.1021/la902237y>.
- (127) Krinsky, N.; Kaduri, M.; Zinger, A.; Shainsky-roitman, J.; Goldfeder, M.; Benhar, I.; Hershkovitz, D.; Schroeder, A. Synthetic Cells Synthesize Therapeutic Proteins inside Tumors. *Adv. Health. Mat.* **2018**, *1701163*, 1–10. <https://doi.org/10.1002/adhm.201701163>.
- (128) Tsuji, G.; Fujii, S.; Sunami, T.; Yomo, T. Sustainable Proliferation of Liposomes Compatible with Inner RNA Replication. *PNAS.* **2016**, *113* (3), 1–3. <https://doi.org/10.1073/pnas.1516893113>.

- (129) Fujii, S.; Matsuura, T.; Yomo, T. Membrane Curvature Affects the Formation of α -Hemolysin Nanopores. *A.C.S. Chem. Bio.* **2015**.
<https://doi.org/10.1021/acschembio.5b00107>.
- (130) Sato, K.; Obinata, K.; Sugawara, T.; Urabe, I.; Yomo, T. Quantification of Structural Properties of Cell-Sized Individual Liposomes by Flow Cytometry. *J. Biosci. Bioeng.* **2006**, *102* (3), 171–178. <https://doi.org/10.1263/jbb.102.171>.
- (131) Matsushita-Ishiodori, Y.; Hanczyc, M. M.; Wang, A.; Szostak, J. W.; Yomo, T. Using Imaging Flow Cytometry to Quantify and Optimize Giant Vesicle Production by Water-in-Oil Emulsion Transfer Methods. *Langmuir* **2019**, *35* (6), 2375–2382. <https://doi.org/10.1021/acs.langmuir.8b03635>.
- (132) Parigoris, E.; Dunkelmann, D. L.; Murphy, A.; Wili, N.; Kaech, A.; Dumrese, C.; Jimenez-Rojo, N.; Silvan, U. Facile Generation of Giant Unilamellar Vesicles Using Polyacrylamide Gels. *Sci. Rep.* **2020**, *10* (1), 0–10.
<https://doi.org/10.1038/s41598-020-61655-2>.
- (133) Woodle, M. C.; Papahadjopoulos, D. Liposome Preparation and Size Characterization. *Methods Enzymol.* **1989**, *171* (C), 193–217.
[https://doi.org/10.1016/S0076-6879\(89\)71012-0](https://doi.org/10.1016/S0076-6879(89)71012-0).
- (134) Graham, M. D. The Coulter Principle: Foundation of an Industry. *JALA - J. Assoc. Lab. Autom.* **2003**, *8* (6), 72–81. [https://doi.org/10.1016/S1535-5535\(03\)00023-6](https://doi.org/10.1016/S1535-5535(03)00023-6).
- (135) Van Amersfoort, E. S.; Van Strijp, J. A. G. Evaluation of a Flow Cytometric Fluorescence Quenching Assay of Phagocytosis of Sensitized Sheep Erythrocytes by Polymorphonuclear Leukocytes. *Cytometry* **1994**, *17* (4), 294–301.
<https://doi.org/10.1002/cyto.990170404>.
- (136) Nolan, J. P. Flow Cytometry of Extracellular Vesicles : Potential , Pitfalls , and Prospects. *Curr. Protocols in Cytom.* **2015**, No. July, 1–16.
<https://doi.org/10.1002/0471142956.cy1314s73>.
- (137) Kogan, M.; Feng, B.; Norde, B.; Rocha, S. Shear-Induced Membrane Fusion in Viscous Solutions. *Langmuir.* **2014**, *30*, 4875-4878.
- (138) Göpfrich, K.; Haller, B.; Staufer, O.; Dreher, Y.; Mersdorf, U.; Platzman, I.; Spatz, J. P. One-Pot Assembly of Complex Giant Unilamellar Vesicle-Based Synthetic Cells. *ACS Synth. Biol.* **2019**, *8* (5), 937–947.
<https://doi.org/10.1021/acssynbio.9b00034>.
- (139) Jørgensen, I. L.; Kemmer, G. C.; Pomorski, T. G. Membrane Protein Reconstitution into Giant Unilamellar Vesicles: A Review on Current Techniques. *Eur. Biophys. J.* **2017**, *46* (2), 103–119. <https://doi.org/10.1007/s00249-016-1155-9>.
- (140) Sugihara, K.; Chami, M.; Zambelli, T. Directed Self-Assembly of Lipid Nanotubes from Inverted Hexagonal. *A.C.S. Nano.* **2012**, No. 8, 6626–6632.
<https://doi.org/10.1021/nm300557s>.

- (141) Herold, C.; Chwastek, G.; Schwille, P.; Petrov, E. P. Efficient Electroformation of Supergiant Unilamellar Vesicles Containing Cationic Lipids on ITO-Coated Electrodes. *Langmuir* **2012**, *28* (13), 5518–5521. <https://doi.org/10.1021/la3005807>.
- (142) Nagle, J. F.; Tristram-Nagle, S. Structure of Lipid Bilayers. *Biochem. Biophys. Acta* **2000**, *1469*.
- (143) Kresse, K.; Xu, M.; Pazzi, J.; Subramaniam, A. B. Novel Application of Cellulose Paper As a Platform for the Macromolecular Self-Assembly of Biomimetic Giant Liposomes. *A.C.S. Appl. Mater. Interfaces* **2016**, *8*, 47, 32102–32107. <https://doi.org/10.1021/acsami.6b11960>.
- (144) Wüstner, D.; Modzel, M.; Lund, F. W.; Lomholt, M. A. Imaging Approaches for Analysis of Cholesterol Distribution and Dynamics in the Plasma Membrane. **2016**, *199*, 106–135. <https://doi.org/10.1016/j.chemphyslip.2016.03.003>.
- (145) Park, J. Y.; Kricka, L. J. Interferences in Immunoassay. *Immunoass. Handb.* **2013**, *1*, 403–416. <https://doi.org/10.1016/B978-0-08-097037-0.00027-0>.
- (146) Elliott, A. D. Confocal Microscopy: Principles and Modern Practices. *Curr. Protoc. Cytom.* **2020**, *92* (1), 1–11. <https://doi.org/10.1002/cpcy.68>.
- (147) Pawley, J. B. *Handbook of Biological Confocal Microscopy*, 3rd ed.; 2006.
- (148) Smith, C. L. Basic Confocal Microscopy. *Curr. Protoc. Mol. Biol.* **2008**, No. SUPPL. 81, 1–18. <https://doi.org/10.1002/0471142727.mb1411s81>.
- (149) Jonkman, J.; Brown, C. M.; Wright, G. D.; Anderson, K. I.; North, A. J. Tutorial: Guidance for Quantitative Confocal Microscopy. *Nat. Protoc.* **2020**, *15* (5), 1585–1611. <https://doi.org/10.1038/s41596-020-0313-9>.
- (150) Stefan Wilhelm, Bernhard Gröbler, Martin Gluch, H. H. *Confocal Laser Scanning Microscopy Principles*; 2009.
- (151) Microscopy, O. L. *Microscopy Optical Sectioning*. **2010**.
- (152) Gröbler, B.; Heinz, H. *LSM 880 Operating Manual*. **2014**.
- (153) Dimitrov, D. S.; Angelova, M. I. Lipid Swelling and Liposome Formation on Solid Surfaces in External Electric Fields. *Prog. Colloid. Polym. Sci.* **1987**, *56*, 48–56.
- (154) Okumura, Y.; Iwata, Y.; Engineering, M. Electroformation of Giant Vesicles on Indium Tin Oxide (ITO)-Coated Poly(Ethylene Terephthalate) (PET) Electrodes. **2011**, 109–118. <https://doi.org/10.3390/membranes1020109>.
- (155) Pazzi, J.; Subramaniam, A. B. Nanoscale Curvature Promotes High Yield Spontaneous Formation of Cell-Mimetic Giant Vesicles on Nanocellulose Paper. *A.C.S. Appl. Mater. Interfaces* **2020**, *12*, 56549–56561.
- (156) Aulin, C.; Gällstedt, M.; Lindström, T. Oxygen and Oil Barrier Properties of

- Microfibrillated Cellulose Films and Coatings. *Cellulose* **2010**, *17* (3), 559–574. <https://doi.org/10.1007/s10570-009-9393-y>.
- (157) Qing, Y.; Sabo, R.; Wu, Y.; Zhu, J. Y.; Cai, Z. Self-Assembled Optically Transparent Cellulose Nanofibril Films : Effect of Nanofibril Morphology and Drying Procedure. *Cellulose*. **2015**, 1091–1102. <https://doi.org/10.1007/s10570-015-0563-9>.
- (158) Zan, G. H.; Tan, C.; Deserno, M.; Lanni, F.; Lösche, M. Hemifusion of Giant Unilamellar Vesicles with Planar Hydrophobic Surfaces: A Fluorescence Microscopy Study. *Soft Matter* **2012**, *8* (42), 10877–10886. <https://doi.org/10.1039/c2sm25702e>.
- (159) Hamai, C.; Cremer, P. S.; Musser, S. M. Single Giant Vesicle Rupture Events Reveal Multiple Mechanisms of Glass-Supported Bilayer Formation. *Biophys. J.* **2007**, *92* (6), 1988–1999. <https://doi.org/10.1529/biophysj.106.093831>.
- (160) Pazzi, J.; Subramaniam, A. B. Nanoscale Curvature Promotes High Yield Spontaneous Formation of Cell-Mimetic Giant Vesicles on Nanocellulose Paper. *ACS Appl. Mater. Interfaces* **2020**, *12* (50), 56549–56561. <https://doi.org/10.1021/acsami.0c14485>.
- (161) Stein, H.; Spindler, S.; Bonakdar, N.; Wang, C.; Sandoghdar, V. Production of Isolated Giant Unilamellar Vesicles under High Salt Concentrations. *Front. Physiol.* **2017**, *8* (FEB), 1–16. <https://doi.org/10.3389/fphys.2017.00063>.
- (162) Peruzzi, J.; Gutierrez, M. G.; Mansfield, K.; Malmstadt, N. Dynamics of Hydrogel-Assisted Giant Unilamellar Vesicle Formation from Unsaturated Lipid Systems. *Langmuir* **2016**, *32* (48), 12702–12709. <https://doi.org/10.1021/acs.langmuir.6b01889>.
- (163) Weinberger, A.; Tsai, F. C.; Koenderink, G. H.; Schmidt, T. F.; Itri, R.; Meier, W.; Schmatko, T.; Schröder, A.; Marques, C. Gel-Assisted Formation of Giant Unilamellar Vesicles. *Biophys. J.* **2013**, *105* (1), 154–164. <https://doi.org/10.1016/j.bpj.2013.05.024>.
- (164) Dao, T. P. T.; Fauquignon, M.; Fernandes, F.; Ibarboure, E.; Vax, A.; Prieto, M.; Le Meins, J. F. Membrane Properties of Giant Polymer and Lipid Vesicles Obtained by Electroformation and Pva Gel-Assisted Hydration Methods. *Colloids Surfaces A Physicochem. Eng. Asp.* **2017**, *533* (July), 347–353. <https://doi.org/10.1016/j.colsurfa.2017.09.005>.
- (165) Has, C.; Sunthar, P. A Comprehensive Review on Recent Preparation Techniques of Liposomes. *J. Liposome Res.* **2019**, No. 0, 1–30. <https://doi.org/10.1080/08982104.2019.1668010>.
- (166) Huang, Z. H.; Abkarian, M.; Viallat, A. Sedimentation of Vesicles: From Pear-like Shapes to Microtether Extrusion. *New J. Phys.* **2011**, *13*. <https://doi.org/10.1088/1367-2630/13/3/035026>.

- (167) Rey Suárez, I.; Leidy, C.; Téllez, G.; Gay, G.; Gonzalez-Mancera, A. Slow Sedimentation and Deformability of Charged Lipid Vesicles. *PLoS One* **2013**, *8* (7). <https://doi.org/10.1371/journal.pone.0068309>.
- (168) Hodnik, V.; Turk, T.; Anderluh, G.; Mikelj, M.; Praper, T.; Demic, R. Electroformation of Giant Unilamellar Vesicles from Erythrocyte Membranes under Low-Salt Conditions. *Anal. Biochem.* **2013**, *435*, 174–180. <https://doi.org/10.1016/j.ab.2013.01.001>.
- (169) Bagatolli, L. A.; Parasassi, T.; Gratton, E. Giant Phospholipid Vesicles: Comparison among the Whole Lipid Sample Characteristics Using Different Preparation Methods - A Two Photon Fluorescence Microscopy Study. *Chem. Phys. Lipids* **2000**, *105* (2), 135–147. [https://doi.org/10.1016/S0009-3084\(00\)00118-3](https://doi.org/10.1016/S0009-3084(00)00118-3).
- (170) Mathivet, L.; Cribier, S.; Devaux, P. F. Shape Change and Physical Properties of Giant Phospholipid Vesicles Prepared in the Presence of an AC Electric Field Characterization of Giant Vesicles. *Biophys. Journ.* **1996**, *70* (March), 1112–1121.
- (171) Telis, V. R. N.; Telis-Romero, J.; Mazzotti, H. B.; Gabas, A. L. Viscosity of Aqueous Carbohydrate Solutions at Different Temperatures and Concentrations. *Int. J. Food Prop.* **2007**, *10* (1), 185–195. <https://doi.org/10.1080/10942910600673636>.
- (172) Paper, O. Fluorescent Quantification of Size and Lamellarity of Membrane Nanotubes. *Eur. Biophys. Journ.* **2014**, 595–602. <https://doi.org/10.1007/s00249-014-0989-2>.
- (173) Russ, John C.; Neal, F. B. *The Image Processing Handbook*, 7th ed.; CRC Press, 2016.
- (174) Beucher, S. The Watershed Transformation Applied to Image Segmentation. *Proc. 10th Pfefferkorn Conf. Signal Image Process. Microsc. Microanal.* **1992**, 299–314. <https://doi.org/10.1.1.24.5229>.
- (175) He, Y.; Gong, H.; Xiong, B.; Xu, X.; Li, A.; Jiang, T. ICut : An Integrative Cut Algorithm Enables Accurate Segmentation of Touching Cells. *Nat. Publ. Gr.* 1–17. <https://doi.org/10.1038/srep12089>.
- (176) Koyuncu, C. F.; Akhan, E.; Ersahin, T.; Cetin-atalay, R. Iterative H-Minima-Based Marker-Controlled Watershed for Cell Nucleus Segmentation. **2016**. <https://doi.org/10.1002/cyto.a.22824>.
- (177) Chen, S. Chaotic Spread Spectrum Watermarking for Remote Sensing Images. *J. Electron. Imaging* **2004**, *13* (1), 220. <https://doi.org/10.1117/1.1631316>.
- (178) Otsu, N. A Threshold Selection Method from Gray-Level Histograms. *IEEE Trans. Syst. Man. Cybern.* **1979**, *9* (1), 62–66. <https://doi.org/10.1109/TSMC.1979.4310076>.

- (179) Thresholding, O.; Pages, B. Otsu Thresholding. *The Lab Book Pages*. **2010**, No. June, 1–8.
- (180) Ueno, T.; Ueno, S.; Kakazu, Y.; Akaike, N.; Nabekura, J. Image Processing ToolboxTM 6 User ' s Guide. *Image Process.* **2001**, 78 (0022-3042 LA-eng PT-Journal Article), 1009–1018.

Chapter 3: A Comprehensive Characterization of Populations of Giant Unilamellar Vesicles Assembled through Surface-Assisted Techniques

1. Introduction

Giant unilamellar vesicles (GUVs) are cell-sized, enclosed phospholipid membranes that have proven to be instrumental tools in biological membrane research¹⁻³. Preparation methods used to assemble GUVs fall into one of two categories: i) surface-assisted methods and ii) solvent-based methods. Of the two, surface-assisted methods are the most commonly employed since they are easier to implement, require less equipment, and do not leave behind residual solvents that could alter the GUV membrane. Regarding applications, questions of whether to use surface-assisted methods versus solvent-based methods only arise in situations where a precise control of the yields and distribution of the sizes of the GUVs is desirable. These questions are further complicated since much about the mechanism of GUV formation and what controls the sizes and yields of GUVs from surface-assisted methods is unknown. In this chapter, I conduct a comprehensive series of experiments following the standardized protocols I developed in Chapter 2 that provide crucial quantitative data on the populations of GUVs assembled through the surface-assisted techniques. The results of the data lead to a wealth of information with highlights including the novel discovery of the use of surfaces composed of nanoscale cylindrical fibers to assemble high yields of GUVs, a budding and merging thermodynamic model that describes the assembly of GUVs at surfaces and allows for the rationale optimization of assembly parameters, and the development of a one-step method that overcomes current challenges associated with obtaining high yields of GUVs in physiological salt conditions.

1.1 Approach for analysis

Using the novel confocal microscopy based methods developed in Chapter 2, I systematically characterize the populations of GUVs that can be assembled from the most commonly used surface-assisted methods. I briefly review these methods in section 1.2 and introduce recent methods that use cellulose paper to assemble GUVs in section 1.3. In section 1.4, I use a new concept, the molar yield⁴, which allows for the first time rationale quantitative comparisons of the sizes and yields of the GUVs. In section 2, the materials and methods used in this work are thoroughly detailed. In section 3, I show the effect of the properties of three physically different cellulose papers and one cotton fabric on the sizes and yields of GUVs. Using these results, I determine the optimal cellulose paper substrate to assemble GUVs and compare the sizes and molar yields with other commonly used substrates in sections 4.1–4.3. In section 4.4, the experimental data can be explained and supported by the budding and merging thermodynamic model⁴. In section 5, I optimize the various parameters involved in the assembly of GUVs such as the time allowed for assembly and the concentration of salts present during hydration and develop a novel one-

step modulation of the ionic strength method to obtain high yields of GUVs in physiological salt conditions from tracing paper.

1.2 Commonly used methods to assemble GUVs

1.2.1 Gentle hydration

The earliest method used for the preparation of vesicles is called gentle hydration and was first discovered by Bangham in 1965⁵. The method has since been adapted⁶ and typically involves the deposition of a lipid solution in an organic solvent such as chloroform onto a glass surface (Figure 51a). The lipid film is allowed to completely dry and is then hydrated in an aqueous solution⁶. Observations of the surface after hydration reveal the spontaneous assembly of the lipids into buds of GUVs above the glass⁷. Once formed, the buds can be released from the surface through the manual application of shear flow using a pipette⁸. Although the method does not require a considerable amount of materials or preparatory steps, from qualitative studies it has been reported to suffer from long incubation times and low yields^{3,9,10}.

1.2.2 Electroformation

To overcome some of these issues, Angelova and Dimitrov¹¹ discovered that an externally applied electric field can be used to produce giant vesicles from the hydrated films of lipids deposited on platinum wires. Subsequently, other electrode surfaces such as indium tin oxide (ITO covered slides) and steel plates have been used^{12,13}. The method using ITO covered slides in particular, known as the electroformation method (Figure 51b), is currently the most widely used method for preparing giant vesicles^{3,10,14}. Experimental conditions such as, amount of lipids used, the applied electric field parameters, and the substrate patterns, can be tuned to produce vesicles with varying compositions and population sizes¹⁴. However, from qualitative studies, it appears challenging to form vesicles from films with excess charged lipids or in solutions of physiological ionic strengths³. There are also concerns that exposure to the electric field causes partial lipid oxidation¹⁵ thus altering the membrane properties.

1.2.3 Gel-assisted rehydration

Since biological membranes are typically found in around 150 mM salts, methods to produce GUVs in similar solutions are desirable^{3,12,16,17}. However, the yields of GUVs obtained from the gentle hydration and electroformation methods have been qualitatively reported to be significantly lowered when the lipids are hydrated in physiological conditions¹⁸.

More recently, gel-assisted formation techniques (Figure 51c) have proven useful for preparing giant vesicles at higher ionic strengths^{19,20}. Following similar procedures as gentle hydration, giant vesicles are formed when a dry lipid film is deposited onto a glass surface that has been covered by a gel such as, agarose²¹, polyvinyl alcohol¹⁹, or cross-linked dextran(ethylene glycol)²⁰. After hydration, the dissolution of the gel during the

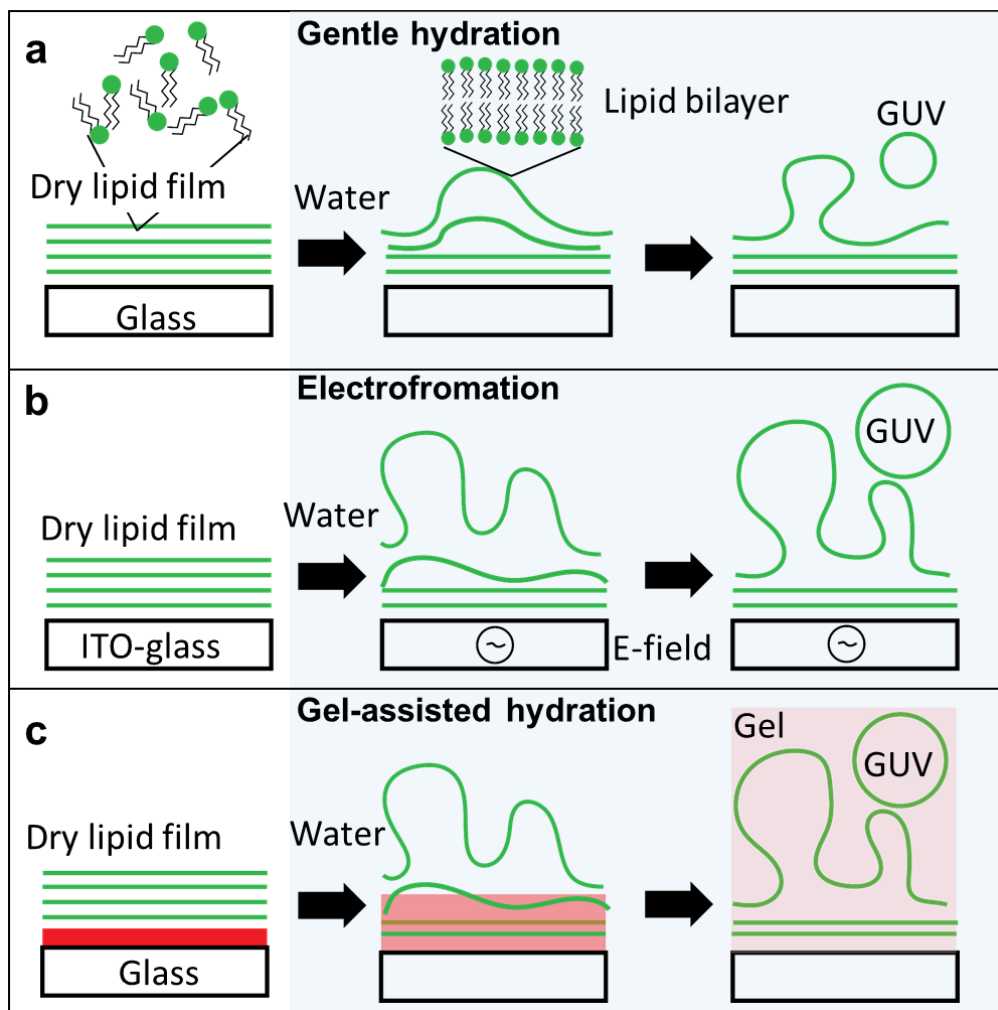


Figure 51: Schematic showing an overview of the most common methods used to obtain GUVs. Methods to obtain GUVs typically begin with the deposition of lipids to obtain a dry lipid film on a surface (left). **a** The gentle hydration is the most straightforward to implement and involves only the hydration of a glass surface in water (light blue). However, the gentle hydration method is reported to result in smaller and fewer GUVs. **b** The electroformation method is reported to improve the sizes and yields of the GUVs produced from the gentle hydration method by using a conductive (typically indium tin oxide or ITO) coated glass surface and connecting the surface to a power supply (E-field symbol). **c** The gel-assisted rehydration method is also reported to increase the sizes and yields of GUVs compared to gentle hydration due to the presence of a gel that dissolves into solution (light red).

assembly of the lipid film is reported to increase the yields of GUVs in high salts. The main drawback with the gel-assisted methods is that the dissolution of the gels into the solution can cause an unwanted contamination of the vesicles^{19,22,23}.

1.2.4 Solvent-based methods

Microfluidic methods have also been used to prepare giant vesicles^{10,24–26}. These methods often employ the use of a water/oil/water double emulsion to bring together two stabilized lipid monolayers in an emulsion droplet. Encapsulation of water soluble molecules into the inner droplet is efficient and the final vesicle size is controlled by the size of the inner water droplet allowing for good control over final vesicle sizes³. However, not only do these methods require a significantly high cost of materials and preparatory steps, the solvent that remains in the membranes after formation of the GUVs can significantly alter properties of the final bilayer membrane and removal of the solvent is difficult¹⁰.

1.3 Novel use of cellulose paper as a substrate to assemble GUVs

Following similar procedures as the gentle hydration method, a novel method to produce giant vesicles using cellulose paper termed the POPYRUS (for Paper Abetted liPid hYdRation in aqUeous Solutions) method was developed²⁷. The POPYRUS method allows for the growth of vesicles without the degradation or incorporation of the cellulose even at higher temperatures (85 °C). Lipids dissolved in chloroform can be deposited onto a small piece of filter paper and the volatile solvent is allowed to evaporate. Subsequent rehydration of the lipid-coated paper in an aqueous solutions leads to the formation of vesicles in under an hour as seen in Figure 52a. One of the advantages of the POPYRUS method is its versatility to a variety of different amphiphiles and different growth conditions²⁸. The growth of vesicles exhibiting phase behavior (Figure 52b) as well as vesicles composed of various lamellar phase forming amphiphiles including lipids, polymers, and fatty acids have all been observed²⁸. Up until the work discussed in this dissertation, physiologically relevant salt buffers such as phosphate-buffered saline (PBS) and Tris had shown to suppress vesicle formation. In section 5 of this chapter, I develop a new method to address and overcome these challenges.

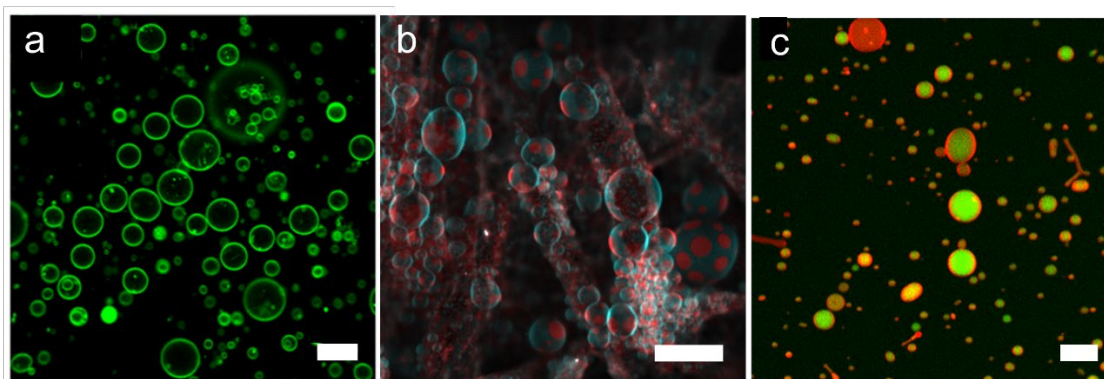


Figure 52: Paper-based method to form giant vesicles. **a** Giant vesicles (green circles) formed on cellulose paper are extracted after an hour incubation and imaged using a confocal fluorescence microscopy. Typical sizes of the vesicles observed are between 5 and 20 μm . **b** Giant vesicles exhibiting phase coexistence (separate liquid phases) can be seen growing on cellulose fibers. Two different membrane dyes are added to the lipid mixtures where one partitions into the areas shown in blue and the other partitions into the

areas shown in red. **c** Giant vesicles extracted from paper exhibiting encapsulation of bovine serum albumin protein tagged with fluorescent molecule. Scale bars: **a,c** 20 μm , **b** 50 μm . Images were published²⁷ and reproduced here with permission from the American Chemical Society.

1.4 Molar yield as a standardized metric to compare populations of GUVs assembled from different techniques

1.4.1 Definition of molar yield

As discussed in Chapter 2, comparisons of the different populations of GUVs produced from the different techniques (and different conditions) has predominantly been conducted through the manual counting of an insignificant portion of the GUV population and reproducing a size distribution. Although useful if a statistically significant percentage of the population is analyzed, the size distributions can ultimately become cumbersome when trying to compare more than one population of GUVs at a time due to the wide range in magnitudes of both the vesicle sizes and counts in a typical population. In addition, since the counts of the largest GUVs are significantly smaller than the total counts (up to 5 orders of magnitude smaller), and since the amount of lipid stored in a GUV scales nonlinearly with the diameter of the GUV (membrane surface area is proportional to the GUV diameter squared), it can be difficult to fairly appreciate the effect the largest GUVs have on the yields considering only the counts. Thus, to allow more rational comparisons of GUV populations, a metric termed the molar yield is used to describe the molar percentage of lipid that is converted into GUV membrane during a single growth cycle⁴. More specifically, the molar yield is defined as the ratio of the total moles of lipid that are composed into GUV membrane over the total moles of lipid that was initially deposited⁴.

To calculate the moles of lipid that are composed into GUV membrane I use the distributions of sizes (most accurately obtained using the methods described in Chapter 2) to collect the diameter of each of the GUVs harvested from an experiment. I then determine the total surface area of all of the GUVs analyzed assuming the surface area of each GUV to be equal to the surface area of an equivalent sphere (πd^2). To calculate the number of moles of lipid from the total surface area, I simply use the typical head group area of each lipid ($\sim 70 \text{ \AA}^2$ for the most commonly used lipid, DOPC) and Avogadro's number. Thus, as long as the total moles of lipid initially deposited is controlled for the molar yield can be calculated using Equation 11⁴:

$$Y = 100 \left(\frac{2\pi m V_h}{N_A A_{hg} M V_{al}} \sum_{i=1}^n (d_i)^2 \right) \quad (11)$$

where, m is the molecular weight of the lipid, V_h is the volume of the harvested solution, N_A is Avogadro's number, A_{hg} is the headgroup area of the lipid, M is the mass of lipid deposited, V_{al} is the volume analyzed, n is the number of GUVs analyzed, and d_i is the

diameter of vesicle i . The factor of 2 accounts for the 2 lipid leaflets in a bilayer. I typically break the molar yield out into three size ranges to help better analyze the GUV population. The three size ranges I typically break the molar yield into are small GUVs with diameters that range between $1 \leq d_i < 10 \mu\text{m}$, large GUVs with diameters that range between $10 \leq d_i < 50 \mu\text{m}$ and very large GUVs with diameters $d_i \geq 50 \mu\text{m}$.

$$mol_{GUV} = mol_{\text{small GUVs}} + mol_{\text{large GUVs}} + mol_{GUVs \geq 50} \quad (12)$$

$$mol_{GUV} = \frac{2\pi V_h}{N_A A_{hg} V_{al}} \left(\sum_{i=1}^{N_{d<10}} (d_i)^2 + \sum_{i=d \geq 10}^{N_{d<50}} (d_i)^2 + \sum_{i=d \geq 50}^N (d_i)^2 \right) \quad (13)$$

In the work conducted in this chapter, I find the molar yield of GUVs typically ranges somewhere between 1 – 30 % depending on the technique.

1.4.2 Statistical comparisons of the molar yields

I develop a statistical testing method to make quantitative comparisons between the molar yields obtained from different samples. These tests are used to ensure that any differences between the conditions are correctly interpreted and that the apparent relationships are meaningful and are not merely due to random chance. Since I am interested in comparing the population means of the molar yields from more than 2 different preparation conditions, I use a one-way analysis of variation (ANOVA) test. The one-way ANOVA test is a hypothesis test that can be used to make quantitative comparisons between the population means of 2 or more groups that differ in only one way (experiments controlled to test only one independent variable)²⁹. The test starts with a null hypothesis (or initial hypothesis) that the population means between the unrelated groups are equal²⁹. The test mathematically determines the statistical significance (p-value) that estimates the likelihood that the null hypothesis will be rejected due to random chance²⁹. A p-value of less than 0.05 for example, would mean there is less than a 5 % chance that the null hypothesis will be rejected due to random chance.

To conduct the one-way ANOVA, I confirm that the molar yield data meets the statistical assumptions underlying the test. The first assumption is that the variance between the populations are not statistically different²⁹. The variance is a mathematical description of how far a set of numbers spread out from an average value and is given by Equation 14²⁹:

$$\sigma^2 = \frac{\sum_{i=1}^N (x_i - \mu)^2}{N} \quad (14)$$

where σ^2 is the population variance, x_i is the molar yield of sample i , μ is the mean molar yield of the population, and N is the number of samples. To compare the variances, I conduct a Bartlett's test on the molar yields using a Matlab built-in function *vartestn*. The Bartlett's test performs a hypothesis test with a null hypothesis that the variance is the same

between all groups²⁹. Thus, if the Bartlett's test returns a p-value of greater than 0.05 (fails to reject the null hypothesis) the data meets the variance criteria for the ANOVA test²⁹.

The second assumption is that each sample must be drawn from a normally distributed population²⁹. A normal distribution is a probability density function that describes a symmetric distribution of values that cluster around one central peak. The general probability density function for a normal distribution is given by Equation 15²⁹:

$$f(x) = \frac{1}{\sigma} e^{-\frac{1}{2} \left(\frac{x-\mu}{\sigma} \right)^2} \quad (15)$$

where $f(x)$ is the probability density function, σ is the standard deviation, and μ is the mean. I conduct another hypothesis test called the Anderson-Darling test that returns a p-value from each different group with a null hypothesis that each sample is from a normally distributed population³⁰. Using the built-in *adtest* Matlab function with the molar yield data, the test returns a p-value with a null hypothesis that each sample is from a normally distribution population.

The third assumption is that the observations I make of populations of GUVs are independent of each other. In other words, the data that is being evaluated statistically is all collected in the same manner and only one aspect of the experiment is different between all of the samples. I expect the third assumption to also be met since I follow a standardized protocol to conduct each of the experiments in the same manner.

With the assumptions for a one-way ANOVA met, I conduct the tests using the null hypothesis that the population means of the molar yields from the different conditions are all equal. I set the significance value to reject the null hypothesis for the different tests at a value of $p < 0.05$. An ANOVA test outputs a matrix with various values that are involved in the computation of a test-statistic. Each row breaks down the overall variability in the experiment into different components with the first being the variability between the different conditions (independent variable), the second being variability between all of the samples (i.e. all of the replicates of all of the conditions), and the third being the variability between the residuals (difference between the observed value for each sample and the expected value). The columns of the ANOVA comprise of the computations that include the degrees of freedom (DF), the sum of squares (SS), the mean of the sum of squares (MS), the test statistic (F), and the p-value of the test statistic. The test statistic, which is a likelihood estimate that the variation between the conditions is not due to random chance, is calculated using Equation 16²⁹:

$$F = \frac{\frac{\sum n_j (\mu_j - \mu)^2}{k - 1}}{\frac{\sum \sum (x_{ij} - \mu_j)^2}{N - k}} \quad (16)$$

where F is the test statistic, n_j is the sample size per group j , μ is the overall mean molar yield, μ_j is the mean molar yield of each group, x_{ij} is the molar yield of each sample ij , k is the number of conditions, and N is the total number of samples. I conduct the ANOVA

calculations by inputting all of the molar yield data from all of the samples from one independent variable using the built-in *anova1* function. The function outputs an ANOVA table with all of the important calculations including the p-value of the test statistic. If the p-value of the test statistic is less than 0.05, there is less than a 5 % chance that the null hypothesis that the molar yields are all equal is rejected due to random chance. Since the ANOVA only provides a likelihood estimate on whether all of the molar yields between the groups are equal but does not provide any information on how the molar yields compare with one another, I use a post-hoc test following the TukeyHSD criteria (Tukey's Honestly-Significant Difference) to determine the statistical significance of the differences between the conditions. The Tukey test runs pairwise comparisons among each of the conditions using the honestly significant criteria given by Equation 17²⁹:

$$HSD = \frac{\mu_i - \mu_j}{\sqrt{\frac{SS_{ij}}{df_{ij}} \frac{1}{n}}} \quad (17)$$

where μ_i is the mean of condition i , μ_j is the mean of condition j , SS_{ij} is the sum of squares between the conditions i and j , df_{ij} is the degrees of freedom of the conditions i and j , and n is the number of samples conducted for each condition. I conduct the Tukey test using the built-in *multcompare* function to compare each combination of the conditions and determine the significance of the differences between the conditions. I reject the null hypothesis that the means are equal if the p-value that is returned from the Tukey test is less than 0.05.

1.4.3 Calculation of molar yields reported in the literature

Until the introduction of the molar yield, the characterization of a population of GUVs was done almost exclusively by quantifying the sizes of a portion of the GUV population and reporting histograms showing the distribution of sizes^{12,17,19,20,23,31–40}. Direct comparisons between these histograms are extremely difficult due to the sheer number of experimental parameters involved in both a single GUV harvest as well as the consequent analysis. I show for the first time fair comparisons of GUV populations from data across important contributions in the literature for surface-assisted methods in Table 5 and for solvent-based methods in Table 6.

For both tables, I collect the data from each publication in rows that are signified by the numbers in column (a). The table consists of 16 rows with 15 unique columns (distributed on multiple pages to improve readability). The columns contain a comprehensive collection of the important parameters relevant to the assembly of GUVs from each (b) literature source when they are mentioned including (c) the method of growth, (d) the substrate used, (e) the composition of lipids, (f) the total mass of lipids deposited, (g) the mass per area of substrate covered with lipid, (h) the volume of the hydration solution used, (i) the solution conditions, (j) the incubation parameters such as the time and the temperature during growth, (k) the size range of GUVs analyzed, (l) the largest size analyzed, (m) whether the histogram of sizes was reported, (n) the percentage of the total population analyzed (typically reported as the volume of the harvested solution

over the volume analyzed), and (o) the counts per microgram of lipid deposited. In the final column (p), I report the molar yield of GUVs for the literature sources that provide enough information for it to be calculated.

To calculate the molar yields in the final column, I require at minimum the amount of lipid that is initially deposited, the fraction of the GUV population that is analyzed, and the histograms showing the distribution of sizes of the GUVs. I extract the counts of the GUVs from the size distribution histograms using an online “WebPlotDigitizer” tool⁴¹. I consider the size of the GUVs in each bin to be equal to the size at the bin center. I then calculate the molar yield by plugging the sizes, counts, total lipid used, and fraction of the population analyzed (given as the volume of the aliquot, V_a , over the total volume harvested, V_h) into Equation 11⁴. The rows in the tables are organized by the method used to prepare the GUVs. Although it is generally considered that the electroformation and gel-assisted hydration methods can be used to obtain high yields of GUVs compared to the gentle hydration method in the literature⁴², the calculations in the Table 5 indicate that using the current data available, molar yields above 1% are not obtainable. These lower than expected molar yields are also observed in Table 6 where data from various solvent-based assembly methods is collected. Following the standardized protocols, I find in the work conducted in section 4 of this chapter, the gentle hydration method on glass in aqueous solutions is expected to result in molar yields of around 15% as a baseline.

Surface-assisted GUV formation methods in literature

(a)	(b) Lit. (First Author, Year)	(c) Method	(d) Substrate	(e) Lipid
1	Akashi, 1996	Gentle hydration	glass only	Egg PC/egg PG/Rhodamine18 (90:10:0.2%)
2	Yamashita, 2002	Gentle hydration	glass only	DOPC/PEG2kPE/NBD-PC (98:2:0.5%)
3	Tsumoto, 2009	Gentle hydration (sugar doped)	glass + 25 μ L of 20 mM fructose	DOPC
4	Estes, 2005	Electroformation	ITO coated glass	Egg PC/Egg PG (50:50)
5	Montes, 2006	Electroformation	Pt wires	Erythrocyte ghosts
6	Pott, 2008	Electroformation	Pt wires	PC lipid
7	Zupanc, 2014	Electroformation	2 platinum electrodes	POPC/Cholesterol (80:20%)
8	Li, 2016	Electroformation	Plasma cleaned ITO	DOPC:TR-DHPE (99.5:0.5)
9	Lefrancois, 2018	Electroformation	ITO or Pt wires	Egg PC
10	Parigoris, 2020	Electroformation	Glass coated with PAA	DOPC:RhoPE (99.5:0.5%)
11	Mora, 2014	Gel-assisted (cross-linked dextran polyethylene glycol)	1.2 mg Dex-PEG crosslinked on glass (75 mm x 25 mm)	POPC/ATTO-488-PE (99.5:0.5%)
12	Horger, 2009	Gel-assisted (Agarose)	Agarose on glass slides (50 mm x 70 mm)	POPC/PEG2kPE/RhoPE (95:5:0.5%)
13	Weinberger, 2013	Gel-assisted (PVA)	PVA on glass slides (30 mm diameter)	POPC/RhoPE (99.5:0.5%)
14	Mora, 2014	Gel-assisted (cross-linked dextran polyethylene glycol)	1.2 mg Dex-PEG crosslinked on glass (75 mm x 25 mm)	POPC/ATTO-488-PE (99.5:0.5%)
15	Peruzzi, 2016	Gel-assisted (Agarose)	Agarose on glass slides (25 mm x 25 mm)	POPC/ATTO-488-PE (99.5:0.5%)
16	Blosser, 2016	Solvent-based (CDICE)	500 μ L centrifuge tube	DOPC

Surface-assisted GUV formation methods in literature

(a)	(f) Mass	(g) Area	(h) Hydration Volume	(i) Hydration Buffer	(j) Incubation parameters
1	1000 μg	176.7 mm^2	1000 μL	100 mM NaCl + 100 mM sucrose	Sealed under argon at 37C for 12 hours
2	79.2 μg	176.7 mm^2	200 μL	150 mM NaCl + 100 mM sucrose	Room temperature for 3 hours
3	39.6 μg	176.7 mm^2	500 μL	100 mM NaCl	Room temperature for 24 hours
4	40 μg	400 mm^2	Not specified	300 mM Sucrose	Room temperature 2 hours
5	12.5 μg	5 mm^2	Not specified	100 mM NaCl	45 deg C for 2 hours
6	19.8 μg	Not specified	Not specified	1X PBS	Room temp overnight
7	Not specified	Not specified	Not specified	Overnight	Room temperature overnight
8	Not specified	Not specified	Not specified	1X PBS + 300 mM sucrose	Room temp for 2 hours
9	1.9 μg	Not specified	Not specified	150 mM NaCl	Room temp for 2 hours
10	Not specified	Not specified	Not specified	100 mM NaCl	Room temp for 90 minutes
11	111 μg	1875 mm^2	300 μL	1XPBS	Room temperature for 1 hour
12	113 μg	3500 mm^2	Not specified	1XPBS	Room temperature for 3 hours
13	20 μg	706.9 mm^2	Not specified	1X PBS	Room temperature for 3 hours
14	111 μg	1875 mm^2	300 μL	1XPBS	Room temperature for 1 hour
15	30 μg	625 mm^2	Not specified	1XPBS + 200 mM sucrose	Room temperature for 30 minutes
16	1400 μg	Not specified	Not specified	1X PBS	Centrifuge petri dish

Surface-assisted GUV formation methods in literature

(a)	(k) Harvested sizes analyzed (um)	(l) Largest size	(m) Histogram provided	(n) Total counts	(o) GUV counts per μg lipid deposited	(p) Molar Yield (%)
1	>25	300	N	1000	1	Not calculable
2	> 10	65	Y	690	8.7	0.0047
3	> 10	79	Y	150	39.8	0.035
4	>10	Not specified	N	Not harvested	Not calculable	Not calculable
5	>10	50	N	Not specified	Not calculable	Not calculable
6	>1	Not specified	N	Not specified	Not calculable	Not calculable
7	>1	41	Y	582,380	14,500	0.78
8	>1	16	N	Not harvested	Not calculable	Not calculable
9	>10	Not specified	N	Not harvested	Not calculable	Not calculable
10	>6.9	36	N	Not specified	Not calculable	Not calculable
11	>1	30	Y	75	0.68	0.00020
12	None	Not specified	N	Not harvested	Not calculable	Not calculable
13	None	Not specified	N	Not harvested	Not calculable	Not calculable
14	>1	Not specified	N	1483	49.4	Not calculable
15	>10	Not specified	N	Not specified	Not calculable	Not calculable
16	>6.9	36	N	Not specified	Not calculable	Not calculable

Table 5: Surface-assisted GUV formation methods in literature. Collection of data from literature on different surface-based GUV formation methods. The important parameters necessary to compare the populations of GUVs produced between the different techniques are collected where reported. The final column (molar yield %) is a percent calculation that allows for a quantitative comparison between the techniques based on the amount of lipid that converted into GUV for each technique.

Solvent-based GUV formation methods in literature

(a)	(b) Lit. (First Author, Year)	(c) Method	(d) Substrate	(e) Lipid
1	Kim, 1981	Solvent-based (mechanical shaking)	glass vial	PC/C/PG/TO (40:40:20:10%)
2	Tan, 2006	Solvent-based (droplet microfluidics)	shear-focusing droplet device	DOPC
3	Nishimura, 2012	Solvent-based (microfluidic and centrifugation)	shear-focusing droplet device and centrifuge	POPC/POPG/ Chol (90:05:05%)
4	Arriaga, 2013	Solvent-based (Biphasic flow with two capillaries to produce w-o-w emulsion)	Glass capillaries	DOPC:Chol DPPC:RhPE (35:35:30:0.5%)
5	Lu, 2015	Solvent-based (w-o-w microfluidic)	shear-focusing droplet device	DOPC:Chol:NBD-PC (70:30:0.5%)
6	Morita, 2015	Solvent-based (Centrifugal capillary based microfluidic device)	Glass capillary in centrifuge tube	DOPC:Egg PC (50:50%)
7	Desphande, 2016	Solvent-based (Octanol used in biphasic flow)	microfluidic device, 1-octanol solvent	DOPC:RhoPE (99.9:0.1%)
8	Blosser, 2016	Solvent-based (droplet interface eDICE)	Appartus requiring custom plastic disk, glass capillaries, petri dish, centrifuge	DPPC:DiPhyPC (80:20%)
9	Tsumoto, 2016	Solvent-based (w-o-w centrifugation)	500 μ L centrifuge tube	Egg PC

Solvent-based GUV formation methods in literature

(a)	(f) Mass	(g) Frequency	(h) Volume	(i) Hydration buffer	(j) Incubation parameters
1	5200 μg	Not specified	Not specified	Chloroform+200 mM Sucrose in water	10 min shaking, 45 minutes evaporated, 37C
2	240 μg	240 μg / hour	Not specified	Ethanol+water	Room temperature
3	2500 μg	2500 μg / hour	500 μL	100 mM Hepes, 500 mM glucose, 2.5 wt % PEG6k in water	Microfluidic device and centrifugation
4	2500 μg	2500 μg / hour	Not specified	36% vol Chloroform, 64% vol hexane, 8 wt% PEG, 2 wt% PVA in water	Biphasic flow using two capillaries
5	3200 μg	3200 μg / hour	400 μL	Oleic acid, 0.6 M glucose, 1 wt% PVA, 14% ethanol, 10% glycerol in water	Prepare 2 lipid in oil solutions, and pump in microfluidic device for 1 hour
6	130 μg	130 μg / hour	170 μL	Ultrapure water	Centrifuge emulsion inside capillary
7	200 μg	200 μg / hour	100 μL	Poloxamer 188 50 mg/mL, 15 wt% glycerol, 15 wt% ethanol in water	Biphasic flow using octanol as solvent
8	1400 μg	1400 μg / hour	Not specified	100 mM sucrose, 30% decane	Flow through spinning disk
9	500 μg	Not specified	500 μL	Ultra pure water	Centrifuge emulsion

Solvent-based GUV formation methods in literature

(a)	(k) Harvested sizes analyzed (um)	(l) Largest size	(m) Histogram provided (Y/N)	(n) Total counts	(o) GUV counts per ug lipid deposited	(p) Molar Yield (%)
1	>1	17	Y	Not specified	Not calculable	Not calculable
2	>20	80	N	Not specified	Not calculable	Not calculable
3	>1	20	Y	~50,000	20	0.0010
4	>80	90	N	Not specified	Not calculable	Not calculable
5	>50	65	Y	~6,000	112.5	0.46
6	>1	30	Y	329	2.5	0.00067
7	>15	30	Y	~3,000	855	0.21
8	>1	Not specified	N	Not specified	Not calculable	Not calculable
9	>1	66	N	~10,000	16.5	Not calculable

Table 6: Solvent-based GUV formation methods in literature. Table showing a collection of data from solvent-based formation methods in literature. Compared to the surface-assisted methods, solvent-based methods require a much larger amount of lipid to produce a similar number of GUVs.

2. Materials and methods

To allow fair comparisons between the populations of GUVs assembled using different substrates, I carefully follow protocols that standardize the GUV assembly process and minimize any effects from experimental variation. In this section, I provide details on the materials and chemicals used to conduct the experiments, the methods used where necessary to fabricate the substrates, the methods used to clean the substrates, the standard composition of the lipid mixture used for experiments, the procedures used to assemble the GUVs, the methods used to characterize the different populations of GUVs (also detailed extensively in Chapter 2), the methods used to characterize the different substrates, and any other methods referred to in the remaining sections.

2.1 Materials

I purchased indium tin oxide (ITO) coated-glass slides (25×25 mm squares with a surface resistivity of 8-12 Ω /sq) from Sigma-Aldrich (St. Louis, MO). A 3 wt % (w/v) aqueous suspension of nanofibrillated cellulose was obtained from the University of Maine Process Development Center. (Seattle, WA). Whatman Ashless Grade 1, Grade 41, and Grade 42 Filter Papers (70 mm diameter, 200 μ m thickness), Fisherbrand Regenerated Cellulose Dialysis Tubing (MWCO-12 000–14 000), glass coverslips (Gold Seal™, 22 mm x 22 mm), premium plain glass microscope slides (75 mm x 25 mm), glass media bottles (Pyrex™, 100 mL), and glass Petri dishes (Pyrex™, 150 mm diameter) were purchased from Thermo Fischer Scientific (Waltham, MA). Unbleached cotton fabric composed of 100 % organic cotton (Organic Cotton Plus (Lubbock, Texas), artist quality tracing paper (Jack Richeson & Co., Inc.), circular hole punches (EK Tools Circle Punch, 3/8 in.), and a hollow punch cutter kit (Amon Tech) were all purchased from Amazon Inc.

2.2 Chemicals

Sucrose (BioXtra grade with purity $\geq 99.5\%$), glucose (BioXtra grade with purity $\geq 99.5\%$), dextran from Leuconostoc (average mol wt $\sim 100,000$), low gelling temperature agarose (BioReagent grade), and casein from bovine milk (BioReagent grade) were all purchased from Sigma-Aldrich (St. Louis, MO). I purchased chloroform (ACS grade with a purity $\geq 99.8\%$ and 0.75% ethanol added as preservative) and acetone (ACS grade, purity $\geq 99.5\%$) from Thermo Fischer Scientific (Waltham, MA). I obtained 18.2 M Ω ultrapure water from an ELGA Pure-lab Ultra water purification system (Woodridge, IL). I purchased lipids 1,2-dioleoyl-sn-glycero-3-phosphocholine (18:1 ($\Delta 9$ -cis) PC (DOPC)) and 23-(dipyrrometheneboron difluoride)-24-norcholesterol (TopFluor-Cholesterol), from Avanti Polar Lipids, Inc. (Alabaster, AL).

2.3 Fabrication of the substrates

2.3.1 Fabrication of nanocellulose paper

Using a 3 wt % (w/v) suspension of nanofibrillated cellulose, I fabricate nanocellulose paper using solution casting^{43,44}. I dilute the suspension of nanofibrillated cellulose to 0.7 wt % using ultrapure water and then fill a 150 mm diameter glass Petri dish with 60 mL of the 0.7 wt % suspension. I obtain smooth sheets of nanocellulose by allowing the water to

evaporate over the course of 2 – 3 days at room temperature (approximately 25 °C.) The process can be accelerated if the Petri dish is placed in a 65 °C oven where the water evaporates within 2 hours instead of 2 – 3 days. However, I find that the faster drying process causes wrinkles in the dry nanocellulose sheet. These wrinkles can be smoothed by refilling the Petri dish with around 30 mL of ultrapure water and allowing the water to evaporate at room temperature for about 12 hours. This process can be used to decrease the time necessary to fabricate nanocellulose paper suitable for PAPYRUS to about 14 hours.

2.3.2 Fabrication of nanohybrid paper

I obtain hybrid cellulose-nanocellulose paper substrates (nanohybrid paper) by dehydrating films of nanocellulose on pristine grade 1 Whatman™ filter papers. The films are dehydrated through vacuum filtration by placing a circular piece of the filter paper of size 70 mm in diameter into a vacuum funnel of size 70 mm in diameter. I then pour 40 mL of a the desired concentration of a suspension of nanocellulose (typically around 0.05 wt% (w/v) to obtain surface densities of nanocellulose around 5.2 g/mm²) on top of the filter paper. The filter paper and suspension are held under vacuum for 30 minutes until the paper is completely dry and a mat of nanocellulose fibers remain at the surface of the filter paper.

2.4 Procedures for cleaning the substrates

2.4.1 Cleaning of the paper substrates

In an abundance of caution, I develop standard procedures to clean the substrates before use in experiments. In a 500 mL glass beaker in a chemical fume hood, I soak the nanocellulose paper, artist grade tracing paper, and filter paper substrates in 100 mL of chloroform while applying occasional manual agitation with a glass stir rod. The substrates are allowed to soak for 30 minutes and then the chloroform is carefully discarded in a waste container. I repeat the process once more with fresh chloroform. Before removing the substrates from the chemical fume hood, I set the pieces of paper down on glass Petri dishes and allow any residual solvent to evaporate for 1 hour. I then soak the pieces of paper in 100 mL of ultrapure water for 30 minutes. I discard the water and repeat the process once more with fresh ultrapure water. The papers are then placed in a glass Petri dish and then moved to a 65 °C oven for 2 hours to dry.

2.4.2 Cleaning of the ITO-covered glass slides

Previous reports have shown that the electric field degrades ITO-covered slides after each use resulting in GUVs of smaller sizes and lower yields⁴⁵. To reverse these effect it is possible to anneal the slides in air at 150 °C for 20 minutes⁴⁵. To ensure the highest possible yields from electroformation while nominally mimicking the pattern of use of this expensive substrate in a typical laboratory, I reuse pristine ITO-covered slides a maximum of five times. Before each use, I clean the slides by sonicating sequentially for 20 minutes in acetone, ethanol, and ultrapure water. I allow the slides to dry at room temperature for 1 hour and then anneal the slides (with the conductive ITO-coat facing up) on a hot plate set at 150 °C for 20 minutes.

2.4.3 Cleaning of the regenerated cellulose dialysis membranes

I follow the instructions provided by the manufacturer to remove any preservatives and traces of metal that may remain after purchasing the regenerated cellulose dialysis membrane. Briefly, I cut the dry dialysis tubing into 10 cm long pieces (1cm wide) and soak the tubing in 50 mL of ultrapure for 30 minutes providing occasional manual agitation. I then cut the tubing open down the middle along the length and transfer the tubing to new clean glass beaker filled with fresh ultrapure water for 60 minutes. The tubing is then moved to soak in a 10 mM solution of sodium bicarbonate at 80°C for 30 minutes. After 30 minutes, the tubing is moved to a solution of 10 mM EDTA for another 30 minutes at room temperature. The tubing is finally rinsed under flowing ultrapure water for 10 minutes and transferred into a clean glass jar with ultrapure water. The glass jar is placed onto a hot plate set at 80°C and the water is mixed with a magnetic stirrer for 30 minutes. After 30 minutes, I remove the wet membrane from the glass jar and allow it to dry ambiently. I find winding the tubing around a glass slide can prevent excessive wrinkling or shrinking that occurs during drying.

2.5 Standardized procedures used to assemble GUVs

2.5.1 Lipid mixture

Significant degradation of lipids through lipid oxidation, or the spontaneous reaction of lipids with atmospheric oxygen, can alter the overall behavior of a lipid membrane and is associated with numerous diseases *in vivo* such as inflammation, atherosclerosis, and cancer^{15,46-48}. Removed from a larger biological framework containing a wide distribution of natural antioxidant substances, lipids can be particularly susceptible to oxidation^{48,49}. To control for any variation that could be caused by contamination through lipid oxidation or otherwise, I developed standardized protocols and lipid mixtures to be used for experiments. I purchase lipid that has been purified and lyophilized as powder (which is significantly more stable to oxidation than in solution) from Avanti® Polar Lipids. For experiments on various substrates, I purchase a synthetic phosphocholine lipid DOPC (1,2-dioleoyl-sn-glycero-3-phosphocholine) which has enjoyed a significant amount of use in the literature along with a fluorescent lipid TopFluor® Cholesterol (TFC) (23-(dipyrrometheneboron difluoride)-24-norcholesterol) which allows visualization of the lipids through confocal fluorescence microscopy. I prepare stock solutions of the lipids by dissolving the powder in chloroform in a glass vial at a concentration of 25 mg/mL for DOPC and 1 mg/mL for TFC. After working with any lipid solutions, I purge the atmospheric oxygen with argon gas, seal the glass vial, wrap the cap and vial with Teflon tape, and then place the lipids in a -20 °C fridge to minimize degradation. For almost all quantitative experiments in this chapter, I prepare a working lipid mixture (300 µL) of 1 mg/mL of 99.5:0.5 mol % DOPC:TFC in chloroform. When down to the last 20 – 30 µL of any lipid mixture, I discard the remaining solution and prepare a new mixture.

2.5.2 Deposition of lipids

To ensure the same surface area of paper is covered with the same mass of lipid for each experiment, I punch out circular disks with a diameter of 9.5 mm from the cleaned tracing paper, nanocellulose paper, filter paper and regenerated cellulose membrane substrates using a circle hole punch (EK Tools Circle Punch, 3/8 in.). I deposit 10 µL of the working

solution of lipid using a glass syringe (Hamilton) onto the papers. Holding the circular disks of paper with forceps, I carefully spread the lipid at a rate of $2 \mu\text{L}$ every 5 seconds around on the surface of the paper and ensure it is covered evenly. For the glass, electroformation, and agarose gel-assisted hydration techniques, I similarly spread $10 \mu\text{L}$ of the working lipid solution onto a 9.5 mm diameter circular area on each of these substrates. To ensure, the same area of the substrate is covered with the same mass of lipid, I place a 9.5 mm diameter paper cutout on the back surface of the slides to serve as guide for spreading the lipid. Once the lipid is deposited, all of the substrates were placed into a standard vacuum desiccator for a minimum of 1 hour to remove any traces of solvent before proceeding to the GUV assembly stage (Figure 53).

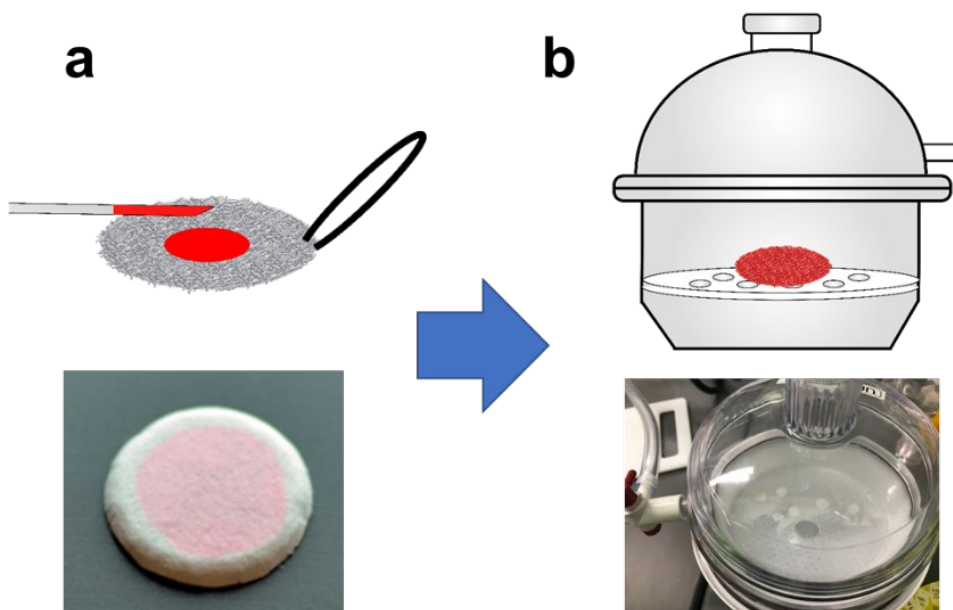


Figure 53: Preparation of substrate. Cartoon (top) and photographs (bottom) showing the **a** deposition of lipids onto circular disks of cellulose paper and **b** placement of the lipid-coated papers under vacuum.

2.5.3 Hydration of the paper substrates

I place the lipid-coated paper substrates into individual wells of a 48-well plate. Using a pipette, I add $150 \mu\text{L}$ of a 100 mM sucrose solution at the bottom corner of the well to fully immerse the substrate with the solution. I cover the 48-well plate with the lid and allow the papers to incubate in the solution for 2 hours.

2.5.4 Hydration of the glass substrates

To hydrate the lipid-coated glass and agarose-coated glass substrates, I affix circular PDMS gaskets (inner diameter \times height = $12 \times 1 \text{ mm}$) to construct a barrier around the lipid films. I then add $150 \mu\text{L}$ of a 100 mM sucrose solution into the gaskets and carefully place a glass

coverslip on the top surface of the PDMS gasket. I allow the samples to incubate for 2 hours.

2.5.5 Hydration of the ITO-coated slides followed by electroformation

I adapt established protocols to prepare GUVs through electroformation^{12,45,50}. I first affix a circular PDMS gasket (inner diameter \times height = 12×1 mm) to construct a barrier around the lipid film. I carefully add 150 μ L of a 100 mM sucrose solution into the chamber and then place a second ITO-coated glass slide (conductive side facing down) on top of the PDMS gasket to form a closed chamber. I then connect the ITO surfaces to leads of a function generator (33120A Agilent) using conductive copper tape and apply a sinusoidal AC field at a field strength of 1.5 V/mm peak-to-peak and frequency of 10 Hz for 2 hours.

2.5.6 One-step modulation of salts

To allow adjustments of the concentration of salts during hydration, I place the lipid-coated tracing paper on a glass slide in a circular PDMS gasket (inner diameter \times height = 12×1 mm) and hydrate in 142.5 μ L of the 100 mM sucrose buffer for 10 minutes. After 10 minutes, 7.5 μ L of 20 \times PBS is carefully expelled beneath the paper and a glass coverslip is placed on top to cover the chamber. Following addition of the salts the paper is allowed to incubate for 1 hour.

2.6 Standardized procedures for harvesting

For the glass, agarose-coated glass, and ITO-coated glass chambers that required a seal, I disassemble the chamber by carefully removing the top cover. For the paper substrates that used the 48-well plate no disassembly was required. To harvest the GUVs attached to each substrate identically I gently aspirate 100 μ L of the sucrose solution into a cut 1000 μ L pipette tip. I repeat this procedure exactly 6 times on different regions to ensure I have applied some gentle shear flow on every region of the substrate. On the seventh time, I aspirate all of the liquid, around 150 μ L, and transfer the harvested GUV solution into an Eppendorf tube. For characterization experiments, aliquots of the GUV solutions were taken immediately for imaging.

2.7 Procedures used to characterize the GUV populations

2.7.1 Confocal microscopy based methods

I collect images of the GUVs following the confocal microscopy based methods detailed in Chapter 2. Briefly, I construct imaging chambers by covalently bonding custom-made PDMS gaskets with a square opening (width \times length \times height = $6 \times 6 \times 1$ mm) to glass microscope slides². Before use, I passivate the chamber with a solution of 1 mg/mL casein to prevent rupture of the GUVs on the bare glass⁵¹. I fill the passivated chamber with 58 μ L of a 100 mM solution of glucose and add a 2 μ L aliquot of the suspension of the harvested GUVs. I allow the GUVs to sediment for 3 hours before imaging. I capture images using an upright confocal laser-scanning microscope (LSM 880, Axio Imager.Z2m, Zeiss, Germany). I excite the TopFluor® dye with a 488 nm argon laser and collected fluorescence using a 10 \times Plan-Apochromat objective with a numerical aperture of 0.45. I collect images of the entire area of the chamber using an automated tilescan routine (64

images [850.19 μm \times 850.19 μm (3212 pixels \times 3212 pixels)]. The routine used an autofocus feature at each tile location. The confocal pinhole is fully opened resulting in a slice thickness of 79.3 μm .

2.7.2 *In situ* confocal microscopy imaging of the vesicles on the substrates

For in-situ imaging, the lipid-coated substrates are placed in PDMS gaskets that is affixed to glass slides (inner diameter \times height = 12 mm \times 1 mm) and is hydrated in 150 μL of 100 mM sucrose. The chamber is sealed with a glass coverslip and imaged using a confocal microscope. I collect z-stack images using a 10 \times Plan-Apochromat objective with a numerical aperture of 0.45. I typically imaged an area of 850.19 μm \times 850.19 μm (3212 pixels \times 3212 pixels) and set the pinhole to 1 Airy Unit which gives a confocal slice thickness of 5.6 μm . To obtain the depth-coded projections from the z-stack images, I select areas of the vesicles on each substrate with width \times length \times height dimensions of 200 μm \times 200 μm \times 88 μm and apply a depth-color coding process to the images using ImageJ (NIH, Bethesda, MD).

2.7.3 Image processing and data analysis

The tilescan images are analyzed using the custom routine detailed in Chapter 2. Briefly, the routine thresholds the images and applies a watershed algorithm to segment the fluorescent objects from the background. I use the native *regionprops* function to obtain the equivalent diameters and mean intensity of the segmented objects. I select the GUVs from the detected objects based on a size-based analysis of the coefficient of variation and mean intensity of the segmented objects. Objects that fall within 1.5 \times times the location of the highest peak in the coefficient of variation and mean intensity histogram for their size class are selected as GUVs. Once selected, I typically obtain histograms of diameters of the GUVs and calculate the molar yield for the different populations of GUVs.

2.8 Comparing size distributions and yields of GUVs across different techniques

2.8.1 Plotting size distributions

Following protocols developed in Chapter 2, I use Matlab to collect and plot histograms of the vesicle diameters into 1 μm wide bins. The bins are normalized to show the GUV counts per μg of lipid deposited (typically 10 μg). I take a mean of the counts in each bin of the histograms from 5 independent repeat samples to obtain the size distribution plots for each of the substrates tested in this work.

2.8.2 Calculation of population size statistics

I calculate the median diameter of the population from 5 independent repeats using the native median command in Matlab. I then take a mean of these values from each of the 5 independent repeats to produce an average median size across the repeats with some standard deviation. I also develop a statistic to provide information on 100 of the largest GUVs in each population called the extreme diameters. To calculate the extreme diameter, I calculate the mean of the largest 100 GUVs for each population and determine an average of the extreme diameter sizes from 5 independent repeats and a standard deviation.

2.8.2 Calculation of substrate costs

To calculate the substrate costs related to GUV formation, I normalize the cost of each substrate by the area (mm^2). To determine the cost of each substrate per area, I use the lowest posted prices in July 2020 from the websites of the largest suppliers of scientific materials and divide by the area that is provided. I then normalize the size histograms from the different substrates by dividing the total counts in each bin by the area of the substrate that lipid was deposited ($70.88 mm^2$). Lastly, I divide the counts per area by the substrate cost per area to obtain the plots of the substrate cost per vesicle. Although not included, other equipment such as the solvent, buffers, lipids, and fluid receptacles can also factor into the total costs but are constant for all of the substrates. For the electroformation procedures, other sources of costs which were not considered include the additional equipment such as the function generator and a source of electrical power, however these factors will only add to the total costs and would not change the conclusions from the cost analysis.

2.9 Other methods

2.9.1 Scanning electron microscopy

To characterize the surface properties of each of the substrates tested in this work, I collect scanning electron microscopy (SEM) images using a field emission scanning electron microscope (Gemini SEM 500, Zeiss, Germany). Typically I cut the substrates into the small squares around $3 mm \times 3 mm$ to minimize the amount of charging that can occur at the surface. For the glass slides I cut relatively larger pieces using a diamond scribe. I place a piece of double-sided copper tape on an aluminum stub and attach the substrates onto the tape. I often also add a piece of copper tape at the surface of the substrates and attach the other end to the stub to allow a conduction pathway for electrons from the top surface to the stub. To image the samples, I use a beam accelerating voltage of 1 kV and collect the secondary electrons using an Everhart-Thornley detector. The lower magnification images were typically captured with a lateral pixel resolution of $1.09 \mu m/pixel$ resulting in an image size of $1120 \mu m \times 840 \mu m$ ($1024 pixels \times 768 pixels$), while the higher magnification images were typically captured with a lateral pixel resolution of $21 nm/pixel$ resulting in an image size of $22.76 \mu m \times 17.07 \mu m$ ($1024 pixels \times 768 pixels$).

2.9.2 Hydrophobic modification of the substrates

For experiments used to understand the effect of the hydrophilicity of the substrates on the assembly of GUVs, I carry out procedures to make glass and tracing paper substrates hydrophobic. To obtain hydrophobic glass slides, I follow previously described protocols⁵² on the vapor phase transfer of silanes onto surfaces. Briefly, I place a $500 \mu L$ solution of methyltrichlorosilane in a 10 mL glass vial. I then place the uncapped glass vial in a laboratory vacuum (contained inside a chemical fume hood) with plasma-cleaned glass slides as well as with a desiccant (DrieRite™). After 12 hours, the silane is fully evaporated and the glass surface is covalently bound with silanes. As a control, I compare the properties of a $5 \mu L$ droplet on the now hydrophobic glass slide compared to the a hydrophilic glass. The droplet on the hydrophobic glass slide forms a bead on the surface while on the hydrophilic glass slide the droplet wets the surface confirming the glass has

been rendered hydrophobic. To obtain hydrophobic tracing paper, I prepare a mixture of the methyltrichlorosilane with anhydrous toluene at a 80 by 20 volume mixture in a glass vial. I then submerge several pieces of tracing paper into the solution and cap the glass vial. I allow the paper to incubate in the silane solution for 30 minute before removing the paper carefully and rinsing the paper in excess toluene for 30 seconds. I allow the paper to dry a chemical fume hood for 30 minutes before transferring to a 65 °C oven for 2 hours.

2.9.3 Recycling tracing paper for repeated use in GUV formation

I follow the standard procedures to assemble GUVs on tracing paper. Once the GUVs are harvested, I rinse the tracing paper under a flowing stream of ultrapure water for around 1 minute and then soak the tracing paper in an excess of ultrapure water. I allow the tracing paper to soak for 30 minutes and occasionally agitate the paper by manually shaking the container. This process removes any water-soluble sugars left behind during hydration. Once clean, I dry the paper at 65 °C in an oven. To remove any lipid left behind on the surface, I soak the tracing paper in 10 mL of chloroform for 30 minutes. I occasionally agitate the paper by manually shaking the container. I then carefully remove the tracing paper, discard the chloroform, and place the tracing paper in a vacuum chamber for 1 hour for 1 hour to remove any traces of chloroform. After 1 hour in vacuum, I start the next growth cycle.

2.9.4 Scaling up the production of GUVs from tracing paper

To evaluate the scalability of tracing paper for the production of GUVs, I use a Paasche airbrush and compressor to spray the lipid onto the whole sheet of tracing paper with size dimension of 12 inches × 8 inches (305 mm × 203 mm). I use PVA-coated gloves when working with the chloroform in large amounts. All experiments were performed inside a chemical fume hood. I prepare a 9.6 mL of a 1 mg/mL solution of the DOPC:TFC (99.5:0.5 mol %) lipid mixture. To spray the lipid onto the surface I fill the lipid solution into a 10 mL Teflon cup attachment that the airbrush takes the solvent from. I use a 0.66 mm cap at the end of the airbrush and set the compressor air pressure to 20 PSI. I airbrush the lipid across the surface at a rate of approximately 1 inch per second and hold the airbrush approximately 2 inches from the surface of the paper. Once the lipid is added to the entire sheet, I place the lipid-coated sheet under vacuum for 1 hour and allow the residual solvent to evaporate. I then place the sheet into a baking sheet with size dimensions of 13 inches × 9 inches and hydrate the entire sheet in a 100 mL solution of 100 mM sucrose. I allow the GUVs to assemble for two hours and then harvest the GUVs by pipetting gently across the entire surface of the paper using a 1 mL plastic transfer pipette with the end cut off. Once harvested, I store the GUVs in 50 mL centrifuge tubes.

2.9.5 Fluorescence recovery after photobleaching (FRAP) experiments on GUV buds and harvested GUVs

To confirm the GUV buds are connected to each other on the surface, I carry out fluorescence recovery after photobleaching (FRAP) experiments on the confocal microscope. Using the 488 nm argon laser at 100 % power, I bleach circular regions of tightly-packed GUV buds on the surface. I collect time lapse images of the fluorescence

recovery at 1 second intervals for 250 seconds setting the laser power for the image acquisition at 0.1 %. The mean intensity of the bleached region was measured in Image J, and the data was normalized by the pre-bleach intensity of the vesicles. To obtain closely-packed harvested GUV samples, I pooled the GUVs from 3 tracing paper samples together. I centrifuge the 450 μL solution of GUVs at $10,000 \times g$ for 3 minutes and then remove the top 300 μL leaving behind a 150 μL solution of concentrated GUVs. To sediment the GUVs, I add a 30 μL aliquot of the concentrated solution to a 30 μL solution of glucose in a PDMS imaging chamber. I allow the vesicles to sediment for 5 hours, and then conduct the FRAP experiments using the same conditions as those used for the GUV buds.

2.9.6 Sodium green assay to evaluate the diffusion of salts inside the GUVs

I follow the one-step modulation of salts procedures but also add 1.5 μL of a 1 mM sodium green indicator solution beneath the paper to obtain a final concentration of 10 μM in the chamber. After 1 hour of growth, I image the vesicles on a glass slide contained within a custom double-sided tape chamber (inner diameter ≈ 13 mm and height ≈ 0.1 mm). I place 20 μL of the undiluted vesicle solution directly within the tape chamber and sealed the chamber with a glass coverslip. To confirm the encapsulation of the salts, I directly compared the interior mean fluorescence of 50 vesicles to the fluorescence of the exterior solution.

3. Results

3.1 Effect of cellulose substrate properties on the populations of GUVs

In this section I determine the effect of properties such as the porosity and the organization of the fibers on the assembly of GUVs. I systematically conduct experiments to test the sizes and yields of GUVs obtained from three different filter papers and one cotton fabric.

3.1.1 Properties of three cellulose filter papers and one cotton fabric

Found in the cell wall of all plant cells, cellulose is considered the most abundant natural polymer on Earth⁵³⁻⁵⁵. Cellulose is composed of monomers of glucose that are joined by a distinctive β - 1,4 glycosidic linkage which causes it to pack closely together into a hierarchy of fibril structures^{56,57}. Figure 54 shows this hierarchy of fibril structures where nanometer fibrils naturally bundle together to form the micrometer scaled cellulose fibers. These micrometer scaled fibers are most commonly extracted from plants that contain a high percentage of cellulose such as cotton (nearly 95% cellulose⁵⁸⁻⁶⁰) and are then processed to form paper. Depending on the manufacturing process, papers with different properties such as varying porosities or liquid flow rates can be obtained. To determine an optimal cellulose substrate to use to assemble GUVs, I conduct experiments using three different types of cellulose filter papers and 1 cotton fabric⁶¹.

The cellulose filter papers are manufactured from fibers that are that are approximately 1.5 mm – 6 mm in length and obtained from bolls that form around the seeds of the cotton plant⁶⁰. During manufacturing these fibers become entangled and form the randomly percolated network of fibers of filter paper⁶². I test three different ‘grades’ of filter paper each

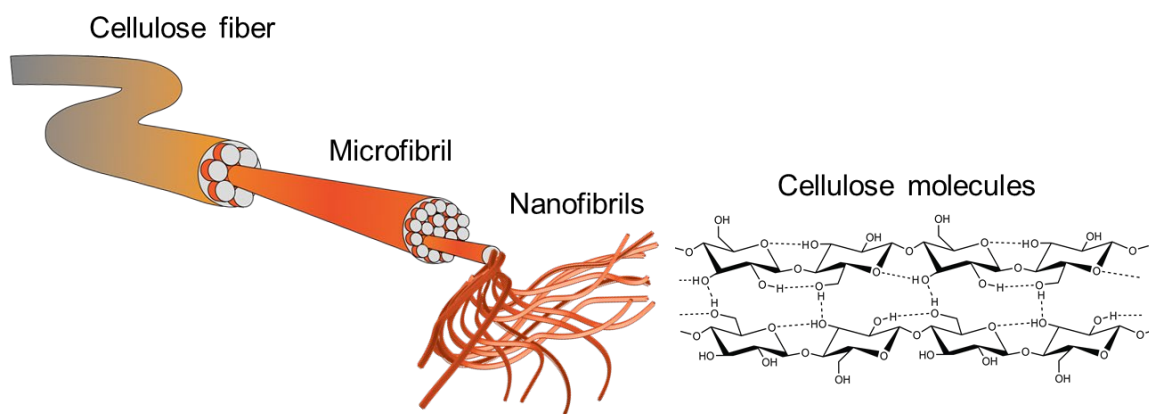


Figure 54: Hierarchical structure of cellulose. Schematic illustrating the hierarchical nature of cellulose fibers which are composed of tightly wrapped bundles of microfibrils, which are each composed of tightly wrapped bundles of nanofibrils, which are composed of polymer chains of glucose monomers that are linked together with many hydrogen bonds.

with different effective porosities and liquid flow rates. The porosities are measured through particle retention⁶³ and reported by the manufacturer. The liquid flow rates are measured using the Herzberg flow rate where the time it takes for 100 mL of water to flow through the paper is measured⁶⁴ and are also reported by the manufacturer. In order of decreasing porosity, I conduct experiments on i) Grade 41 filter paper (G41) with an effective porosity of 25 μm and a Herzberg flow rate of 54 seconds/100 mL, ii) Grade 1 filter paper (G1) with an effective porosity of 11 μm and Herzberg flow rate of 150 seconds/100 mL, and iii) Grade 42 filter paper (G42) with an effective porosity of 2.5 μm and a Herzberg flow rate of 1870 seconds/100 mL. As expected, the decrease in the effective porosity also directly corresponds to the increase in the Herzberg flow rate.

In contrast to the different grades of cellulose paper, the cotton fabric is obtained from only the longer staple fibers present in the cotton bolls which can have lengths between 20 mm – 40 mm⁶⁰. These staple fibers are carefully spun together to form tightly twisted bundles of yarn that is then weaved together to form the interlaced network of fabric⁶⁰. Different than the randomly organized fibers of the filter papers, the cotton fabric is composed of fibers that are highly aligned and have a very uniform size and shape.

To examine the microstructure of the cellulose substrates, I collect scanning electron microscopy (SEM) images of regions at the surfaces (Figure 55a-d). The cellulose fibers at the surface of the papers appear as twisted and flattened cylinders with diameters between around 15 μm – 20 μm . The G41 paper has larger pores between the fibers (dark regions in the images) compared to the G1 paper, and the G1 paper has larger pores than the G42 paper. This observation is consistent to the reported particle retention capacities and flow rates of the filter papers. The cotton fabric however appears as a highly ordered network of twisted cellulose fibers with regions that are devoid of any cellulose where the yarn is intertwined (white arrows). I also characterize the microstructure, in particular the diameters of the fibers, while the substrates are hydrated similar to during the assembly of the GUVs. Figure 55e-h shows the maximum intensity projection from confocal z-stack images of the substrates. I used a bandpass filter on the images to highlight the edges of the fibers and more easily measure the fiber diameters in ImageJ. The histograms of the diameters of the cellulose fibers measured are shown in Figure 55i-l. From the histograms, the average diameter of the fibers, d_f , was $21 \pm 5 \mu\text{m}$ for G41, $20 \pm 6 \mu\text{m}$ for G1, $16 \pm 7 \mu\text{m}$ for G42, and $16 \pm 4 \mu\text{m}$ for the cotton fabric. Thus, the G41 and G1 paper have on average larger diameter fibers, while G42 paper and the cotton fabric have smaller diameter cellulose fibers.

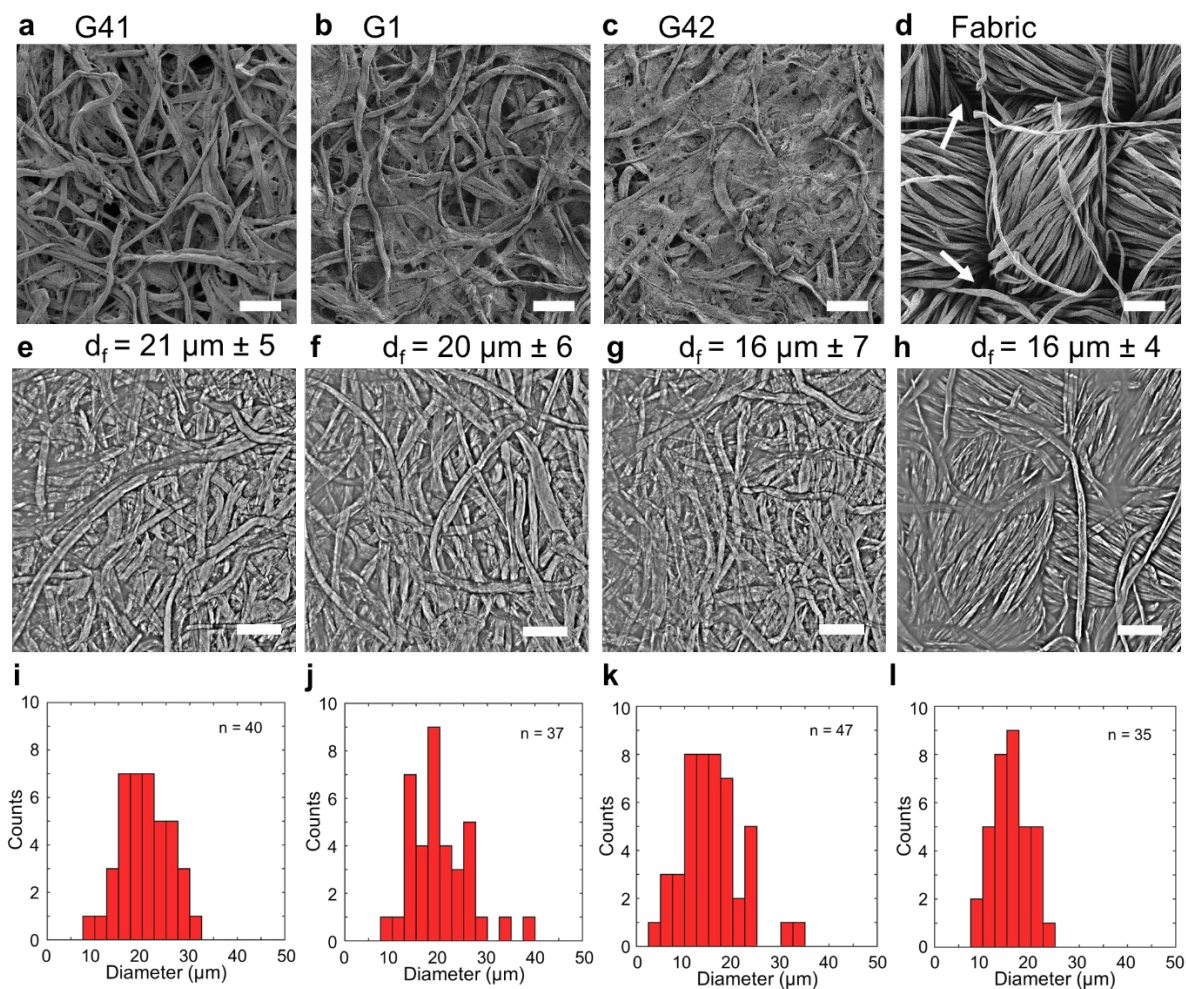


Figure 55: Microstructure of the cellulose filter papers and cotton fabric. a-d SEM images showing the surface structure of a) G41, b) G1, c) G42, and d) cotton fabric substrates. e-h Maximum intensity projections of confocal z-stack images of the hydrated cellulose substrates. The contrast is enhanced using a band pass filter to better observe the width of the fibers. i-l Histograms of the diameters of the fibers in the images. Scale bars (a-h) 100 μm . Images were published⁶¹ and reproduced here with permission from the American Chemical Society.

3.1.2 Size distributions of giant liposomes assembled on G41, G1, G42, and cotton fabric

I standardize the assembly of GUVs on the filter paper and cotton fabric substrates by depositing 3 μg of lipid for every 1 mg of cellulose. I find this adaptation to the normal protocols necessary since the filter papers and cotton fabric are significantly more porous at the surface compared to the other substrates tested in this work. To allow fair

comparisons regarding yields across the techniques, I normalize the data obtained from these experiments by the amount of lipid deposited initially following the standardized protocols detailed in the methods (Section 2.5.2). Figure 56a,b shows the GUVs on the surface of the cellulose fibers before harvesting. The GUVs appear to rest in tight clusters attached only to the fibers and do not span across the pores of the paper. In addition, manual measurements conducted of the sizes of the GUVs that are observable in the images suggest that most of the GUVs have sizes $< 20 \mu\text{m}$ in diameter.

Representative confocal images of the harvested GUV populations produced from the four substrates are shown in Figure 57 a-d. Qualitatively, the GUVs appear similar from each of the substrates. To evaluate the populations quantitatively, I collect tilescan images and characterize more than 100,000 GUVs from each of the different populations of GUVs using the standardized methods developed in Chapter 2. Figure 57e shows a histogram of the diameters of one sample of GUVs assembled from G41 filter paper and normalized to the amount of lipid deposited. The distribution is asymmetric and has a long right tail matching results of populations of GUVs

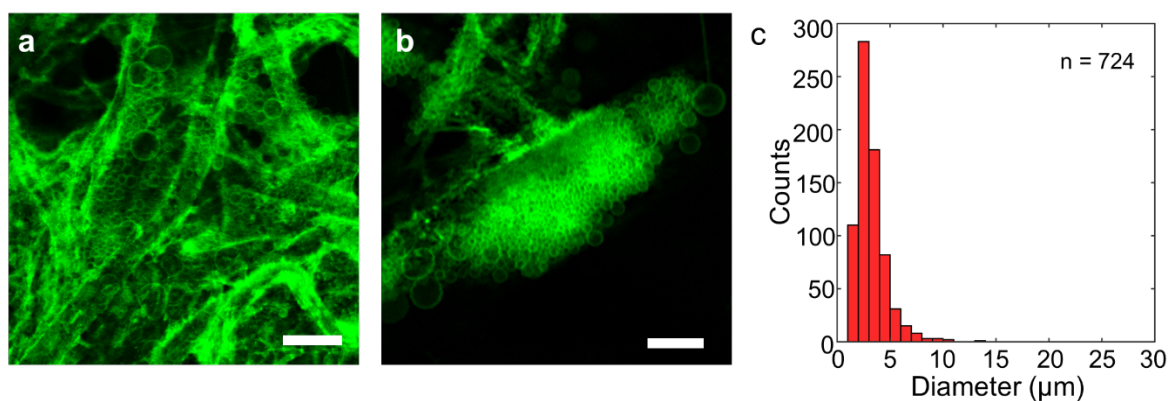


Figure 56: GUV buds rest on the fibers of the cellulose paper. a,b Observation of GUVs on the surface of G1 paper reveal GUVs are only located on the surface of the fibers and do not span the pores of the paper. Manual measurements of the GUVs on the surface reveal right-tailed size distributions. Scale bar: a $50 \mu\text{m}$ b $25 \mu\text{m}$. Images were published⁶¹ and reproduced here with permission from the American Chemical Society.

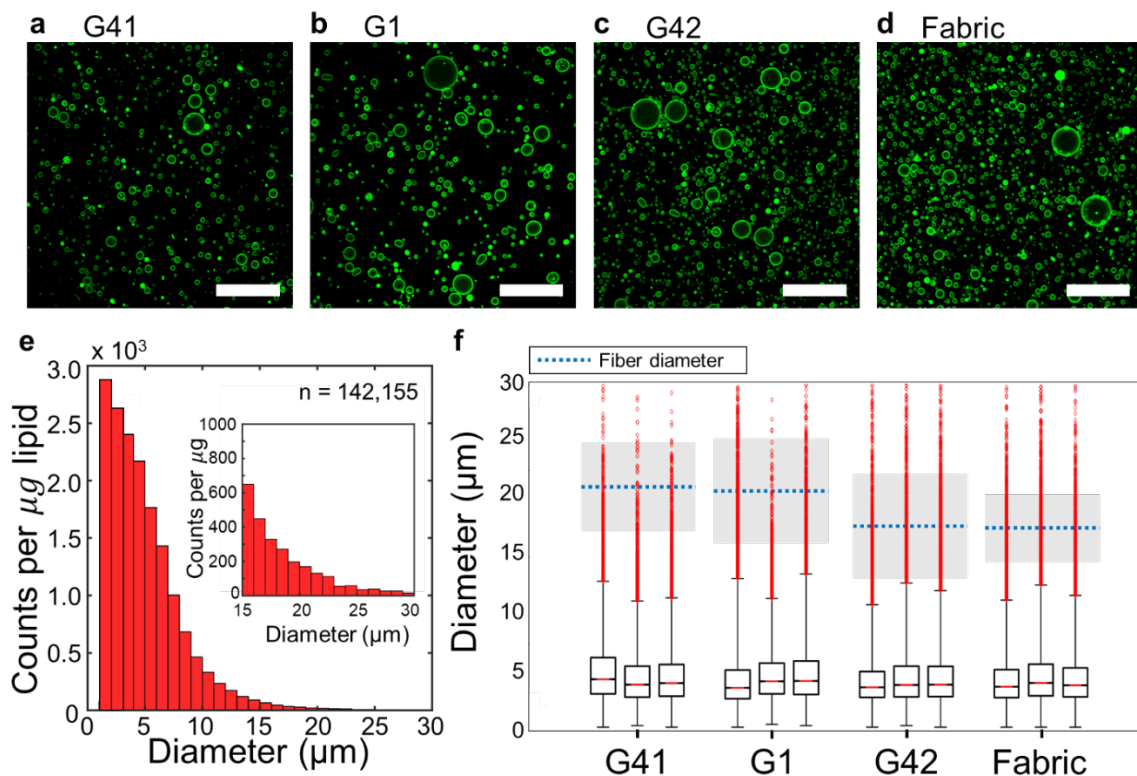


Figure 57: Characterization of populations of GUVs produced from the cellulose substrates. **a-d** Representative confocal images of the GUVs (green rings) harvested from **a** G41, **b** G1, **c** G42, and **d** Fabric substrates. **e** Size distribution from one sample of cotton fabric. Inset shows a zoom in of the right tail. **f** Box and whisker plots of the distribution of sizes of GUVs assembled from the different samples. The bottom whisker shows the lowest GUV size, the bottom line of the box shows the 25th percentile, the red line of the box shows the 50th percentile, the top line of the box shows the 75th percentile and the top line shows the 98th percentile. The red diamonds show the outlier points, and the gray boxes show the diameter of the fibers of the different papers. Scale bars: **a-d** $50 \mu\text{m}$. Images were published⁶¹ and reproduced here with permission from the American Chemical Society.

obtained from other thin film hydration techniques^{7,11,31,32,65} as well as the results obtained in Chapter 2. Populations with an extended right-tail have also been reported for other colloidal systems⁶⁶ such as small unilamellar vesicles⁶⁷, raindrops⁶⁸, and draining foam bubbles⁶⁹. These right-tailed fits have been used to develop theoretical models to help describe fundamental processes such as coalescence, fragmentation and nucleation^{66,68-71}. Similar models for GUVs have previously not been reported but will, however, be discussed later in this chapter.

In Figure 57f, I show box and whisker plots of the distribution of sizes of GUVs obtained from 3 replicate samples of each of the four cellulose substrates. The lowest

whisker of the box represents the minimum size of the GUVs analyzed which is $1.1 \mu\text{m}$. The bottom, middle (red), and top line of the box shows the 25th, 50th, and 75th percentile respectively. The top whisker indicates the 98th percentile of the GUVs, and the red diamonds represent the remaining points which consists of less than 2 % of the GUVs. The plots are overlaid with the data on the diameter of the fibers measured in Figure 55 where the mean diameter is marked as a blue dashed line and the standard deviation is marked in gray.

Comparing the box and whisker plots from different samples of the same substrate, it is clear that there is little sample-to-sample variation. Comparing the box and whisker plots from the samples from different substrates, it is also clear that the size distributions are extremely similar between the three different grades of filter paper and the cotton fabric. For each different substrate, the median diameter of the GUVs was between $3 \mu\text{m} - 4 \mu\text{m}$ and more than 98% of the GUVs were below the fiber diameter of the substrates.

3.2 Lower porosity cellulose substrates produce higher yields of GUVs

3.2.1 Comparison of yields from G1, G41, G42 papers and cotton fabric

To compare the yields of GUVs obtained between the substrates I normalize the GUV counts by the mass of lipid deposited. Figure 58 shows a bar plot of the average number of GUVs obtained per μg of lipid deposited for each of the four substrates. The error bars show the standard deviation of the mean from 3 replicate samples, and the inset shows the

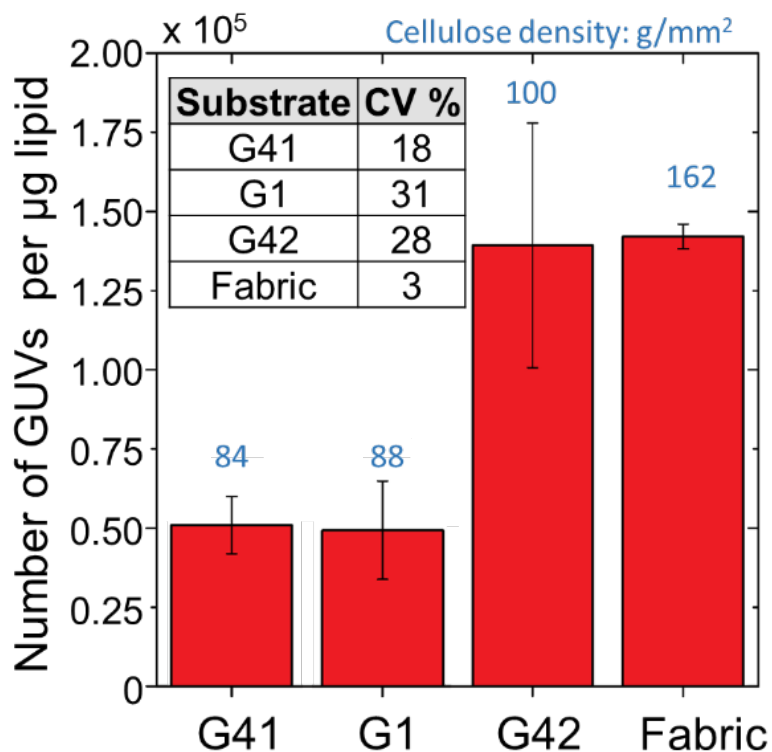


Figure 58: Yields of GUVs produced from the cellulose substrates. Bar plot showing the yields of GUVs from the different substrates. Each bar is an average of the number of GUVs obtained from 3 samples. The average is normalized per μg of lipid deposited on each of the substrates. The error bars show the standard deviation of the samples from the mean. The inset shows the coefficient of variation between the samples. Images were published⁶¹ and reproduced here with permission from the American Chemical Society.

coefficient of variation. Both the G41 and G1 substrates produced much lower yields of GUVs compared to the G42 and cotton fabric substrates. Compared to the G41 and G1 substrates, the G42 and cotton fabric substrates also have smaller average fiber sizes which can be more densely packed together. This result suggests that it may be possible to increase GUV yields using cellulose substrates with lower porosity. Interestingly, the highly ordered cellulose fabric substrate results in the lowest variation in the yields of GUVs between samples.

3.2.2 Assembly of GUVs on hybrid cellulose-nanocellulose papers

To test the hypothesis that decreasing the pore size of the cellulose paper increases the yields of GUVs, I design an experiment to incrementally fill the pores of G1 filter paper using small nanometer-sized cellulose fibrils that can pack much more tightly together than ordinary cellulose fibers. I call these hybrid papers composed of cellulose and nanocellulose fibers nanohybrid paper. To prepare the nanohybrid papers with decreasing porosity, I first prepare suspensions of nanocellulose fibrils in ultrapure water at concentrations of 0.2 wt %, 0.35 wt %, and 0.7 wt % (w/v). I then place a circular piece of the G1 filter paper of size 70 mm in diameter into a vacuum funnel and turn on the vacuum. To obtain the nanohybrid paper with the desired porosity, I pour the 40 mL of the nanocellulose suspension on top of the filter paper. The 0.2 wt %, 0.35 wt %, and 0.7 wt % suspensions result in a surface density of nanocellulose of 2.6 g/mm^2 , 5.2 g/mm^2 , and 10.4 g/mm^2 respectively. The filter paper and nanocellulose suspension are held under vacuum for 30 minutes until the paper is completely dry and a mat of nanocellulose fibers remain at the surface of the filter paper.

Figure 59a-d shows SEM images of the nanohybrid papers (NHP) after drying. The pores (dark regions) that are clearly present in the G1 paper image appear almost completely filled by nanocellulose in the NHP images confirming the vacuum filtration method of forming nanohybrid paper was successful. To observe the effects of incrementally filling the pores of G1 paper using nanocellulose on the assembly of the GUVs, I conduct *in situ* experiments and collect confocal images after 2 hours of hydration of the GUVs present at the surface of each of the different nanohybrid papers (Figure 59e-h). The samples are prepared using the exact same conditions and the exact same amount of lipids. The images show a remarkable increase in the sizes of the GUVs at the surface

of the papers as the surface density of nanocellulose increases. The GUVs at the surface of the G1 filter paper appear to be no larger than around $20\ \mu\text{m}$ in diameter as expected. In addition, large pores and fibers are clearly visible in the G1 image. The vesicles appear to be only coating the fibers and do not span over the distance of the pores of the paper. In the image of the nanohybrid paper with a surface density of $2.6\ \text{g}/\text{mm}^2$ nanocellulose, more GUVs appear to be present on the surface and some of the GUVs appear to have larger sizes around $30\ \mu\text{m}$ in diameter. The fibers are still clearly visible, however, and there are still regions devoid of lipid similar to the G1 paper. In the image of the nanohybrid paper with a surface density of $5.2\ \text{g}/\text{mm}^2$ nanocellulose, the GUVs are both more in number and larger in size compared to the lower surface density nanohybrid paper sample, with the largest GUVs reaching sizes of more than $50\ \mu\text{m}$ in diameter. In the image of the $10.4\ \text{g}/\text{mm}^2$ nanohybrid paper, which has the same surface density of nanocellulose as nanopaper, the entire surface is covered with GUVs. Remarkably, some of the largest GUVs reach sizes of more than $100\ \mu\text{m}$ in diameter which was a size previously inaccessible to the filter paper substrates. Compared to the papers with a lower surface density of nanocellulose, the $10.4\ \text{g}/\text{mm}^2$ nanohybrid paper appears to have the most counts and largest sizes of GUVs. At this magnification the fibers and pores at the surface of the paper are not visible and the GUVs appear to span areas larger than the fibers and pores of the paper.

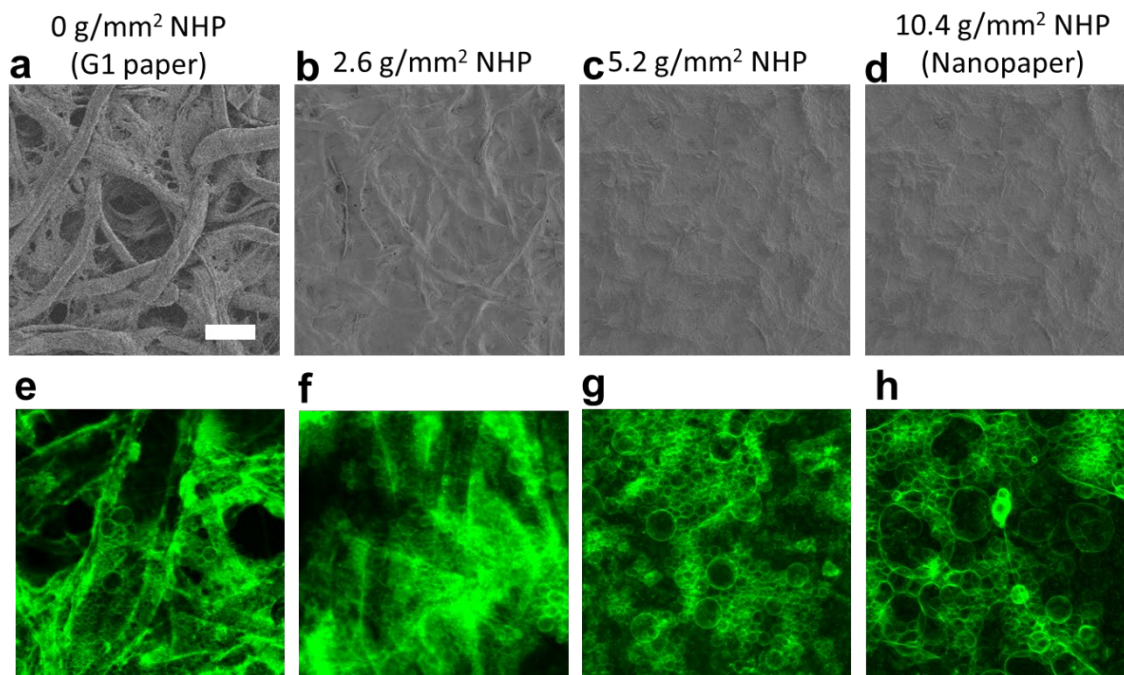


Figure 59: Effect of the density of nanocellulose on the assembly of GUVs at the surface. **a-d** SEM images of the surfaces of the various nanohybrid papers. The pores and larger fibers become hidden on the surface of the nanohybrid papers with higher surface concentrations. **e-h** Representative confocal images showing the GUVs resting on the surface of the different substrates 1 hour after hydration. Scale bars: **a-h** $100\ \mu\text{m}$.

3.2.3 Sizes and molar yields of GUVs produced from various nanohybrid papers

Following the confocal microscopy methods developed in Chapter 2, I characterize the populations of GUVs produced from the four nanohybrid paper samples. Figure 60a shows the distribution of sizes from each of the four nanohybrid paper samples. The GUVs per μg lipid from each nanohybrid sample is plotted as an average from 3 replicates. The distributions are significantly different from one another. Clearly the extension of the right tail present in the distributions increases significantly as the density of nanocellulose increases. The G1 sample appears to have almost no GUVs with diameters $\geq 50 \mu\text{m}$ in diameter whereas the higher density nanohybrid paper samples appear to have GUVs with diameters up to around $130 \mu\text{m}$.

Since the distributions are heavy-tailed, I use the molar yield metric to quantify the populations of GUVs instead of the counts per μg lipid as before. The molar yield metric allows for more clear comparisons between the different populations assembled from the nanohybrid substrates since the large GUVs are only produced in some of the nanohybrid samples and are comprised of a significantly larger amount of the lipid compared to the small GUVs. This difference is much more difficult to appreciate in a counts plot. Figure 60b shows the bar plots of the molar yields are $3.1 \pm 1\%$ for the G1 paper, $6.9 \pm 1\%$ for the 2.6 g/mm^2 nanohybrid paper, $15.2 \pm 3\%$ for the 5.2 g/mm^2 nanohybrid paper, and $30.3 \pm 2\%$ for the nanopaper samples. The significant differences in the molar yields between the samples confirm that increasing the density of the nanocellulose at the surface of the paper directly responds to increasing yields of GUVs.

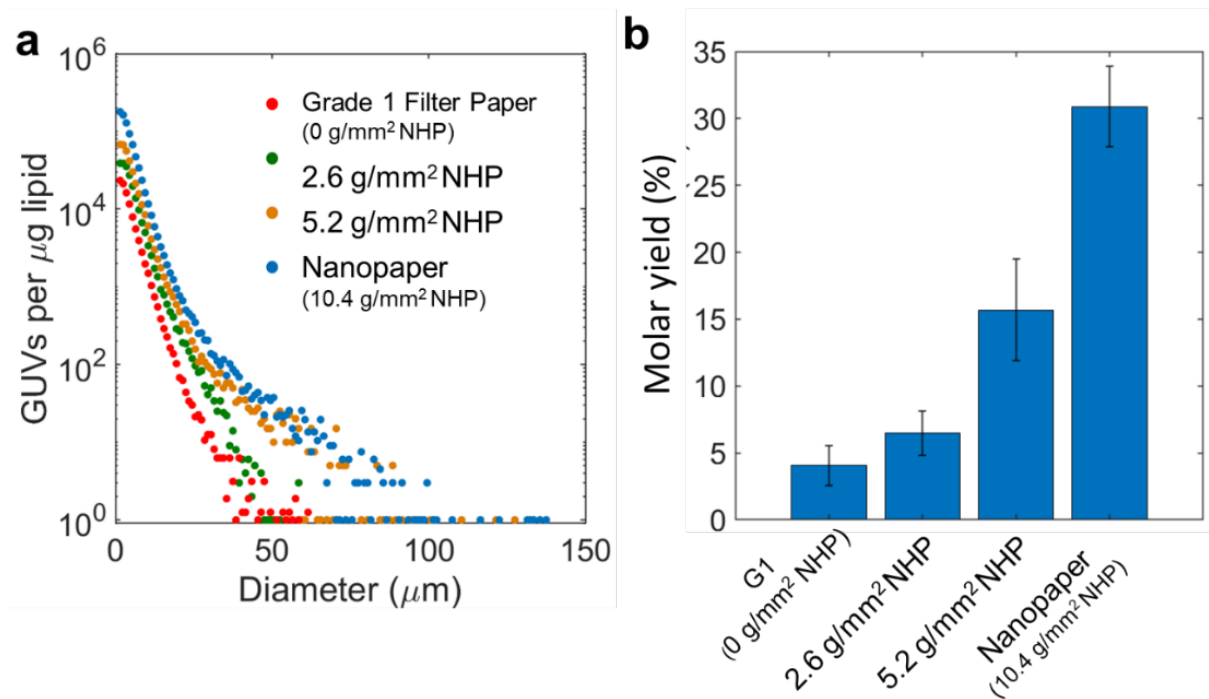


Figure 60: Sizes and yields of GUVs assembled on nanohybrid paper. a Distributions of sizes of the GUVs assembled from various nanohybrid paper substrates. Each point is

an average of the counts of GUVs obtained from 5 samples and is normalized per μg of lipid deposited. The inset shows the color assignment of the points from each paper. **b** Bar plot showing the molar yields of GUVs assembled from the various nanohybrid paper substrates. Each bar shows the average from 5 samples and the error bars show the standard deviation of the samples from this average.

3.2.4 Losses of GUVs in pores of cellulose papers

To confirm that the increases in molar yield are due to decreasing losses of lipids in the less porous nanocellulose papers and are not a product of the nanocellulose fibers themselves, I collect images of the dry nanohybrid papers coated with lipids (Figure 61).

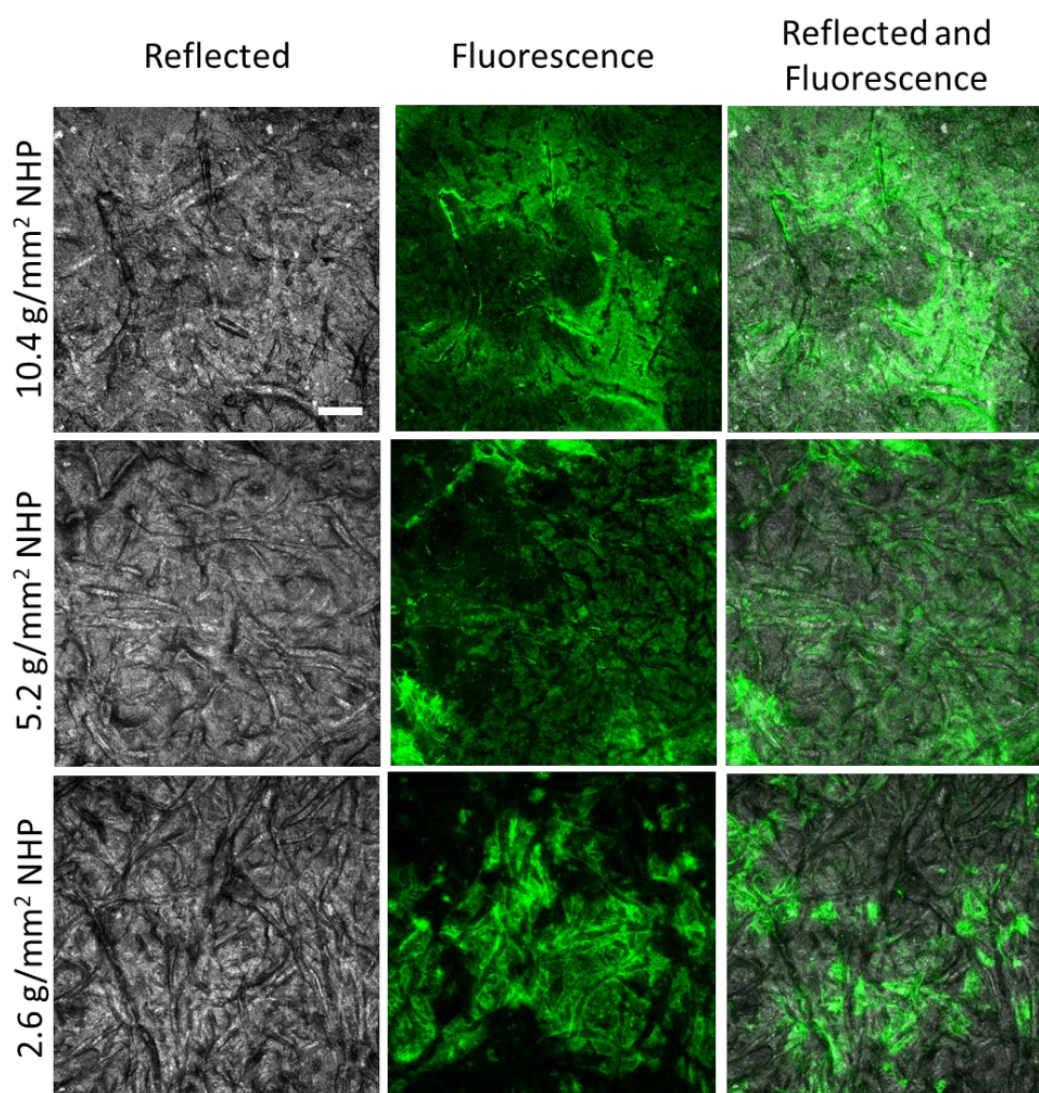


Figure 61: Characterization of the penetration of lipid into the surface of the various nanohybrid papers. The left column shows reflected confocal images of the surface

structure of the dry nanohybrid papers covered with nanocellulose. The larger fibers are more visible on the surfaces with less nanocellulose, differences in porosities are unclear. The middle column shows fluorescence confocal images of the coverage of the lipids at the surface of the paper while dry. The lipids do not coat the surface as evenly on the less nanocellulose dense substrates. This is likely due to the lipid penetrating deeper within the papers. A composite image combining the reflected and fluorescence images are shown in the rightmost column. Scale bar: 50 μm .

The first column shows the reflected channel image of the fibers from the three nanohybrid papers. The second column shows the fluorescence channel image of the lipids after depositing 10 μg of the lipid solution onto each of the nanohybrid papers. The third column shows a composite of the images in the first two rows. From the images it is clear that there is significantly less lipid (green) at the surface of the less densely-packed nanohybrid paper substrate suggesting that some of the lipid becomes lost in the pores. As a second line of evidence that the pores are an important factor leading to the lower yields of GUVs, I also collect images inside the pores of G1 paper after hydrating and harvesting the GUVs. This is possible since I expect some amount of the solution to remain trapped in the pores after harvesting to keep the GUV intact until I can carefully add more solution and collect images. Figure 62a shows the maximum intensity projection of confocal z-stacks of the vesicles on G1 paper before harvesting. The vesicles are stratified on fibers that range from the lowest point inside of a pore where vesicles are visible in the image surface to the top surface 80 μm above the pore. Figure 62b,c show representative regions inside pores of the G1 paper after harvesting. Clearly a significant fraction of the GUVs that have formed remained trapped in the pores of the paper.

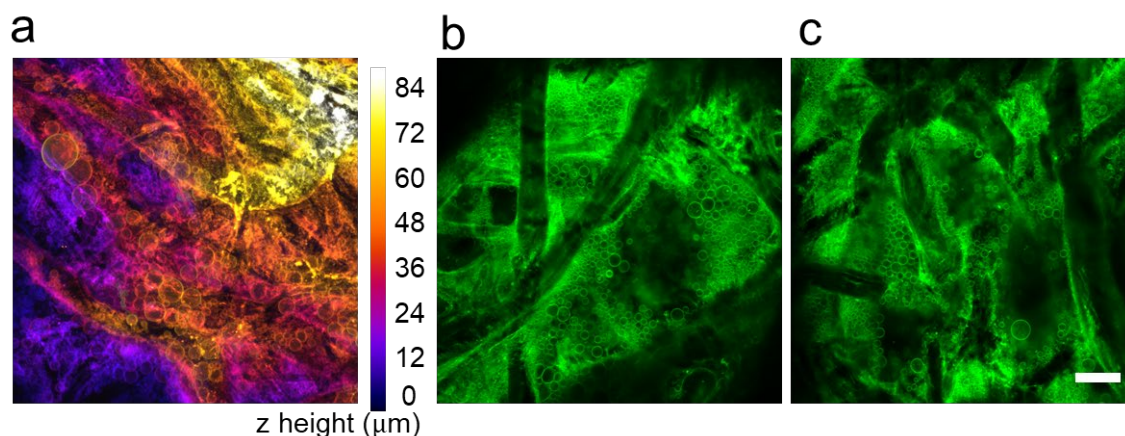


Figure 62: GUVs remain trapped in the pores of the G1 paper after harvesting. **a** Depth coded z-projection showing that the vesicular buds on G1 paper are distributed within the open porous matrix of the cellulose fibers. **b,c** Representative images taken a few micrometers into the pores of the filter paper showing that many GUVs remain trapped in the pores of the G1 paper after harvesting. Scale bars: 25 μm .

3.3 Reusability of cotton fabric to assemble GUVs

Since cotton fabrics are much more resilient to mechanical stresses that occur during washing than ordinary cellulose papers, I also conduct experiments to determine if I can obtain multiple populations of GUVs from reusing the same piece of cotton fabric. I follow the standard procedures to prepare and harvest the vesicles. After harvesting, I rinse and soak the fabric in ultrapure water to remove traces of dissolved salts and sugars. I then allow the fabric to dry in a 65 °C oven for 1 hour. Once dry I then follow standard washing procedures detailed in the methods section and use the fabric once again to assemble the GUVs. Figure 63 shows that the cotton fabric can be cleaned and reused to assemble multiple populations of GUVs without any significant changes in the sizes and yields of the GUVs. The harvested populations between the first and fifth cycle appear similar visually. The number of GUVs produced in each cycle remain similar with between 1.4×10^5 – 1.6×10^5 GUVs per μg lipid produced, and the size distributions all appear similar with most of the GUVs having sizes smaller than $5 \mu\text{m}$. In addition, the fabric appears unaffected at the surface even after 5 cycles of washing and rehydration. This demonstration of the reusability of the fabric provides an economical route for the large-scale production of GUVs.

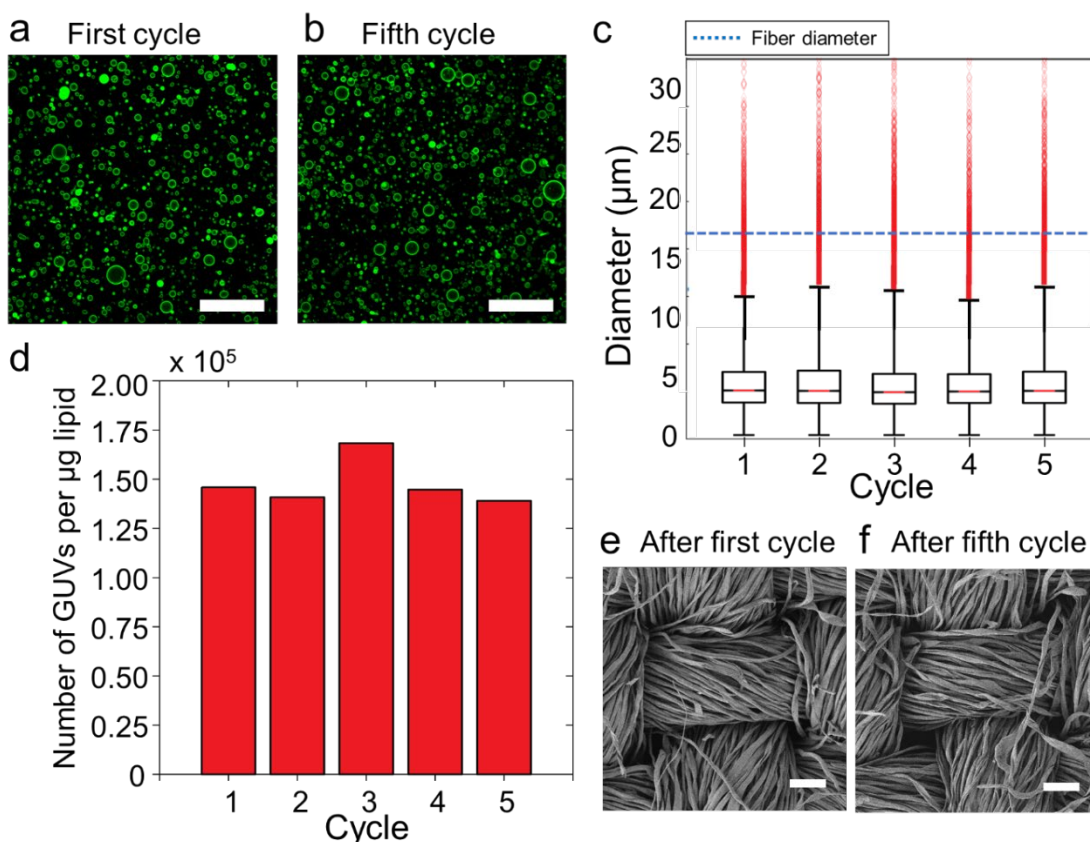


Figure 63: Cotton fabric supports the assembly of multiple cycles of GUVs. a,b Confocal images showing the appearance of the harvested vesicle populations obtained

after **a** the first cycle and **b** the fifth cycle. **c** Distribution of sizes of the populations of GUVs obtained after each cycle. The bottom whisker represents the GUVs with sizes of 1 μm , the bottom of the box represents the 25th percentile, the middle of the box represents the 50th percentile, and the top of the box represents the 75th percentile. The top whisker represents the 98th percentile and the red diamonds represent outliers. The fiber diameter of the cotton fabric is marked with the blue dashed line. **d** Bar plot showing the yield of GUVs normalized per μg of lipid deposited after each cycle. **e,f** SEM images showing the appearance of the cotton fabric after the first cycle and after the fifth cycle. Images were published⁶¹ and reproduced here with permission from the American Chemical Society.

4. Effect of substrate properties on the assembly of GUVs

4.1 Properties of the substrates tested

To evaluate the effect of the substrate properties on the assembly of GUVs, I conduct a systematic series of experiments on specifically selected substrates. In this section, I extend previous work (Publication 3) and examine effects such as the curvature of the substrate, the manufacturing methods used to obtain the substrate, the permeability of the substrate, the hydrophilicity of the substrate, and the application of electric fields using each of the following i) lab-made nanocellulose paper, ii) commercially available tracing paper, iii) commercially available regenerated cellulose dialysis membranes, iv) silanized tracing paper, v) pristine glass slides, and vi) indium tin oxide (ITO)-coated glass slides.

4.1.1 Tracing paper as potential substrate to assemble GUVs

Overall, the nanohybrid paper experiments (Sections 3.2.2–3.2.4) reveal that the molar yields of GUVs are significantly improved upon when the lipid does not become trapped in the pores of the cellulose paper. Following procedures detailed in the methods (Section 2.3.2), I fabricate whole sheets of pure nanocellulose paper through solution casting to confirm the significant increase in molar yields of GUVs observed in nanohybrid paper is also observed in pure nanocellulose paper. Figure 64a shows a photograph of the nanocellulose paper (outlined by black dashed lines) on top drawings of the UC Merced bobcat mascot. The drawings are clearly visible through the nanocellulose paper highlighting the translucency of the paper. The opaque properties of normal paper are due to the filling of the pores in the paper with air⁷². Since the pores are significantly smaller and more compact on the nanocellulose paper compared to more ordinary cellulose paper (visible in SEM images Figure 64b,c), the paper appears translucent. A commercially available alternative to nanocellulose paper, artist-grade tracing paper, is also identified as a potential substrate to assemble GUV. Since tracing paper is manufactured to be translucent, I expect the pore sizes to also be much smaller and more compact in comparison to ordinary cellulose paper. I confirm that the artist-grade tracing paper both has smaller pores than ordinary cellulose paper and is also transparent in Figure 64d,e.

To obtain the solutions of nanocellulose, the nanocellulose fibers must be liberated from the micrometer-sized cellulose fibers that are present naturally in plants⁷³. For the solutions of nanocellulose used in this work, this process involves the mechanical homogenization under high pressures of pulps of cellulose^{58,74,75}. This homogenization process liberates the nanocellulose fibers from the bundles of cellulose fibers and allows for the regeneration of these smaller fibers into films (nanopaper) with pore sizes on a similar scale to the fibers which typically have widths between 20–100 nm^{43,76,77}. Different than nanopaper, tracing paper is typically fabricated by mechanically pressing out the air in the fibers of ordinary cellulose paper and allowing the paper to soak in sulfuric acid to obtain flattened paper with smaller pores⁷³. These flattened fibers have

similar dimensions to the cellulose fibers and remain on the surface after manufacturing (red arrows in Figure 64d). Overall, due to its widespread use, tracing paper is a much more economical and commercially available substrate in comparison to nanocellulose paper. Figure 64f-h show a higher magnification view of regions of the filter paper, nanocellulose paper, and tracing paper. As expected, when observing a fiber from the filter paper at a higher magnification the bundles of nanocellulose fibers become apparent. These fibers randomly entangle leaving behind nanometer sized pores (red arrows). The nanocellulose fibers and nanometer sized pores appear to be a similar size and scale on the nanocellulose paper and tracing paper substrates confirming the physical properties that effect the assembly of the GUVs (in particular the porosity) should be similar. Using ImageJ to quantify the fiber dimensions, I find the nanocellulose fibers appear to be around 17 ± 6 nm in radii and around 5000 ± 2000 nm in length.

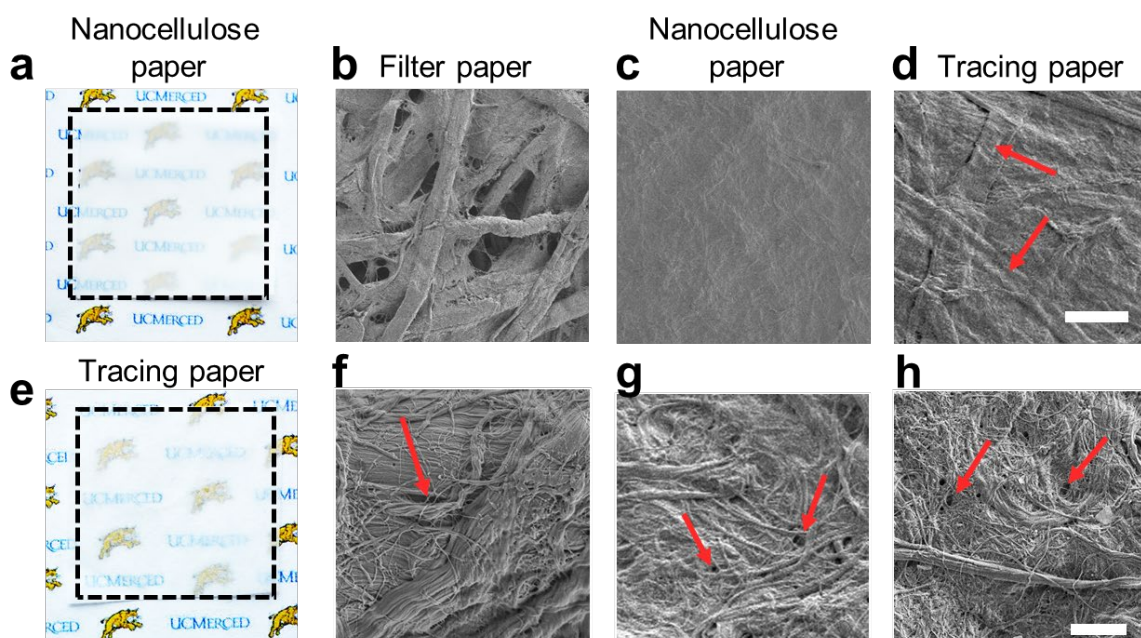


Figure 64: Characterization of nanocellulose and tracing paper **a** Photograph of nanocellulose paper (outlined by black dashed lines) resting on top of a separate piece of paper with a printed logo. **b-d** Lower magnification SEM images of the **b** filter paper, **c** nanocellulose paper, and **d** tracing paper surfaces. The filter paper is composed of micrometer scale fibers and pores, whereas the fibers and pores are not visible at this magnification on the nanocellulose paper. The tracing paper has some micrometer scale fibers (red arrows), but the pores are not visible. **e** Photograph of tracing paper (outlined by black dashed lines) also resting on top of a separate piece of paper with a printed logo. **f-h** Higher magnification images of **f** a fiber from the filter paper, **g** the nanocellulose paper surface, **h** the tracing paper surface. At this magnification the nanoscale fibers and pores (red arrows) are visible on all three substrates. Scale bars: **b-d** $100 \mu\text{m}$, **f-h** $2 \mu\text{m}$. Images were published⁴ and reproduced with permission from the American Chemical Society.

4.1.2 Regenerated cellulose membranes and hydrophobic nanocellulose paper as potential substrates to assemble GUVs

Using chemical processes it is possible to convert natural cellulose (cellulose I) into a dissolvable chemical derivative called cellulose II⁷⁸⁻⁸⁰. This cellulose II can then be regenerated together to form a polymer that results in smooth cellulose membranes that do not contain cylindrical nanofibers⁷⁸⁻⁸⁰. These membranes are typically used for processes such as dialysis since the pore size can be carefully controlled down to the nanometer scale to allow only molecules with small sizes to pass⁸¹⁻⁸³. Previously, I was a part of work that showed fabrics composed of hydrophilic cylindrical fibers with distinct chemistries could be used as novel substrates to assemble GUVs (Publication 4)⁸⁴. Populations of GUVs obtained from cellulose I cotton fabric membranes and cellulose II spun into rayon fabric membranes were not significantly different emphasizing that the slight chemical difference between cellulose I and cellulose II membranes does not have an effect on the assembly of the GUVs.

To allow direct comparison on the effect of the nanoscale curvature of the nanocellulose fibers in the absence of significant chemical differences, I conduct experiments using completely smooth regenerated cellulose membranes with pore sizes that result in the exclusion of molecules (molecular weight cut-off) of around 13kDa. This molecular weight cut-off is similar to values reported for nanocellulose papers^{55,74}. Along with the physically distinct cellulose substrates with nanoscale pores, I also test the effect of the hydrophilicity of the substrate by grafting methyl groups onto the tracing paper surface using a silanization reaction⁸⁵. This treatment results in the fabrication of a hydrophobic nanocellulose paper substrate that allows for the probing of the effect of hydrophilicity in the absence of significantly altering the geometry of the surface. Figure 65a-d shows SEM images of the surfaces of the nanocellulose paper, tracing paper, silanized tracing paper, and regenerated cellulose membranes. As expected the nanoscale fibers are apparent in the images of the nanocellulose paper, tracing paper, and silanized tracing paper substrates but are not present in the regenerated cellulose membrane. The nanoscale pores are just becoming visible on this scale for all four substrates as well with the regenerated cellulose appearing more as bumps than pores in most places at this scale suggesting the pores are slightly smaller than the other papers. The silanized tracing paper also appears to have some additional flat pieces of surface that are left behind from the grafting procedure.

Before quantitative experiments, I qualitatively examine the assembly of the GUVs on the surface of each of these cellulose substrates 2 hours after the initial hydration (Figure 65e-h). As expected, dense and stratified layers of GUVs with sizes reaching more than 100 μm are present at the surface of the nanocellulose paper. The surface of the tracing paper is also covered with these dense and stratified layers of GUVs and appears similar to the nanocellulose paper. Compared to the nanocellulose and tracing paper substrates, the silanized nanocellulose paper surface is covered in significantly fewer GUVs with the

largest sizes observable around $20\ \mu\text{m}$ in diameter. The flat regenerated cellulose membranes also have significantly smaller GUVs present on the surface with a more sparse coverage of the GUVs over the surface of the membrane. Before quantitative experiments it appears that all four substrates do in fact produce GUVs, however, the nanocellulose paper and tracing paper substrates appear to produce more in number and more with larger sizes. In addition, the nanocellulose paper and tracing paper surfaces appear to be able to assemble GUVs more than $200\ \mu\text{m}$ in diameter (Figure 66) which had not observed in any of the other surfaces I tested up until this point and are uncommon in the literature⁴⁵.

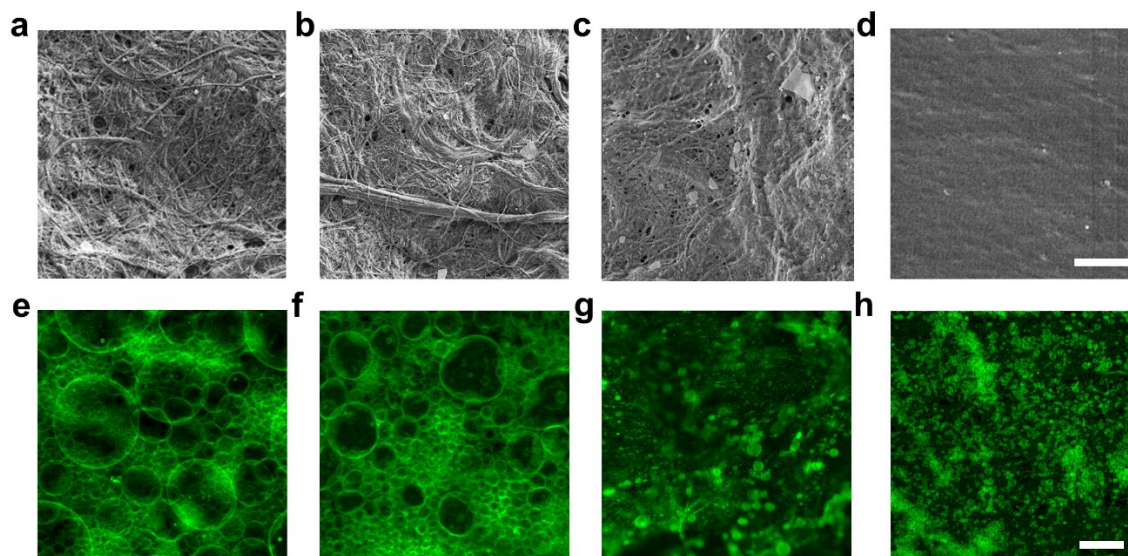


Figure 65: Characterization of the substrates and the assembled giant vesicle buds. **a–d** SEM images showing the microstructure of the **a** nanocellulose paper, **b** tracing paper, **c** silanized nanocellulose paper, and **d** regenerated cellulose dialysis membranes. **e–h** Confocal images of the lipid film after 2 hours of hydration in aqueous solutions on the **e** nanocellulose paper, **f** tracing paper, **g** silanized nanocellulose paper, and **h** regenerated cellulose dialysis membranes. Scale bars: **a–d** $2\ \mu\text{m}$, **e–h** $50\ \mu\text{m}$. Images were published⁴ and reproduced here with permission from the American Chemical Society.

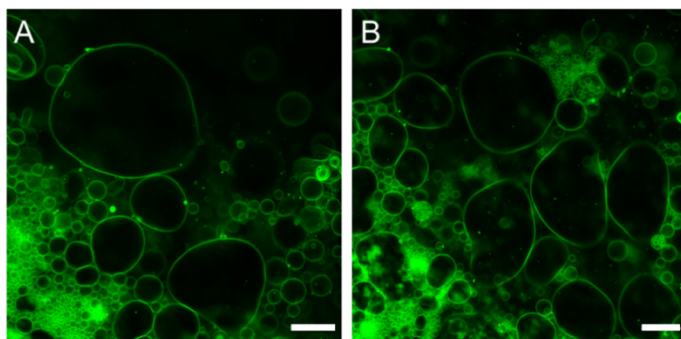


Figure 66: Supergiant vesicles growing on nanocellulose paper and tracing paper. Selected regions on the surface of **a** nanocellulose paper and **b** tracing paper during vesicle

growth showing that supergiant vesicles with sizes as large as 200 μm in diameter are observed. Scale bars: **a,b** 100 μm . Images were published⁴ and reproduced here with permission from the American Chemical Society.

4.1.3 Characterization of GUV buds on the surfaces

To compare the populations of GUVs with the most commonly employed methods in the field as well as quantitatively evaluate the effect of their different properties, I conduct additional experiments using glass slides and indium tin oxide (ITO)-coated glass slides. These substrates are completely flat and are devoid of any features on the surface in SEM images. I qualitatively examine the assembly of the GUVs on each of the surfaces collecting representative images of 400 $\mu\text{m} \times 400 \mu\text{m}$ regions of the lipid film at the surface after 2 hours of hydration. Figure 67a shows confocal images of lipids covering the glass surface in regions of low and high coverage. The coverage of the GUVs is sparse in both images and the membranes of the GUVs are unclear since the sizes are mostly smaller than 10 μm . Clearly within the surface area where the lipid is deposited on the glass there are large regions where not enough lipid is deposited to form GUVs (dark regions in low coverage images). As a comparison I also show images of low and high coverage from the flat regenerated cellulose membrane (Figure 67b). As seen on the glass surface, there are large regions on the regenerated cellulose surface where there is not enough buds to form GUVs in the low coverage area. In the high coverage area, although there appears to be a few, less than 10, large GUVs with sizes more than 10 μm in diameter, a vast majority of the GUVs appear to have sizes smaller than 10 μm .

Similar to the glass slides and regenerated cellulose surfaces, the ITO-coated glass slides are also flat surfaces. However, these slides are used to conduct an electric current following protocols from the gold standard method of producing vesicles that is termed electroformation. This application of an electric field is reported to increase the sizes and yields of the vesicles in comparison to the gentle hydration on the glass slides^{12,50,86}. Observations of the various regions of the surface of the ITO-coated glass slides after 2 hours of electroformation reveal a significant difference in comparison to the other flat substrates where many, more than 100, GUVs with sizes larger than around 10 μm appear visible and stratified above the surface over the same area of image. Although appearing less sparse than the other flat surfaces, the electroformation sample still contains some regions with a low coverage of GUVs.

As a comparison, Figure 67d-f shows 400 $\mu\text{m} \times 400 \mu\text{m}$ representative areas where there are low and high coverage of the GUVs on the curved nanocellulose substrates. The silanized nanopaper appears to have mostly smaller vesicles with sizes less than around 10 μm , but does have a few, less than 10, that are more than 10 μm . The counts of the GUVs depend on the coverage of the lipid with lower coverage having lower counts, and higher coverage having higher counts. However, even in the higher coverage areas, there is still a sparse coverage of GUVs. Both the nanopaper and tracing paper appear similar on

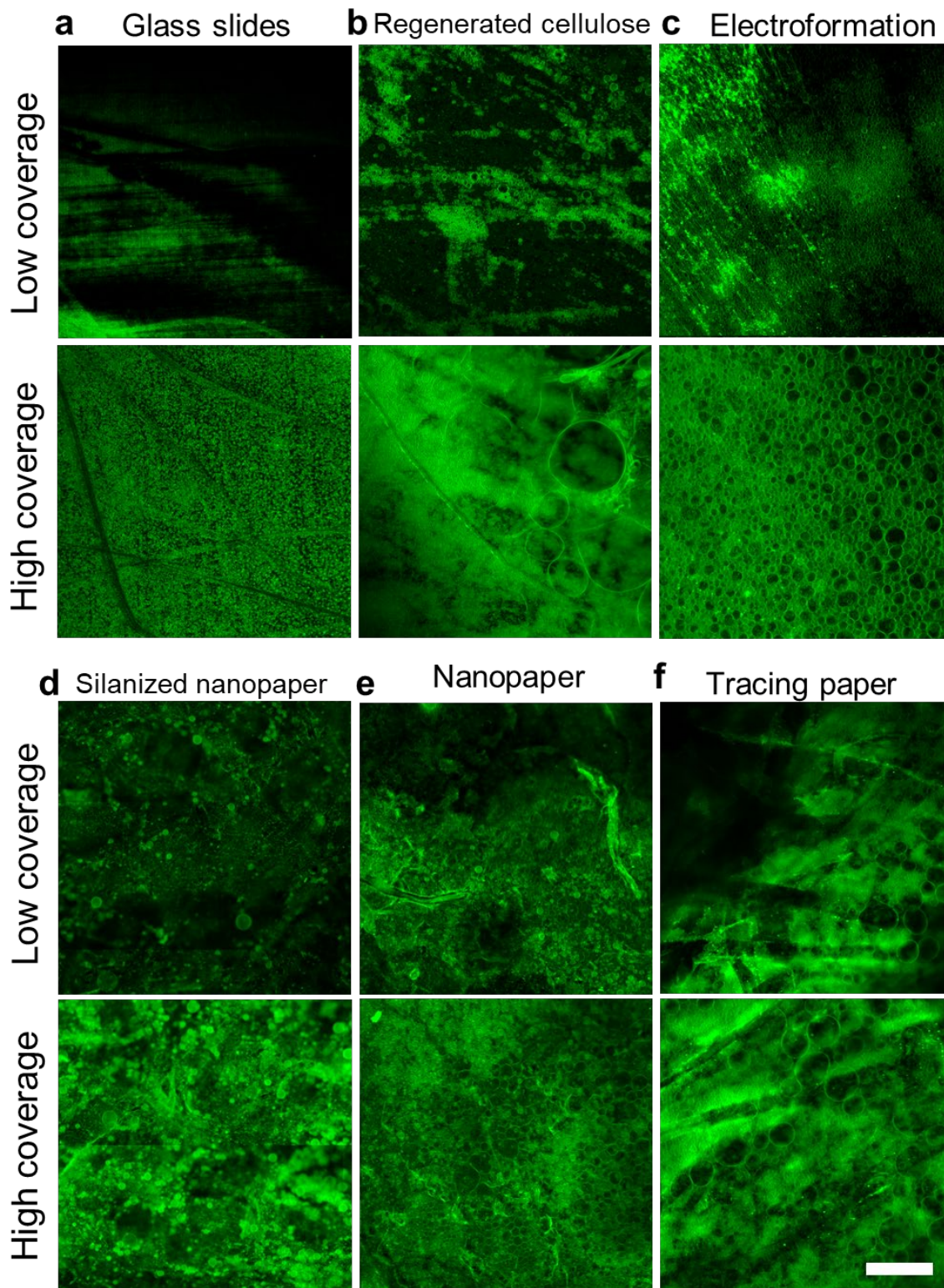


Figure 67: Characterization of the coverage of vesicle buds on the substrates. a-d Confocal images of regions with low and high vesicle bud coverage on a silanized glass

slides, **b** glass slides, **c** regenerated cellulose and **d** electroformation. **e-g** Images of regions with low and high vesicle coverage on **e** silanized tracing paper, **f** nanopaper, and **g** tracing paper. Scale bar 100 μm . Images were published⁴ and reproduced here with permission from the American Chemical Society.

the surface with both low coverage and high coverage areas being covered in GUVs Similar to the electroformation there are significantly more counts of larger GUVs with more than 100 GUVs in each of the images, including the low coverage images, with sizes larger than 10 μm in size.

I perform a qualitative analysis of the GUVs over the entire surface of each of the substrates by collecting tilescan images over the 9.5 mm area where the lipid is deposited after 2 hours of growth. The bud coverage is initially manually scored in each image as a percentile from 0 to 100%. As a second qualitative metric, I also threshold the images in ImageJ since regions where GUV buds are present typically leave behind a fluorescence signature with intensities above around 30 A.U. I find a good correlation between the GUV bud coverage scores, within 3%, between the manually scored and automatically thresholded images. Figure 68a,b shows an example of a 7 mm \times 7 mm tilescan at the center of the tracing paper substrate along with a magnified view of individual tiles each of the tilescans. The bud coverage that was determined using the threshold is written onto each image. Figure 68c-h shows the results of the qualitative analysis over the area at the center of the surfaces. The heatmaps show the amount of bud coverage in each of the images. Only the nanopaper and tracing paper substrates have almost their entire surfaces, more than 96%, being covered with GUV buds. The other substrates have more frequent regions that are devoid of GUV buds with the bud coverage in order from highest to lowest at 83% for electroformation, 72% for regenerated cellulose, 21% for silanized tracing paper and 18% for the glass slides.

From the tilescans of the buds at the surface of the different substrates it is clear that the coverage of the buds is nonhomogeneous. However along with being laterally nonhomogeneous, the buds are also often tightly packed and distributed at different z-heights. Figure 69 shows depth-coded maximum intensity projects of confocal z-stack images on the surfaces where this axial distribution is most noticeable. Larger GUV buds often appear further away from the surface (lighter colors) and obstruct the view of smaller buds beneath them. This axial packing of the buds makes it difficult to quantitatively determine the boundaries and sizes of the GUVs on surface images highlighting the importance of standardized harvesting procedures that allow for the collection of the GUV buds free into solution. Once the GUV buds are harvested and free in solution, they are free to diffuse around and do not pack tightly together making them much easier to identify. Along with the technical challenges that make quantification of the buds on the surface difficult, the buds are also not particularly useful for applications while the harvested GUVs are much more desirable¹⁻³.

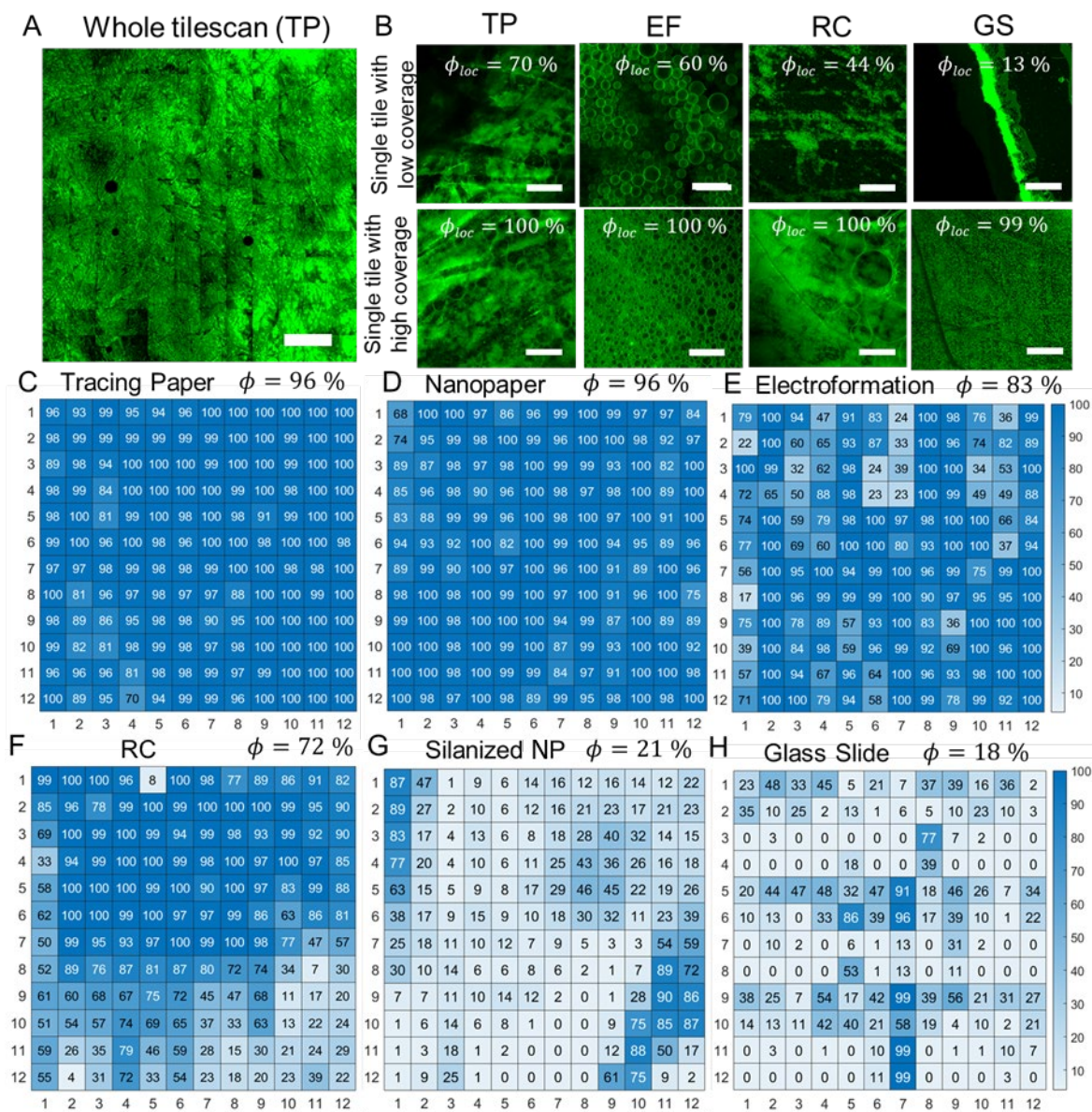


Figure 68: GUV bud coverage on each of the substrates. **a** An example of a whole tilescan covering a 7 mm \times 7 mm area at the center of the tracing paper (TP). **b** Selected tiles showing examples of regions with lower and higher bud coverage from the tracing paper (TP), electroformation (EF), regenerated cellulose (RC) and glass slide (GS) surfaces. The qualitative score given to the image is written at the top of each image. **c-h** Heat maps showing the results from the qualitative score on each of the tiles for each of the substrates. Dark blue represents complete bud coverage, whereas white represents no bud coverage. The total GUV bud coverage from the tilescan images is written at the top. Scale bars: **a** 1 mm, **b** 100 μ m.

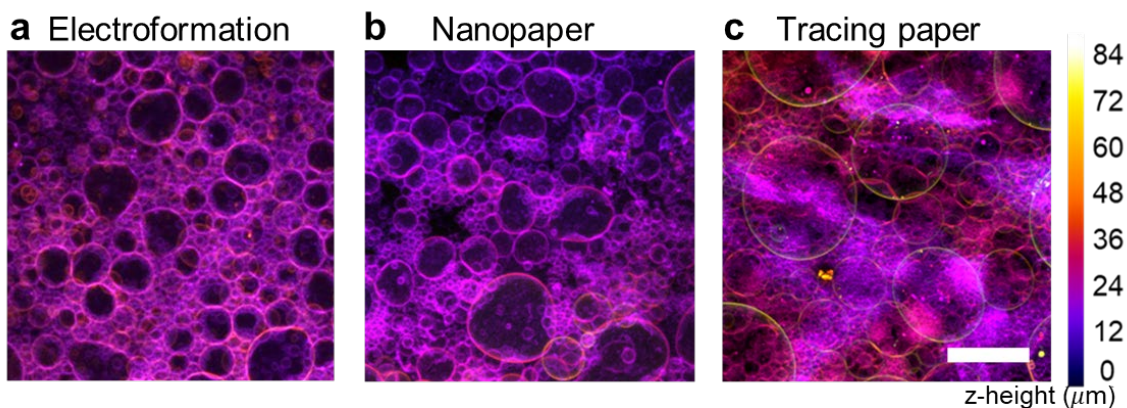


Figure 69: Axial distribution of GUVs on surface. Depth-coded maximum intensity projections of the axial distribution of the vesicles on the surface of the **a** nanopaper, **b** tracing paper, **c** glass slides, and **d** electroformation. The color bar shows the z-height of the objects above the surface. Scale bar: **a-d** 100 μm .

4.2 Quantitative analysis of populations of GUVs from the selected substrates

4.2.1 Characterization of populations of GUVs using confocal microscopy based methods

Using the standardized conditions developed in Chapter 2, I find that on nanopaper a typical harvest of GUVs results in the collection of more than 5 million GUVs. Current comparisons of the sizes and yields of GUVs from even the most commonly employed formation methods such as gentle hydration on glass slides and electroformation on ITO-coated glass slides are unclear due to the lack of data on a statistically relevant portion of the population where typically less than a thousands GUVs are counted^{16,32,86–89}. However, in the cases where a statistically significant amount of data is collected^{31,35,88,90} experimental variables are often not carefully controlled for to allow fair comparisons with other techniques including factors collected in Table 5 such as the amount of lipid deposited, the type of lipid used, the surface area where the lipid is deposited, the hydration solution, the percentage of the population analyzed, whether the population is forced to concentrate near the bottom of the imaging chamber due to sedimentation, or the percentage of the population that is non-GUV structures.

In the previous chapter, I carefully developed methods to standardize the conditions used to assemble the GUVs and optimize the confocal tilescan methods used to characterize of populations of GUVs. These standardized methods provide for the first time a framework to allow fair comparisons on the properties of the different populations of GUVs obtained from different formation methods. I reproduce some of the images from Chapter 2 in Figure 70 to show the general overview of these confocal microscopy based

methods. The important procedures are standardized including the careful deposition of 10 μg of lipid over a 9.5 mm diameter area of the substrate, the hydration of the lipid in 100 mM sucrose solution for 2 hours, the controlled harvesting of the GUVs from each substrate, the sedimentation of the GUVs for 3 hours to the bottom of an imaging chamber, the standard confocal tilescan imaging routine, and the selection of GUVs from other non-GUV objects in the images using an automated image analysis code (refer to the materials and methods section for the complete standardized methods involved in production of the GUVs).

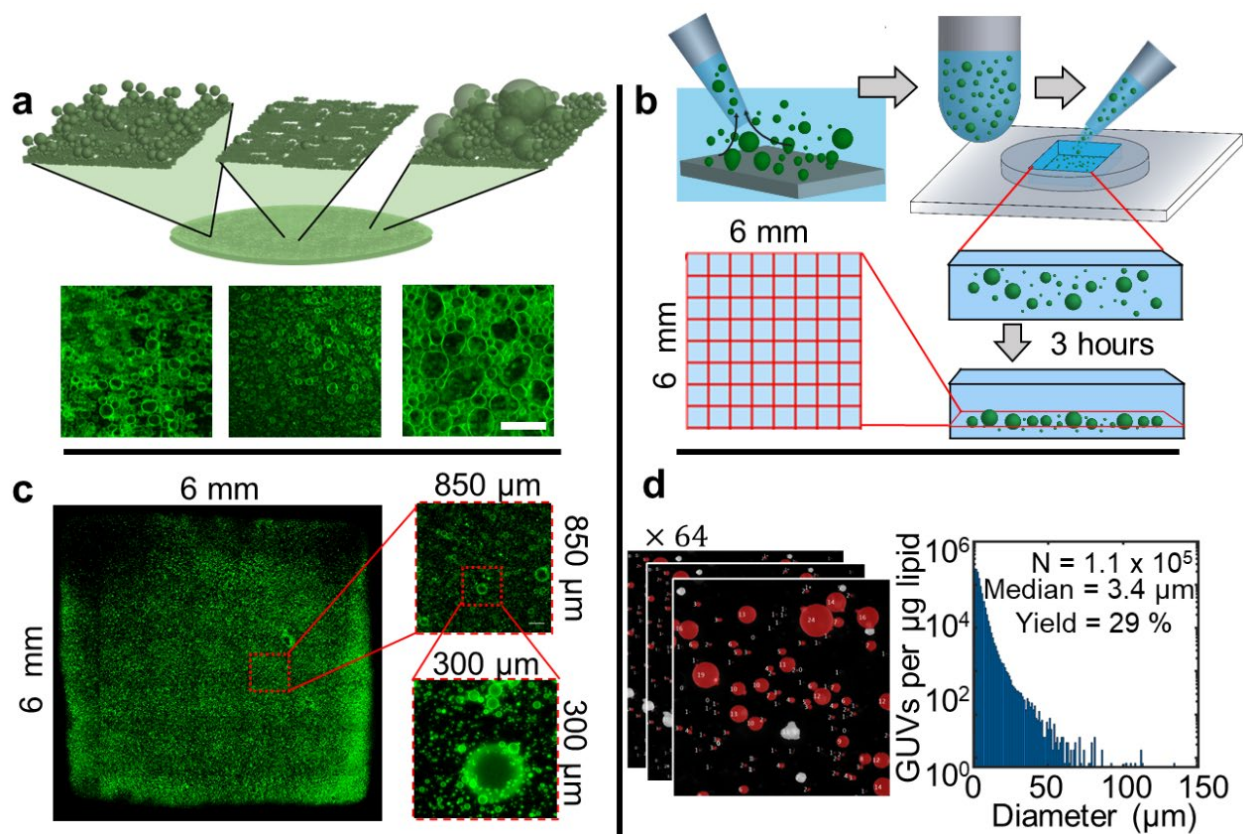


Figure 70: Quantitative analysis of populations of GUVs. **a** Schematic of the buds resting on the surface. The schematic was based on an example of typical experimental images from the assembly on a glass slide (below). **b** Schematic showing the procedures used to measure the distribution of sizes and molar yields of GUVs. **c** Stitched confocal images from a single tilescan imaging experiment. The insets show progressive zoomed in views of a single tile and a region within the tile. **d** (Left) Montage showing an example of the objects selected by the image analysis code as GUVs (red). (Right) A histogram of the diameters of GUVs obtained from on tracing paper sample. The counts were normalized by the total mass of lipid deposited on the surface. Bin widths are 1 μm . Note the logarithmic scale on the y-axis. Scale bar: **a** 50 μm . Images were published⁴ and reproduced here with permission from the American Chemical Society.

4.2.2 Nanocellulose and tracing paper produce the highest counts of GUVs

The typical appearance of an aliquot of the harvested populations of GUVs obtained following the standardized methods are shown in Figure 71. As detailed in Chapter 2, GUVs often appear in the images as a circular bright object with a single distinct ring at the edge and a dim interior. Some of the larger GUVs, which were not nearly as common in the previous filter paper samples characterized in Section 3, appear to have a less pronounced bright ring and instead a more diffuse halo at the edges. This appearance is expected due to their equatorial planes being further above the focal plane and is characterized extensively in Chapter 2. The images show a $200\ \mu\text{m} \times 200\ \mu\text{m}$ area that is representative of the typical counts and sizes of the GUVs obtained from a $2\ \mu\text{L}$ aliquot of the harvested GUV solution obtained from each substrate. The flat substrates are placed in the top row and the substrates composed of nanoscale cylindrical fibers are placed in the bottom row. Compared to the hydrophilic surfaces, both the silanized glass and silanized tracing paper surfaces appear qualitatively to have significantly fewer and smaller GUVs. The glass surface appears to produce fewer and smaller GUVs in comparison to the electroformation, nanopaper and tracing paper samples, but appears similar to the regenerated cellulose surface. The electroformation surface appears to produce more GUVs than the other flat surfaces but fewer GUVs than the nanopaper and tracing paper surfaces. The GUVs obtained from the nanopaper and tracing paper surfaces appear overall similar in the images.

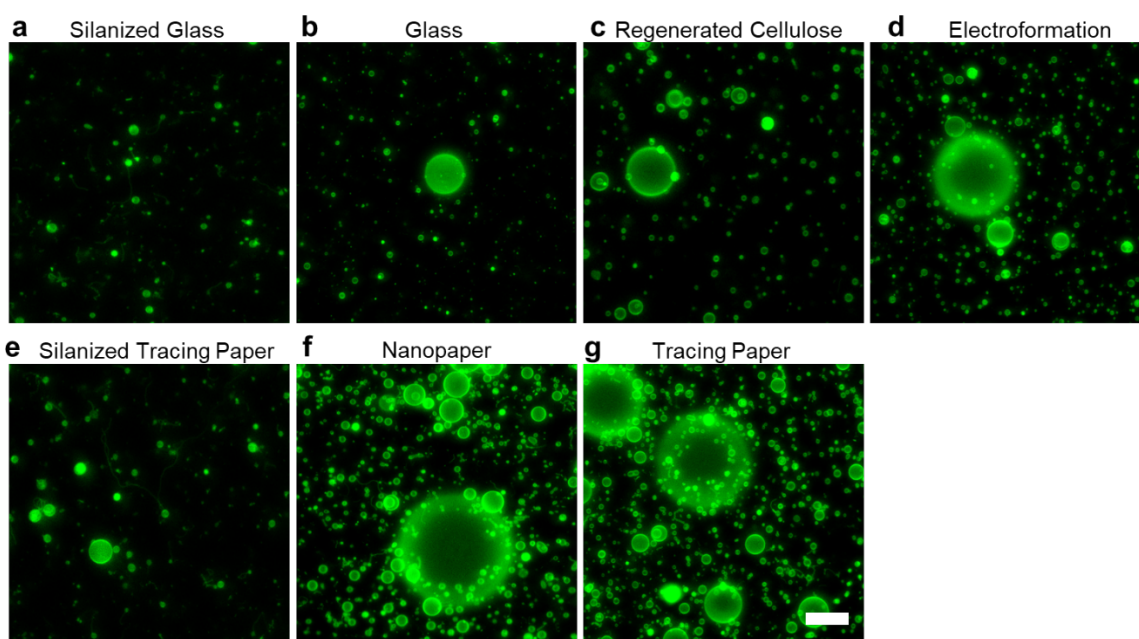


Figure 71: Images of the GUVs harvested from each of the different substrates. Confocal images showing qualitatively the differences in the sizes and yields of vesicles obtained from **a-d** the flat substrates **a** silanized glass, **b** glass, **c** regenerated cellulose, and

d electroformation, and **e-g** the substrates composed of nanoscale cylindrical fibers **e** silanized glass, **f** nanopaper, and **g** tracing paper. Scale bar: **a-g** 50 μm .

To determine quantitatively the differences between the populations of GUVs obtained from each of the different substrates, I characterize the GUVs in the images using the automated image analysis routine developed in Chapter 2. For each of the 7 substrates, I obtain 5 replicate samples repeating the standard growth and characterization procedures exactly. Figure 72 shows histograms of the resulting distribution of sizes of the GUVs obtained from each of the substrates normalized by the amount of lipid initially deposited (10 μg). Note the logarithmic scaling of the y-axis. The height of each bin represents the average number of counts obtained from the 5 replicate samples and the step size of the each bin is 1 μm wide. The average total counts of the GUVs (N) for each substrate is shown inside each plot.

For all of the surfaces, the size distributions appear similar with a single peak that occurs in the first bin at 1 μm and then an extended right-tail where the counts decrease as a function of increasing diameter. The extension of the tail varies significantly between the techniques with the shorter tails, which correlate to the amount of larger GUVs, apparent in the hydrophobic surfaces and the longer tails more apparent in the electroformation, nanopaper and tracing paper surfaces which produce a significant more number of GUVs greater than around 50 μm than the other surfaces. However, overall smaller GUVs are clearly much more abundant than larger GUVs.

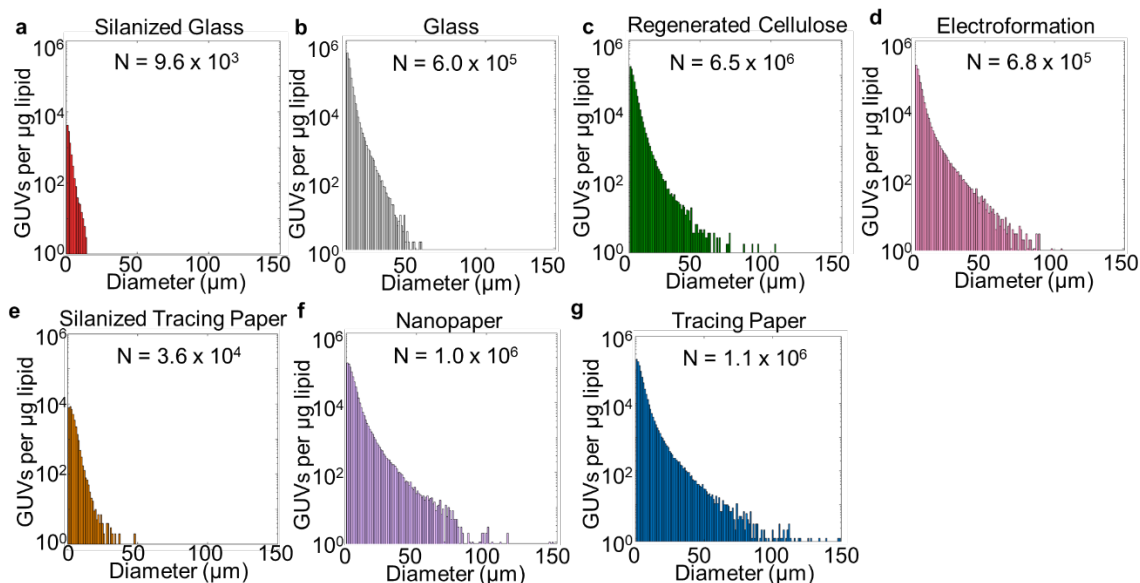


Figure 72: Size distributions of GUVs obtained from the surfaces tested. a-g Normalized histograms of the diameters of the GUVs harvested from **a** silanized glass, **b** glass, **c** regenerated cellulose, **d** electroformation, **e** silanized tracing paper, **f** nanocellulose

paper, and g tracing paper. Each bin shows the average normalized counts from 5 replicate samples. The total number of GUVs per μg lipid (N) is added to each plot. Bin widths are $1\ \mu\text{m}$. Note the logarithmic scale of the y axis. Images were published⁴ and reproduced here with permission from the American Chemical Society.

Figure 73a shows a bar plot of the average counts of GUVs obtained from each surface. The flat surfaces are marked in red while the surfaces composed of nanoscale cylindrical fibers are marked in blue. The counts are split into three size classes that include small GUVs which have diameters (d) from $1 \leq d < 10$, large GUVs with diameters from $10 \leq d < 50$, and very large GUVs with diameters from $d \geq 50$. The error bars show one standard deviation of the mean. Of the flat substrates, the electroformation surface clearly produces a higher number of counts of the larger GUVs while maintaining a similar number of counts of the smaller GUVs when compared to the regenerated cellulose and glass surfaces. The number of GUVs produced by the regenerated cellulose surface appears to increase slightly overall for all of the size ranges when compared to glass, and the glass only produces more GUVs than the hydrophobic silanized glass surface. The tracing paper and nanopaper surfaces appear to produce significantly more counts of all different size ranges of the GUVs when compared to the flat substrates. In addition, the tracing paper and nanopaper substrates do not appear to result in significant differences in the counts of the different size classes of GUVs. The counts of GUVs obtained from silanized tracing paper appear to be significantly lower than all of the other surfaces except the silanized glass. Figure 73b,c shows the average median diameter and the average extreme diameter, which I define as the average diameter of the largest 100 GUVs, for each of the surfaces. Overall the median diameters are all within $1\ \mu\text{m}$ of each other and appear slightly higher on the curved surfaces with the largest disparity ranging from $2.6 \pm 0.5\ \mu\text{m}$ on glass to $3.4 \pm 0.4\ \mu\text{m}$ on nanopaper. The extreme diameters, however, vary by a much more significant amount with the largest extreme diameters produced by the tracing paper and nanopaper surfaces at $65 \pm 4\ \mu\text{m}$ and $64 \pm 5\ \mu\text{m}$ respectively. After the hydrophobic surfaces which produce the smallest extreme diameters (both less than $25\ \mu\text{m}$), the extreme diameters of the GUVs from glass were smallest at $30 \pm 4\ \mu\text{m}$. The regenerated cellulose and electroformation were both larger with extreme diameters at $42 \pm 9\ \mu\text{m}$ and $55 \pm 12\ \mu\text{m}$ respectively.

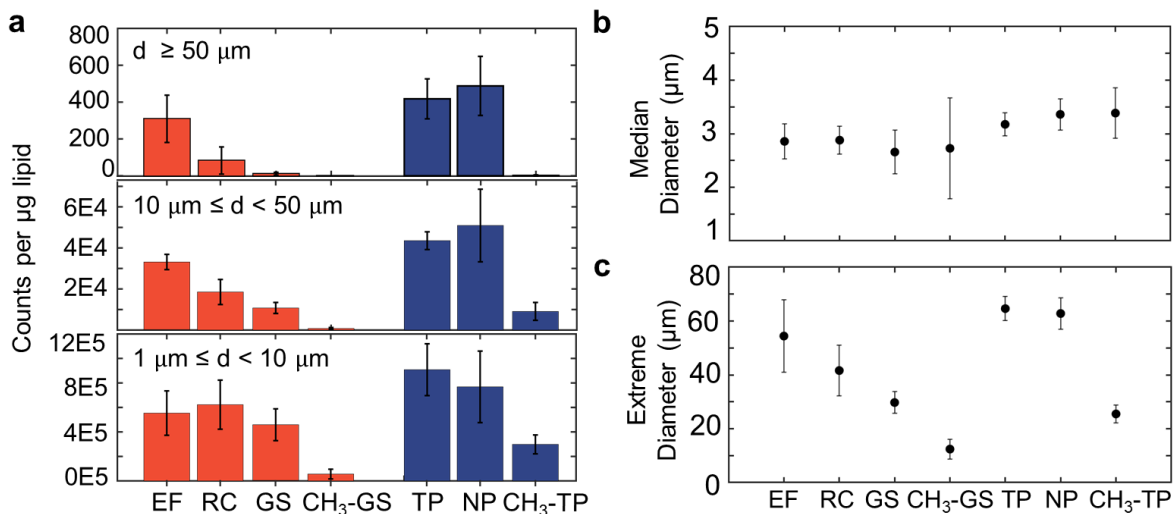


Figure 73: Counts and size statistics of GUVs obtained from the substrates tested. **a** Bar plots showing the average GUV counts normalized by the amount of lipid deposited. The bars colored in red show the flat surfaces which include electroformation (EF), regenerated cellulose (RC), glass (GS) and silanized glass (CH₃ – GS). The bars colored in blue show the surfaces composed of nanoscale cylindrical fibers which include tracing paper (TP), nanocellulose paper (NP) and silanized tracing paper (CH₃ – TP). The bar plots are split different into diameter ranges that are indicated in the plots. **b** Scatter plot showing the median diameter of the populations of GUVs obtained from the surfaces. **c** Scatter plot showing the extreme diameters, which is the mean of the largest 100 GUVs in each distribution. Error bars are standard deviations of the mean obtained from the 5 replicate samples for all of the plots. Images were published⁴ and reproduced here with permission from the American Chemical Society.

4.2.3 Nanocellulose paper and tracing paper produce highest molar yields of GUVs

To evaluate the differences in the GUV yields, I calculate the average molar yield obtained for each substrate. As detailed in Section 1, the molar yield is the ratio between the mols of lipid within the GUVs over the mols of lipid initially deposited. I then determine the statistical significance of the differences between the molar yields from these experiments following the methods detailed in Section 1. The results of the average molar yield calculations obtained from each substrate are shown in the stacked bar plot in Figure 74a. The bars colored in red indicate the flat surfaces and the bars colored in blue indicate the surfaces composed of nanoscale cylindrical fibers. Each bar is split into three size classes which include small GUVs which have diameters (d) from $1 \leq d < 10$, large GUVs with diameters from $10 \leq d < 50$, and very large GUVs with diameters from $d \geq 50$. The error bars show one standard deviation from the mean. I also show the statistical significance between the molar yields determined from a one-way analysis of variance (ANOVA) test and a post-hoc test using Tukey’s honestly significant difference criteria

(HSD). I show the results of the Anderson Darling and Bartlett's test used to confirm the samples meet the underlying assumptions required to use the ANOVA in Table 7 and the show results of the ANOVA and post-hoc test in Table 8.

The average molar yields of GUVs obtained from the tracing paper and nanopaper samples were highest at $31 \pm 4 \%$ and $31 \pm 3 \%$ respectively and were not significantly different from each other ($p = 0.99, NS$). The molar yields of GUVs obtained from the electroformation, regenerated cellulose, and glass surfaces were $22 \pm 2 \%$, $19 \pm 2 \%$, and $16 \pm 1 \%$ respectively. This decrease in molar yield compared to the tracing paper and nanopaper surfaces was statistically significant for all three samples (all $p < 0.001, ***$). The difference between the molar yield of the electroformation and the glass surface was also statistically significant ($p = 0.005, **$), while the difference between the molar yield of the regenerated cellulose and glass surface was not statistically significant ($p = 0.383, NS$). The silanized tracing paper and silanized glass samples produced the lowest molar yields at $8 \pm 2 \%$ and $1 \pm 0.4 \%$ and were both significantly different when compared to their respective hydrophilic substrates (both $p < 0.001, ***$). Overall these results are also all in agreement with the trends expected from the qualitative images as well as the size histogram data on the counts and size statistics.

The results of the molar yield data reveal the effects of several different properties of these substrates that were systematically selected including i) the differences in manufacturing of the tracing paper and nanocellulose paper do not have a significant effect on the yields of GUVs, ii) the substrates composed of nanoscale cylindrical fibers produce significantly higher yields of GUVs in comparison to the flat substrates, iii) the application of an electric field during hydration does significantly increase the yields of GUVs, iv) the increased permeability of water at a surface does not lead to a significant increase in yields of GUVs, and v) lastly the hydrophobic modification of a surface results in a significant loss in the yields of GUVs.

The correspondence between the percentage of the molar yield occupied by the large GUVs versus the total molar yield is also shown in Figure 74b. The x and y error bars at each point show the standard deviation from the mean from the 5 replicate samples. The orange dashed line shows the point where half of the total lipid contained in GUVs (molar yield) is from GUVs greater than $10 \mu\text{m}$ in diameter. The substrates with the highest yields, electroformation, tracing paper, and nanopaper are the only substrates where more than half of the molar is from GUVs larger than $10 \mu\text{m}$.

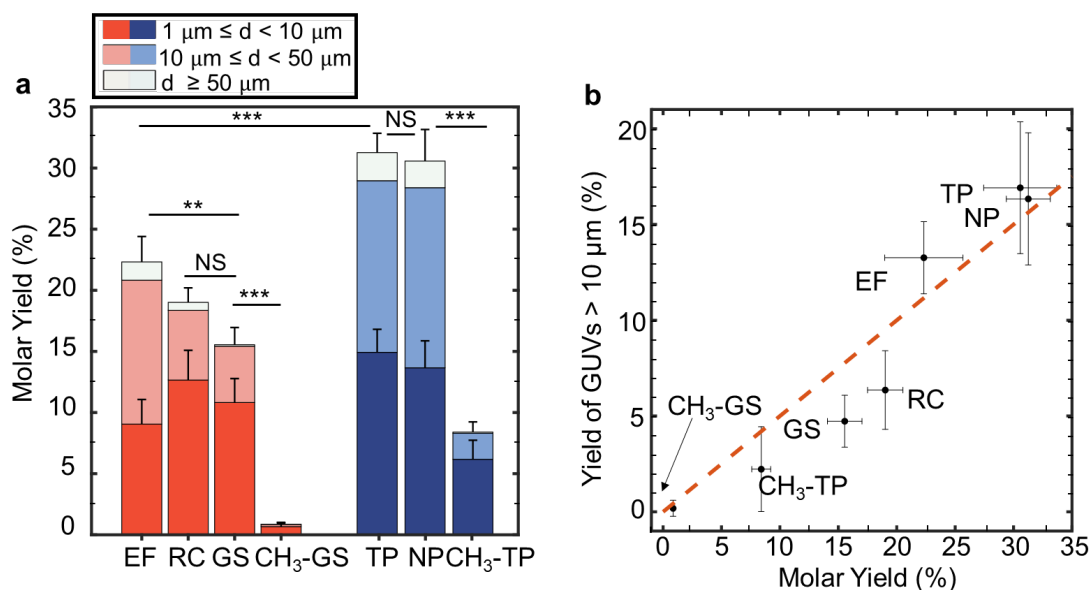


Figure 74: Molar yields of GUVs obtained from the substrates tested. **a** Stacked bar plots showing the molar yields of the GUVs obtained from the flat substrates (red) which include the electroformation (EF), regenerated cellulose (RC), glass (GS) and silanized glass (CH₃ – GS) surfaces, and substrates composed of nanoscale cylindrical fibers (blue) which include the tracing paper (TP), nanopaper (NP) and silanized tracing paper (CH₃ – TP) surfaces. Each bar shows the average molar yield from 5 replicate samples and is split into the three size categories described in the legend. The error bars show one standard deviation from the mean of the smallest size category (bottom) and the two largest size categories (top). The statistical significance between the molar yields determined from a one-way ANOVA and Tukey’s HSD posthoc test is shown where the significance is given by * = $p < 0.05$, ** = $p < 0.01$, *** = $p < 0.001$, and NS = not significant. **b** Scatter plot showing the molar yield of the GUVs larger than 10 μm versus the total molar yield. The orange dashed line corresponds to half of the molar yield coming from GUVs larger than 10 μm . The x and y error bars show one standard deviation from the mean. Images were published⁴ and reproduced here with permission from the American Chemical Society.

	Value	Electro.	Regen. Cellulose	Glass	Silanized Glass	Tracing Paper	Nano-paper	Silan. Tracing Paper
Anderson Darling	p	0.5241	0.3831	0.847	0.4885	0.5251	0.3119	0.3739
Bartlett's Test	p	0.3462						

Table 7: Satisfying ANOVA assumptions. Results of the Anderson-Darling and Bartlett tests confirming the populations have enough experimental variation to accurately perform a one-way ANOVA. NS not significant, * $p < 0.05$, ** $p < 0.01$ *** $p < 0.001$. Table was published⁴ and reproduced here with permission from the American Chemical Society.

Source	SS	df	MS	F	Prob > F, (p-value)
Columns	3725.24	6	620.873	90.53	5.0591E-17
Error	192.04	28	6.858		
Total	3917.27	34			

Group 1	Group 2	p-value	Significance	Comments
Glass	Electro-formation	0.00542	**	Effect of electric field significant
Glass	Regenerated Cellulose	0.383	NS	Effect of permeability not significant
Glass	Nanopaper	5.28E-08	***	Effect of curvature significant
Glass	Tracing Paper	4.31E-08	***	Effect of curvature significant
Glass	Silanized Glass	6.23E-08	***	Effect of hydrophilicity significant
Glass	Silanized TP	0.00304	**	Effect of hydrophilicity significant
Electro-formation	Nanopaper	5.22E-04	***	Effect of curvature significant
Electro-formation	Tracing Paper	1.72E-04	***	Effect of curvature significant
Electro-formation	Regenerated Cellulose	0.439	NS	Effect of electric field not significant
Electro-formation	Silanized Glass	3.71E-08	***	Effect of hydrophilicity significant
Electro-formation	Silanized TP	1.14E-07	***	Effect of hydrophilicity significant
Tracing Paper	Nanopaper	0.999	NS	Effect of manufacturing paper not significant
Tracing Paper	Regenerated Cellulose	9.63E-07	***	Effect of curvature significant
Tracing Paper	Silanized Glass	3.71E-08	***	Effect of curvature significant
Tracing Paper	Silanized TP	3.71E-08	***	Effect of hydrophilicity significant

Nanopaper	Regenerated Cellulose	2.71E-06	***	Effect of curvature significant
Nanopaper	Silanized Glass	3.71E-08	***	Effect of curvature significant
Nanopaper	Silanized TP	3.71E-08	***	Effect of hydrophilicity significant
Regenerated Cellulose	Silanized Glass	3.73E-08	***	Effect of hydrophilicity significant
Regenerated Cellulose	Silanized TP	1.18E-05	***	Effect of hydrophilicity significant
Silanized TP	Silanized Glass	0.00162	**	Effect of curvature significant

Table 8: Statistical significance of differences between molar yields of substrates. ANOVA table and table of p-values from post hoc Tukey's HSD tests of the molar yields of GUVs obtained from the glass, regenerated cellulose, nanopaper, tracing paper, silanized glass, silanized tracing paper and electroformation surfaces. Tables were published⁴ and reproduced here with permission from the American Chemical Society.

4.3 Insights from the substrate molar yield data

4.3.1 Practical advantages of using tracing paper to assemble GUVs

The quantitative data obtained on the populations of GUVs from the different substrates allows for a more practical consideration of parameters such as cost or technical difficulty. Table 9 shows the lowest online prices in US dollars of the glass, ITO-glass, regenerated cellulose, and tracing paper substrates across the largest suppliers of scientific materials. Following the protocols described in the methods section, I normalized the substrate costs by the area. I use the size distributions to obtain the GUV counts and calculate the cost per GUV produced from each substrate. The average costs per GUV as a function of the GUV diameter are shown in Figure 75. Note the logarithmic scaling of the y-axis. The shaded regions around the points show one standard deviation from the mean ($N = 5$). The differences between the distributions are large with the costs associated with obtaining GUVs using tracing paper (blue circles) falling significantly lower than all of the other substrates. The tracing paper also provides a larger range in the sizes of the GUVs that are accessible compared to the other substrates ranging from $1 \mu\text{m}$ up to around $150 \mu\text{m}$ in diameter. The electroformation samples also regularly produce GUVs up to around $110 \mu\text{m}$, but the difference in substrate cost is large where obtaining a single $100 \mu\text{m}$ GUV using electroformation costs around 0.16 USD while using tracing paper it costs around 1.3×10^{-6} USD. The differences between the substrate costs can also be appreciated at the lower sizes considering a scalable example of producing 1L of red blood cell-sized GUVs as potential compartments for substitutes for blood, an area of research currently of unsolved^{91,92}. Since the equivalent mean spherical diameter of the biconcave cells is around $5.6 \mu\text{m}$ ⁹³, I consider the GUVs with sizes between $5.0 \mu\text{m}$ and $5.9 \mu\text{m}$ for each of the

Substrate	Cost (USD)	Unit of measure	Cost (USD) per mm^2	Source of cost
Glass Slide	733.61	1440 glass slides, 25 mm \times 75 mm	2.72E-04	Fischer Scientific
ITO-slide	144	10 slides, 25 mm \times 25 mm	2.30E-02	Sigma Aldrich
Regenerated Cellulose	224.5	1 roll, 30,000 mm \times 90 mm	8.31E-05	Fischer Scientific
Tracing paper	26.93	500 sheets, 228.6 mm \times 304.8 mm	7.73E-7	Amazon

Table 9: Material costs of the substrates used to assemble GUVs. The costs (USD) per area (mm^2) were calculated using the lowest price available online across different large scientific supply companies. Table published⁴ and reproduced here with permission from the American Chemical Society.

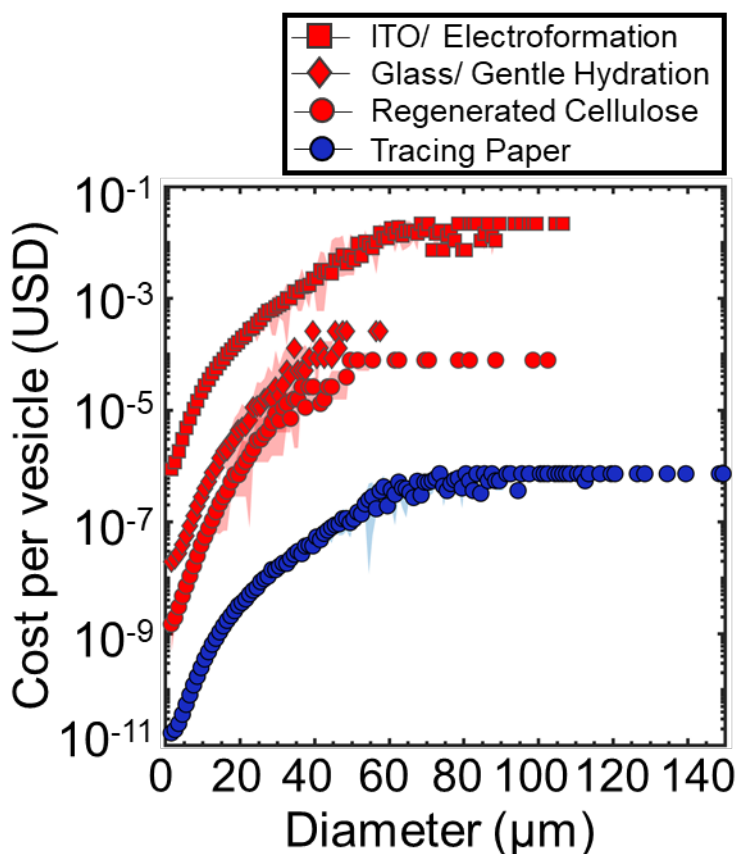


Figure 75: Comparison of substrate costs. Plots showing the substrate costs in USD associated with obtaining GUVs of different sizes. The cost is normalized as USD per vesicle in each size bin. Each bin is 1 μm wide and shows the average cost from 5 samples. The shaded regions show one standard deviation from the mean. The red colors show the costs associated with the flat substrates and the blue colors show the costs associated with

the substrates with nanoscale cylindrical fibers. The legend shows the symbol and color correspondence to the different substrates.

substrates in the distributions. At a typical red blood cell concentration⁹³ of around million USD for electroformation, 230,000 USD for the glass surfaces, 43,000 USD for the regenerated cellulose, and 270 USD for the tracing paper. Compared to previous formation methods, the tracing paper significantly lowers the substrate cost barrier associated with scaling up the production of GUVs.

Another practical advantage offered by the tracing paper substrate is the ease with which cellulose materials can be adapted for scale-up applications. Similar to the reusability experiments conducted on cotton fabric in Section 3, I test the ability of tracing paper to assemble multiple populations of GUVs. Due to the increased mechanical resilience of nanocellulose substrates^{94,95} and the similarities I show in the properties between the tracing paper and nanocellulose papers, I expect the tracing paper to be able to sustain the washing cycles required to be reused for GUV formation. Following the protocols detailed in the methods section, I hydrate, wash, and then reuse the same piece of tracing paper for five experiments. Figure 76a-d shows the appearance of the populations of GUVs as well as the appearance of the tracing paper at the surface after one cycle and after five cycles. Qualitatively the populations appear similar with no large differences in the counts or sizes of the GUVs. Additionally, the tracing paper surface appears unchanged after 5 cycles. Figure 76e shows quantitatively the molar yield of GUVs obtained from each of the cycles. The variation between the samples is small overall and the molar yield does not change significantly with cycle, confirming the tracing paper can be reused for multiple growth cycles.

Along with recyclability, paper can be easily manipulated in ways that make scale-up more straightforward. To demonstrate as a proof of concept, I adapt the typical procedures that use a small 9.5 mm diameter circular area of tracing paper and a 48-well plate to assemble GUVs for an around 800× scaled experiment. To scale the experiment, I use a whole sheet of tracing paper which has size dimensions of 12 inches × 8 inches (305 mm × 203 mm). Following the procedures in methods section, I deposit the lipids evenly across the surface of the whole sheet using a commercial air-brush that is suitable for spraying volatile solvents. I then hydrate the entire paper in a baking tray with size dimensions of 13 inches × 9 inches (330 mm × 229 mm). After 2 hours of growth, I harvest solution of GUVs and store the GUVs in a centrifuge tube. Figure 77 shows stacked bar plots of the average molar yields obtained from 3 replicate 48-well plate sized experiments and 3 replicate whole sheet sized experiments. Note the logarithmic scaling of the y-axis which compresses the stacks within the bars. I find that compared to the 48-well plate the yields obtained from the whole sheet increase by more than two orders of magnitude by a factor of around 600 times, measured as the total mols of lipid harvested as GUVs.

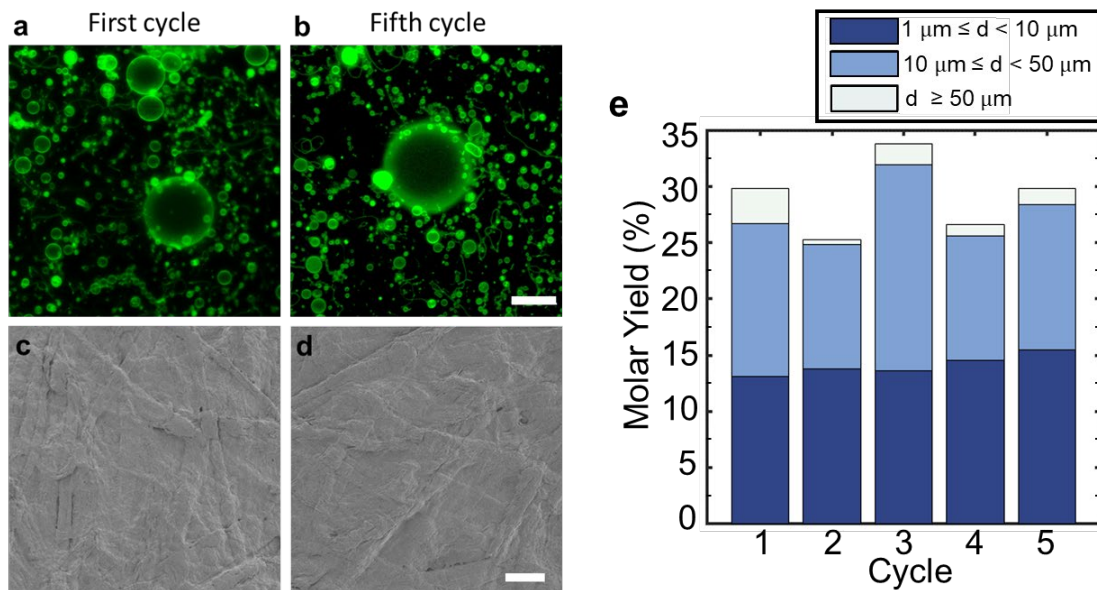


Figure 76: Characterization of the GUV populations obtained from the reused tracing paper surface. **a,b** Confocal images of the harvested GUVs obtained from tracing paper after **a** the first cycle and **b** the fifth cycle. **c,d** SEM images showing the surface structure of the tracing paper remains unchanged after **c** the first growth cycle and after **d** the fifth growth cycle. **e** Stacked bar plot showing the yields of GUVs obtained from each of the five cycles. The legend marks the color correspondence of the molar yield from GUVs from each size classification. Scale bars: **a,b** $50 \mu\text{m}$, **c,d** $50 \mu\text{m}$. Images were published⁴ and reproduced here with permission from the American Chemical Society.

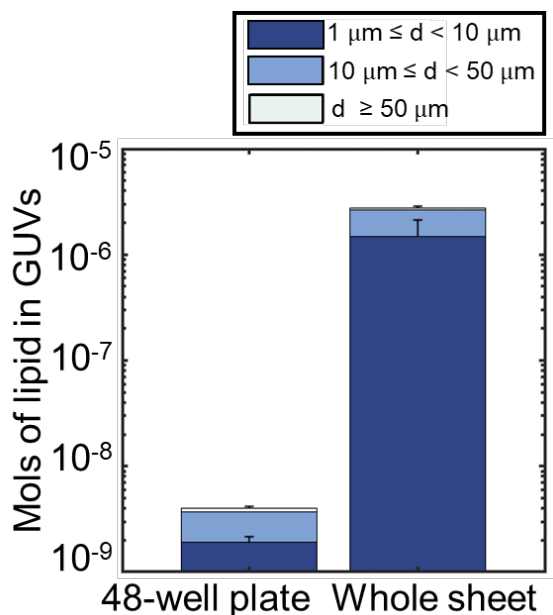


Figure 77: Scale-up of yields from tracing paper. Stacked bar plots showing the mols of lipids obtained from a small piece of tracing paper in a 48-well plate and an entire sheet of

tracing paper. Note the logarithmic scaling of the y-axis. The legend marks the color correspondence of the molar yield of GUVs from each size classification. Images were published⁴ and reproduced here with permission from the American Chemical Society.

4.3.2 GUV buds are attached through membrane connections on the surfaces

Current proposed models that describe the GUV formation mechanism^{21,96–99}, do not explain the new molar yield data I obtain from the different substrates. Thus, the quantitative data that I collected was used to build and test the budding and merging thermodynamic model which was published in ACS AMI⁴. To start to develop a model that could be used to inform experiments and rationalize the results from the molar yield data, the morphology of the lipid film on the surfaces was examined. Figure 78a,b shows a schematic of two possible configurations of the GUV buds on the surface and the two possible scenarios that could result from each configuration after a fluorescence recovery after photobleaching¹⁰⁰ (FRAP) experiment. FRAP experiments to bleach the all of the

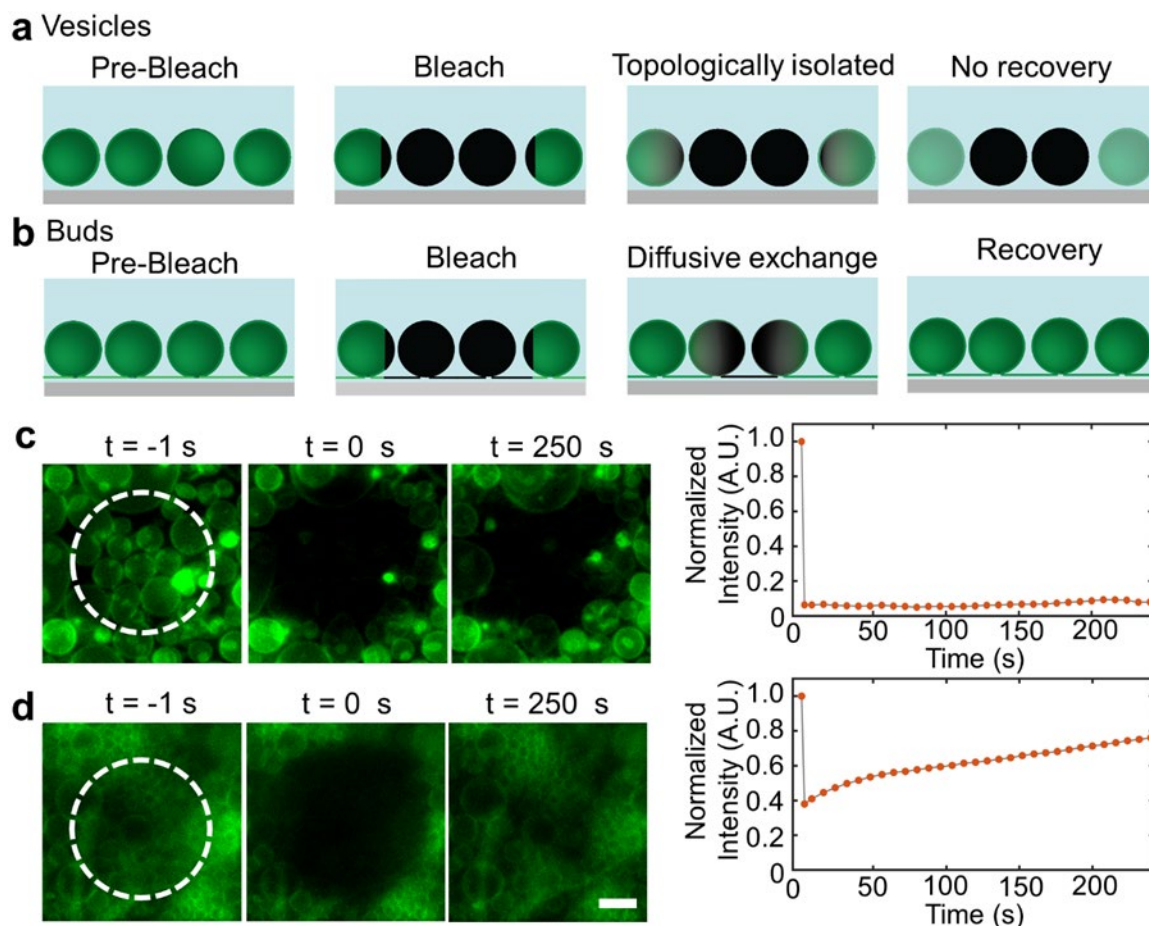


Figure 78: GUV buds on the surface are connected. **a,b** Schematic illustrating the expected results of a FRAP experiment where **a** the fluorescence of vesicles remains

bleached over time (black) and **b** the fluorescence of buds recovers over time (green). Confocal images from FRAP experiments where **c** harvested GUVs are imaged after photobleaching and **d** budding GUVs on the surface of tracing paper are imaged after photobleaching. The white dashed regions show the regions where the average mean intensities were calculated (right) corresponding to each experiment. The scatter plots are normalized to the initial intensity from the image at $t = -1$ s. Scale bar: **c,d** 10 μ m. Images were published⁴ and reproduced here with permission from the American Chemical Society.

fluorescence dye within multiple vesicles on the surface and observe the recovery of the fluorescence over time were conducted. If the vesicles are closely packed together but do not share any membrane connections with each other the vesicles will remain bleached and there will be no recovery of the fluorescence signal over time. However, if the membranes of the vesicles are connected to each other on the surface, diffusive lipid exchange occurs between the vesicles and lipids that were not bleached diffuse into the region that was bleached. If the second scenario occurs, an increase in the fluorescence signal over time is observed and confirms that the vesicles do share membrane connections with each other. Figure 78c shows a control experiment of performing FRAP on the GUVs after harvesting from tracing paper. The first panel on the left shows the appearance of the GUVs before bleaching with the region where the bleach was made outlined in white dashed circle. The second panel shows the appearance of the GUVs directly after bleaching and the third panel shows the appearance of the GUVs 250 s after bleaching. The GUVs do not appear to recover their fluorescence over time. The fourth panel shows normalized fluorescence intensity within the white dashed circle region over time confirming that the fluorescence of the GUVs does not recover with time. Figure 78d shows the FRAP experiment of the buds on the surface of the tracing paper after hydration. The fluorescence of the buds on the surface is bleached and then recovers with time confirming that the buds were indeed still connected to each other through membrane connections on the surface before being harvested.

4.3.3 Assembly of GUV buds occurs through energetically favorable merging

From observations of the buds after hydration on the surfaces, one dynamical phenomena that can be commonly observed is the apparent merging of GUV buds together. This bud merging process has also been described by others^{32,101}. Merging is distinct from another dynamical phenomena, vesicle fusion, which assumes the vesicle membranes are initially fully sealed before fusing together to form one bud¹⁰²⁻¹⁰⁵. Figure 79 shows as a control that even in tightly packed groups of the GUVs harvested from tracing paper fusion does not occur. This result is expected since forming an opening in the membrane in an aqueous environment costs a significant amount of energy¹⁰⁶. In the merging process the buds are not fully sealed and are free to move laterally along the lipid membrane which is a configuration that is in agreement with the FRAP experiments.

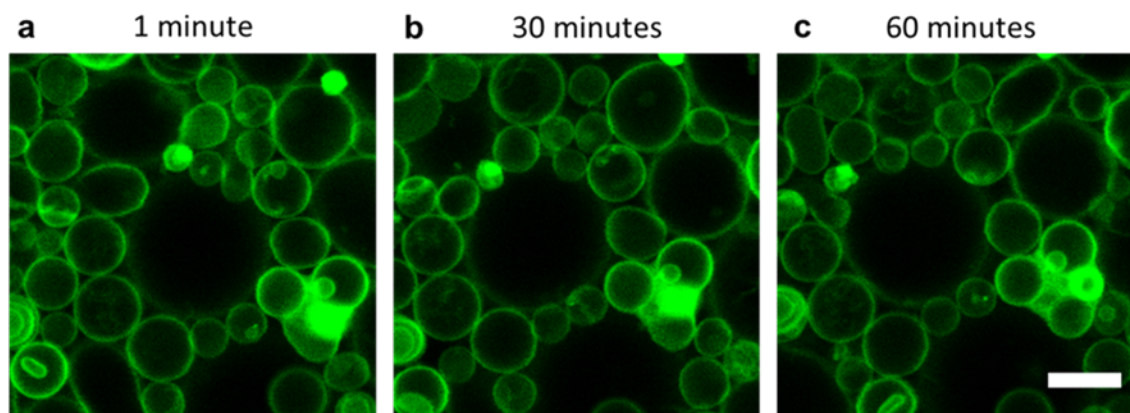


Figure 79: Appearance of harvested GUVs remains constant over course of 1 hour. Confocal images from time lapse experiments of the harvested GUVs resting on the surface of the glass over the course of 60 minutes. Scale bar: **a-c** 10 μm . Images were published⁴ and reproduced here with permission from the American Chemical Society.

Figure 80 shows the dynamics of 7 GUV buds on the tracing paper surface merging together over the course of the first 500 s of hydration. At the first time frame, 242 s, all 7 buds are marked with numbers, and the location of the buds that will merge together between the next time frame are marked with white arrows. At the second time frame, 284 s, bud 1 and bud 2 merge together forming the larger GUV bud that now occupies the area where both buds occupied previously. This is also the case for bud 3 and bud 4 which merge together as well. In the third time frame, 372 s, buds 6 and buds 7 appear to have merged together, and in the fourth time frame at 463 s, the new bud that was at the first time point buds 3 and 4 now merge together with bud 5. In the fifth time frame at 472 s, only 2 of the 7 buds remain, and in the final point at 501 s all 7 buds appear to have merged together into a single bud.

The data can be understood by using principles from membrane thermodynamics and by considering the lipid membrane as an elastic sheet that has some preferred equilibrium state^{107,108}. Any deviation from a preferred equilibrium state requires an input of energy¹⁰⁷. This process can be thought of as analogous to a spring which also has some preferred equilibrium position where if energy is added through pulling and then releasing, the spring will spring back into its preferred equilibrium position. In the case of the bilayer forming lipid membranes, the membranes are expected to prefer flat configurations at equilibrium¹⁰⁷. Thus, with the prior knowledge from observations that the initial state of the lipid membrane after hydration is to have many buds on the surface that are merging together, the system is not at an equilibrium state. To describe the energy cost associated to each bud, a membrane bending modulus, κ_b (analogous to a spring constant), is used to describe the amount of energy it costs to pull the membrane away from equilibrium. This

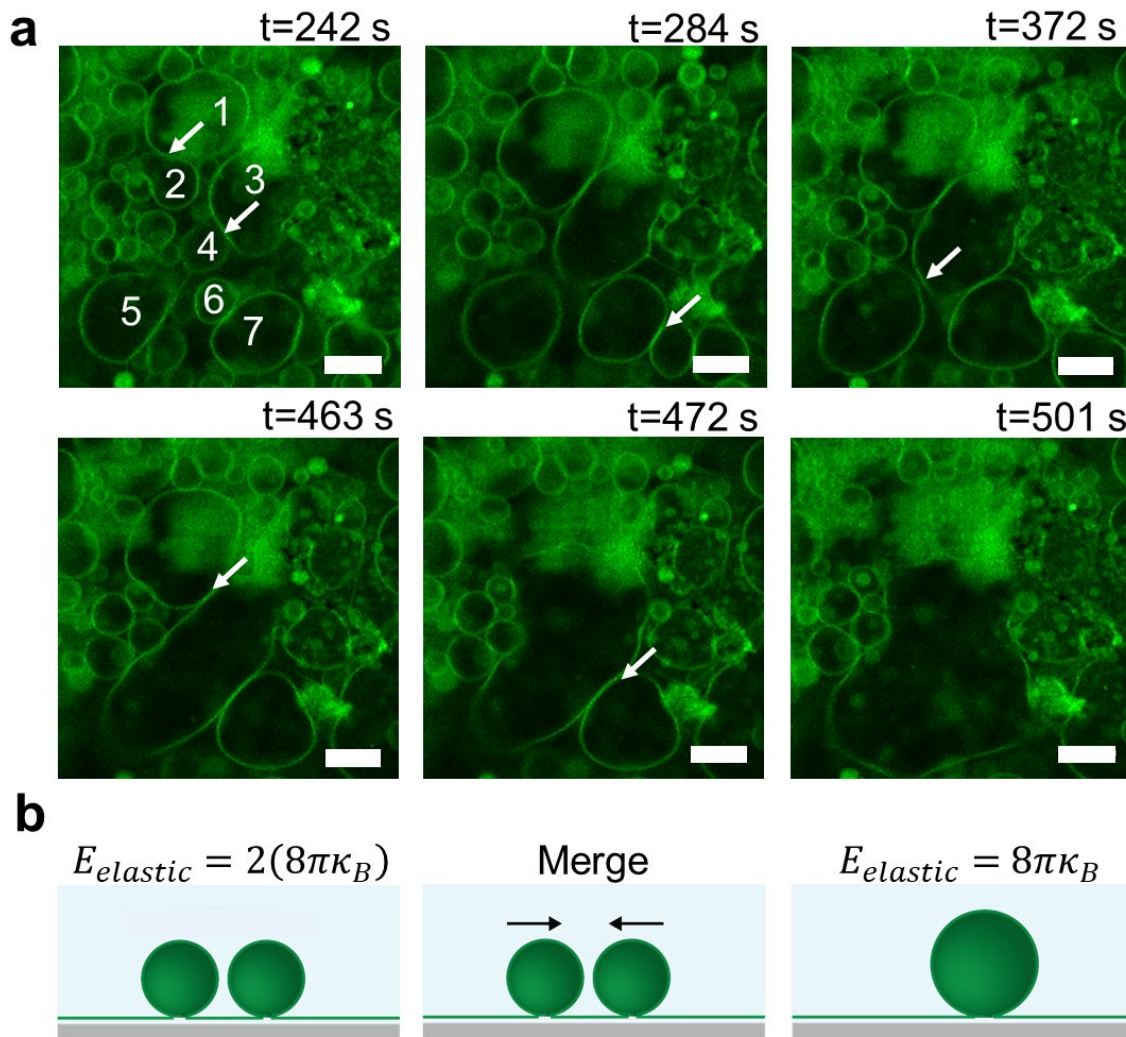


Figure 80: Merging of buds on the surface of tracing paper. a Confocal time lapse images showing the merging of the 7 number buds marked in the top left image over time. The white arrows indicate the buds that merge before the next image. **b** Schematic showing the energy cost to wrap the membrane into two spherical buds (left), through diffusion and a minimization of the free energy of the system merging for the buds is favorable (middle) resulting in a single larger bud (right). Scale bar: **a** 10 μm . Images were published⁴ and reproduced here with permission from the American Chemical Society.

elastic energy due to the curvature of the lipid film can be described using the membrane curvature equation in Equation 18¹⁰⁹

$$E_{curvature} = \int_S dS \left[\frac{\kappa_b}{2} (2H - H_0)^2 + \kappa_G G + \kappa_a \right] \quad (18)$$

where κ_b is the bending modulus, κ_G is the Gaussian bending modulus, $H = \frac{1}{2}(\kappa_1 + \kappa_2)$

is the mean curvature of the membrane, where κ_1 and κ_2 are the principle curvatures on the surface, $G = \kappa_1\kappa_2$ is the Gaussian curvature, H_0 is the spontaneous curvature, and κ_a is the area expansion modulus. For the GUV buds where bending an initially flat membrane ($H_0 = 0$) into a sphere results in equal radii along both principle axes and a Gaussian curvature of zero¹¹⁰ ($G = 0$), Equation 18 can be simplified to Equation 19:

$$E_{vesicle} = 8\pi\kappa_b \quad (19)$$

Since the energy stored in a vesicle bud is independent of the radius of the vesicle, the number of buds that are present at the surface is directly related to the global energy cost of the system, or in other words when a higher number of buds are present the energy in the system is also higher. Thus, merging of the buds together into fewer total buds would result in the relaxation of the total energy of the system and would be energetically favorable (Figure 80b).

4.3.4 Emergence of nanobuds is energetically favorable on substrates composed of nanoscale cylindrical fibers

Considering only the membrane thermodynamics discussed in Section 4.3.3, it would be expected that all of the GUV buds, if given enough time, would eventually merge together and form one single supergiant GUV to minimize the curvature energy⁴. However, from observations of the buds at the surface over longer incubation times (discussed in detail in Section 5), it appears the GUV buds become kinetically trapped and the dynamics at the surface slow considerably likely due to an unknown dissipative mechanism⁴. Assuming that the dissipative mechanism acts universally across all of the substrates, the only parameter that could cause the differences in the molar yields of GUVs observed in experiments is the number of buds that initially emerge from the surface⁴.

Since the molar yields were significantly higher from surfaces composed of nanoscale cylindrical fibers compared to flat surfaces (Figure 74a), the model to describe the bud emergence first includes the effects of curvature⁴. Along with substrate geometry, a term that allows for the adjustment of the surface chemistry due to rendering the surfaces hydrophobic is also included⁴. Finally, although there are no osmotic gradients in the experiments conducted in this section, since the effect of osmotic pressure on budding of lipid membranes is well documented^{104,106,106,111–113}, a term for the osmotic pressure difference is also included⁴. In total, the energy of a vesiculating membrane supported by a surface can be modeled using Equation 20⁴

$$E_1 = \int_S dS \left[\frac{\kappa_b}{2} (2H - H_0)^2 + \kappa_G G + \kappa_a \right] + \int_S dS [\xi(h)] + \int_V dV \Delta p \quad (20)$$

where the first term is related to the curvature of the surface and is the same as Equation 19. The second term is related to the surface chemistry of the surface where $\xi(h)$ is the

microscopic interaction potential normal to the surface and includes the effects from the intermolecular forces, electrostatic forces, van der Waals forces and structural forces¹¹⁴. Lastly, the third term is related to the osmotic pressure where Δp is the osmotic pressure gradient. The terms are integrated over either S the surface of the membrane or V the volume that the membrane encloses.

For the flat surfaces, the first term in Equation 20 is set equal to 0 since the membrane is considered in its preferred equilibrium state. For the nanocellulose and tracing paper surfaces, the energy associated with wrapping an elastic sheet around a cylindrical fiber is given by Equation 21⁴

$$E_{cylinder} = \frac{\pi\kappa_b L_c}{R_c} \quad (21)$$

where L_c is the length of the cylindrical fiber and R_c is the radii of the cylindrical fiber. For the second term in Equation 20, the membrane interaction potential $\xi(h)$ is simplified following work by Helfrich^{109,115} and considers only the adhesion potential between the lipid bilayer and the surface. For the adhesion potential a value of $-1 \times 10^{-5} J m^{-2}$ for each of the surfaces, which is reported for phosphocholine lipid bilayers in aqueous solutions^{116,117}, is typically used, and the osmotic pressure gradient is set equal to 0 for each of the surfaces.

The change in energy caused by lifting a spherical bud from the surface is the difference between curvature energy cost of the a spherical bud and the energy cost of the lipid remaining on the surface and can be given by Equation 22⁴:

$$\Delta E = E_2 - E_1 = \int_{S_2} dS(2\kappa_b H^2) - \int_{S_1} dS(2\kappa_b H^2) - \int_{S_1} dS(\xi) + \int_{C_1} dr(\lambda) \quad (22)$$

The first three terms are for curvature of the spherical bud, curvature of surface, and the adhesion energy respectively. The additional fourth term adds a constraint that if there is no source of lipid for the membrane to draw from, for a section of a membrane to transition into a bud it must form breaks which have edges that cost energy (λ)⁴.

To show the budding energies associated for the possible surfaces and scenarios plots of the change in energy calculated from the model were collected. The plots are normalized relative to the thermal energy scale, $k_B T$ and are plotted on a logarithmic scale on both the x and y axes. First the change in energy from lifting a spherical bud with radius R_B from a flat membrane disk with a radius R_d is reproduced from published work⁴. Note that following geometric constraints the radii are related by $R_B = \frac{R_d}{2}$. Solving Equation 22 for this scenario results in Equation 23⁴

$$\Delta E_{R_B,d} = 8\pi\kappa_B - \pi R_d^2 \xi \quad (23)$$

which only depends on the curvature energy of the bud and the adhesion energy. Plugging in the values of five different adhesion energies $\xi = 0, -1 \times 10^{-7}, -1 \times 10^{-6}, -1 \times 10^{-5}$, and -1×10^{-4} , and solving for various bud sizes ranging from 10^{-8} m and 10^{-5} m

using Matlab, the curves in Figure 81a⁴ can be reproduced. The adhesion energy used for each curve from is marked by color (lowest is brightest, and highest is darkest). Considering the curves, regardless of bud size and adhesion energy the model predicts that the formation of buds is positive above $100k_bT$ and thus not favorable. The change in energy from lifting a spherical bud from a flat membrane disk with an additional $2\pi R_d\lambda$ term added to consider the scenario without a lipid source where λ is the edge energy is reproduced in Figure 81b⁴. Similar to the first scenario, regardless of bud size or adhesion energy the model predicts that the formation of buds is positive (around or above $1000k_bT$) and is not favorable.

Isolines where the change in energy due to lifting a spherical bud from a cylindrical section of the membrane is zero, $\Delta E_{R_B,c} = 0$, and where the lipid is drawn from a source are reproduced in Figure 81c⁴. The isolines are plotted as a function of the length of the cylindrical fiber (L_c) versus the radius of the cylindrical fiber (R_c). In this case the geometric constraints for the radii are related by $R_B = \sqrt{\frac{R_c L_c}{2}}$. Resolving Equation 22 for this scenario results in Equation 24⁴

$$\Delta E_{R_B,c} = \pi\kappa_B \left(8 - \frac{L_c}{R_c} \right) - 2\pi R_c L_c \xi + 4\pi R_c \lambda \quad (24)$$

where the first term balances the curvature energy cost of i) a spherical bud and ii) a cylindrical nanofiber, the second term considers the energy cost of the adhesion to a cylindrical nanofiber, and iii) considers the energy cost if the system were to form breaks in the membrane. Considering Equation 24, a negative first term relates to a higher energy cost of wrapping the membrane around a cylindrical fiber than the energy cost for forming a bud⁴. As the fiber becomes longer in length and smaller in radii, or more specifically when $\frac{L_c}{R_c} \geq 8$, the first term becomes negative and the formation of buds from the surface becomes more favorable⁴. Looking at the isolines for the different adhesion values, any regions above (higher L_c) and to the left (lower R_c) of the isolines indicate the regions where the energy for the formation of a spherical bud is negative and is favorable⁴. Using the dimensions of typical nanocellulose fibers^{63,74,118,119} which have a radius of around 12 nm (and a length of around 2000 nm), the radius of the outer membrane (R_c) should be around 20 nm. Interestingly, comparing the dimensions of $R_c = 20$ nm and $L_c = 2000$ nm to the isolines, the formation of buds is favorable for all adhesion energies except the highest value at $1 \times 10^{-4} J m^{-2}$. Considering the scenario where the lipid membrane forms edges and using the same cylindrical membrane dimensions as previously the formation of buds is again favorable for all adhesion energies except the highest value (Figure 81d)⁴. Lastly, since the adhesion potential for membranes on hydrophobic surfaces can be as high as $-1 \times 10^{-1} J m^{-2}$ due to the formation of depleted membranes¹²⁰, the plots also show that the formation of buds would be unfavorable on the hydrophobic rendered tracing paper surfaces⁴.

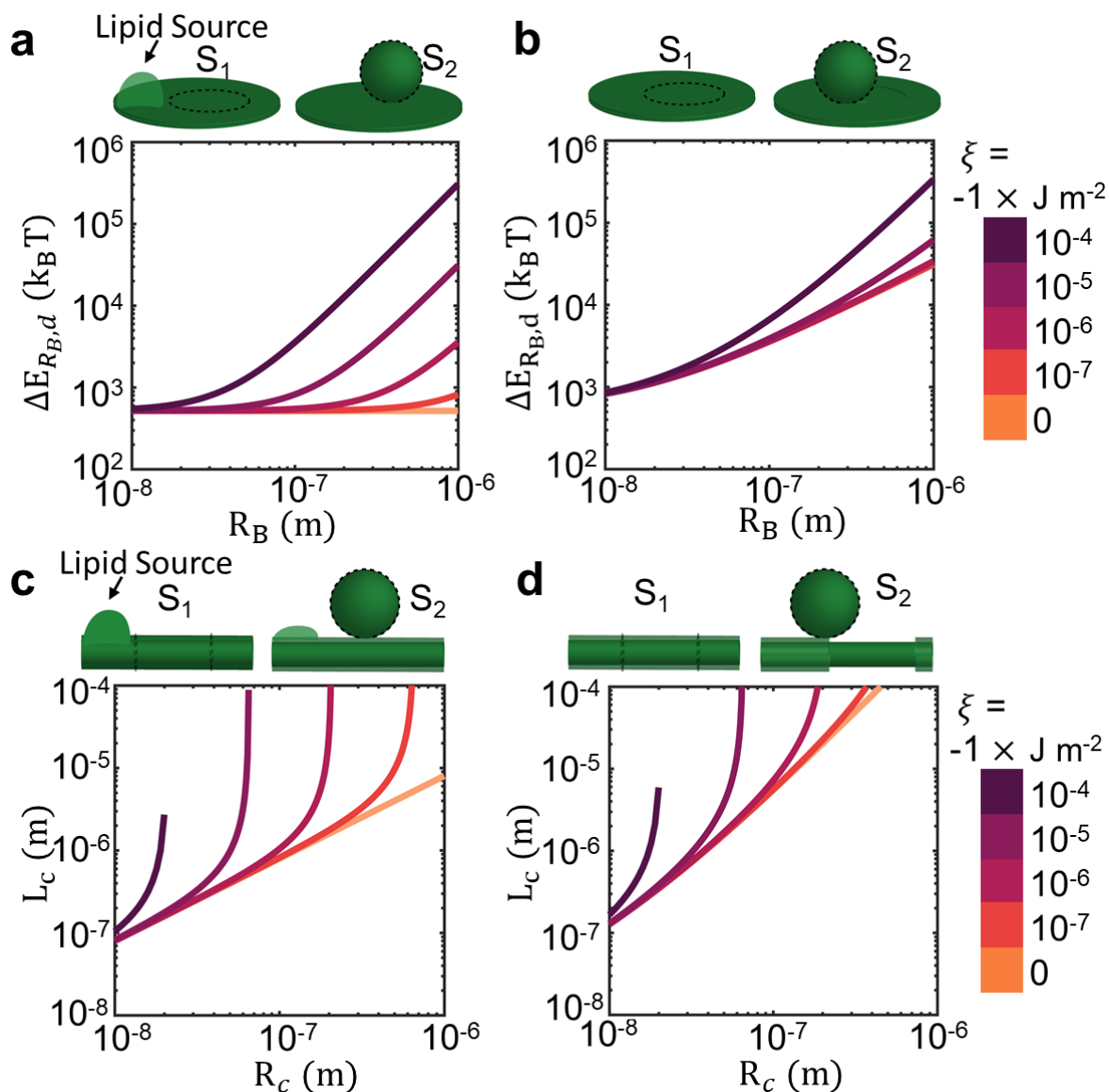


Figure 81: Change in energy associated with forming a spherical bud on the substrates. The schematics above each plot show the scenario being modeled where if a lipid source is involved it is marked, the surface area that transitions into a bud is marked in black dashed lines and labeled, and the configuration of the membrane on the surface is illustrated. **a,b** Plots showing the change in energy associated with forming a spherical bud (R_B) from **a** a flat surface with a lipid source and **b** a flat surface without a lipid source. **c,d** Plots showing the isoenergy lines where the change in energy for forming a spherical bud from a cylindrical fiber is zero. The plots are shown in R_c and L_c phase space where the magnitude and sign of $\Delta E_{R_b,d}$ can be calculated using Equation 24. The colors of the lines mark the adhesion energies, ξ , used to obtain each plot. The energies are shown relative to the thermal energy scale $k_b T$. Note the logarithmic scaling of both the x and y axis. Images were published⁴ and reproduced here with permission from the American Chemical Society.

Parameter	Description	Magnitude	Source
κ_a	Area expansion modulus	$80 - 200 \times 10^{-3} \text{ J m}^{-2}$	114
ξ	Adhesion energy	$-1 \times 10^{-1} -$ $-5 \times 10^{-9} \text{ J m}^{-2}$	114,117,121
λ	Membrane edge energy	$1 \times 10^{-11} \text{ J m}^{-1}$	114
κ_b	Bending modulus	$8.22 \text{ to } 82.2 \times 10^{-20} \text{ J}$	114
κ_G	Gaussian bending modulus	$-0.9\kappa_B \text{ to } -1.0\kappa_B$	110

Table 10: Parameters for budding and merging model. Values for the physical parameters of phosphocholine membranes reported in the literature. Table was published⁴ and reproduced here with permission from the American Chemical Society.

Other factors such as the process of hydration could introduce external energy into the system and might explain the assembly of GUVs on the flat glass and regenerated cellulose surfaces⁹⁷. Assuming the external factors involved in the formation of buds on glass is constant between the other techniques, the budding and merging model provides a basis to explain the differences in molar yields observed from the substrates tested in this section that could not be explained otherwise. Figure 82 shows an overview of the budding and merging model on tracing paper. The idealized dimensions and configuration of the nanocellulose fibers with a length, L_f , and a radius, R_f are shown on the left. Once hydrated, the lipid film wraps around the cylindrical fiber resulting in a membrane radius of R_c . Due to the curvature energy stored in the wrapped cylindrical membrane, the formation of a spherical nanobud at every critical length L_c is favorable. The size of the nanobud is directly related to the critical length that results in a free energy change equal to 0. Once formed, the buds begin to merge together to lower the total global curvature energy of the system. The nanobuds merge together and form the micrometer-scaled GUV buds that are observable and more abundant on the tracing paper surface. One advantage of the model is that an exact size range per area of lipid membrane can be correlated to a the initial size of the nanobud before merging. Since the amount of lipid membrane on the surface is controlled and the movement of the buds is expected to be diffusion-limited, this framework provided by the budding and merging model opens avenues for understanding the evolution of the buds on the surfaces through different approaches such as through simulations that allow for the testing of parameters like fiber dimensions. These new avenues could contribute to further insights on the continuing understanding of the mechanism of the surface-assisted formation of GUVs.

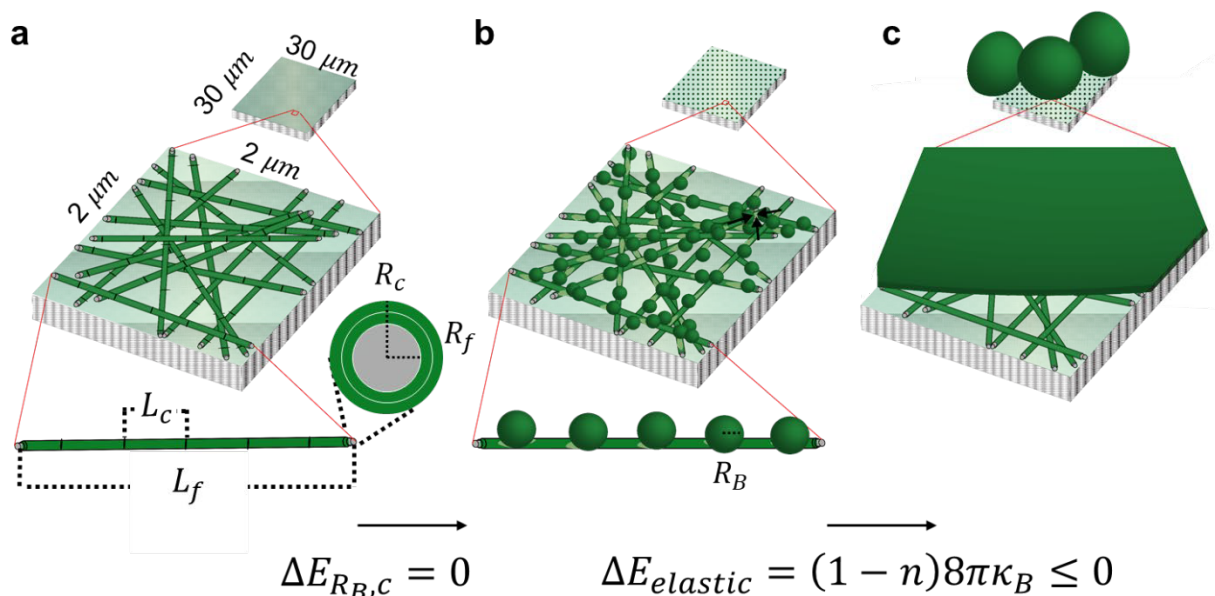


Figure 82: Overview of budding and merging model. Schematic showing the concept of a budding and merging framework that results in the assembly of GUVs from nanocellulose fibers. Illustrations of the lipid membranes on the surface at the micrometer scale is shown on the top with a magnified illustration (red lines) shown coming down. **a** Lipid membranes coat cylindrical nanocellulose fibers with dimensions of lengths L_f and radii of R_f . When the lipid membrane dimensions are equal to R_c and L_c the energy cost to form a spherical bud falls to zero. **b** Buds with a radii R_b are expected to emerge from the fibers. Once merged the buds are free to diffuse and can minimize the global curvature energy through merging resulting in **c** micrometer-scaled GUV buds that are observed on the surface. Images were published⁴ and reproduced here with permission from the American Chemical Society.

5. Optimization of assembly of GUVs in physiological conditions

For both biophysical studies as well as potential practical applications relevant to biological systems, obtaining GUVs in physiological conditions is desirable³. In this section, I characterize the effect of factors such as the sample incubation time and the ionic strength of the solution on the populations of GUVs obtained from surface-assisted techniques. Through these experiments, I develop novel methods to obtain high yields of physiological GUVs using tracing paper.

5.1 Effect of incubation time on the sizes and yields of the GUVs

5.1.1 *In situ* characterization of bud dynamics reveals bud merging and bud growth

Following previous observations of the tracing paper surface during the first 10 minutes of incubation (Figure 83), I expect that buds will merge together and result in more larger buds as the incubation time is allowed to increase. I qualitatively determine the timescales over which I expect significant merging to occur by observing the evolution of the buds after 5 minutes, 30 minutes, 60 minutes, and 120 minutes of gentle hydration on glass slides, electroformation, and gentle hydration on tracing paper. Figure 83a shows the evolution of the same buds over a typical $200\ \mu\text{m} \times 200\ \mu\text{m}$ region of the glass slide. The buds on the glass slide appear to be less than around $25\ \mu\text{m}$ in diameter at all time points and do not significantly increase in size at any point between 5 minutes and 120 minutes. This suggests that most of the bud merging occurs rapidly after the initial hydration on glass. In contrast, the GUV buds at the surface during both electroformation (Figure 83b) and gentle hydration on tracing paper (Figure 83c) appear to increase in size significantly between the 5 minute and 30 minute time points with some buds reaching sizes larger than $50\ \mu\text{m}$ in diameter. After 30 minutes the sizes of the buds appear to mostly stabilize and increase only slightly in size over the course of 120 minutes. This observation of an increase in bud sizes for only the electroformation and tracing paper surfaces but not for the glass surface is in agreement with the quantitative data on the counts of large GUVs ($d \geq 10\ \mu\text{m}$) from Section 4).

To quantitatively examine whether most of the observable bud merging occurs before 60 minutes on each of the surfaces, I collect time lapse images of the buds merging with one time lapse starting after 10 minutes of hydration and a second time lapse starting after 60 minutes of hydration. In each time lapse, I collect images of a representative $150\ \mu\text{m}^2$ area of buds for 7 minutes. The interval between each image is 3 seconds. Using ImageJ, I then manually count the number of merging events that occur during the 7 minute time lapse and determine a merging rate as observable merging events per minute. Figure 84 shows a bar plot of the merging rate determined from the time lapse images. For each surface, I obtain an average from 3 independent replicate samples (error bars show one standard deviation from the mean). The merging rate observed at the surface of the glass

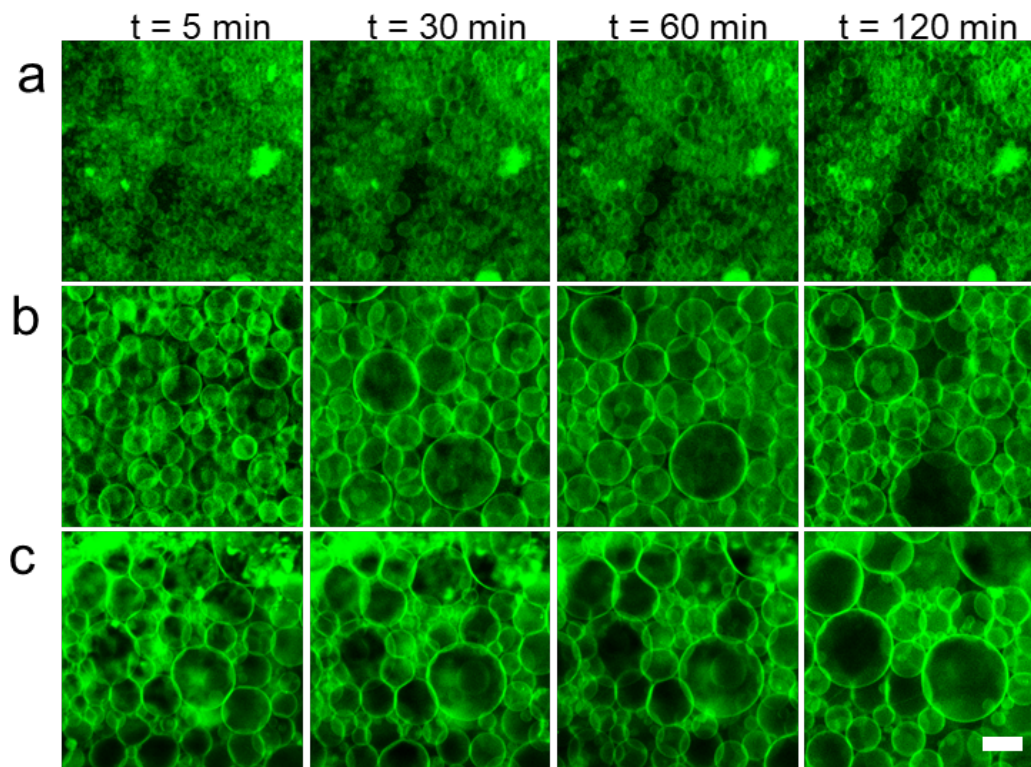


Figure 83: Evolution of GUV buds during common surface-assisted hydration techniques. Confocal images showing the typical evolution of buds after 5 minutes, 30 minutes, 60 minutes, and 120 minutes of incubation through **a** gentle hydration on glass slides, **b** electroformation, and **c** gentle hydration on tracing paper. The sizes of the vesicle buds appear to increase with time for electroformation and tracing paper, while there appears to be no change in the buds with time on glass. Scale bar: **a-c** 25 μm .

at 10 minutes is less than 1 observable event per minute and is around 8 times lower than the rate observed on the electroformation surfaces and 10 times lower than the rate observed on the tracing paper surfaces. After 60 minutes, the merging rate from the electroformation and tracing paper surfaces also fall to below 1 observable event per minute. Interestingly, the merging rate observed in the electroformation samples appears to only fall by a factor of around 8 while in comparison the tracing paper falls by a factor of around 13 which could be due to the effects of the continuous electric field.

Along with micrometer-scale bud merging, bud growth without observable merging is also common at the surface. Figure 85 shows the growth of specific buds over the course of 60 minutes. As expected the buds overall appear to increase in size from 3 minutes (Figure 85a) to 60 minutes (Figure 85). A closer look at specific buds reveals that some buds appear to increase in size without any observable bud merging (Figure 85c). Other buds can be observed merging together as expected (Figure 85d). Analyzing the time

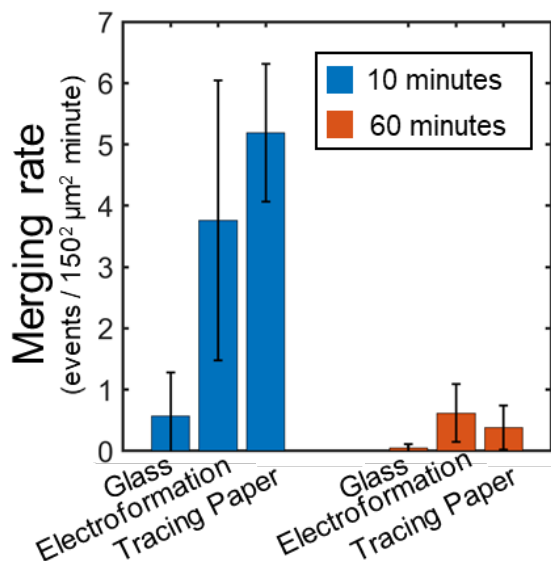


Figure 84: Decrease in the rate of bud merging at 60 minutes. Bar plot of the average merging rate for the buds on the three surfaces. Error bars show one standard deviation from the mean ($N = 3$). At 10 minutes (blue), tracing paper had the highest initial merging rate followed by electroformation and then glass. At 60 minutes (orange), the merging rates all fall to below 1 observable event per minute.

lapse images in ImageJ, I quantify the change in size of the buds where no bud merging is apparent in Figure 85e. Most of the buds are visible 3 minutes after the initial hydration and increase only slightly in size over the course of 60 minutes. Two buds (buds 3 and 5) appear in the time lapse images after around 10 minutes and grow rapidly to around $10 \mu\text{m}$ in size and then grow slowly similar to the others. I also quantify the change in size of the buds that grow due to observable merging (Figure 85f). Although these merging events are clearly visible in the plots as spikes in the bud size, even these buds appear to slowly increase in size at times where observable merging events are not present. Following the predictions of the budding and merging model which was developed using the data in Section 4, I expect that the bud growth that I observe without micrometer-scale merging is due to the merging of nanometer-scaled buds that are below the resolution of the images.

Although much more rare, occasionally I also observe the disappearance of buds from the surface in the absence of clear merging. Figure 86 shows an example of a bud disappearing back into the surface 55 minutes after the initial hydration along with a plot of the sizes of all of the vesicles that were observed to disappear in a $150 \mu\text{m}^2$ over the course of 60 minutes. Disappearance appears to typically be caused in places where the vesicles appear strained and either contained inside another vesicle bud or overcrowded between other vesicle buds. The buds can be observed retracting back onto the surface. Since the disappearance of micrometer-scaled buds is so rare however, it likely does not play a major role in the dynamics of the buds at the surface.

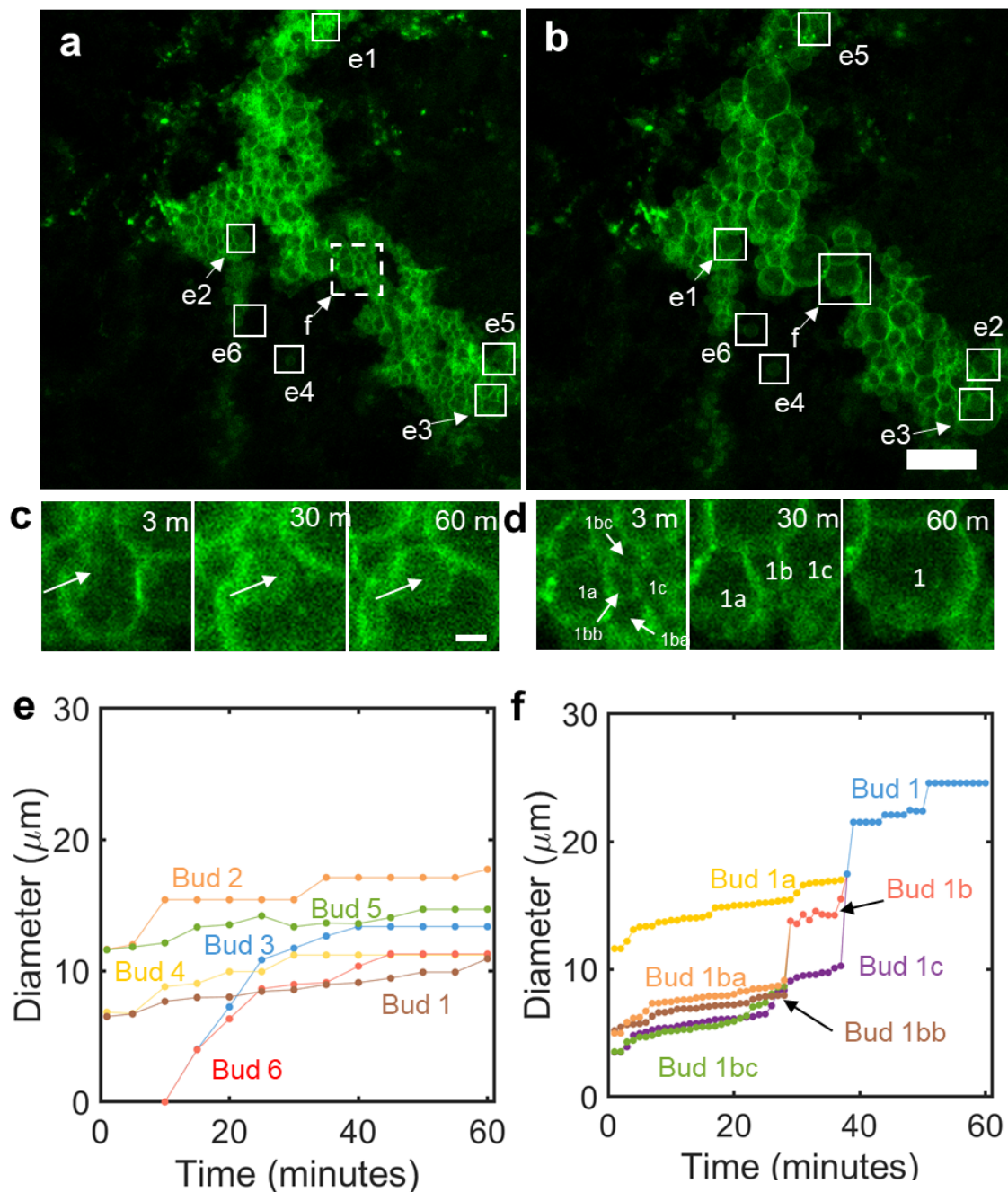


Figure 85: Buds increase in size over the course of 60 minutes. Stills from confocal time lapse images of buds growing on the surface of tracing paper at **a** 3 minutes and **b** 60 minutes after initial hydration. **c,d** Magnified stills of buds **c** growing without observable merging, and **d** with observable merging at 3 minutes, 30 minutes, and 60 minutes after initial hydration. **e,f** Plots showing the increasing diameter (μm) of the buds from the time lapse images **e** without observable merging (buds marked in **a,b** as e1–e6) and **f** with observable merging (area marked in **a,b** as f). Scale bars: **a,b** 50 μm , **c,d** 10 μm .

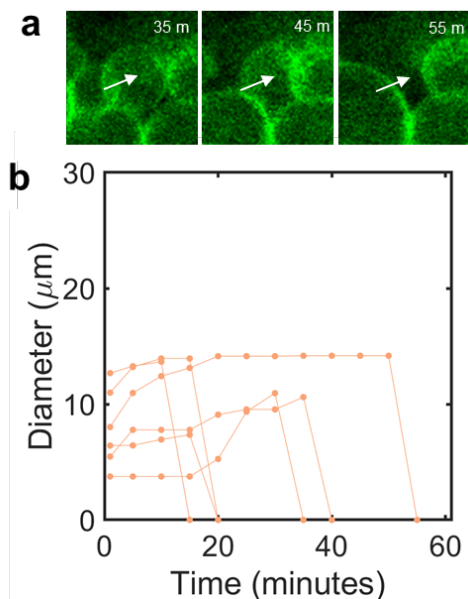


Figure 86: Disappearance of buds over time. **a** Stills from confocal time lapse images of a bud (marked with white arrow) disappearing on the surface of tracing paper at 55 minutes. **b** Plots showing the change in diameter (μm) of various disappearing buds over time. Scale bar: **a** $10 \mu\text{m}$.

5.1.2 Stopped-time technique reveals size distributions broaden with increasing incubation time

The studies of the dynamics of the buds at the surfaces reveal that the incubation time can have an effect on the sizes of the buds. Since the harvesting procedures to obtain GUVs are designed to free these same buds from their membrane connections at the surface, I also expect the sizes of the GUVs can be controlled by the incubation time. To confirm quantitatively that the incubation time will have a significant effect on the populations of GUVs obtained from the glass, electroformation and tracing paper substrates, I conduct experiments to harvest and stop the assembly of GUVs at various time points. I characterize the populations of GUVs obtained by stopping the growth at various time points using the confocal tilescan methods. Using this stopped-time technique, I arrest the dynamics of the buds and provide a snapshot of the populations of GUVs obtained at stopping times of 1, 10, 30, 60, and 120 minutes. Figure 87 shows a schematic of the stopped time technique along with representative images of the GUVs harvested from each of the substrates after 1 minute, 10 minutes and 120 minutes. Qualitatively, the sizes and counts of the GUVs obtained from all 3 surfaces clearly increase with longer incubation times. It also appears that the largest GUVs, greater than $50 \mu\text{m}$ in diameter, are much more common after 120

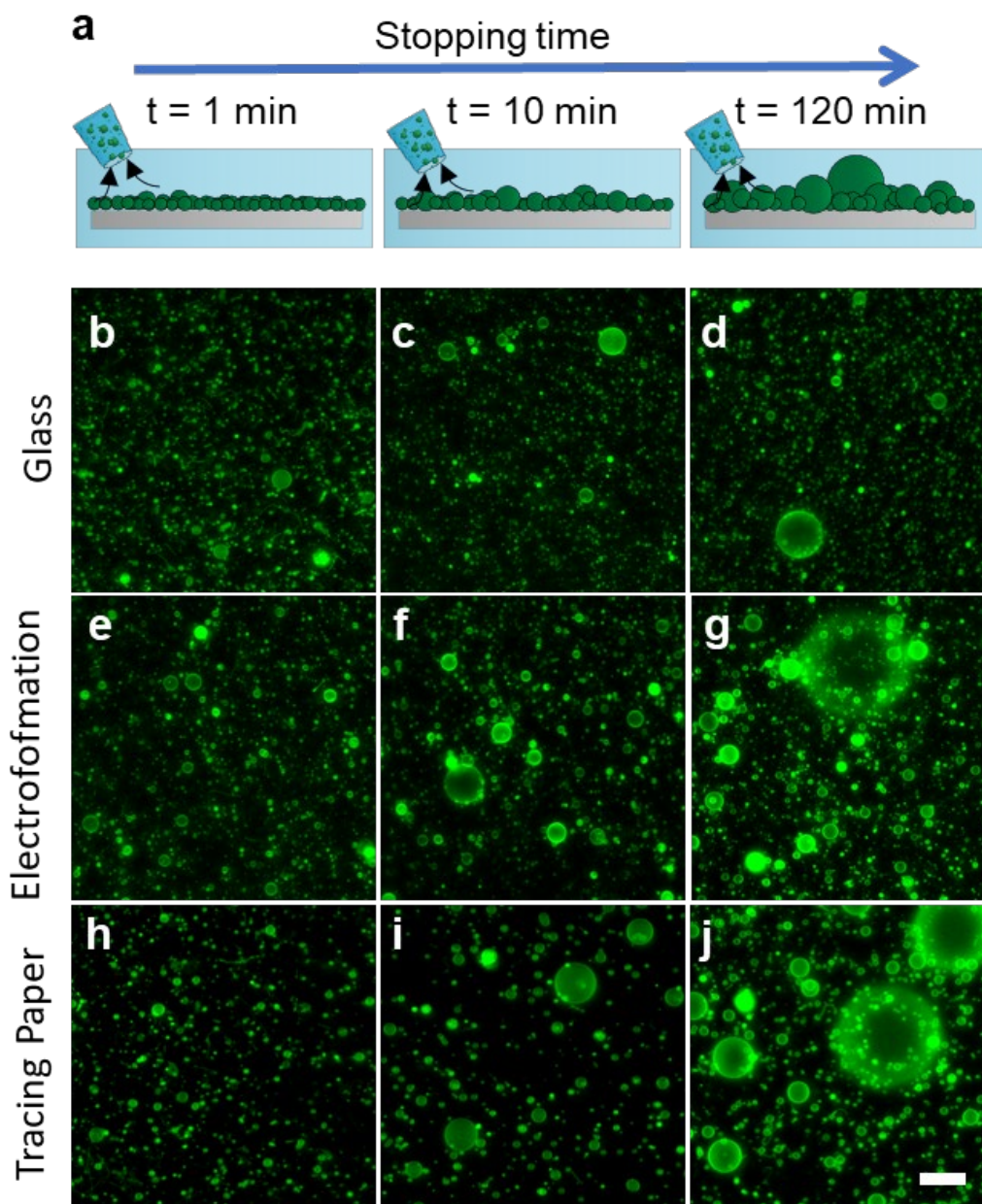


Figure 87: Larger vesicles appear more abundant at later stopping times. a Schematic showing the effect of stopping time on the sizes of vesicles harvested. b-j Representative confocal images of GUVs harvested from b-d glass, e-g electroformation, and h-j tracing paper surfaces. From left to right, the columns of the schematic correspond to the images of the harvested GUVs obtained after 1 minute (left), 10 minutes (middle) and 120 minutes (right) of incubation. Scale bar: b-j 50 μm .

minutes of incubation. These results are both in agreement with the observations of the dynamics at the surface.

For each substrate and each stopping time point, I collect data from 3 independent replicate samples. Figure 88a-c shows the average counts of GUVs obtained from the samples normalized by the amount of lipid initially deposited (which was $10\ \mu\text{g}$ lipid for all of the samples). The error bars show one standard deviation from the mean. The average counts of GUVs obtained from glass do not change significantly with time and remain between 6×10^5 and 7×10^5 counts per μg lipid for each time point over the course of 120 minutes. The average counts of GUVs obtained from electroformation start out at around 6×10^5 counts per μg lipid at 1 minute and then increase significantly to above 9×10^5 counts per μg lipid for the 30 minute and 60 minute time points, before falling back down to an average of 6×10^5 counts per μg lipid at 120 minutes. The average counts of GUVs obtained from tracing paper start higher at around 9×10^5 counts per μg lipid at 1 minute, increase to above 11×10^5 counts per μg lipid at 30 minutes, and then fall back down to an average of around 9×10^5 counts per μg lipid at 120 minutes.

At both the 1 minute and 120 minute time points the glass and electroformation samples have similar average counts of GUVs. However, after around 30–60 minutes of electroformation there are on average significantly more GUVs that are harvested suggesting that the presence of the electric field leads to the emergence of more buds during the first hour of growth. At 120 minutes the average counts fall significantly likely due to both a limit being reached of emerging buds as well as the merging of the additional buds into fewer but larger buds. This explanation that the decrease in counts is due to the emergence and consequent merging of additional buds assembled through electroformation and is not an effect of the buds disappearing entirely from the surface is also in agreement with the data from Figure 88 showing the counts of large and very large GUVs is significantly higher from the electroformation samples compared to the glass samples. The tracing paper samples also produce higher average counts of GUVs over the course of the first 30 minutes of growth in comparison to the glass and electroformation samples suggesting that the effect of the curvature energy leads to the emergence of more buds. After 30 minutes the average counts begin to decrease likely due to the merging of the additional buds into fewer larger buds. For all 3 substrates, the average counts at the 120 minute time point are also within the ranges expected.

The distribution of sizes of the GUVs obtained from the stopped-time samples are plotted in Figure 88d–f. The size distribution plots show the average GUVs counts normalized per μg of lipid with the counts distributed into $1\ \mu\text{m}$ sized diameter bins. Note the log scale of the axes. The legend shows the color correspondence of the sample stopping time to the size distribution obtained (the lighter colors show the earlier time points and the darker colors show the later time points). The size distribution of the glass sample harvested after 1 minute of incubation appears to have more smaller GUVs than all of the other time points since the points corresponding to the $1-3\ \mu\text{m}$ diameter bins are slightly

above all the other time points. The 1 minute sample also appears to have fewer counts of the larger GUVs in comparison to the rest of the other time points since the bins from around $8 \mu\text{m}$ and larger are visible below all of the other time points. The largest GUVs obtained at 1 minute appear to have sizes of around $30 \mu\text{m}$ in diameter. The size distributions from 10 minutes to 120 minutes appear to mostly overlap with one another suggesting that the incubation time only effects the size distributions of the GUVs obtained on glass during the course of the first 10 minutes. The tail of the size distributions of the electroformation and tracing paper samples at 1 minute, which I define as GUVs with diameters greater than $10 \mu\text{m}$ in diameter, appear to have similar slopes to the size distribution from the glass slide at 1 minute. All three tails approximate to a straight line in the log-log plot which is a characteristic of power law distributions^{66,122}. At the 1 minute time point, the slope of the lines are all similar starting at around 1.2×10^3 GUV counts per μg lipid at the $10 \mu\text{m}$ diameter bin and falling to around 5 GUV counts per μg lipid at the $30 \mu\text{m}$ diameter bin. Power law fits to all 3 distributions at 1 minute result in a negative power law exponent of 3. Different than the glass samples however, the electroformation

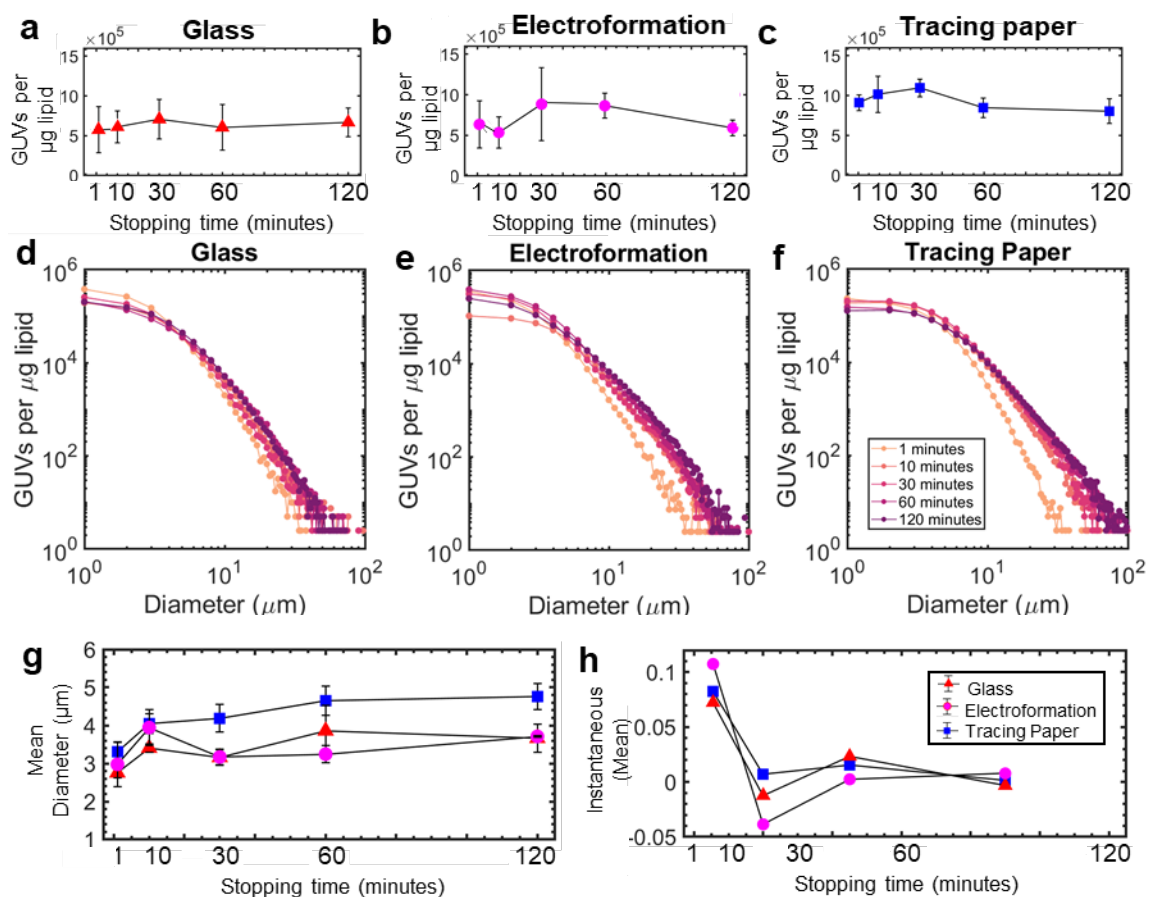


Figure 88: Effect of stopping time on the counts and size properties of the GUVs. a-c Average counts of the GUVs obtained from **a** glass, **b** electroformation, and **c** tracing paper

substrates plotted as a function of stopping time. The counts are normalized per μg of lipid deposited for each sample. **d-f** Distribution of sizes of GUVs obtained from **d** glass, **e** electroformation, and **f** tracing paper substrates. The stopping time is shown by the color indicated in the legend. The bin widths are $1\ \mu\text{m}$. **g,h** Size statistics showing **g** the mean diameter and **h** the instantaneous mean diameter of the populations of GUVs obtained from each of the substrates. The points associated with each substrate are indicated in the legend. In all of the plots each point represents an average from 3 independent replicate samples. Error bars show one standard deviation from the mean.

and tracing paper size distributions appear to broaden significantly more with increasing stopping time. For both plots the tails of the 10 minute, 30 minute, and 120 minute size distributions are visible with each distribution broadening with increasing incubation time. Interestingly, it appears that extra incubation time between 60 minutes and 120 minutes does not have a significant effect on the size distributions from the electroformation and tracing paper substrates, confirming that the size distributions do not appear to broaden after 60 minutes of incubation. Between the plots, the incubation time has the largest effect on the distribution of sizes of the GUVs obtained from tracing paper where the tail of the 60 minute and 120 minute size distributions are the broadest compared to all of the other distributions and are the only one that appear to reach sizes of $100\ \mu\text{m}$ in diameter without any gaps.

I characterize the broadening of the size distributions by calculating the mean diameter of the GUVs as a function of time (Figure 88g). Since the size distributions broaden for each of the substrates with increasing stopping time, the mean diameter also increases with stopping time. As expected this increase in mean diameter is largest for the tracing paper samples which broaden the most with increasing stopping time. Figure 88h shows the instantaneous mean diameter, which is just the rate of change of values from the mean diameter plot. The plot shows that the rate of increase of the mean diameter of the GUVs from all of the samples is mostly similar around $0.1\ \mu\text{m}$ per minute during the first 10 minutes and then remains mostly constant at $0\ \mu\text{m}$ per minute after 30 minutes.

5.1.3 Highest yields of GUVs reached within one hour for all substrates

Rationalizing the observed dynamics of the buds at the surface using the budding and merging model, the process of bud merging can be described using three supplementary mechanisms. The first mechanism is when nanobuds merge together with other nanobuds to form micrometer-scaled buds. This process results in the rapid emergence of the more than 1 million micrometer-scaled buds that can be harvested within the first minute from a typical sample. The emergence of new micrometer-scaled buds is also observed in time lapse images during the first 60 minutes of hydration (Figure 85). The second mechanism is when a nanobud merges with micrometer-scaled bud. This process results in the bud

growth in the absence of any observable merging events that is commonly observed during the first 60 minutes of hydration (Figure 85). The last mechanism is when a micrometer-scaled bud merges with another micrometer-scaled bud. This process is often described in literature as coarsening of the buds^{32,101} and is the most common dynamical phenomena observed during the first 60 minutes of hydration (Figure 80).

To characterize the dynamics of nanobud-nanobud merging a higher spatiotemporal resolution than is currently feasible would be needed^{123–125}. Quantitative metrics such as the amount of lipid (molar yield) that converted to nanobud could be measured by preserving the small unilamellar vesicles (SUVs) that are produced and characterizing the SUV populations. Challenges using these techniques arise, as addressed in Chapter 2, due to the presence of other non-unilamellar lipid structures as well as the losses of vesicles that are unavoidable during sample preparation. However, quantification of the amount of lipid (molar yield) that converted into buds due to nanobud-microbud and microbud-microbud merging is more straightforward since both mechanisms result in GUVs that can be quantified using the confocal microscopy tilescan methods developed in Chapter 2. Since the molar yield directly corresponds to the amount of lipid in GUVs, which corresponds to the amount of microbuds that emerge, the molar yield provides a quantitative metric on the amount of nanobud-microbud merging that occurs for a sample. Differences in the amount of microbud-microbud merging that occurs only results in changes in the size distributions. In addition to providing a key insight into quantifying the amount of nanobud-microbud, quantification of the molar yield also makes direct comparisons of the yields obtained from different stopping times, as well as from the different substrates, much more clear in contrast to analyzing the size distributions which often are difficult to compare.

I report the molar yield data obtained from the stopped-time experiments in Figure 89. The area plots show the average molar yield of GUVs produced from the glass, electroformation, and tracing paper substrates as a function in time. Each point is an average of 3 samples (same samples as Figure 88) and the error bars show one standard deviation of the mean. Each area plot is divided into three subsections that show portion of the total molar yield that is comprised of i) the small GUVs that have diameters between $1 \mu\text{m} \leq d < 10 \mu\text{m}$ (dark blue), ii) the large GUVs that have diameters between $10 \mu\text{m} \leq d < 50 \mu\text{m}$ (light blue), and iii) the very large GUVs that have diameters greater than $50 \mu\text{m}$ (white). The molar yield of the GUVs produced from the glass increases slightly with stopping time going from $11.7 \pm 1.7 \%$ at 1 minute, $13.0 \pm 2.3 \%$ at 10 minutes, $12.2 \pm 2.7 \%$ at 30 minutes, $15.5 \pm 1.4 \%$ at 60 minutes and to $16.0 \pm 1.7 \%$ at 120 minutes. The molar yield of the GUVs produced from electroformation increases significantly with stopping time going from $9.2 \pm 1.1 \%$ at 1 minute, $10.9 \pm 2.0 \%$ at 10 minutes, $16.1 \pm 4.8 \%$ at 30 minutes, $22.4 \pm 1.4 \%$ at 60 minutes and to $21.7 \pm 1.2 \%$ at 120 minutes. The molar yield of the GUVs produced from tracing paper increases the most dramatically with stopping time going from $13.4 \pm 1.2 \%$ at 1 minute, $24.8 \pm 2.7 \%$ at 10 minutes,

$31.0 \pm 1.4 \%$ at 30 minutes, $31.3 \pm 1.7 \%$ at 60 minutes and to $31.2 \pm 1.4 \%$ at 120 minutes.

For all three surfaces the average molar yield of GUVs reaches a peak within 60 minutes and does not increase significantly after. These results for each surface are in excellent agreement with the average molar yield data collected in Section 4 (collected at 120 minutes). In addition, for all three surfaces the average molar yields at the earliest, 1 minute, time point are all similar at around 10 %. This result is in agreement with the size distributions at the 1 minute time point (Figure 88) which were similar and suggests that there is likely some commonality shared between the hydration of the lipid films on hydrophilic surfaces devoid of large pores. This hydration process appears to drive the formation of approximately 10 % of the yield of giant vesicles as long as the surface is hydrophilic and devoid of large pores.

After the first minute of hydration, the average molar yields from glass remain relatively constant increasing by no more than 5 %. This result suggests that the emergence of new micrometer-scaled buds after the initial hydration of the film is rare. The average molar yields from electroformation however, climb steadily increasing by more than 10 % over the course of 60 minutes before stabilizing at around 22 % for the 60 minute and 120 minute time points. The average molar yields from tracing paper climb rapidly increasing by around 20 % within the first 30 minutes before stabilizing at around 31 % for the 30 minute, 60 minute and 120 minute time points. Thus, the emergence of new micrometer scaled buds appears to become more rare after the first 60 minutes on the electroformation surface and after the first 30 minutes on the tracing paper surface. In addition, since the molar yield directly correlates to the amount of nanobuds that merge into micrometer-scaled buds, these results suggest that the effects of the electric-field appear to drive the formation of around 10 % more nanobuds on the surface and the effects of the nanoscale curvature of the fibers appear to drive the formation of around 20 % more nanobuds on the surface.

Since the area plots indicate the percentage of the total molar yield that comes from small and large GUVs, the amount of micrometer-scaled bud merging, or coarsening, that occurs can also be understood. Most simply, coarsening of the buds can be observed in the molar yield plot as a widening in the portion of the large GUVs (light blue and white) compared to the small GUVs (dark blue) when moving from left to right. For glass, the area occupied by the large GUVs widens slightly after 10 minutes and then stays relatively constant over the course of 120 minutes increasing slightly between the 30 minute and 60 minute time points. This result suggests that the majority of the coarsening that occurs on glass happens within the first 10 minutes and becomes less prominent with time. From the electroformation plots it is clear that the area occupied by the large GUVs widens constantly over the course of 120 minutes reaching the largest percentage of the molar yield at the 120 minute point. This result suggests that coarsening continues during the course of 120 minutes as a result of the electric-field. The area occupied by the large GUVs in the

tracing paper plots widens over the course of 60 minutes and then appears to stabilize at 120 minutes suggesting that coarsening occurs for around 60 minutes as a result of the nanoscale curvature of the substrate and then slows down significantly at around 60 minutes.

The relationship between the percentage of the molar yield occupied by the large GUVs from the total molar yield is shown in scatter plots in Figure 89d–f. The arrows connect the data between each stopping time point and the x and y error bars at each point show the standard deviation from the mean ($N = 3$). Points above the gray dashed line show samples that have more than half of the total lipid (molar yield) contained in in large GUVs. The scatter plots supplement the data from the area plots emphasizing the time points where coarsening is apparent as any movement up along the y-axis, and emphasizing the time points where the amount of new emerging micrometer-scaled buds is apparent as any

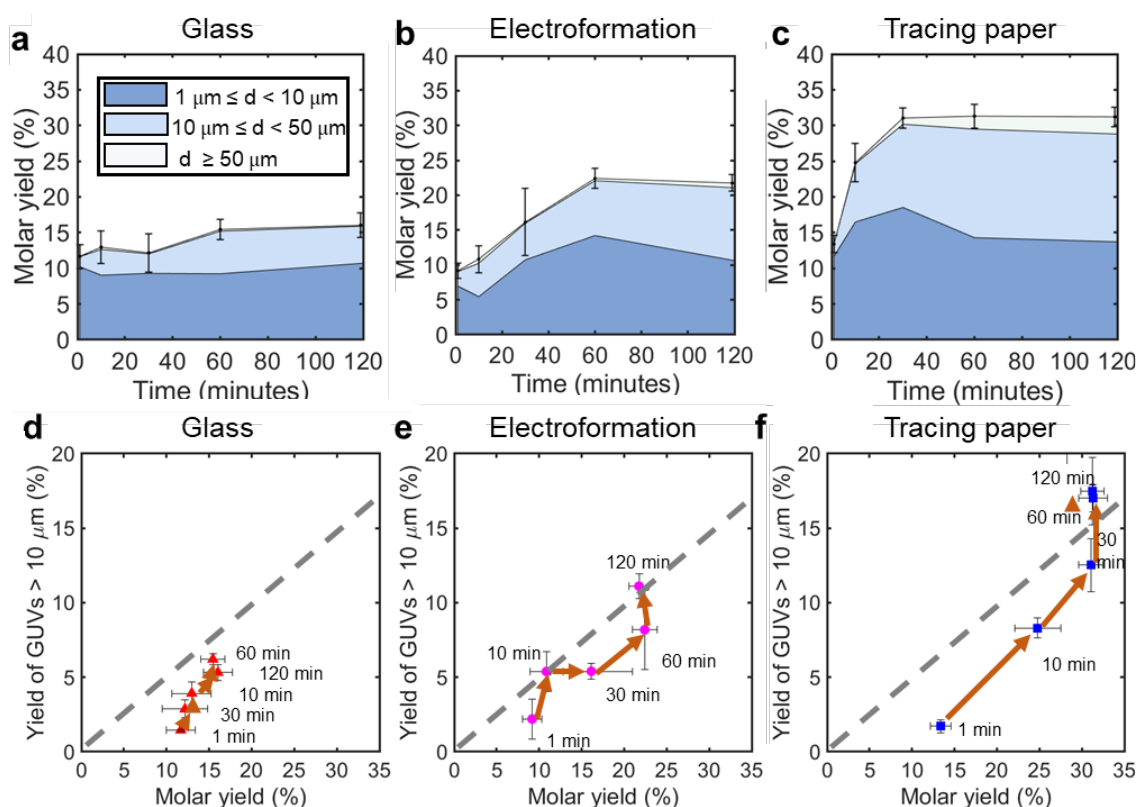


Figure 89: Effect of stopping time on molar yield and coarsening of vesicles. a-c Area plots showing the average molar yield from 3 replicate samples harvested from a glass, b electroformation, and c tracing paper surfaces at 1 minute, 10 minutes, 30 minutes, 60 minutes and 120 minutes of incubation. The error bars show one standard deviation of the mean. The colors of the plots show the percentage of the molar yield that is comprised from the different size classifications listed in the label. d-f Scatter plots showing the average percentage of the molar yield from large GUVs (sizes greater than $10 \mu\text{m}$) versus the

average total molar yield for the **d** glass, **e** electroformation, **f**, and tracing paper surfaces. Points above the gray dashed lines are points where more than 50 % of the molar yield comes from large GUVs. The arrows show the sequential organization points from each sample. The x and y error bars show one standard deviation from the mean.

movement along the x-axis. In agreement with the area plots, the scatter plots show for the glass, electroformation and tracing paper surfaces that the emergence of new buds ends at around 10 minutes, 60 minutes and 30 minutes for each substrate respectively and the coarsening of buds ends at around 60 minutes, 120 minutes, and 60 minutes for each substrate respectively. Additionally, the scatter plots show that amount of lipid present in large GUVs compared to the total amount in GUVs never reaches more than half on the glass surface, while for electroformation and tracing paper it reaches more than half at around 120 minutes and 60 minutes respectively.

5.1.4 Budding and merging process is diffusion-limited

To explain the results from the dynamic molar yield data, I show schematically the effect of the emergence of a higher number of nanobuds on the amount of GUVs produced in a diffusion-limited model (Figure 90). Starting with the glass surface, nanobuds emerge as a result of the exogenous energy input from hydration. These nanobuds, which are depicted in the magnified view of the surface (dashed lines), merge when they are close enough in proximity (arrows) to form microbuds that can emerge within the first minute of hydration. Note that since the buds are in the nanoscale and the lipid film behaves as a liquid laterally, the buds are expected to be able to diffuse as well following Brownian motion. The growth of microbuds as a result of nanobuds merging into microbuds and the coarsening as a result of microbuds merging with other microbuds is also depicted. When the number of nanobuds decreases to low enough numbers that the nanobuds are not close enough in proximity to merge together by diffusion, new micrometer-scaled buds stop emerging. On the electroformation and tracing paper surfaces a similar number of nanobuds are expected to emerge from the exogenous energy input from hydration (red buds). However, an additional number of nanobuds are also expected to emerge due to the energy inputs from the electric field and the curvature of the fibers (green buds). The additional buds that emerge due to the effects of the electric field are fewer in number compared to the additional buds that emerge due to the effects of curvature. Similar to glass, the buds from the electroformation and tracing paper surfaces merge together until there are not enough buds close in proximity to merge. The additional nanobuds produced initially by the two substrates result in more micrometer-scaled buds, with the most micrometer-scaled buds being produced by the tracing paper.

The data from the stopping time experiments can also be used to optimize the GUV formation methods to obtain specific populations of GUVs. A scalable example of this is to produce populations of GUVs that mimic the membrane size characteristics of red blood cells. Table 11 shows the average counts of red blood cell sized GUVs ($5.0 \mu\text{m} - 5.9 \mu\text{m}$)

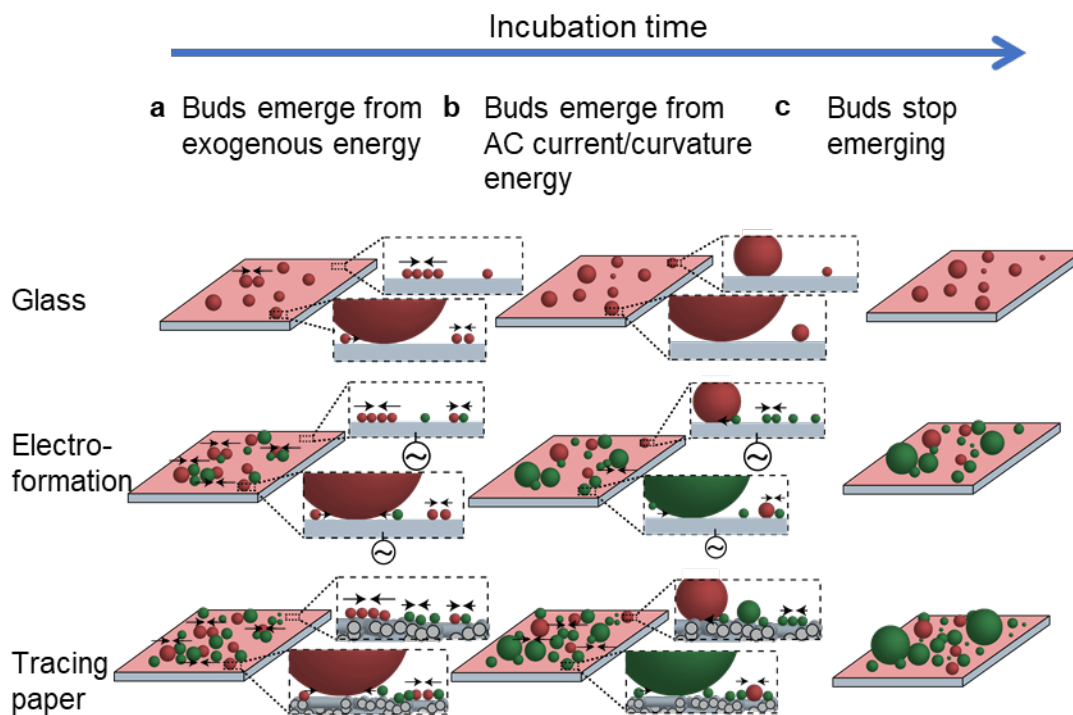


Figure 90: Diffusion limited budding and merging model. Schematic showing the evolution of the buds on the glass (top), electroformation (middle) and tracing paper (bottom) as predicted by the budding and merging model. **a** Initially after hydration buds emerge from the exogenous energy input during hydration of the lipids (red). A magnified view of an empty region of the surface on the glass (dashed box at top) reveals the formation of nanobuds which can diffuse and merge together if close enough (arrows). **b** Application of an electric field (AC symbol in middle) result in more nanobuds (green) from electroformation. Curvature energy of fibers results in even more nanobuds on tracing paper. **c** Once buds are far apart and limited by diffusion the system reaches equilibrium.

produced from the glass, electroformation, and tracing paper surfaces at the different incubation times tested. The counts on glass appear to increase slightly with time, while the counts from electroformation and tracing paper appear to peak at around 60 minutes and 30 minutes respectively and then fall back down due to coarsening. The highest counts of $5\ \mu\text{m}$ sized GUVs can be obtained on tracing paper over the course of a 30 minute incubation. However, since in a practical scale-up problem, samples prepared with shorted incubation times can be repeated multiple times within the same time frame needed by the longer incubation time, I also show the amount of $5\ \mu\text{m}$ GUVs that are produced per minute for each sample. For all three samples the highest amount of $5\ \mu\text{m}$ GUVs produced per minute occurs in the 1 minute samples (orange) with the total highest amount being produced from the tracing paper surface at 1 minute. Along with being able to optimize

Average counts of red blood cell-sized GUVs (5 μm bin)						
Stopping time (minute)	Glass	Glass (per minute)	Electro-formation	Electro-formation (per minute)	Tracing paper	Tracing paper (per minute)
1	3.49E+04	3.49E+04	2.78E+04	2.78E+04	5.16E+04	5.16E+04
10	3.64E+04	3.64E+03	3.53E+04	3.53E+03	7.42E+04	7.42E+03
30	3.55E+04	1.18E+03	3.82E+04	1.27E+03	8.13E+04	2.71E+03
60	3.63E+04	6.06E+02	4.88E+04	8.14E+02	5.83E+04	9.72E+02
120	4.44E+04	3.70E+02	3.43E+04	2.86E+02	5.70E+04	4.75E+02

Table 11: Counts of red blood cell-sized GUVs. Table showing a prototypical example of the time required to produce red blood cell sized GUVs. The first column shows which row corresponds to which stopping time for each of the consequent columns. The second and third columns show the average total number of counts of GUVs and the average normalized number of counts per minute (second column divided by first column) for glass. The next four rows show the electroformation counts and normalized counts and tracing counts and normalized counts respectively. The boxes colored in orange show the highest average counts of red blood cell-sized GUVs that can be obtained in each minute from each technique.

features of the size distributions, information on the incubation times necessary to maximize the yields of GUVs from the different surfaces was also determined from the stopping time data. Using the fits to the data the molar yield was determined to reach a maximum (within 0.5 %) at 21 minutes of incubation time on glass, 50 minutes of incubation time on electroformation, and 24 minutes of incubation time on tracing paper. Knowledge of these parameters allows for the optimization of experimental time without compromising yields.

One remaining question is whether coarsening has a significant effect on the molar yields after 120 minutes. Figure 91 shows bar plots of the molar yields from electroformation and tracing paper at 180 minutes. For the electroformation sample, the molar yield drops slightly where the amount of small GUVs remains relatively constant and the amount of large GUVs decreases slightly. For the tracing paper sample the molar yield also drops slightly, where the amount of small GUVs drops slightly while the amount of large GUVs appears increase slightly. These results confirm that although coarsening may continue after 120 minutes, increasing the incubation time to time points longer than 120 minutes does not result in any significant increase in the molar yields and may result in an overall decrease in the molar yields.

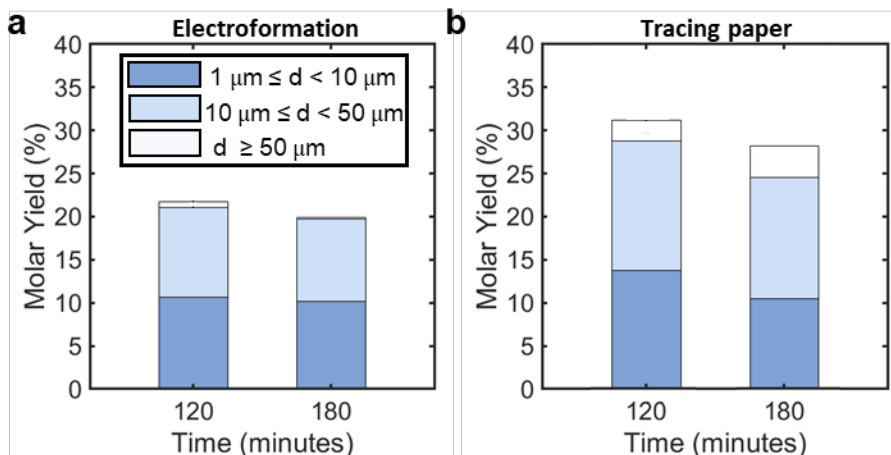


Figure 91: Molar yields at longer incubation times. Molar yield of GUVs obtained after 120 minutes and after 180 minutes of growth on **a** electroformation and **b** tracing paper surfaces. The colors correspond to the amount of the molar yield that comes from the different size classifications of shown in the legend.

5.2 A one-step modulation of the ionic strength results in high yields of GUVs in physiological salt solutions

5.2.1 Physiological concentrations of salts significantly lower the yields of GUVs from surface-assisted assembly techniques

All previous quantitative experiments I conducted on the surface-assisted assembly of GUVs (Sections 3, 4, and 5.1) have been in low salt conditions. Since obtaining physiological concentrations of salts in the aqueous environment on the inside and outside of the GUVs is desirable^{3,12,16,17}, I conduct quantitative experiments to optimize the formation of GUVs in high salt conditions. Figure 92 shows the dramatic effect of adding a commonly used physiological buffer, phosphate-buffered saline (PBS)^{21,34,126,127} directly to the lipid-coated glass and tracing paper substrates at a concentration of 1× PBS (the typical concentration of 1× PBS contains 137 mM NaCl, 2.7 mM KCl, 10 mM Na₂HPO₄, and 1.8 mM KH₂PO₄). The large number of GUV buds that are typically present at the surface during hydration in low salt conditions do not appear at both the glass and tracing paper surface during hydration in 1× PBS. The few GUVs that are observable in the 1× PBS appear to be smaller than around 5 μm in diameter and appear to be less circular. I also observe this result in other physiological buffers such as tris suggesting that the mechanism for GUV formation through surface-assisted assembly is suppressed in physiological concentrations of salts.

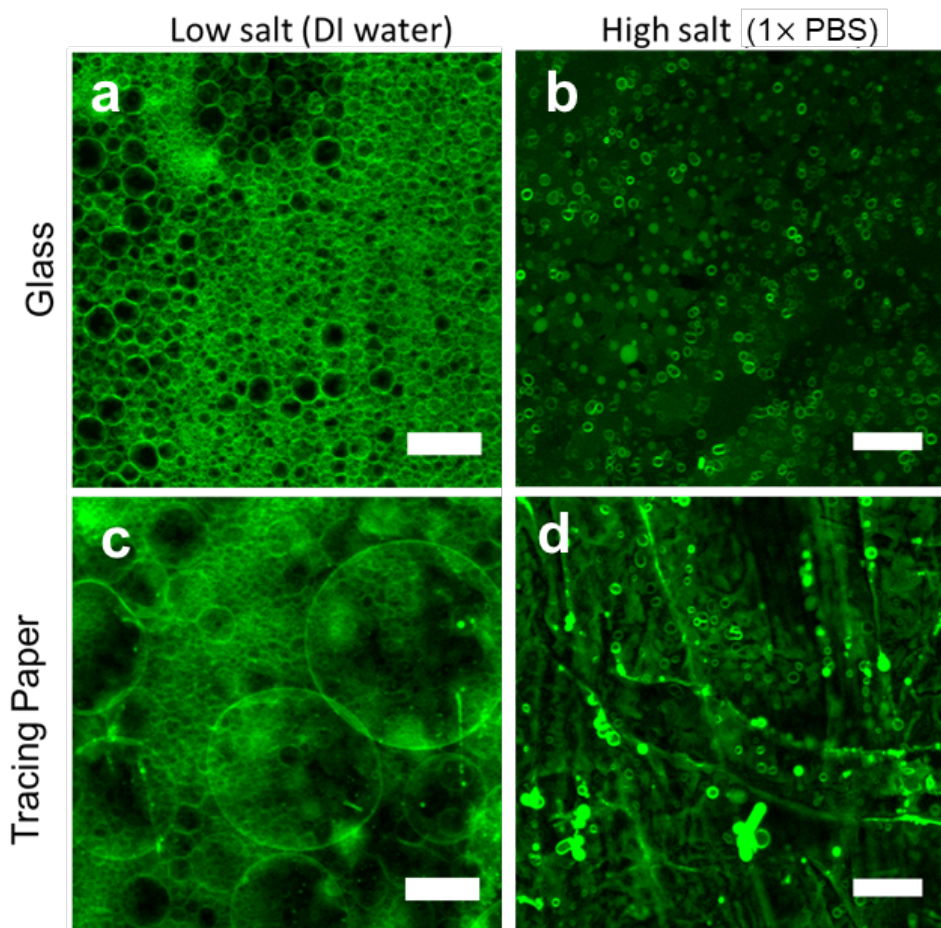


Figure 92: Suppression of formation of GUV buds in physiological concentrations of salts. Confocal images showing representative regions of GUV buds after 2 hours of assembly on **a,b** glass in **a** low salt and **b** high salt conditions and on **c,d** tracing paper in **c** low salt and **d** high salt conditions. Scale bars: **a-d** 25 μm

Referring to the framework offered by the budding and merging model, I expect that the initial emergence of nanobuds is being suppressed due to the presence of physiological concentrations of salts. In section 4, I show on surfaces with fixed geometry that changing the surface chemistry to be hydrophobic results in a significant decrease in yields likely due to the increased adhesion between the membranes^{120,128}. It has also been shown that the adhesion energy of zwitterionic membranes with similar lipid compositions as the compositions I use for quantitative experiments (99.5:0.5 mol % DOPC:TFC) can change in different ionic strength solutions^{8,117,129–131}. Since the zwitterionic DOPC lipid is expected to have a slightly negative surface potential in low salt environments, one possible explanation for the observed suppression of GUV bud formation is that the additional ions in solution cause an electrostatic screening of the negative charges of the membrane^{132–134}. This electrostatic screening could change the adhesion energy of the membrane making the formation of GUVs unfavorable.

To test this hypothesis, I allow the buds to assemble normally in low salt environments for 2 hours on tracing paper. I then add salts and collect images of the buds on the surface during incubation. Figure 93a,b shows the difference between the appearance of the DOPC buds at the surface with and without salts. When the GUV buds are pre-formed and then the $1\times$ PBS is added the GUV buds can be seen adhering strongly together. This is clear since the GUV buds begin to take on non-spherical shapes due to the presence of long, flattening sections where the membranes adhere to one another. One solution to minimize the adhesion of the membranes is to incorporate a small amount of PEGylated lipid (lipid molecule conjugated to a PEG molecule) into the DOPC membrane composition to provide steric repulsion^{88,135,136}. Repeating the experiment with a new lipid mixture that incorporates 3 mol % of a PEGylated lipid molecule (PEG-2000-PE described in the methods section) into the membrane, I find the GUV buds return to their spherical morphologies on the surface and do not adhere to one another with the addition of salts.

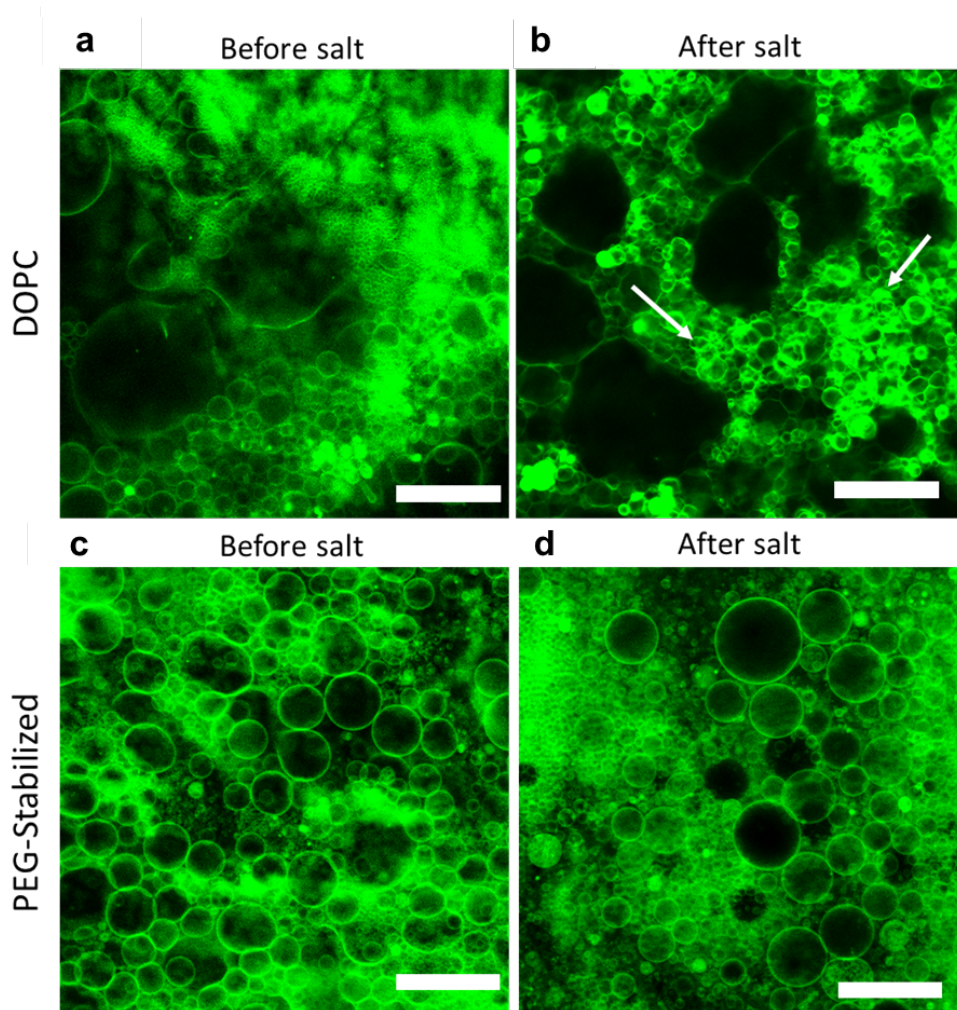


Figure 93: Adhesion between zwitterionic GUV buds in $1\times$ PBS. Confocal images showing representative regions of GUV buds on the tracing paper being assembled from

DOPC membranes **a** before addition of $1\times$ PBS and **b** after addition of $1\times$ PBS. The white arrows indicate the regions where buds appear to become much more tightly packed. The images for the PEG-stabilized membranes are shown in **c** before addition of $1\times$ PBS and **d** after addition of $1\times$ PBS. Scale bars: **a-d** $50\ \mu\text{m}$.

5.2.2 Assembly of GUVs from PEG-modified membranes and anionic membranes in physiological salts

To determine quantitatively the effect of the $1\times$ PBS on the molar yields of GUVs obtained from the glass and tracing paper surfaces, I conduct confocal tilescan experiments to characterize the populations of GUVs obtained through direct hydration in both low salt (sucrose only) and physiological salt ($1\times$ PBS) conditions. I also collect data on the effect of adding 3 mol% of a PEGylated lipid to the membrane on the molar yields from each substrate and salt condition. Figure 94 shows a bar plot of the average molar yields from each of these experiments. The error bars are split to show one standard deviation from the mean from the portion of the molar yield from the small GUVs ($1 \leq d < 10$) and large GUVs ($d \geq 10$). The difference between the low salt and physiological salt conditions is impressive. For the $1\times$ PBS samples where the typical DOPC membrane mixture was used the molar yields were below 1% for both the glass and tracing paper samples resulting in more than a $15\times$ and $30\times$ drop in molar yield. Since all of the other conditions were held

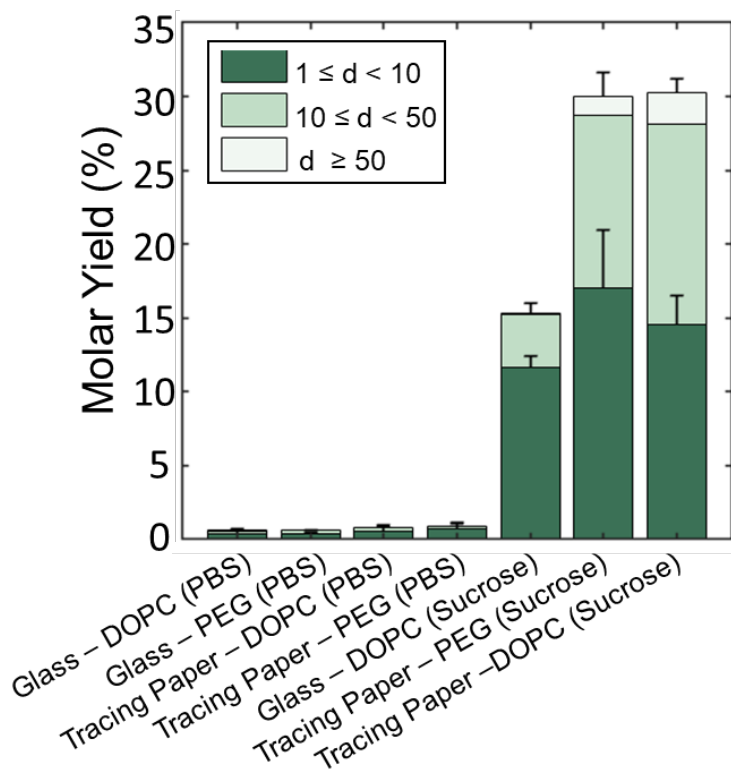


Figure 94: Significant decrease in molar yields of GUVs during formation in physiological salts. Stacked bar plots showing the average molar yield of the GUVs

obtained from the different substrate, buffer and lipid compositions listed. Each bar is an average of 3 replicate samples and the error bars show one standard deviation of the mean. The colors of the bars correspond to the amount of the molar yield that comes from the size classification of GUVs shown in the legend.

constant this result should be due solely to the addition of physiological salts. Although addition of the PEGylated lipid prevented the adhesion between the buds on the surface, it appears the additional steric repulsion is not enough to overcome the increased adhesion of the membranes still on the surface, and the resulting molar yields from the samples where the PEG-modified membrane was incorporated are still low at less than 2 %. Notably, comparing the sucrose tracing paper samples the addition of the PEGylated lipid does not appear significantly change the molar yields. Comparing the portions of the molar comprised of small GUVs however, it appears addition of the PEGylated lipid does slightly increase the number of small GUVs and decrease the number of large GUVs that are produced. This decrease in the amount of large GUVs is likely due to some change in the membrane properties that is caused by the presence of PEG such as the additional repulsion¹³⁷ or even the bending rigidity¹³⁸ which would result in a decrease in the amount of coarsening, but overall the differences are still small.

Since the DOPC GUV membranes clearly adhere to one another on the surface, I perform control experiments before conduction more quantitative experiments to ensure the molar yields are not underreported since adhering GUVs may appear to be aggregates of lipids in the images. Figure 95a-d shows images of GUVs prepared in low salt conditions and then transferred into 1× PBS solutions. Qualitatively the harvested DOPC samples appear to have many bright aggregates and no large GUVs whereas the harvested PEG-modified samples appear more similar to typical low salt harvested images. Adjusting the imaging settings away from the normal tilescan settings to allow investigation of the bright spots in the harvested images, I find the bright spots in the DOPC images are mostly all aggregates of GUVs that are adhered to one another (Figure 95c). The bright spots in the PEG-modified images however, appear to be more typical examples of MLVs and MVVs and do not appear to be aggregates of GUVs. Thus, even when the DOPC GUVs are present in the sample, the 1× PBS concentration results in the aggregation of the GUVs making them difficult to quantify. I estimate the amount of lipid that is stored in bright spots (MLVs, MVVs, aggregates) in Figure 95e and confirm that compared to the low salt conditions, which have around 5 % of the total lipid contained in bright spots, the 1× PBS samples have around 35% of the total lipid contained in bright spots. Interestingly, even for the samples with the PEG-modified membrane the percentage of bright spots also increases compared to the low salt conditions. Overall, however, since adhesion of isolated GUVs does not appear common from PEG-modified membranes I don't expect the molar yield to be underreported due to aggregates of GUVs. Thus, for the quantitative experiments in salts I use the PEG-modified membranes (96.5:3.0:0.5 mol % DOPC:PEG-2000-PE:TFC) instead of the DOPC membranes (99.5:0.5 mol % DOPC:TFC) and from this point on refer to the PEG-modified membrane as the zwitterionic membranes.

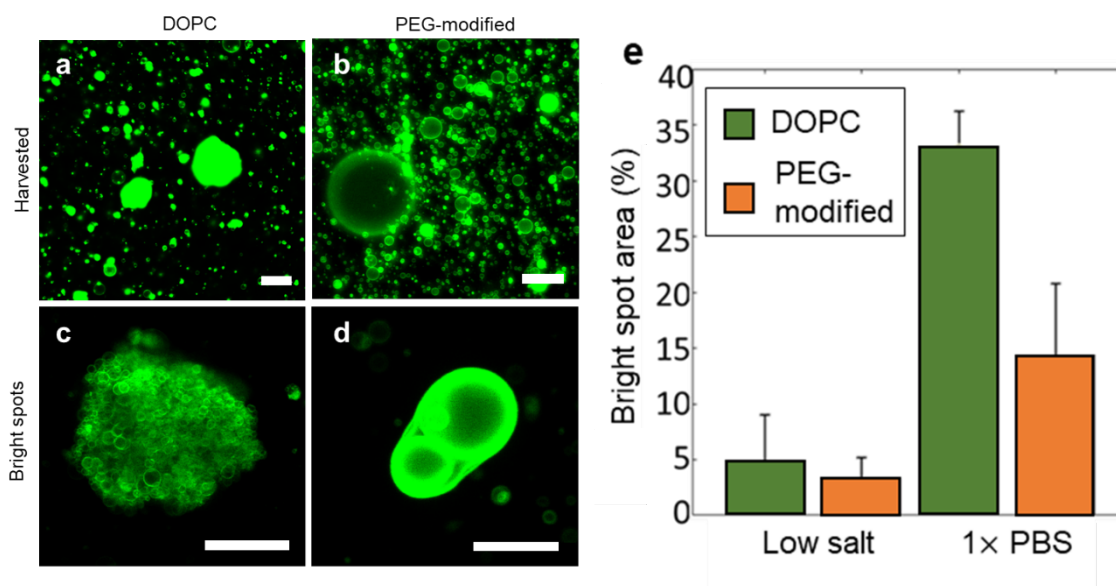


Figure 95: Adhesion between GUVs minimized using PEGylated lipid. **a-d** Confocal images showing the typical sizes and counts of GUVs assembled directly in 1× PBS from **a** DOPC membranes and **b** PEG-modified membranes. **c** The bright spots in the images from DOPC membranes are typically aggregates of GUVs whereas the bright spots in images from PEG-modified membranes are typically **d** MLVs or MVVs. **e** Bar plot showing the percentage of the lipid that is characterized as being too bright by the image analysis code. Error bars show one standard deviation from the mean. The color correspondence is shown in the legends. Scale bars: **a,b** 50 μm , **c,d** 10 μm .

In physiological systems many biological membranes have a significant amount of negative lipids^{139,140}, which may change the electrostatic and adhesive properties of the membranes in physiological concentrations of salts. Along with the zwitterionic membranes, I also prepare anionic membranes with a concentration of 75:25 mol % DOPC:DOPG for quantitative experiments. Control experiments with these anionic membranes indicate that the additional negative charges on the membrane can prevent adhesion of the free-floating GUVs without the need to add PEGylated lipid likely due to an increase in the electrostatic repulsion between the membranes⁸. From control experiments, I also determine that the optimal molar yield that can be produced on tracing paper using the anionic membranes is around 30 %, around the same range as the zwitterionic membranes. One difference however, is to achieve optimal yields, the amount of lipid initially deposited needs to be much higher at 50 μg lipid instead of 10 μg lipid. Since the molar yield metric accounts for differences of lipids initially deposited on the substrates, the plots of anionic and zwitterionic membranes can be read normally and do not require any additional normalization. Similar to the zwitterionic GUVs, the formation of anionic GUVs in 1× PBS is also significantly reduced compared to in low salt conditions (Figure 96).

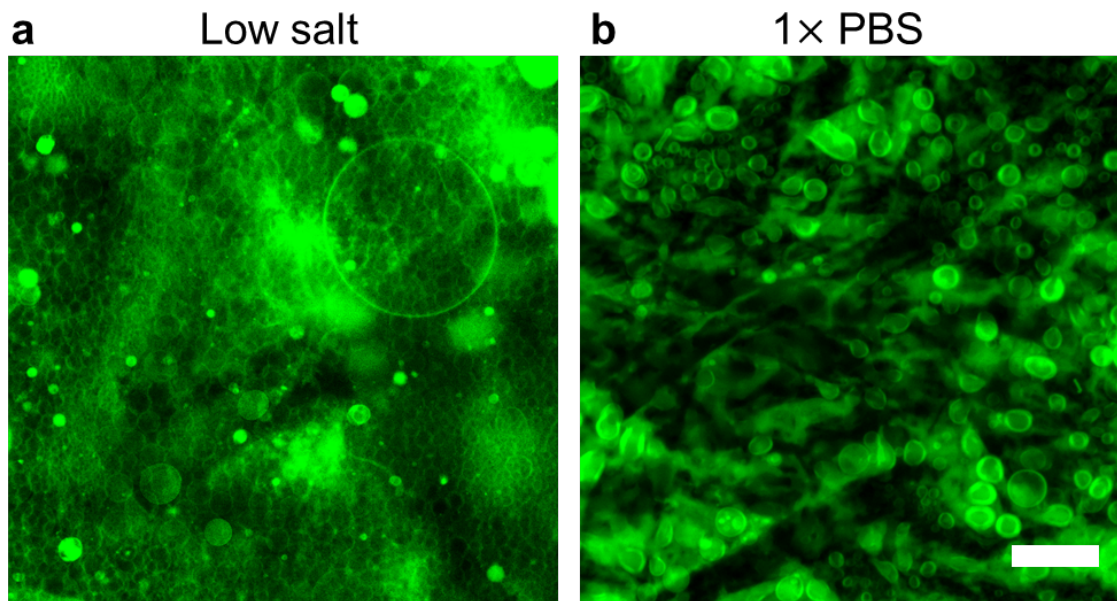


Figure 96: Formation of GUVs from anionic membranes suppressed in physiological salt conditions. Confocal images showing typical appearance of GUVs at the surface of tracing paper assembled from anionic membranes in **a** low salt conditions and **b** 1× PBS. Scale bars: **a,b** 25 μm .

5.2.3 Effect of salt concentration on the molar yields of GUVs

To characterize the concentration range where salts have a significant effect on the molar yield of the GUVs, I design experiments to control the ionic strength of the solution during hydration. Figure 97 shows a scatter plot of the average molar yields as a function of the concentration of ions. Note the logarithmic scaling of the x-axis. The error bars show one standard deviation from the mean from 3 replicate samples at each point, and all samples were prepared and quantified following the standard confocal tilescan procedures (Chapter 2). Using sodium chloride solutions ranging in concentration from 0 mM, 0.14 mM, 0.3 mM, 0.4 mM, 0.65 mM, 1.4 mM, 14 mM, 140 mM, to 1400 mM NaCl, I control the ionic strength of the solution. Starting with the zwitterionic tracing paper sample (orange circles), the average molar yield of the leftmost point at 0.003 mM, which corresponds to the concentration of ions present in ultrapure water due to the pH, is at $30.0 \pm 1.9\%$ which is in good agreement with all previous low salt tracing paper data. Moving from left to right following the orange dashed lines the average molar yields remain constant at 0.14 mM ions at $32.0 \pm 3.4\%$, and then begin to decrease to $28.5 \pm 3.7\%$ at 0.3 mM ions, $24.1 \pm 3.4\%$ at 0.4 mM ions, $20.8 \pm 0.7\%$ at 0.65 mM ions, $13.7 \pm 1.1\%$ at 1.4 mM ions, $6.3 \pm 0.9\%$ at 14 mM, $2.5 \pm 0.6\%$ at 140 mM ions, and to $1.4 \pm 0.8\%$ at 1400 mM ions. The average molar yields from anionic tracing paper samples (green circles) follow an almost identical trend staying relatively constant at $31.2 \pm 3.0\%$ at 0.003 mM ions and $29.7 \pm 2.7\%$ at 0.14 mM ions, and then decreasing to $14.2 \pm 3.8\%$ at 1.4 mM ions, $1.7 \pm 0.8\%$ at 140 mM ions, and $1.0 \pm 0.4\%$ at 1400 mM ions. The average

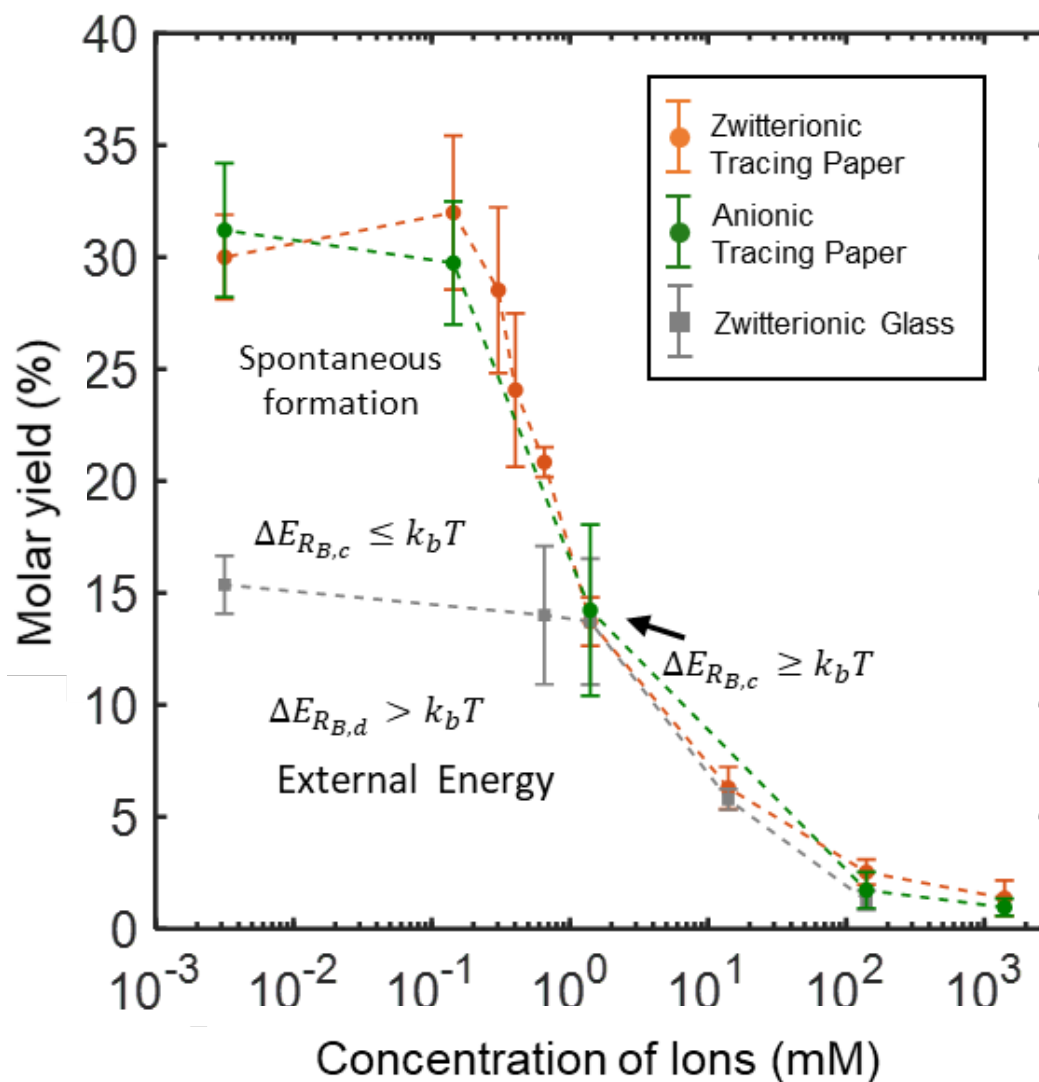


Figure 97: Effect of salts on molar yields. Scatter plot showing the average molar yield of GUVs as a function of the concentration of ions present during the initial hydration. The molar yields were obtained from samples of i) zwitterionic membranes on tracing paper (orange circles), ii) anionic membranes on tracing paper (green circles), and iii) zwitterionic membranes on glass (gray squares). Each point shows an average of 3 replicates and the error bars show one standard deviation from the mean. Note the logarithmic scaling of the x-axis.

molar yields from the zwitterionic glass samples stay relatively constant from 15.4 ± 1.3 % at 0.003 mM ions to 14.0 ± 3.1 % at 0.65 mM ions to 13.8 ± 2.8 % at 1.4 mM ions and then decrease to 5.8 ± 0.5 % at 14 mM ions and 1.3 ± 0.4 % at 140 mM ions.

From ion concentrations of 1 mM and above, the molar yield from all three samples is the same. This result is interesting since the glass appears to behave exactly like tracing paper at these higher ion concentrations supporting the prediction that the favorable formation of buds due to the curvature energy of the substrate ($\Delta E_{R_{B,c}} \leq k_b T$) and the favorable formation of the buds due to the exogenous energy input during hydration are distinct mechanisms. This is because while the yields from the glass samples only start decreasing at concentrations of ions of around 10 mM, the yields from tracing paper appear to start decreasing at concentrations of ions of around 0.4 mM. Corresponding these results to predictions from the budding and merging model, it appears the effect of the ions on the ability for the external energy to produce buds is not significant until around 10 mM ions whereas the effect of the ions on the ability for the curvature energy to produce buds appears to be significant at much lower values of around 0.4 mM ions. The decrease of the molar yields from tracing paper is gradual instead of a sharp cut-off likely since in practice the fibers have a range of sizes that result in a range of different L_c over R_c ratio, and it is not until at around 1 mM ions, where the formation of buds from the curvature energy is positive everywhere ($\Delta E_{R_{B,c}} \geq k_b T$). Additionally, although the electrostatic repulsion between the bilayers is expected to be higher for the anionic membranes compared to the zwitterionic membranes^{8,133}, the difference does not result in a significant shift in the molar yields. I replot the results from these molar yields experiments in stacked area plots in Figure 98 to show the effect of the ionic concentration on the size distributions as well. The higher ionic concentrations appear to decrease the sizes of GUVs overall for all of the samples as observed by a thinning, when moving from left to right along the plots, of the white and light blue regions that show the percentage of the molar yield from the GUVs $\geq 10 \mu\text{m}$. Interestingly, the initial decrease in the sizes of the GUVs appears to precede the decreases in the molar yields of the GUVs for all of the samples.

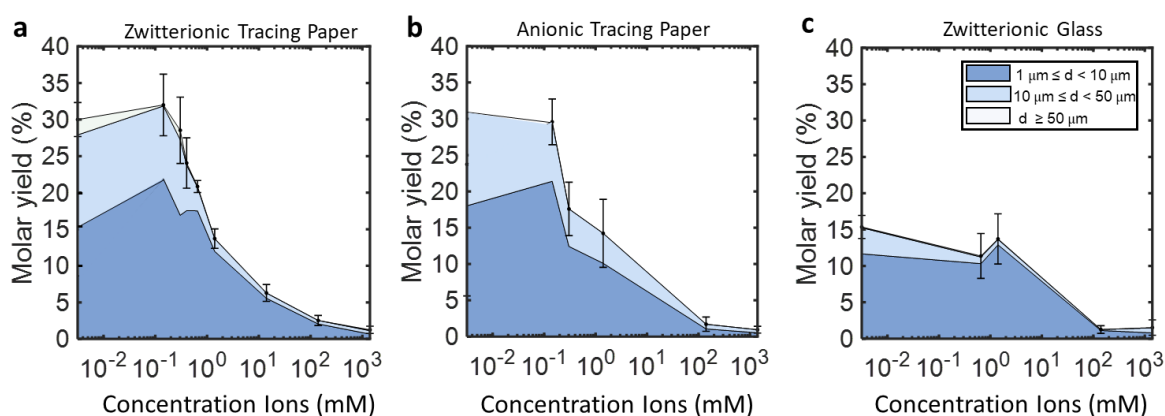


Figure 98: Effect of salts on size breakdown of molar yields. a-c Stacked area bar plots of the a zwitterionic tracing paper, b anionic tracing paper, and c zwitterionic glass data from Figure 97. The colors correspond to the amount of the molar yield that comes from the different size classifications of GUVs shown in the legend.

5.2.4 Novel one-step methods to modulate the ionic strength of the solution

Since the decrease in the molar yields at around 1 mM salts is likely due to the increased adhesion between the membranes, high yields of GUVs in physiological salt solutions may be obtained by modulating the ionic strength of the solution in one step. To develop methods to modulate the ionic strength, I conduct preliminary experiments and find that addition of osmolytes (1× PBS) above the surface of the paper results in lower yields of GUVs than addition below the paper (Figure 99). Considering the potential effects of the additional hydrodynamic flow or the osmotic pressure gradient against the direction of GUV growth from the surface, I develop protocols for the one-step addition of a concentrated salt beneath the paper and show the process schematically in Figure 100.

The one-step modulation process begins with the hydration of the lipid-coated paper in a 142.5 μL solution of low salts in a chamber. After an initial incubation period in low salts, τ_{mod} , a concentrated solution of 7.5 μL of 20× PBS is added beneath the paper. The chamber is then sealed with a glass slide and the sample is allowed to incubate for a total time, τ_{tot} . For the experiments conducted on the effect of the modulation of the salts, the total duration of the time allowed for the assembly of the GUVs is fixed to 1 hour. Once the incubation time is reached, the glass slide is carefully removed and the GUVs are harvested and stored into an Eppendorf tube following normal procedures.

I expect the concentration of the salt to equilibrate throughout the chamber through diffusion. Since, the nanocellulose paper is porous and permeable to ions, and the lipid bilayer coverage is nonhomogeneous likely with defects, I expect the salt to be able to diffuse freely and reach an equilibrium concentration of 1× PBS. To estimate the time for diffusion, I model the system using the one-dimensional diffusion equation¹⁴¹. I use the

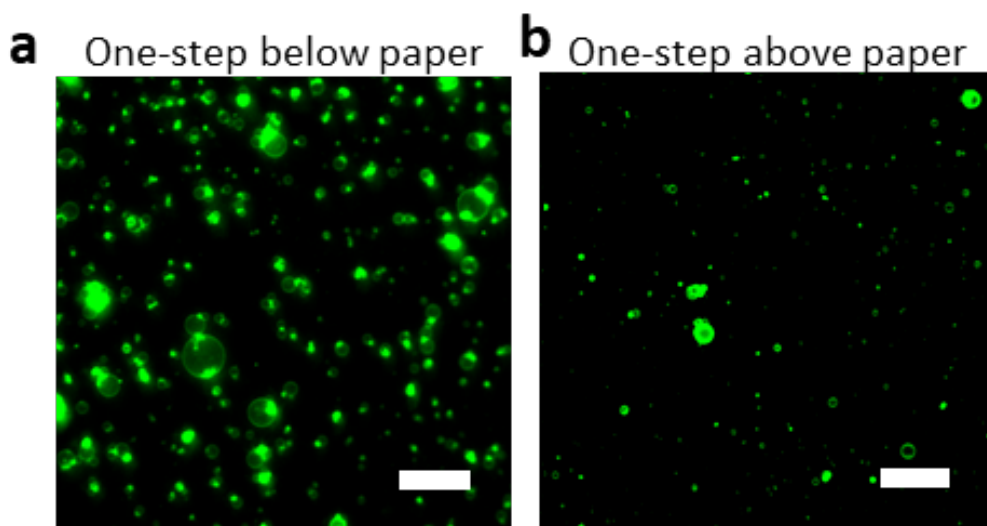


Figure 99: Effect of addition of salts above the paper. Confocal images showing the qualitative differences in the yields of GUVs obtained from the addition of salts **a** below the paper and **b** above the paper. Scale bars: **a,b** 50 μm .

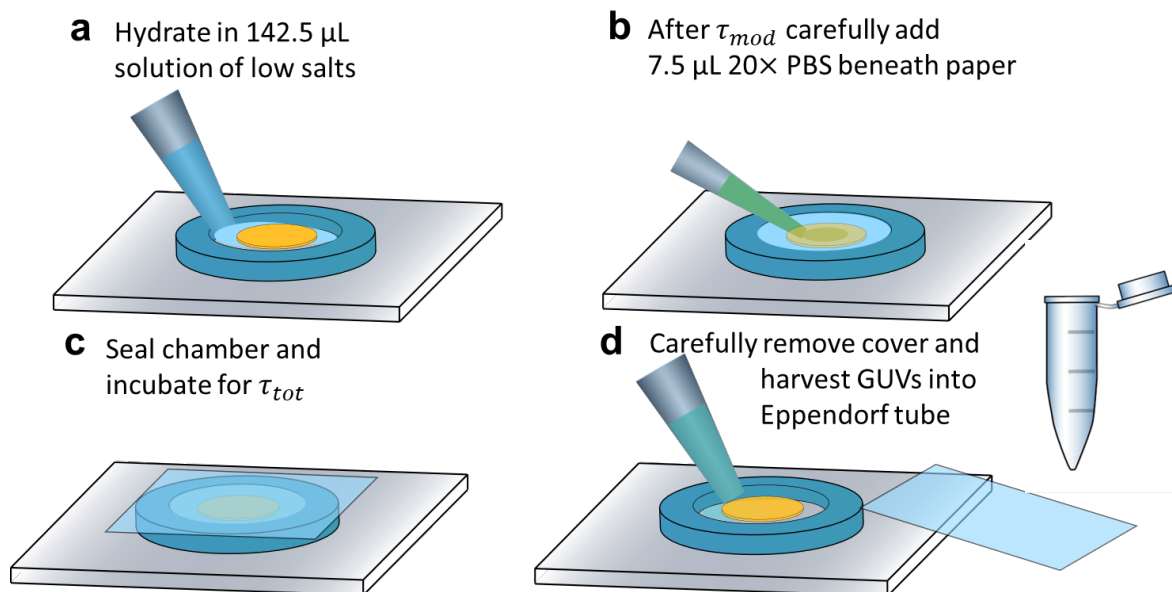


Figure 100: One-step methods to modulate the solution ionic strength. Schematic showing the novel one-step modulation of salts methods where the **a** lipid-tracing paper is placed in a PDMS gasket (same dimensions as the ones used for gentle hydration on glass in the methods section) and hydrated in 142.5 μL low salt buffer. **b** At some time τ_{mod} a concentrated solution of 7.5 μL of 20 \times PBS added beneath the paper. **c** The chamber is sealed and assembly is continue. **d** After 60 minutes the GUVs are harvested and stored in an Eppendorf tube to be taken for imaging.

quasi-steady state approximation, valid for thin membranes where the time for diffusion of the solute across the membrane is much faster than the time for the concentration to change on either side of the membrane, to solve the diffusion equation in one dimension. I set the volume the first chamber, V_1 , equal to 7.5 μL (0.0075 cm^3) corresponding the volume of the concentrated 20 \times PBS added beneath the paper, and I set the volume of the second chamber, V_2 , equal to 142.5 μL (0.1425 cm^3) corresponding the remaining volume where the concentration of PBS is zero (Figure 101). I determine the length of the tracing paper membrane, L_m , from SEM images to be approximately 30 μm (0.003 cm), and set the area, A_m , corresponding to the area of the 9.5 mm diameter disk (0.7088 cm^2). The concentration profile of the quasi-steady state solution is given by Equation 28¹⁴¹

$$C_1(t) = C_0 \frac{V_1}{V_1 + V_2} + C_0 \left(1 - \frac{V_1}{V_1 + V_2} \right) e^{\left[-\left(\frac{A_m D_m \Phi}{V_1 L_m} + \frac{A_m D_m \Phi}{V_2 L_m} \right) t \right]} \quad (28)$$

where C_1 is the concentration of the first chamber, C_0 is the initial concentration of the first chamber, V_1 and V_2 are the volume of the first and second chambers respectively, A_m and L_m is the area and length of the tracing paper membrane, D_m , is the diffusivity constant of

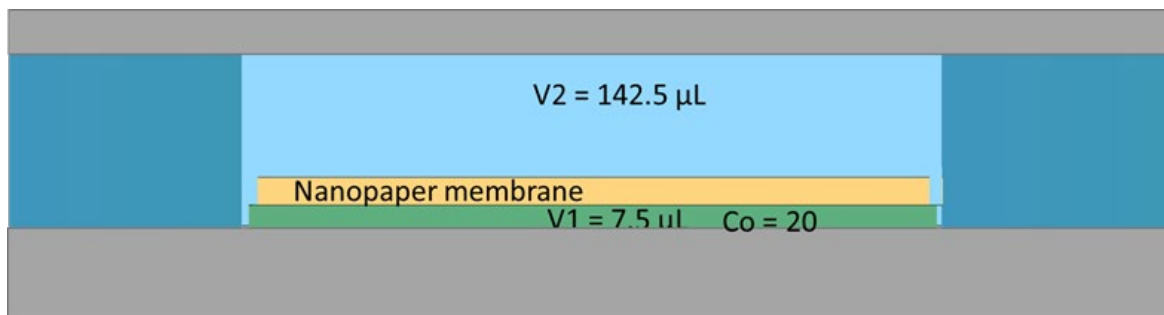


Figure 101: Diffusion of salts through the nanopaper. Schematic showing an idealized model of the diffusion of salts through the nanocellulose paper membrane. Using the quasi-steady state approximation, the system is split into two chambers where one 7.5 μL in volume and has an initial concentration of 20 and the other is 142.5 μL in volume and has an initial concentration of 0.

the solute in the membrane, Φ is the partition coefficient of the solute to the membrane, and t is time. I rearrange and simplify Equation 29 to isolate time, t , which gives

$$t = \frac{-\ln \left[\frac{C_1}{C_0} \left(1 + \frac{V_1}{V_2} \right) - \frac{V_1}{V_2} \right]}{\frac{A_m P}{V_1} \left(1 + \frac{V_1}{V_2} \right)} \quad (29)$$

where P is equal to $\frac{D_m \Phi}{L_m}$ and describes the permeability of the membrane in centimeters per second to the solute. Setting C_1 equal to 1 and C_0 equal to 20, I solve for the time it takes for the system to reach equilibrium as a function of the nanocellulose permeability. Although nanocellulose membranes are often highlighted for their barrier properties in dry conditions, in wet conditions nanocellulose membranes are reported to display similar permeabilities as regular cellulose filter paper^{76,142} and higher permeabilities than regenerated cellulose membranes^{83,143}. I use the values reported from the least permeable cellulose membrane, regenerated cellulose membranes, which are reported to be between $1 \times 10^{-3} \text{ cm s}^{-2}$ ⁸¹ and $1 \times 10^{-4} \text{ cm s}^{-2}$ ¹⁴⁴, and find the time for equilibration of the salts should be between 3 and 30 minutes.

As a control, I also conduct experiments to evaluate the concentration of salts inside the GUVs after harvesting using a sodium sensitive dye, sodium green, that fluoresces in the presence of sodium¹⁴⁵. Figure 102 shows the results of the sodium green experiments. I use a rhodamine-labeled lipid dye to allow visualization of the membrane in the red channel since the sodium green dye is fluorescent in the green channel. From the images, all of the GUVs appear to have the same fluorescence inside their lumens as the outside environment. I measure the fluorescence signal by drawing a line profile through the GUVs in both channels and show the results from measuring four typical GUVs with different sizes in Figure 102d. The fluorescence signal in the red channel has two peaks that mark the edges of the GUVs with the lumen between these peaks. The fluorescence signal in the

green channels remains constant both inside and outside of these peaks suggesting that the concentrations are equal. I repeat this process for 50 randomly chosen vesicles and find that the fluorescence intensity of the lumens is the same as the exterior for all of the vesicles. This result is in agreement with the expectations from the model.

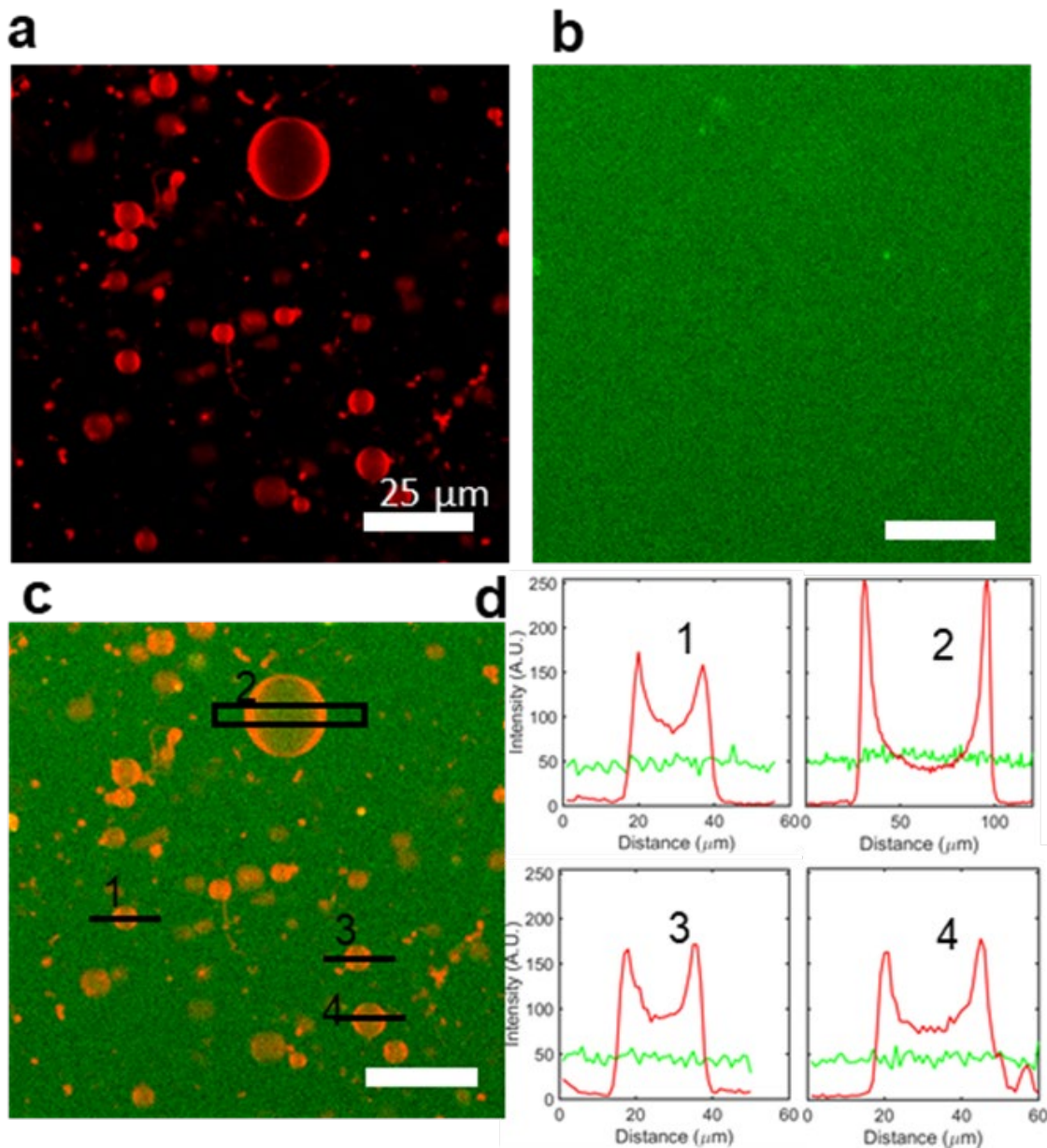


Figure 102: Confirmation of sodium inside the GUVs. a-c False-colored confocal images showing the a red channel, b green channel, and c overlay of both channels of a single image of GUVs assembled using the one-step methods with 1× PBS. The fluorescence signal from the GUV membranes is shown in red and the fluorescence signal of the sodium green indicator is shown in green. d Line profiles showing the fluorescence intensities of the regions marked in black and numbered in c.

5.2.5 One-step modulation of salts experiments

To test the effects of the modulation time on the molar yields of GUVs, I conduct experiments by modulating the time the salt is added τ_{add} . Using a non-dimensional modulation time $\tau_{mod} = \frac{\tau_{add}}{\tau_{tot}}$, I normalize the relationship between the time the salt is added by the total time before harvesting. This allows for a rational inclusion of the conditions when the salt is present in hydration, where $\tau_{mod} = 0$, as well as the conditions when salt is not ever added $\tau_{mod} = 1$. The remaining timepoints that are tested are 1 minute, 5 minutes and 10 minutes after the initial hydration which correspond to τ_{mod} values of 0.02, 0.08, and 0.17 respectively.

Figure 103 shows the effect of the modulation time on the sizes and counts of GUVs obtained from tracing paper. The data is split between experiments conducted from the zwitterionic membranes as well as experiments conducted from the anionic membranes. I collect data from 3 independent replicate samples at each modulation time point. Histograms showing the distribution of sizes from zwitterionic membranes are shown in Figure 103a. Each point represents the average counts from 3 samples normalized by the amount of lipid initially deposited, and the bin widths are $1 \mu\text{m}$. Note the logarithmic scaling of the y-axis. The shading of the colors indicate the modulation time where brighter colors show the earlier modulation times and darker colors show the later modulation times. As expected all of the size distributions have a single peak that is located at $1 \mu\text{m}$ and have a long right tail. The size distributions of the $\tau_{mod} = 0$ and $\tau_{mod} = 0.02$ overlap remarkably closely and appear much more steep with a shorter tail compared to the other distributions. This shape highlights the sharp drop in size and counts of the GUVs due to the addition of salts within 1 minute of hydration. At $\tau_{mod} = 0.08$, the distribution shifts slightly up and to the right, indicating an increase in counts and sizes. Following this same trend, at $\tau_{mod} = 0.17$ the distribution shifts even further up and to the right appearing to overlap completely with the low salt conditions, $\tau_{mod} = 1$. This suggests that the addition of salts after 10 minutes of hydration in low salt conditions results in no differences with the entirely no salt conditions. Figure 103b shows the size distributions from the anionic membranes. The shapes of the distributions are similar but with a more truncated tail than the zwitterionic membranes suggesting that anionic membranes form vesicles with smaller sizes. Compared to the other distributions, at $\tau_{mod} = 0$ the distribution is significantly shifted down and to the left corresponding to the sharp decrease in sizes and counts of GUVs in the presence of salts. Since overall the histograms from anionic membranes have less prominent right tails, even at $\tau_{mod} = 0.02$ corresponding to 1 minute in low salt conditions, the distribution begins to overlap well with the low salt conditions. The other time points $\tau_{mod} = 0.08$, and $\tau_{mod} = 0.017$ appear mostly indistinguishable from the distribution in low salt, $\tau_{mod} = 1$.

The breakdown of the counts between the small (diameters, $1 \leq d < 10$), large ($10 \leq d < 50$), and very large GUVs ($d \geq 50$) is shown for the zwitterionic membranes in Figure 103c and for the anionic membranes in Figure 103d. The average counts are normalized per μg lipid and the error bars show one standard deviation from the mean. The counts from the samples in high salts are colored orange and the counts from the low salt

samples are colored green. For the zwitterionic membranes, the counts of the small vesicles increase steadily with modulation time, starting at 1.2×10^5 small GUVs at $\tau_{mod} = 0$ until reaching 1.1×10^6 small GUVs at $\tau_{mod} = 0.07$. The counts of the large and very large vesicles appear to increase sharply between $\tau_{mod} = 0.08$ and $\tau_{mod} = 0.017$. At $\tau_{mod} = 0.017$ the counts appear to have reached values similar to the low salt conditions at 4×10^4 large GUVs and 150 very large GUVs. For the anionic membranes the counts of the small GUVs also steadily increase from 0.5×10^5 small GUVs at $\tau_{mod} = 0$ to 1.6×10^6 small GUVs at $\tau_{mod} = 0.07$, matching the low salt data. The large GUVs also steadily rise until reaching counts of 2.9×10^4 at $\tau_{mod} = 0.07$. The counts of the very large GUVs remain below 50 for all of the time points.

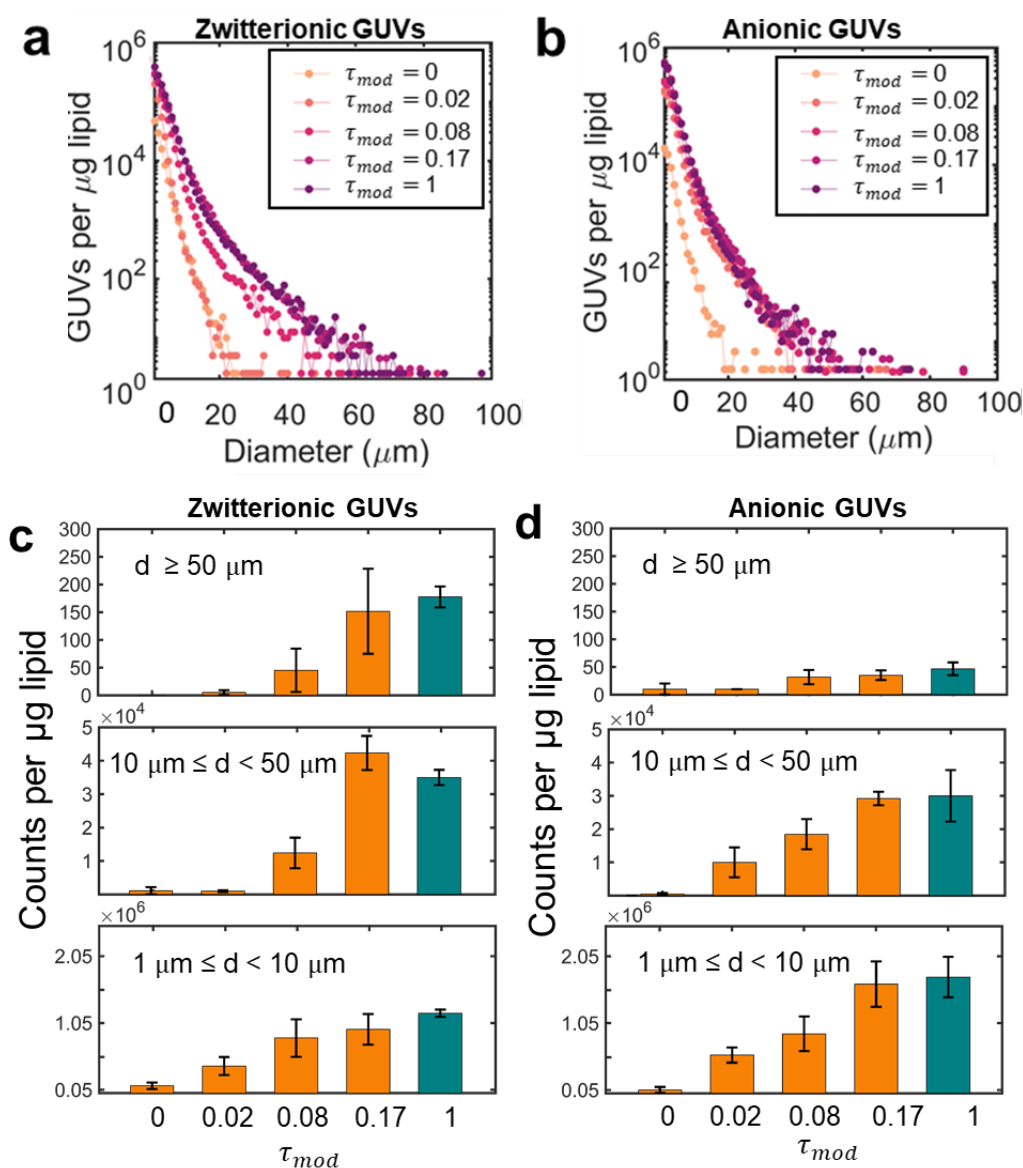


Figure 103: Sizes and counts of GUVs obtained from the one-step modulation of salts experiments. a,b Histograms showing the distributions of sizes of the populations of

GUVs obtained from **a** zwitterionic GUVs and **b** anionic GUVs assembled in $1\times$ PBS using the one-step modulation of salts methods. The various modulation times marked in the legend where the brighter colors indicate the earlier modulation times and the darker colors indicate the later modulation times. Each point represents an average of the counts from 3 replicate samples and is normalized by the amount of lipid deposited. The bin widths are $1\ \mu\text{m}$. Note the logarithmic scaling of the y-axis. **c,d** Plots showing the counts of GUVs normalized by the μg of lipid for the **c** zwitterionic GUVs and **d** anionic GUVs at each of the different modulation times. Samples where salts are added are marked in orange and the samples without salt are marked in green. The plots are split into the counts from each of the size categories labeled in each plot.

I show the stacked bar plots of the molar yield as a function of the modulation time for both the zwitterionic and anionic GUVs in Figure 104. Each bar is split into the small, large, and very large size classifications marked in the legend. The red colors represent the samples with salt added, the blue colors represent the low salt samples. The molar yields of the zwitterionic GUVs increase from $0.6 \pm 0.2\%$ at $\tau_{mod} = 0$, to $7.6 \pm 1\%$ at $\tau_{mod} = 0.02$, to $18.5 \pm 3\%$ at $\tau_{mod} = 0.08$, and then remain constant from $29.3 \pm 4\%$ at $\tau_{mod} = 0.17$ to $31.1 \pm 2\%$ at $\tau_{mod} = 1$. The molar yields of the anionic GUVs trend similarly increasing from $0.8 \pm 0.5\%$ at $\tau_{mod} = 0$, to $11.1 \pm 1\%$ at $\tau_{mod} = 0.02$, to $18.8 \pm 3\%$ at $\tau_{mod} = 0.08$, and then remaining constant from $30.5 \pm 2\%$ at $\tau_{mod} = 0.17$ to $31.2 \pm 2\%$ at $\tau_{mod} = 1$. For the zwitterionic GUVs, the addition of salts any time within the first

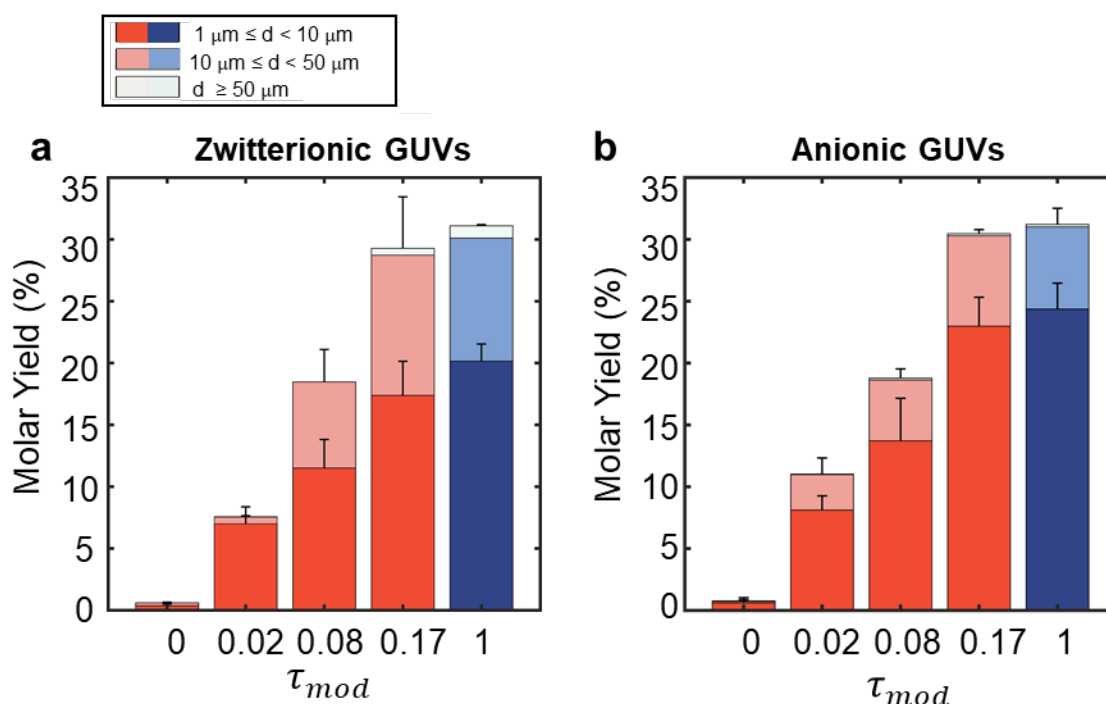


Figure 104: Molar yield of GUVs from one-step modulation of salts experiments. Stacked bar plots showing the average molar yield of GUVs from **a** zwitterionic GUVs and **b** anionic GUVs assembled in $1\times$ PBS using the one-step modulation of salts methods. The

molar yield is plotted as a function of increasing modulation time (τ_{mod}). The red colors indicate the samples that have $1\times$ PBS and the blue colors represent the samples in low salts. Each bar shows the average of 3 samples and the error bars show one standard deviation of the mean. The amount of the molar yield from each size classification of GUVs is marked in the legend.

5 minutes, which correlates to $\tau_{mod} = 0.08$, results in a decrease in the molar yields compared to low salt conditions. This decrease is directly proportional to the time the salt is added with earlier times resulting in lower yields. After 10 minutes of hydration in low salts ($\tau_{mod} = 0.17$), addition of salts does significantly decrease the yields. As a control, I also conduct experiments adding salts at time points after 10 minutes, including at 60 minutes after the initial hydration, and find this also does not lead to a decrease in the yields. The anionic GUVs appear to follow the same trend as the zwitterionic GUVs with the only major difference being that there appear to be fewer GUVs larger than $10\ \mu\text{m}$. Figure 105 shows a plot of the yield of the GUVs larger than $10\ \mu\text{m}$ versus the total molar yield. The blue points represent the zwitterionic GUVs and the red points represent the anionic GUVs. The error bars are 1 standard deviation from the mean. All of the samples fall below the dashed red line which indicates that the less than half of the total molar yield for each sample comes from GUVs larger than $10\ \mu\text{m}$. The final time-addition points ($\tau_{mod} = 0.17$) match closely with the low salt points ($\tau_{mod} = 1$) for both lipid compositions, suggesting that salt does not have an effect on the sizes of the GUVs. Since previous data from DOPC membranes on tracing paper showed a little more than half of the yield came from GUVs with diameters larger than $10\ \mu\text{m}$, likely the PEGylated lipid and negatively charged lipid result in slightly smaller sizes of the GUVs.

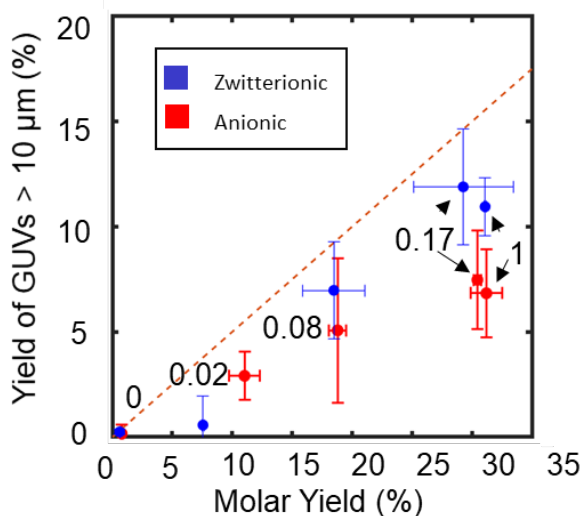


Figure 105: Molar yield of large GUVs. Scatter plot showing the molar yield of the GUVs larger than $10\ \mu\text{m}$ versus the total molar yield. The red dashed line corresponds to half of the molar yield coming from GUVs larger than $10\ \mu\text{m}$. The x and y error bars show one standard deviation from the mean. The zwitterionic GUVs are marked in blue and the anionic GUVs are marked in red. The modulation time is written next to each point.

Overall the molar yield experiments confirm that to obtain high yields of GUVs in physiological salt solutions, the GUV buds need to be allowed a short 10 minute period, τ_{bud} , to emerge. Once this period is reached, concentrated salt solutions can be added beneath the paper and allowed to equilibrate in the solution and do not have any apparent effects on the merging or the sizes of the GUVs compared to entirely low salt conditions. It also appears the suppression of the emergence of buds from the direct addition of high salts is due to increased adhesion between the membranes. I show these three scenarios schematically in Figure 106.

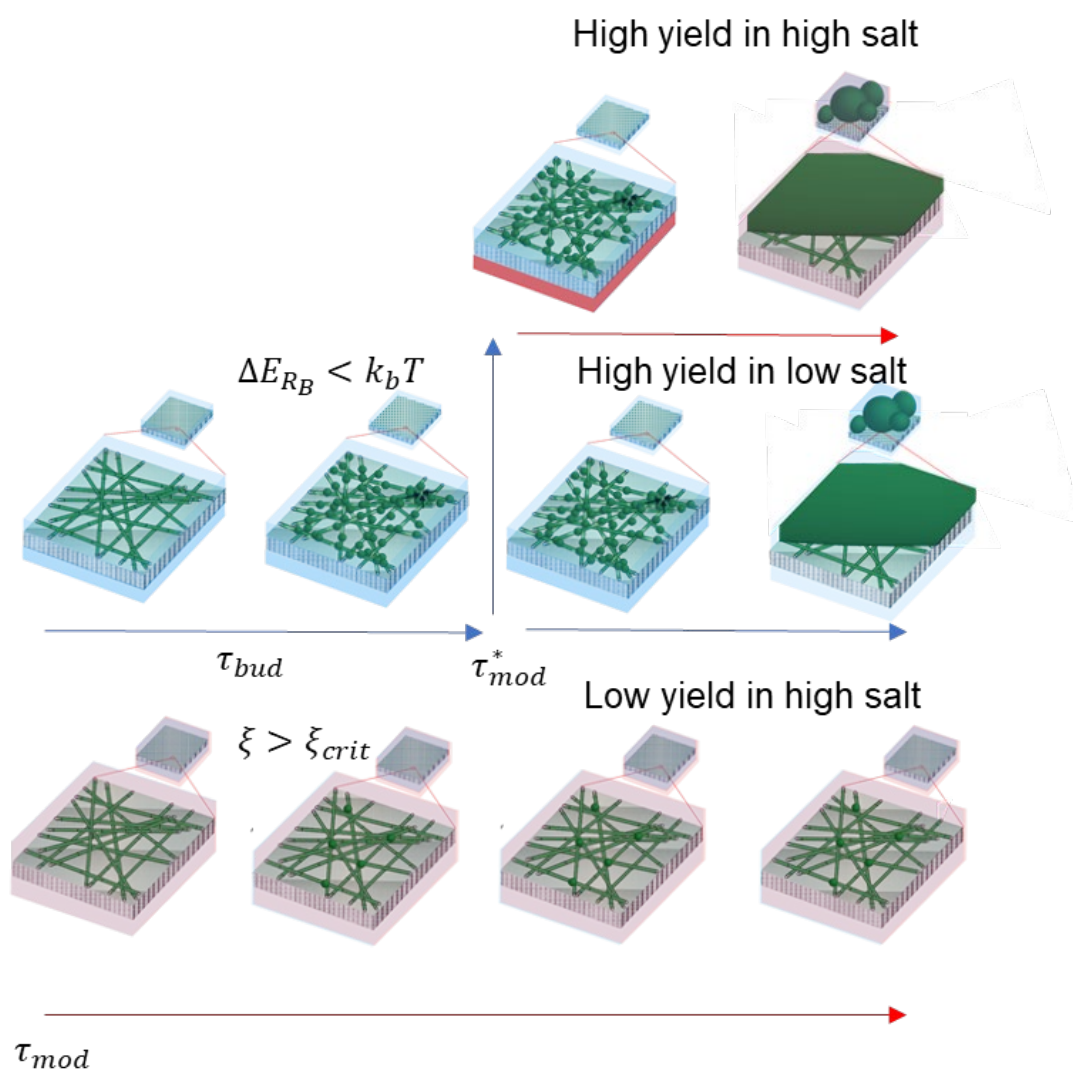


Figure 106: Budding and merging model in salts. Schematic showing the different scenarios of budding and that can occur due to the salts. Starting in the middle row, when the buds are allowed to emerge in the absence of salts high yields can be obtained in low salts (middle right) as well as in high salts through the one-step method (top right). When high salts are added immediately during hydration higher adhesion prevents the formation of buds and leads to low yields in high salts.

5.2.6 One-step tracing paper methods to assemble GUVs are general

With the one-stepped modulation of salts method, a much larger range of different experimental parameters can be used during the assembly of GUVs on tracing paper than previously. For example, Figure 107 shows GUVs assembled in physiologically relevant salt concentrations from various lipid extract mixtures. Lipid extract mixtures are lipid mixtures that are directly from natural membranes^{146,147}. Forming GUVs from lipid extract mixtures in physiological salt solutions allows for the controllable experimentation of more natural-like membrane systems and has resulted in discoveries related to lateral interactions of lipids and as well as membrane protein interactions^{87,146,148}. In addition working with proteins, which are often extremely sensitive to salt conditions^{149–151}, is much more straightforward. Figure 108 shows an example of the incorporation of a salt sensitive globular actin protein into GUVs using the one-step method. In the presence of around 50 mM salts the globular actin which is around 60 kDa in size can polymerize and form micrometer-long filaments of actin¹⁵². Thus, the one-step method allows for the loading of the actin into the vesicles at low salts and then consequent filling of the vesicles with high salts to initiate the polymerization of the actin resulting in the containment of cytoskeleton-like frameworks inside the GUVs.

Figure 109 shows an overview of the generality of the GUVs that can be assembled from tracing paper. Figure 100a shows the high yields that can be obtained in physiological salts using anionic GUVs composed of negatively charged lipids which are found commonly in biological membranes^{140,153}. Figure 109b shows GUVs obtained from phase separating mixtures that contain the lipids 1,2-dipalmitoyl-sn-glycero-3-phosphocholine (DPPC), which has two saturated alkyl chains, DOPC, cholesterol, 1,2-dioleoyl-sn-glycero-3-phosphoethanolamine-N-(lissamine rhodamine B sulfonyl) (Rhod-PE), and the

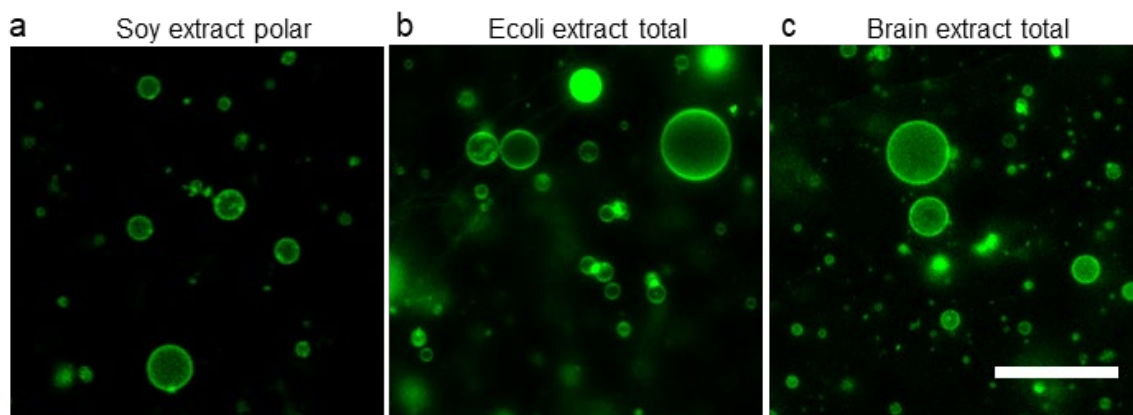


Figure 107: One-step modulation of salts method using tracing paper allows for the assembly of GUVs composed from biologically relevant lipid compositions in physiological salts. a-c Harvested GUVs assembled in physiological salts using the one-step modulation of salts method. The membrane compositions of the GUVs that can be assembled are **a** soy extract polar, **b** E. coli extract total, and **c** brain extract total. Scale bar: **a-c** 50 μm .

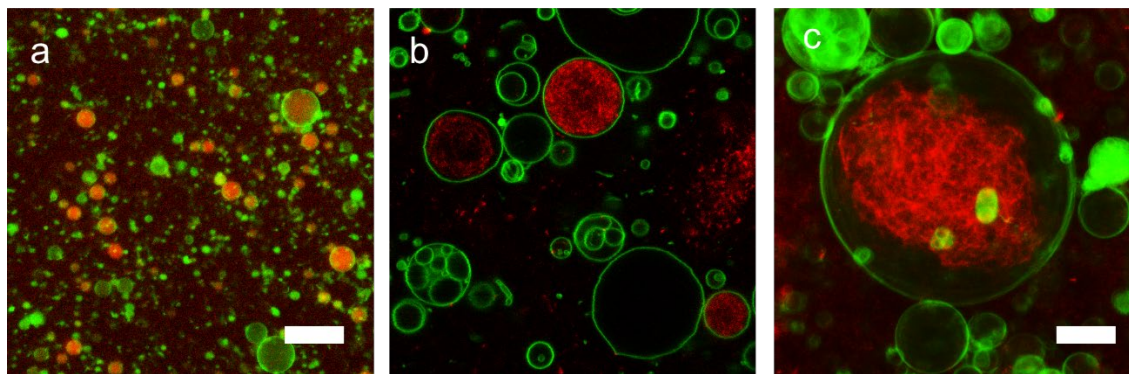


Figure 108: Encapsulation of actin inside GUVs. Confocal images showing a practical use of the modulation of salts method to obtain GUVs encapsulated **a** with globular actin and **b,c** with actin filaments. The images are each false colored with the red channels showing the fluorescence signal from a rhodamine labeled actin and the green channels showing the fluorescence signal of the lipid membrane. Scale bars: **a** 50 μm , **b,c** 10 μm .

ganglioside GM1 at molar ratio of 36:36:27.5:0.25:0.25. When the GUVs are prepared from the tracing paper in solutions while on a hot plate set to temperatures above 40 °C and then quickly cooled to room temperature, the lipids phase separate into coexisting liquid ordered, L_o , and liquid disordered, L_d , domains¹⁵⁴. The coexistence can be easily visualized since the Rho-PE partitions in the L_d phase and the GM1 partitions into the L_o phase. The GM1 although not fluorescent binds with the fluorescently labeled cholera toxin subunit B. Phase separation in GUVs is studied extensively and has aided in the understanding of various membrane related phenomena such the effect the membrane has on protein function and organization in membranes^{140,153}. Lastly, for proteins that can denature in low salt conditions, the one-step tracing paper methods allow for the initial assembly of GUV buds, the loading of buds with proteins in their required high salt conditions, and the harvesting of high yields of protein-filled GUVs. Figure 109c shows the loading of zwitterionic GUVs with a labeled bovine serum albumin (FITC-BSA) protein. The ease, efficiency, and accessibility of the one-step tracing paper methods open avenue for the large-scale production of protein-filled GUVs that could potentially deliver large payloads of drugs¹⁵⁵. In tandem with the confocal microscopy methods, large sample sizes of GUVs containing proteins can be studied over time as containers to carry out biological chemical reactions relevant to creating synthetic cells^{156–159}. Overall the demonstrations shown here are extremely significant since up until now methods to obtain GUVs in physiologically relevant environments are reported to either result in low yields or result in the contamination of the GUVs with osmolytes^{17,42}.

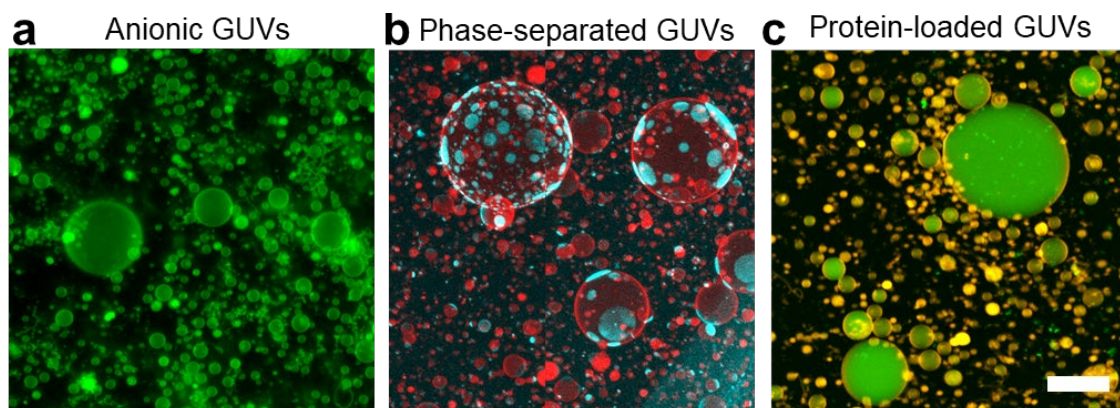


Figure 109: Methods developed to assemble GUVs from tracing paper are general to a wide variety of conditions. Representative confocal images showing the wide variety of GUVs that can be obtained using the novel methods developed and studied in this dissertation including **a** anionic GUVs (green rings), **b** phase-separated GUVs (L_d domains are false colored red and L_o domains are false colored blue), and **c** protein-loaded GUVs (membrane is colored red and protein is colored green). Scale bar: **a-c** 50 μm . Images were published⁴ and reproduced here with permission from the American Chemical Society.

6. Conclusion

Using the novel confocal microscopy methods I developed in Chapter 2, I show the systematic characterization of the populations of GUVs from the most commonly used surface-assisted techniques in Chapter 2. I collect data from ~100,000 GUVs from each different substrate tested and quantitatively compare important features of the populations using metrics including the counts, the distributions of sizes, and the newly introduced metric termed the molar yields. From these quantitative experiments, I show the advantages of using tracing paper over other commonly used methods to assemble GUVs due to the high yields of GUVs that can be produced and the commercial availability of the substrate. Comparing the molar yields from different substrates systematically, I show the molar yield data can be explained using the budding and merging model⁴ that considers the effect that the nanoscale cylindrical fibers at the surface of tracing paper could have on the lipid membrane. I then optimize the assembly of the GUVs from tracing paper studying a variety of different conditions such as the time allowed for assembly and the concentration of salts present during hydration. Finally, I show that high yields of GUVs with various properties such as being composed of anionic lipids or encapsulating proteins, can be obtained in physiological concentrations of salts through a one-step modulation of the ionic strength of the solution during the assembly on tracing paper. The work conducted in this dissertation has resulted in a wealth of information on the process of surface-assisted assembly of GUVs and has open avenues for the large-scale production of GUVs for quantitative biophysical studies and for potential practical applications in drug delivery and synthetic cells.

7. Bibliography

- (1) Wesolowska, O.; Michalak, K.; Maniewska, J.; Hendrich, A. B. Giant Unilamellar Vesicles - a Perfect Tool to Visualize Phase Separation and Lipid Rafts in Model Systems. *Acta Biochim. Pol.* **2009**, *56* (1), 33–39. <https://doi.org/20091772> [pii].
- (2) Dimova, R.; Aranda, S.; Bezlyepkina, N.; Nikolov, V.; Riske, K. a; Lipowsky, R. A Practical Guide to Giant Vesicles. Probing the Membrane Nanoregime via Optical Microscopy. *J. Phys. Condens. Matter* **2006**, *18* (28), S1151–S1176. <https://doi.org/10.1088/0953-8984/18/28/S04>.
- (3) Walde, P.; Cosentino, K.; Engel, H.; Stano, P. Giant Vesicles: Preparations and Applications. *ChemBioChem* **2010**, *11* (7), 848–865. <https://doi.org/10.1002/cbic.201000010>.
- (4) Pazzi, J.; Subramaniam, A. B. Nanoscale Curvature Promotes High Yield Spontaneous Formation of Cell-Mimetic Giant Vesicles on Nanocellulose Paper. *ACS Appl. Mater. Interfaces* **2020**, *12* (50), 56549–56561. <https://doi.org/10.1021/acsami.0c14485>.
- (5) Bangham, A. D.; Standish, M. M.; Watkins, J. C. Diffusion of Univalent Ions across the Lamellae of Swollen Phospholipids. *J. Mol. Biol.* **1965**, *13* (1), 238–252, IN26–IN27. [https://doi.org/10.1016/S0022-2836\(65\)80093-6](https://doi.org/10.1016/S0022-2836(65)80093-6).
- (6) Bagatolli, L. A.; Parasassi, T.; Gratton, E. Giant Phospholipid Vesicles: Comparison among the Whole Lipid Sample Characteristics Using Different Preparation Methods - A Two Photon Fluorescence Microscopy Study. *Chem. Phys. Lipids* **2000**, *105* (2), 135–147. [https://doi.org/10.1016/S0009-3084\(00\)00118-3](https://doi.org/10.1016/S0009-3084(00)00118-3).
- (7) Reeves, J. P.; Dowben, R. M. Formation and Properties of Thin-Walled Phospholipid Vesicles. *J. Cell. Physiol.* **1969**, *73* (1), 49–60. <https://doi.org/10.1002/jcp.1040730108>.
- (8) Akashi, K.; Miyata, H.; Itoh, H.; Kinoshita, K. Formation of Giant Liposomes Promoted by Divalent Cations: Critical Role of Electrostatic Repulsion. *Biophys. J.* **1998**, *74* (6), 2973–2982. [https://doi.org/10.1016/S0006-3495\(98\)78004-X](https://doi.org/10.1016/S0006-3495(98)78004-X).
- (9) Patil, Y. P.; Jadhav, S. Novel Methods for Liposome Preparation. *Chem. Phys. Lipids* **2014**, *177*, 8–18. <https://doi.org/10.1016/j.chemphyslip.2013.10.011>.
- (10) Swaay, D. Van. Microfluidic Methods for Forming Liposomes. *Lab on a Chip* **2013**, *752–767*. <https://doi.org/10.1039/c2lc41121k>.
- (11) Angelova, M. I.; Dimitrov, D. S. Liposome Electroformation. *Faraday Discuss. Chem. Soc.* **1986**, *81*, 303. <https://doi.org/10.1039/dc9868100303>.
- (12) Li, Q.; Wang, X.; Ma, S.; Zhang, Y.; Han, X. Electroformation of Giant Unilamellar Vesicles in Saline Solution. *Colloids Surfaces B Biointerfaces* **2016**, *147*, 368–375. <https://doi.org/10.1016/j.colsurfb.2016.08.018>.

- (13) Angelova, M.; Dimitrov, D. S. A Mechanism of Liposome Electroformation. *Prog. Colloid Polym. Sci.* **1988**, *67*, 59–67.
- (14) Patil, Y. P.; Jadhav, S. Novel Methods for Liposome Preparation. *Chem. Phys. Lipids* **2014**, *177*, 8–18. <https://doi.org/10.1016/j.chemphyslip.2013.10.011>.
- (15) Zhou, Y.; Berry, C. K.; Storer, P. A.; Raphael, R. M. Peroxidation of Polyunsaturated Phosphatidyl-Choline Lipids during Electroformation. *Biomaterials* **2007**, *28* (6), 1298–1306. <https://doi.org/10.1016/j.biomaterials.2006.10.016>.
- (16) Stein, H.; Spindler, S.; Bonakdar, N.; Wang, C. Production of Isolated Giant Unilamellar Vesicles under High Salt Concentrations. *Front. Physiol.* **2017**, *8* (February), 1–16. <https://doi.org/10.3389/fphys.2017.00063>.
- (17) Pott, T.; Bouvrais, H.; Méléard, P. Giant Unilamellar Vesicle Formation under Physiologically Relevant Conditions. *Chem. Phys. Lipids* **2008**, *154* (2), 115–119. <https://doi.org/10.1016/j.chemphyslip.2008.03.008>.
- (18) Morales-pennington, N. F.; Wu, J.; Farkas, E. R.; Lin, S.; Konyakhina, T. M.; Zheng, J. Y.; Webb, W. W.; Feigenson, G. W. Biochimica et Biophysica Acta GUV Preparation and Imaging : Minimizing Artifacts. *BBA - Biomembr.* **2010**, *1798* (7), 1324–1332. <https://doi.org/10.1016/j.bbamem.2010.03.011>.
- (19) Weinberger, A.; Tsai, F. C.; Koenderink, G. H.; Schmidt, T. F.; Itri, R.; Meier, W.; Schmatko, T.; Schröder, A.; Marques, C. Gel-Assisted Formation of Giant Unilamellar Vesicles. *Biophys. J.* **2013**, *105* (1), 154–164. <https://doi.org/10.1016/j.bpj.2013.05.024>.
- (20) López Mora, N.; Hansen, J. S.; Gao, Y.; Ronald, A. a; Kieltyka, R.; Malmstadt, N.; Kros, A. Preparation of Size Tunable Giant Vesicles from Cross-Linked Dextran(Ethylene Glycol) Hydrogels. *Chem. Commun. (Camb).* **2014**, *50* (16), 1953–1955. <https://doi.org/10.1039/c3cc49144g>.
- (21) Horger, K. S.; Estes, D. J.; Capone, R.; Mayer, M. Films of Agarose Enable Rapid Formation of Giant Liposomes in Solutions of Physiologic Ionic Strength. *J. Am. Chem. Soc.* **2009**, *131* (5), 1810–1819. <https://doi.org/10.1021/ja805625u>.
- (22) Lira, R. B.; Dimova, R.; Riske, K. A. Article Giant Unilamellar Vesicles Formed by Hybrid Films of Agarose and Lipids Display Altered Mechanical Properties. *Biophysj* **2014**, *107* (7), 1609–1619. <https://doi.org/10.1016/j.bpj.2014.08.009>.
- (23) Horger, K. S.; Estes, D. J.; Capone, R.; Mayer, M. Films of Agarose Enable Rapid Formation of Giant Liposomes in Solutions of Physiologic Ionic Strength Films of Agarose Enable Rapid Formation of Giant Liposomes in Solutions of Physiologic Ionic Strength. *J.A.C.S.* **2009**, No. 26, 2973–2982. <https://doi.org/10.1021/ja805625u>.
- (24) Deshpande, S.; Caspi, Y.; Meijering, A. E. C.; Dekker, C. Octanol-Assisted Liposome Assembly on Chip. *Nat. Com.* **2016**.

<https://doi.org/10.1038/ncomms10447>.

- (25) Park, Y.; Lee, D.; Park, J. On-Chip Generation of Monodisperse Giant Unilamellar Lipid Vesicles Containing. *Electrophoresis*. **2016**, 1353–1358. <https://doi.org/10.1002/elps.201600035>.
- (26) Hu, P. C.; Li, S.; Malmstadt, N. Microfluidic Fabrication of Asymmetric Giant Lipid Vesicles. *ACS Appl. Mater. Interfaces* **2011**, 3 (5), 1434–1440. <https://doi.org/10.1021/am101191d>.
- (27) Kresse, K. M.; Xu, M.; Pazzi, J.; García-ojeda, M.; Subramaniam A.B. Novel Application of Cellulose Paper as a Platform for the Macromolecular Self-Assembly of Biomimetic Giant Liposomes. *ACS Appl. Mater. Interfaces* **2016**, 8, 47, 32102–32107.
- (28) Li, A.; Pazzi, J.; Xu, M.; Subramaniam, A. B. Cellulose Assisted Assembly and Temporally-Decoupled Loading of Cargo into Vesicles Synthesized from Functionally Diverse Lamellar Phase Forming Amphiphiles. *Biomacromolecules* **2018**. <https://doi.org/10.1021/acs.biomac.7b01645>.
- (29) Robert L. Mason, Richard F. Gunst, J. L. H. *Statistical Design and Analysis of Experiments: With Applications to Engineering and Science*, Second.; Wiley-Interscience: Hoboken, New Jersey, 2003.
- (30) Stephens, M. A. Statistics for Goodness of Fit and Some Comparisons. *J. Am. Stat. Assoc.* **1974**, 69, 730–737.
- (31) Zupanc, J.; Dras, B.; Boljte, S.; Kralj-iglic, V.; Erdogmus, D.; Drobne, D. Lipid Vesicle Shape Analysis from Populations Using Light Video Microscopy and Computer Vision. *PLOS One*. **2014**, 1–14. <https://doi.org/10.1371/journal.pone.0113405>.
- (32) Peruzzi, J.; Gutierrez, M. G.; Mansfield, K.; Malmstadt, N. Dynamics of Hydrogel-Assisted Giant Unilamellar Vesicle Formation from Unsaturated Lipid Systems. *Langmuir* **2016**, 32 (48), 12702–12709. <https://doi.org/10.1021/acs.langmuir.6b01889>.
- (33) Blosser, M. C.; Horst, B. G.; Keller, S. L. CDICE Method Produces Giant Lipid Vesicles under Physiological Conditions of Charged Lipids and Ionic Solutions. *Soft Matter* **2016**, 12, 7364–7371. <https://doi.org/10.1039/C6SM00868B>.
- (34) Lefrançois, P.; Goudeau, B.; Arbault, S. Electroformation of Phospholipid Giant Unilamellar Vesicles in Physiological Phosphate Buffer. *Integr. Biol. (United Kingdom)* **2018**, 10 (7), 429–434. <https://doi.org/10.1039/c8ib00074c>.
- (35) Parigoris, E.; Dunkelmann, D. L.; Murphy, A.; Wili, N.; Kaech, A.; Dumrese, C.; Jimenez-Rojo, N.; Silvan, U. Facile Generation of Giant Unilamellar Vesicles Using Polyacrylamide Gels. *Sci. Rep.* **2020**, 10 (1), 0–10. <https://doi.org/10.1038/s41598-020-61655-2>.

- (36) Akashi, K.; Miyata, H.; Itoh, H.; Kinoshita, K. Preparation of Giant Liposomes in Physiological Conditions and Their Characterization under an Optical Microscope. *Biophys. Journ.* **1996**, *71* (December), 3242–3250.
- (37) Yamashita, Y.; Oka, M.; Tanaka, T.; Yamazaki, M. A New Method for the Preparation of Giant Liposomes in High Salt Concentrations and Growth of Protein Microcrystals in Them. *Biochim. Biophys.* **2002**, *1561* (2), 129–134. [https://doi.org/10.1016/S0005-2736\(02\)00338-3](https://doi.org/10.1016/S0005-2736(02)00338-3).
- (38) Estes, D. J.; Mayer, M. Giant Liposomes in Physiological Buffer Using Electroformation in a Flow Chamber. *Biochim. Biophys. Acta - Biomembr.* **2005**, *1712* (2), 152–160. <https://doi.org/10.1016/j.bbamem.2005.03.012>.
- (39) Montes, L.-R.; Alonso, A.; Goñi, F. M.; Bagatolli, L. a. Giant Unilamellar Vesicles Electroformed from Native Membranes and Organic Lipid Mixtures under Physiological Conditions. *Biophys. J.* **2007**, *93* (10), 3548–3554. <https://doi.org/10.1529/biophysj.107.116228>.
- (40) Tsumoto, K.; Matsuo, H.; Tomita, M.; Yoshimura, T. Colloids and Surfaces B : Biointerfaces Efficient Formation of Giant Liposomes through the Gentle Hydration of Phosphatidylcholine Films Doped with Sugar. *Coll. Surf. Biointer.* **2009**, *68*, 98–105. <https://doi.org/10.1016/j.colsurfb.2008.09.023>.
- (41) Drevon, D.; Fursa, S. R.; Malcolm, A. L. Intercoder Reliability and Validity of WebPlotDigitizer in Extracting Graphed Data. *Behav. Modif.* **2017**, *41* (2), 323–339. <https://doi.org/10.1177/0145445516673998>.
- (42) Has, C.; Sunthar, P. A Comprehensive Review on Recent Preparation Techniques of Liposomes A Comprehensive Review on Recent Preparation Techniques of Liposomes. *J. Liposome Res.* **2019**, *0* (0), 1–30. <https://doi.org/10.1080/08982104.2019.1668010>.
- (43) Aulin, C.; Gällstedt, M.; Lindström, T. Oxygen and Oil Barrier Properties of Microfibrillated Cellulose Films and Coatings. *Cellulose* **2010**, *17* (3), 559–574. <https://doi.org/10.1007/s10570-009-9393-y>.
- (44) Qing, Y.; Sabo, R.; Wu, Y.; Zhu, J. Y.; Cai, Z. Self-Assembled Optically Transparent Cellulose Nanofibril Films : Effect of Nanofibril Morphology and Drying Procedure. *Cellulose.* **2015**, 1091–1102. <https://doi.org/10.1007/s10570-015-0563-9>.
- (45) Herold, C.; Chwastek, G.; Schwille, P.; Petrov, E. P. Efficient Electroformation of Supergiant Unilamellar Vesicles Containing Cationic Lipids on ITO-Coated Electrodes. *Langmuir* **2012**, *28* (13), 5518–5521. <https://doi.org/10.1021/la3005807>.
- (46) Reis, A.; Spickett, C. M. Chemistry of Phospholipid Oxidation. *Biochim. Biophys. Acta - Biomembr.* **2012**, *1818* (10), 2374–2387. <https://doi.org/10.1016/j.bbamem.2012.02.002>.

- (47) Breton, M.; Amirkavei, M.; Mir, L. M. Optimization of the Electroformation of Giant Unilamellar Vesicles (GUVs) with Unsaturated Phospholipids. *J. Membr. Biol.* **2015**, *248* (5), 1–9. <https://doi.org/10.1007/s00232-015-9828-3>.
- (48) Sankhagowit, S.; Wu, S.; Biswas, R.; Riche, C. T.; Povinelli, M. L.; Malmstadt, N. Biochimica et Biophysica Acta The Dynamics of Giant Unilamellar Vesicle Oxidation Probed by Morphological Transitions. *BBA - Biomembr.* **2014**, *1838* (10), 2615–2624. <https://doi.org/10.1016/j.bbamem.2014.06.020>.
- (49) Reis, A.; Spickett, C. M. Chemistry of Phospholipid Oxidation. *Biochim. Biophys. Acta - Biomembr.* **2012**, *1818* (10), 2374–2387. <https://doi.org/10.1016/j.bbamem.2012.02.002>.
- (50) Collins, M. D.; Gordon, S. E. Giant Liposome Preparation for Imaging and Patch-Clamp Electrophysiology. *J. Vis. Exp.* **2013**, No. 76, 1–9. <https://doi.org/10.3791/50227>.
- (51) Faysal, K. M. R.; Park, J. S.; Nguyen, J.; Garcia, L.; Subramaniam, A. B. Lipid Bilayers Are Long-Lived on Solvent Cleaned Plasma-Oxidized Poly(Dimethyl) Siloxane (Ox-PDMS). *PLoS One* **2017**, *12* (1), 1–16. <https://doi.org/10.1371/journal.pone.0169487>.
- (52) Glavan, A. C.; Martinez, R. V.; Subramaniam, A. B.; Yoon, H. J.; Nunes, R. M. D.; Lange, H.; Thuo, M. M.; Whitesides, G. M. Omniphobic “RF Paper” Produced by Silanization of Paper with Fluoroalkyltrichlorosilanes. *Adv. Funct. Mater.* **2014**, *24* (1), 60–70.
- (53) Wada, M.; Nishiyama, Y.; Chanzy, H.; Forsyth, T.; Langan, P. The Structure of Celluloses. **2008**.
- (54) Li, Y.-Y.; Wang, B.; Ma, M.-G.; Wang, B. Review of Recent Development on Preparation, Properties, and Applications of Cellulose-Based Functional Materials. *Int. J. Polym. Sci.* **2018**, *2018*, 1–18. <https://doi.org/10.1155/2018/8973643>.
- (55) Klemm, D.; Kramer, F.; Moritz, S.; Lindström, T.; Ankerfors, M.; Gray, D.; Dorris, A. Nanocelluloses: A New Family of Nature-Based Materials. *Angew. Chemie - Int. Ed.* **2011**, *50* (24), 5438–5466. <https://doi.org/10.1002/anie.201001273>.
- (56) Kontturi, E. Cellulose : Structure , Morphology , and Crystalline Forms. **2015**, No. October, 55.
- (57) Sullivan, A. C. O. Cellulose : The Structure Slowly Unravels. **1997**, 173–207.
- (58) Wang, Y.; Wei, X.; Li, J.; Wang, Q.; Wang, F.; Kong, L. Homogeneous Isolation of Nanocellulose from Cotton Cellulose by High Pressure Homogenization. *J. Mater. Sci. Chem. Eng.* **2013**, *01* (05), 49–52. <https://doi.org/10.4236/msce.2013.15010>.
- (59) Zhao, H.; Kwak, J. H.; Zhang, Z. C.; Brown, H. M.; Arey, B. W.; Holladay, J. E.

- Studying Cellulose Fiber Structure by SEM , XRD , NMR and Acid Hydrolysis. *Carb. Polym.* **2007**, *68*, 235–241. <https://doi.org/10.1016/j.carbpol.2006.12.013>.
- (60) *Cotton: Science and Technology*, 1st ed.; Gordon, S., Hsieh, Y. L., Eds.; Woodhead Publishing: Cambridge, 2007.
- (61) Pazzi, J.; Xu, M.; Subramaniam, A. B. Size Distributions and Yields of Giant Vesicles Assembled on Cellulose Papers and Cotton Fabric. *Langmuir* **2018**, *35* (24), 7798–7804. <https://doi.org/10.1021/acs.langmuir.8b03076>.
- (62) Alava, M.; Niskanen, K. The Physics of Paper. *Reports Prog. Phys.* **2006**, *69* (3), 669–723. <https://doi.org/10.1088/0034-4885/69/3/R03>.
- (63) Ferraz, N.; Leschinskaya, A.; Toomadj, F.; Fellström, B.; Strømme, M.; Mihranyan, A. Membrane Characterization and Solute Diffusion in Porous Composite Nanocellulose Membranes for Hemodialysis. *Cellulose* **2013**, *20* (6), 2959–2970. <https://doi.org/10.1007/s10570-013-0045-x>.
- (64) Bogaty, H.; T., C. F. Measurement of Rate of Flow of Water through Filter Paper. *J. Res. Natl. Bur. Stand. (1934)*. **1944**, *33*, 353–362.
- (65) Huang, C.; Quinn, D.; Sadovsky, Y.; Suresh, S.; Hsia, K. J. Formation and Size Distribution of Self-Assembled Vesicles. *Proc. Natl. Acad. Sci. U. S. A.* **2017**, *114* (11), 2910–2915. <https://doi.org/10.1073/pnas.1702065114>.
- (66) Clauset, A.; Shalizi, C. R. Power-Law Distributions in Empirical Data *. **2009**, *51* (4), 661–703.
- (67) Lasic, D. D. The Spontaneous Formation of Unilamellar Vesicles. *J. Colloid Interface Sci.* **1988**, *124* (2), 428–435. [https://doi.org/10.1016/0021-9797\(88\)90181-6](https://doi.org/10.1016/0021-9797(88)90181-6).
- (68) Best, A. C. The Size Distribution of Raindrops. *Quarterly Journal of the Royal Meteorological Society*. 1950, pp 16–36. <https://doi.org/10.1002/qj.49707632704>.
- (69) Kostoglou, M.; Lioumbas, J.; Karapantsios, T. A Population Balance Treatment of Bubble Size Evolution in Free Draining Foams. *Colloids Surfaces A Physicochem. Eng. Asp.* **2015**, *473*, 75–84. <https://doi.org/10.1016/j.colsurfa.2014.11.036>.
- (70) Teran, A. V.; Bill, A.; Bergmann, R. B. Time-Evolution of Grain Size Distributions in Random Nucleation and Growth Crystallization Processes. *Phys. Rev. B - Condens. Matter Mater. Phys.* **2010**, *81* (7), 1–19. <https://doi.org/10.1103/PhysRevB.81.075319>.
- (71) Letters, E. Truncated Power Laws : A Tool for Understanding Aggregation Patterns in Animals ? *Ecol. Letters* **2000**, 90–94.
- (72) Golmohammadi, H.; Morales-Narváez, E.; Naghdi, T.; Merkoçi, A. Nanocellulose in Sensing and Biosensing. *Chem. Mater.* **2017**, *29* (13), 5426–5446. <https://doi.org/10.1021/acs.chemmater.7b01170>.

- (73) Lu, Z.; Fan, L.; Zheng, H.; Lu, Q.; Liao, Y.; Huang, B. Preparation, Characterization and Optimization of Nanocellulose Whiskers by Simultaneously Ultrasonic Wave and Microwave Assisted. *Bioresour. Technol.* **2013**, *146*, 82–88. <https://doi.org/10.1016/j.biortech.2013.07.047>.
- (74) Mautner, A.; Lee, K. Y.; Tammelin, T.; Mathew, A. P.; Nedoma, A. J.; Li, K.; Bismarck, A. Cellulose Nanopapers as Tight Aqueous Ultra-Filtration Membranes. *React. Funct. Polym.* **2015**, *86*, 209–214. <https://doi.org/10.1016/j.reactfunctpolym.2014.09.014>.
- (75) Wågberg, L.; Decher, G.; Norgren, M.; Lindström, T.; Ankerfors, M.; Axnäs, K. The Build-up of Polyelectrolyte Multilayers of Microfibrillated Cellulose and Cationic Polyelectrolytes. *Langmuir* **2008**, *24* (3), 784–795. <https://doi.org/10.1021/la702481v>.
- (76) Lavoine, N.; Desloges, I.; Dufresne, A.; Bras, J. Microfibrillated Cellulose - Its Barrier Properties and Applications in Cellulosic Materials: A Review. *Carbohydr. Polym.* **2012**, *90* (2), 735–764. <https://doi.org/10.1016/j.carbpol.2012.05.026>.
- (77) Ahola, S.; Salmi, J.; Johansson, L. S.; Laine, J.; Österberg, M. Model Films from Native Cellulose Nanofibrils. Preparation, Swelling, and Surface Interactions. *Biomacromolecules* **2008**, *9* (4), 1273–1282. <https://doi.org/10.1021/bm701317k>.
- (78) Tanaka, M.; Wong, A. P.; Rehfeldt, F.; Tutus, M.; Kaufmann, S. Selective Deposition of Native Cell Membranes on Biocompatible Micropatterns. *J. Am. Chem. Soc.* **2004**, *126* (10), 3257–3260. <https://doi.org/10.1021/ja038981d>.
- (79) Mohan, T.; Kargl, R.; Doliška, A.; Vesel, A.; Köstler, S.; Ribitsch, V.; Stana-Kleinschek, K. Wettability and Surface Composition of Partly and Fully Regenerated Cellulose Thin Films from Trimethylsilyl Cellulose. *J. Colloid Interface Sci.* **2011**, *358* (2), 604–610. <https://doi.org/10.1016/j.jcis.2011.03.022>.
- (80) Navard, P. Rotation and Contraction of Native and Regenerated Cellulose Fibers upon Swelling and Dissolution : The Role of Morphological and Stress Unbalances. *Cellulose.* **2010**, 507–519. <https://doi.org/10.1007/s10570-009-9395-9>.
- (81) Klein, E.; Smith, J. K.; Holland, F. F. Permeability Studies With Hemodialysis Membranes. *Journ. Biomed. Mater. Res.* **1974**, *5*, 423–439.
- (82) Michie, R. I. C. The Fine Structure of Regenerated Cellulose as Revealed by Chemical Swelling. *British Rayon Res. Assoc.* 41–55.
- (83) Bedane, A. H.; Eić, M.; Farmahini-Farahani, M.; Xiao, H. Water Vapor Transport Properties of Regenerated Cellulose and Nanofibrillated Cellulose Films. *J. Memb. Sci.* **2015**, *493*, 46–57. <https://doi.org/10.1016/j.memsci.2015.06.009>.
- (84) Girish, V.; Pazzi, J.; Li, A.; Subramaniam, A. B. Fabrics of Diverse Chemistries Promote the Formation of Giant Vesicles from Phospholipids and Amphiphilic Block Copolymers. *Langmuir* **2019**, *35*, 9264–9273.

<https://doi.org/10.1021/acs.langmuir.9b01621>.

- (85) Yadav, A. R.; Sriram, R.; Carter, J. A.; Miller, B. L. Comparative Study of Solution-Phase and Vapor-Phase Deposition of Aminosilanes on Silicon Dioxide Surfaces. *Mater. Sci. Eng. C* **2014**, *35* (1), 283–290. <https://doi.org/10.1016/j.msec.2013.11.017>.
- (86) Rodriguez, N.; Cribier, S. Giant Vesicles Formed by Gentle Hydration and Electroformation : A Comparison by Fluorescence Microscopy. **2005**, *42*, 125–130. <https://doi.org/10.1016/j.colsurfb.2005.01.010>.
- (87) Montes, L. R.; Alonso, A.; Goñi, F. M.; Bagatolli, L. A. Giant Unilamellar Vesicles Electroformed from Native Membranes and Organic Lipid Mixtures under Physiological Conditions. *Biophys. J.* **2007**, *93* (10), 3548–3554. <https://doi.org/10.1529/biophysj.107.116228>.
- (88) Shohda, K.; Takahashi, K.; Suyama, A. A Method of Gentle Hydration to Prepare Oil-Free Giant Unilamellar Vesicles That Can Confine Enzymatic Reactions. *Biochem. Biophys. Reports* **2015**, *3*, 76–82. <https://doi.org/10.1016/j.bbrep.2015.07.005>.
- (89) Reeves, J. P.; Dowben, R. M. Formation and Properties of Thin-Walled Phospholipid Vesicles. *J. Cell. Physiol.* **1969**, *73* (1), 49–60. <https://doi.org/10.1002/jcp.1040730108>.
- (90) Nishimura, K.; Hosoi, T.; Sunami, T.; Toyota, T.; Fujinami, M.; Oguma, K.; Matsuura, T.; Suzuki, H.; Yomo, T. Population Analysis of Structural Properties of Giant Liposomes by Flow Cytometry. **2009**, *25* (10), 11443–11447. <https://doi.org/10.1021/la902237y>.
- (91) Cells, R. B. Oxygen Carriers (“ Blood Substitutes ”). *Chemistry and Some*. **2001**. <https://doi.org/10.1021/cr970143c>.
- (92) Chen, J.-Y.; Scerbo, M.; Kramer, G. A Review of Blood Substitutes: Examining the History, Clinical Trial Results, and Ethics of Hemoglobin-Based Oxygen Carriers. *Clinics* **2009**, *64* (8), 803–814. <https://doi.org/10.1590/S1807-59322009000800016>.
- (93) Bartels, P.; Helleman, P. Evaluation of Red Blood Cell Size Distribution Histograms: The Fraction of Microcytes. *Ann. Clin.* **1988**, 680–687.
- (94) Lin, N.; Dufresne, A. Nanocellulose in Biomedicine: Current Status and Future Prospect. *Eur. Polym. J.* **2014**, *59*, 302–325. <https://doi.org/10.1016/j.eurpolymj.2014.07.025>.
- (95) Salas, C.; Nypelö, T.; Rodriguez-Abreu, C.; Carrillo, C.; Rojas, O. J. Nanocellulose Properties and Applications in Colloids and Interfaces. *Curr. Opin. Colloid Interface Sci.* **2014**, *19* (5), 383–396. <https://doi.org/10.1016/j.cocis.2014.10.003>.

- (96) Dimitrov, D. S.; Angelova, M. I. Lipid Swelling and Liposome Formation Mediated by Electric Fields. *Bioelectrochemistry Bioenerg.* **1988**, *253*, 323–336.
- (97) Lasic, D.; June, R.; Press, A. The Spontaneous Formation of Unilamellar Vesicles. **1988**, *1* (2), 428–435.
- (98) Hishida, M.; Seto, H.; Yamada, N. L.; Yoshikawa, K. Hydration Process of Multi-Stacked Phospholipid Bilayers to Form Giant Vesicles. **2008**, *455*, 297–302. <https://doi.org/10.1016/j.cplett.2008.02.065>.
- (99) Yamada, N. L.; Hishida, M.; Seto, H.; Tsumoto, K.; Yoshimura, T. Unbinding of Lipid Bilayers Induced by Osmotic Pressure in Relation to Unilamellar Vesicle Formation. *Epl* **2007**, *80* (4). <https://doi.org/10.1209/0295-5075/80/48002>.
- (100) Kang, M.; Day, C. a.; Drake, K.; Kenworthy, A. K.; DiBenedetto, E. A Generalization of Theory for Two-Dimensional Fluorescence Recovery after Photobleaching Applicable to Confocal Laser Scanning Microscopes. *Biophys. J.* **2009**, *97* (5), 1501–1511. <https://doi.org/10.1016/j.bpj.2009.06.017>.
- (101) Micheletto, Y. M. S.; Marques, C. M.; Silveira, N. P. Da; Schroder, A. P. Electroformation of Giant Unilamellar Vesicles: Investigating Vesicle Fusion versus Bulge Merging. *Langmuir* **2016**, *32* (32), 8123–8130. <https://doi.org/10.1021/acs.langmuir.6b01679>.
- (102) Schroder, A. P. Electroformation of Giant Unilamellar Vesicles: Investigating Vesicle Fusion versus Bulge Merging. *Langmuir* **2016**, *32* 8123-8130. <https://doi.org/10.1021/acs.langmuir.6b01679>.
- (103) Rørvig-lund, A.; Bahadori, A.; Semsey, S.; Bendix, P. M.; Oddershede, L. B. Vesicle Fusion Triggered by Optically Heated Gold Nanoparticles. **2015**. <https://doi.org/10.1021/acs.nanolett.5b01366>.
- (104) Menger, F. M.; Lee, S. J. Induced Morphological Changes in Synthetic Giant Vesicles : Growth , Fusion , Undulation , Excretion , Wounding , and Healing. *Langmuir* **1995**, 3685–3689.
- (105) Ishmukhametov, R. R.; Russell, A. N.; Berry, R. M. A Modular Platform for One-Step Assembly of Multi-Component Membrane Systems by Fusion of Charged Proteoliposomes. *Nat. Commun.* **2016**, *7*, 1–10. <https://doi.org/10.1038/ncomms13025>.
- (106) Terasawa, H.; Nishimura, K.; Suzuki, H.; Matsuura, T.; Yomo, T. Coupling of the Fusion and Budding of Giant Phospholipid Vesicles Containing Macromolecules. **2012**. <https://doi.org/10.1073/pnas.1120327109/-/DCSupplemental.www.pnas.org/cgi/doi/10.1073/pnas.1120327109>.
- (107) Lasic, D. D.; Joannic, R.; Keller, B. C.; Frederik, P. M.; Auvray, L. Spontaneous Vesiculation. *Adv. Colloid Interface Sci.* **2001**, *89–90*, 337–349. [https://doi.org/10.1016/S0001-8686\(00\)00067-1](https://doi.org/10.1016/S0001-8686(00)00067-1).

- (108) Almeida, P. F. F. Thermodynamics of Lipid Interactions in Complex Bilayers. *Biochim. Biophys. Acta - Biomembr.* **2009**, *1788* (1), 72–85. <https://doi.org/10.1016/j.bbamem.2008.08.007>.
- (109) Helfrich, W. Elastic Properties of Lipid Bilayers: Theory and Possible Experiments. *Z. Naturforsch* **1973**, *28c*, 693–703.
- (110) Dharmavaram, S.; She, S. B.; Lázaro, G.; Hagan, M. F.; Bruinsma, R. Gaussian Curvature and the Budding Kinetics of Enveloped Viruses. *PLoS Comput. Biol.* **2019**, *15* (8), 1–22. <https://doi.org/10.1371/journal.pcbi.1006602>.
- (111) Claessens, M. M. A. E.; Leermakers, F. A. M.; Hoekstra, F. A.; Stuart, M. A. C. Osmotic Shrinkage and Reswelling of Giant Vesicles Composed of Dioleoylphosphatidylglycerol and Cholesterol. *Biochim. Biophys. Acta - Biomembr.* **2008**, *1778* (4), 890–895. <https://doi.org/10.1016/j.bbamem.2008.01.019>.
- (112) Menger, F. M. Giant Vesicles : Imitating the Cytological Processes of Cell Membranes. **1998**, *31* (12), 789–797. <https://doi.org/10.1021/ar970103v>.
- (113) Kas, J.; Sackmann, E. Shape Transitions and Shape Stability of Giant Phospholipid Vesicles in Pure Water Induced by Area-to-Volume Changes. **1991**, (October), 825–844. [https://doi.org/10.1016/S0006-3495\(91\)82117-8](https://doi.org/10.1016/S0006-3495(91)82117-8).
- (114) Israelachvili, J. N. *Intermolecular and Surface Forces: Third Edition*; 2011. <https://doi.org/10.1016/C2011-0-05119-0>.
- (115) Duwe, H. P.; Kaes, J.; Sackmann, E. Bending Elastic Moduli of Lipid Bilayers : Modulation by Solutes. *J. Phys.* **1990**, *51* (10), 945–961. <https://doi.org/10.1051/jphys:019900051010094500>.
- (116) Bailey, S. M.; Chiruvolu, S.; Israelachvili, J. N.; Zasadzinski, J. A. N. Measurements of Forces Involved in Vesicle Adhesion Using Freeze-Fracture Electron Microscopy. *Langmuir* **1990**, *6* (7), 1326–1329. <https://doi.org/10.1021/la00097a024>.
- (117) Sun, Y.; Lee, C.; Huang, H. W. Adhesion and Merging of Lipid Bilayers : A Method for Measuring the Free Energy of Adhesion and Hemifusion. *Biophysj* **2011**, *100* (4), 987–995. <https://doi.org/10.1016/j.bpj.2011.01.013>.
- (118) Tanaka, R.; Saito, T.; Ishii, D.; Isogai, A. Determination of Nanocellulose Fibril Length by Shear Viscosity Measurement. *Cellulose* **2014**, *21* (3), 1581–1589. <https://doi.org/10.1007/s10570-014-0196-4>.
- (119) Varanasi, S.; He, R.; Batchelor, W. Estimation of Cellulose Nanofibre Aspect Ratio from Measurements of Fibre Suspension Gel Point. *Cellulose* **2013**, *20* (4), 1885–1896. <https://doi.org/10.1007/s10570-013-9972-9>.
- (120) Helm, C. A.; Israelachvili, J. N.; McGuiggan, P. Role of Hydrophobic Forces in Bilayer Adhesion and Fusion. *Biochemistry* **1992**, *31* (6), 1794–1805.

<https://doi.org/10.1021/bi00121a030>.

- (121) Servuss, R. M.; Helfrich, W. Mutual Adhesion of Lecithin Membranes at Ultralow Tensions. *J. Phys.* **1989**, *50* (7), 809–827.
<https://doi.org/10.1051/jphys:01989005007080900>.
- (122) Niwa, H. S. Power-Law versus Exponential Distributions of Animal Group Sizes. *J. Theor. Biol.* **2003**, *224* (4), 451–457. [https://doi.org/10.1016/S0022-5193\(03\)00192-9](https://doi.org/10.1016/S0022-5193(03)00192-9).
- (123) Valli, J.; Garcia-Burgos, A.; Rooney, L. M.; Vale de Melo e Oliveira, B.; Duncan, R. R.; Rickman, C. Seeing beyond the Limit: A Guide to Choosing the Right Super-Resolution Microscopy Technique. *J. Biol. Chem.* **2021**, *297* (1), 100791.
<https://doi.org/10.1016/j.jbc.2021.100791>.
- (124) Jonkman, J.; Brown, C. M.; Wright, G. D.; Anderson, K. I.; North, A. J. Tutorial: Guidance for Quantitative Confocal Microscopy. *Nat. Protoc.* **2020**, *15* (5), 1585–1611. <https://doi.org/10.1038/s41596-020-0313-9>.
- (125) Letschert, S.; Göhler, A.; Franke, C.; Bertleff-Zieschang, N.; Memmel, E.; Doose, S.; Seibel, J.; Sauer, M. Super-Resolution Imaging of Plasma Membrane Glycans. *Angew. Chemie Int. Ed.* **2014**, *53* (41), 10921–10924.
<https://doi.org/10.1002/anie.201406045>.
- (126) Ho, W. T.; Chiang, T. H.; Chang, S. W.; Chen, Y. H.; Hu, F. R.; Wang, I. J. Enhanced Corneal Wound Healing with Hyaluronic Acid and High-Potassium Artificial Tears. *Clin. Exp. Optom.* **2013**, *96* (6), 536–541.
<https://doi.org/10.1111/cxo.12073>.
- (127) Tsumoto, K.; Hayashi, Y.; Tabata, J.; Tomita, M. A Reverse-Phase Method Revisited: Rapid High-Yield Preparation of Giant Unilamellar Vesicles (GUVs) Using Emulsification Followed by Centrifugation. *Colloids Surfaces A Physicochem. Eng. Asp.* **2018**, *546* (March), 74–82.
<https://doi.org/10.1016/j.colsurfa.2018.02.060>.
- (128) Zan, G. H.; Tan, C.; Deserno, M.; Lanni, F.; Lösche, M. Hemifusion of Giant Unilamellar Vesicles with Planar Hydrophobic Surfaces: A Fluorescence Microscopy Study. *Soft Matter* **2012**, *8* (42), 10877–10886.
<https://doi.org/10.1039/c2sm25702e>.
- (129) Nakayama, Y.; Slavchov, R. I.; Bavi, N.; Martinac, B. Energy of Liposome Patch Adhesion to the Pipet Glass Determined by Confocal Fluorescence Microscopy. *J. Phys. Chem. Lett.* **2016**, *7* (22), 4530–4534.
<https://doi.org/10.1021/acs.jpcllett.6b02027>.
- (130) Evans, E.; Needham, D. Attraction between Lipid Bilayer Membranes in Concentrated Solutions of Nonadsorbing Polymers: Comparison of Mean-Field Theory with Measurements of Adhesion Energy. *Macromolecules* **1988**, *21* (6), 1822–1831. <https://doi.org/10.1021/ma00184a049>.

- (131) Marra, J.; Israelachvili, J. Direct Measurements of Forces between Phosphatidylcholine and Phosphatidylethanolamine Bilayers in Aqueous Electrolyte Solutions. **1985**, 4608–4618. <https://doi.org/10.1021/bi00338a020>.
- (132) Petrache, H. I.; Tristram-Nagle, S.; Harries, D.; Kučerka, N.; Nagle, J. F.; Parsegian, V. A. Swelling of Phospholipids by Monovalent Salt. *J. Lipid Res.* **2006**, *47* (2), 302–309. <https://doi.org/10.1194/jlr.M500401-JLR200>.
- (133) Hemmerle, A.; Malaquin, L.; Charitat, T.; Lecuyer, S.; Fragneto, G. Controlling Interactions in Supported Bilayers from Weak Electrostatic Repulsion to High Osmotic Pressure. **2012**, *109* (49). <https://doi.org/10.1073/pnas.1211669109>.
- (134) Cevc, G. Membrane Electrostatics. *BBA - Rev. Biomembr.* **1990**, *1031* (3), 311–382. [https://doi.org/10.1016/0304-4157\(90\)90015-5](https://doi.org/10.1016/0304-4157(90)90015-5).
- (135) Nicholas, A. R.; Scott, M. J.; Kennedy, N. I.; Jones, M. N. Effect of Grafted Polyethylene Glycol (PEG) on the Size, Encapsulation Efficiency and Permeability of Vesicles. *Biochim. Biophys. Acta - Biomembr.* **2000**, *1463* (1), 167–178. [https://doi.org/10.1016/S0005-2736\(99\)00192-3](https://doi.org/10.1016/S0005-2736(99)00192-3).
- (136) Allen, T. M.; Cullis, P. R. Liposomal Drug Delivery Systems: From Concept to Clinical Applications. *Adv. Drug Deliv. Rev.* **2013**, *65* (1), 36–48. <https://doi.org/10.1016/j.addr.2012.09.037>.
- (137) Needham, D.; McIntosh, T. J.; Lasic, D. D. Repulsive Interactions and Mechanical Stability of Polymer-Grafted Lipid Membranes. *BBA - Biomembr.* **1992**, *1108* (1), 40–48. [https://doi.org/10.1016/0005-2736\(92\)90112-Y](https://doi.org/10.1016/0005-2736(92)90112-Y).
- (138) Battaglia, G.; Paredes, J. I.; Lopresti, C.; Lomas, H.; Massignani, M.; Smart, T.; Battaglia, G. Polymersomes : Nature Inspired Nanometer Sized Compartments †. **2009**, *19* (22). <https://doi.org/10.1039/b818869f>.
- (139) Marquardt, D.; Geier, B.; Pabst, G. Asymmetric Lipid Membranes: Towards More Realistic Model Systems. *Membranes (Basel)*. **2015**, *5* (2), 180–196. <https://doi.org/10.3390/membranes5020180>.
- (140) Verkleij, A. J.; Zwaal, R. F. A.; Roelofsen, B.; Comfurius, P.; Kastelijn, D.; van Deenen, L. L. M. The Asymmetric Distribution of Phospholipids in the Human Red Cell Membrane. A Combined Study Using Phospholipases and Freeze-Etch Electron Microscopy. *BBA - Biomembr.* **1973**, *323* (2), 178–193. [https://doi.org/10.1016/0005-2736\(73\)90143-0](https://doi.org/10.1016/0005-2736(73)90143-0).
- (141) Truskey, George A.; Yuan, Fan; Katz, D. F. *Transport Phenomena in Biological Systems*; Pearson: Upper Saddle River, New Jersey, 2009.
- (142) Nair, S. S.; Zhu, J.; Deng, Y.; Ragauskas, A. J. High Performance Green Barriers Based on Nanocellulose. *Sustain. Chem. Process.* **2014**, *2* (1), 1–7. <https://doi.org/10.1186/s40508-014-0023-0>.
- (143) Zhang, W.; Jing, Z.; Shan, Y.; Ge, X.; Mu, X.; Jiang, Y.; Li, H.; Wu, P. Paper

- Reinforced with Regenerated Cellulose: A Sustainable and Fascinating Material with Good Mechanical Performance, Barrier Properties and Shape Retention in Water. *J. Mater. Chem. A* **2016**, *4* (44), 17483–17490. <https://doi.org/10.1039/c6ta07681e>.
- (144) Vázquez, M. I.; Benavente, J. A Study of Temperature Effect on Chemical, Structural and Transport Parameters Determined for Two Different Regenerated Cellulose Membranes. *J. Memb. Sci.* **2003**, *219* (1–2), 59–67. [https://doi.org/10.1016/S0376-7388\(03\)00179-0](https://doi.org/10.1016/S0376-7388(03)00179-0).
- (145) Estes, D. J.; Mayer, M. Giant Liposomes in Physiological Buffer Using Electroformation in a Flow Chamber. **2005**, *1712*, 152–160. <https://doi.org/10.1016/j.bbamem.2005.03.012>.
- (146) Dietrich, C.; Volovyk, Z. N.; Levi, M.; Thompson, N. L.; Jacobson, K. Partitioning of Thy-1, GM1, and Cross-Linked Phospholipid Analogs into Lipid Rafts Reconstituted in Supported Model Membrane Monolayers. *Proc. Natl. Acad. Sci. U. S. A.* **2001**, *98* (19), 10642–10647. <https://doi.org/10.1073/pnas.191168698>.
- (147) Méléard, P.; Bagatolli, L. A.; Pott, T. Giant Unilamellar Vesicle Electroformation. From Lipid Mixtures to Native Membranes Under Physiological Conditions. *Methods in Enzymology*. 2009, pp 161–176. [https://doi.org/10.1016/S0076-6879\(09\)65009-6](https://doi.org/10.1016/S0076-6879(09)65009-6).
- (148) Merino, S.; Domenech, O.; Diez, I.; Sanz, F.; Vinas, M.; Montero, M. T.; Hernandez-Borrell, J. Effects of Ciprofloxacin on Escherichia Coli Lipid Bilayers: An Atomic Force Microscopy Study. *Langmuir* **2003**, *19* (17), 6922–6927. <https://doi.org/10.1021/la034232y>.
- (149) Zhang, J. Protein-Protein Interactions in Salt Solutions. *Protein-Protein Interact. - Comput. Exp. Tools* **2012**, No. 6. <https://doi.org/10.5772/38056>.
- (150) Colletier, J.-P.; Chaize, B.; Winterhalter, M.; Fournier, D. Protein Encapsulation in Liposomes: Efficiency Depends on Interactions between Protein and Phospholipid Bilayer. *BMC Biotechnol.* **2002**, *2*, 9. <https://doi.org/10.1186/1472-6750-2-9>.
- (151) Smirnova, I. A.; Ädelroth, P.; Brzezinski, P. Extraction and Liposome Reconstitution of Membrane Proteins with Their Native Lipids without the Use of Detergents. *Sci. Rep.* **2018**, *8* (1), 1–6. <https://doi.org/10.1038/s41598-018-33208-1>.
- (152) Tsai, F. C.; Stuhmann, B.; Koenderink, G. H. Encapsulation of Active Cytoskeletal Protein Networks in Cell-Sized Liposomes. *Langmuir* **2011**, *27* (16), 10061–10071. <https://doi.org/10.1021/la201604z>.
- (153) Devaux, P. F. Static and Dynamic Lipid Asymmetry in Cell Membranes. *Biochemistry* **1991**, *30* (5), 1163–1173. <https://doi.org/10.1021/bi00219a001>.
- (154) Veatch, S. L.; Keller, S. L. Separation of Liquid Phases in Giant Vesicles of Ternary Mixtures of Phospholipids and Cholesterol. *Biophys. J.* **2003**, *85* (5),

3074–3083. [https://doi.org/10.1016/S0006-3495\(03\)74726-2](https://doi.org/10.1016/S0006-3495(03)74726-2).

- (155) Čejková, J.; Štěpánek, F. Compartmentalized and Internally Structured Particles for Drug Delivery - A Review. *Curr. Pharm. Des.* **2013**, *19* (35), 6298–6314. <https://doi.org/10.2174/1381612811319350007>.
- (156) Göpfrich, K.; Haller, B.; Staufer, O.; Dreher, Y.; Mersdorf, U.; Platzman, I.; Spatz, J. P. One-Pot Assembly of Complex Giant Unilamellar Vesicle-Based Synthetic Cells. *ACS Synth. Biol.* **2019**, *8* (5), 937–947. <https://doi.org/10.1021/acssynbio.9b00034>.
- (157) Fischer, A.; Franco, A.; Oberholzer, T. Giant Vesicles as Microreactors for Enzymatic mRNA Synthesis. *ChemBioChem* **2002**, *3* (5), 409–417. [https://doi.org/10.1002/1439-7633\(20020503\)3:5<409::AID-CBIC409>3.0.CO;2-P](https://doi.org/10.1002/1439-7633(20020503)3:5<409::AID-CBIC409>3.0.CO;2-P).
- (158) Kurihara, K.; Tamura, M.; Shohda, K.; Toyota, T.; Suzuki, K.; Sugawara, T. Self-Reproduction of Supramolecular Giant Vesicles Combined with the Amplification of Encapsulated DNA. *Nat. Chem.* **2011**, *3* (10), 775–781. <https://doi.org/10.1038/nchem.1127>.
- (159) Nomura, S. M.; Yoshikawa, Y. Towards Proto-Cells : "Primitive" Lipid Vesicles Encapsulating Giant DNA and Its Histone Complex. *ChemBioChem* **2001**, No. 6, 457–459.

Appendix

1. Introduction

In the appendix section of this dissertation, I include work that is supplemental to the research conducted in the previous chapters. In Section 2, I include the relevant materials and methods used only in the appendix. In Section 3, I present data I collected on the effect of osmolytes on the assembly of GUVs in physiological solutions. In Section 4, I include work related to the use of cellulose paper as a platform for novel biosensing applications. Finally, in Section 5 I include the raw code I used to characterize the populations of GUVs from the confocal images in the previous chapters.

2. Materials and methods

2.1 Materials

Whatman Ashless Grade 1 Filter Papers (12 cm × 12 cm), glass coverslips (Gold Seal™, 22 mm x 22 mm), premium plain glass microscope slides (75 mm x 25 mm), and glass media bottles (Pyrex™, 100 mL) were purchased from Thermo Fischer Scientific (Waltham, MA).

2.2 Chemicals

Rabbit IgG (reagent grade $\geq 95\%$), anti-rabbit IgG (whole molecule) antiserum produced in goat (~ 17 mg/mL), polyethylene glycol (average M_n 6000, premium grade) and erioglaucline disodium salt (analytical standard grade $>97\%$), sucrose (BioXtra grade with purity $\geq 99.5\%$), glucose (BioXtra grade with purity $\geq 99.5\%$), dextran from Leuconostoc (average mol wt $\sim 100,000$), low gelling temperature agarose (BioReagent grade), and casein from bovine milk (BioReagent grade) were all purchased from Sigma-Aldrich (St. Louis, MO). I purchased chloroform (ACS grade with a purity $\geq 99.8\%$ and 0.75% ethanol added as preservative) and acetone (ACS grade, purity $\geq 99.5\%$) from Thermo Fischer Scientific (Waltham, MA). I obtained 18.2 M Ω ultrapure water from an ELGA Pure-lab Ultra water purification system (Woodridge, IL). I purchased lipids 1,2-dioleoyl-sn-glycero-3-phosphocholine (18:1 (Δ^9 -cis) PC (DOPC)) and 23-(dipyrrometheneboron difluoride)-24-norcholesterol (TopFluor-Cholesterol), from Avanti Polar Lipids, Inc. (Alabaster, AL).

2.3 Assembly of GUVs from gel-assisted methods

2.3.1 Fabrication of agarose-coated glass coverslips

I prepare films of agarose on glass coverslips following protocol previously reported by others^{1,2}. I obtain a 1 wt % (w/v) solution of agarose by mixing 0.8 g of low gelling temperature agarose in 80 mL of room temperature ultrapure water. The solution is mixed

in a 100 mL glass media bottle and then set on a hot plate at 100 °C for 30 minutes while being stirred with a magnetic stir bar. I place square glass coverslips (22 mm × 22 mm) onto a sheet of Parafilm, and then spread 300 μ L of the agarose solution onto the coverslips evenly moving the solution around with the pipette. The sheet of Parafilm holding the coated glass coverslips is then placed onto a hot plate set at 40 °C where the agarose gel is allowed to dehydrate for 3 hours^{1,2}.

2.3.2 Fabrication of the polyvinyl alcohol (PVA) coated glass coverslips

To fabricate the polyvinyl alcohol, I followed protocols from others³. I spread 300 μ L of a 5 wt % (w/v) solution of PVA evenly over a glass coverslip (22 mm × 22 mm). I then place the PVA-coated glass coverslip onto a sheet of Parafilm and allow the PVA film to dry at 40 °C for 2 hours.

2.3.3 Fabrication of dextran-tracing paper

I fabricated dextran-tracing paper to approximate the surface concentration of agarose molecules on the surface of glass coverslips used for agarose gel-assisted hydration^{1,2}. Low melting temperature agarose has an average molecular weight of 100,000⁴. Due to its porosity, a piece of tracing with equivalent area to a glass coverslip (22 mm × 22 mm) absorbs ~ 120 μ L of water. I thus deposited 420 μ L of a 1% (w/v) solution of dextran (MW 100,000) onto cleaned pieces of tracing paper. I allowed the solution to dry for 2 hours at 40 °C on a hot plate.

2.3.4 Hydration of the agarose-coated glass and PVA-coated glass substrates

To hydrate the lipid-coated glass and agarose-coated glass substrates, I affix circular PDMS gaskets (inner diameter × height = 12 × 1 mm) to construct a barrier around the lipid films. I then hydrate the surfaces in 150 μ L of buffer and carefully place a glass coverslip on the top surface of the PDMS gasket. I allow the samples to incubate for 2 hours, before carefully removing the coverslip and harvesting the GUVs from the surface normally.

2.4 Pre-hydration with sucrose to obtain GUVs in physiological salts

Controlling the concentration gradients of osmolytes between the substrate surface and the lipid membranes, high yields of GUVs bud from the surface during direct assembly in physiological salts. For experimental ease and working with small volumes the lipid-coated tracing paper surface is placed into a circular PDMS gasket (same as the ones used for gel-assisted methods in section 2.3.4) instead of the standard 48-well plate. To control the gradients, I pre-hydrate the lipid coated tracing paper using 15 μ L of a 1 M solution of sucrose in 1× PBS. Following a 3 minute incubation period, I gently fill the rest of the chamber with 135 μ L of 1× PBS solution, resulting in a final concentration of 100 mM sucrose and 1× PBS. After 60 minutes of growth the GUVs are harvested normally from the surface.

2.5 Quantification of immunoprecipitation reactions

2.5.1 Fabrication of microPADs

I created a template for the devices in Adobe Illustrator. There were 45 devices on a single piece of chromatography paper, each a rectangular channel with a width of 5 mm and length of 30 mm. I printed the channels using a Xerox ColorQube 8580 wax printer with black wax ink. I melted the wax through the thickness of the paper, by placing the wax-printed paper on a hot plate set at 150°C for 3 minutes. During this process, the black wax turned gray and the channels were clearly visible on both sides of the paper. I printed a second layer to create a rectangular slit at the top of each channel (1 mm) and a millimeter scaling ruler along the side of each channel. To seal the bottom surface of the paper, I printed a complete layer of yellow wax and then a complete layer of black wax. The black wax layer visually printed well onto the yellow wax layer.

2.5.2 Fabrication of nanoPADs

I diluted a stock suspension of nanofibrillated cellulose (NFC) from 3 wt % to 0.05 wt % in ultrapure water. I cut off the end of a pipette tip (20-200 μ L) and carefully deposited 40 μ L droplets of the NFC suspension on the entrance of the μ PADs. I allowed the suspension to completely wick into the paper and evaporate for one hour. A mat of nanocellulose formed on top of the entrance.

2.5.3 Procedure for immunoprecipitation reaction

I diluted the anti-rabbit IgG antiserum (nominal concentration \sim 17 mg/mL, manufacturer's data) in PEG buffer (4 w/v % PEG in 1X PBS buffer) to obtain a working concentration of 2 mg/mL of antiserum. To obtain a wide range of antigen concentrations, I serially diluted rabbit IgG in half dilutions 7 times to obtain samples with concentrations ranging from 1.000 mg/mL to 0.016 mg/mL. The final volume for each sample was 320 μ L. I filtered all solutions through a regenerated cellulose syringe filter with a pore size of 0.2 μ m to remove any dust or other large contaminants. After mixing each antigen sample with an equal volume of antiserum solution in 1.5 mL Eppendorf tubes, I allowed the reaction to proceed for 20 minutes.

2.5.4 Procedure for turbidimetric control

After 20 minutes, I gently mixed the reaction to redistribute the precipitates and placed three 200 μ L aliquots from each reaction mixture into a polystyrene flat bottom 96-well plate (Corning Inc.). I measured the optical density using a SpectraMax M2^e plate reader (Molecular Devices). I performed the measurements in the absorbance mode at a wavelength of 340 nm.

2.5.5 Procedure for nanoPAD analysis

I added 5 μ L of FD&C Blue Dye (11 mg/mL erioglaurine disodium salt) to each well in the 96-well plate. I gently mixed the solutions and deposited three 40 μ L droplets onto the entrance of three nanoPADs. I allowed the droplets to imbibe into the devices for 5 minutes

before wiping the excess liquid from the entrance. After the devices completely dried the fluid flow path remained clearly visible as a blue stain against the white paper. I recorded the fluid front length of each of the solutions to the furthest millimeter traveled and then scanned the paper in a scanner.

2.5.6 Characterization of the paper devices

I collected electron microscopy images of the μ PAD and nanoPAD devices using a field emission scanning electron microscope (GeminiSEM 500, Zeiss, Germany). I taped the samples down to a metallic SEM pin stub using copper tape to secure the sample and create a conduction path to minimize charging at the non-conductive paper surface. I used a low beam accelerating voltage (1kV) and collected signal using a secondary electron detector. I collected images at 10 different locations and at three different magnifications for a total of 30 images. The pixel size of the low, middle and high magnifications was 1.09 $\mu\text{m}/\text{pixel}$, 0.24 $\mu\text{m}/\text{pixel}$, and 0.011 $\mu\text{m}/\text{pixel}$ respectively. The dimension of the images was 1024 x 768. Quantitative analysis of the pore size distribution was conducted on these images in Matlab using a custom routine.

2.5.7 Pore size distribution analysis

I wrote a custom Matlab routine to obtain the pore size distribution at the entrance of the paper devices from the SEM images. I used a threshold to convert the grayscale images into binary images. The pores were considered to be the 0-value pixels and the fibers were considered to be the 1-value pixels. I considered connected 0s to be single pores and used the *bwconncomp* routine to return the connected components. I used *regionprops* routine to determine an equivalent diameter for each of the connected components assuming they were circular.

I analyzed 7 low, 10 middle and 10 high magnification images and normalized the pore size data from each magnification to encompass the surface area of the device entrance. I set criteria on the diameter of the pores that were collected from each magnification to prevent double counting. The pore size distributions were plotted in histograms as 24 equal bins between 38 nm and 90,000 nm.

3. Effect of osmolytes on the formation of GUVs

3.1 Molar yields of GUVs obtained from gel-assisted methods in physiological salts

Gel-assisted methods have been reported to be able to result in high yields of GUVs in physiological salts. At the conclusion of Chapter 3, I show that through a modulation of the ionic strength of the solution, tracing paper can be used to produce high yields of biologically-relevant GUVs in physiological salt conditions. This demonstration is significant since up until now methods to obtain GUVs in physiologically relevant conditions are reported to result in either low yields or, in the case of the gel-assisted methods, contamination of the GUVs with osmolytes^{5,6}. However, in cases where contamination of the environment is not an issue, the yields of GUVs from gel-assisted are still quantitatively unknown. Following the procedures in the methods section, I quantitatively evaluate the yields of GUVs in $1\times$ PBS solutions from agarose gels, polyvinyl alcohol (PVA) gels, and surfaces of tracing paper covered with dextran molecules. I select the dextran as a molecule to coat the tracing paper, to compare the effect of osmolytes that are not gels. I coat the surface of the tracing paper with the same surface concentration of dextran the surface concentration used in the agarose gel method. I also include new data relevant to the yields of GUVs in physiological salts from the electroformation method and replot the yields of the glass, tracing paper, and one-step tracing paper methods for comparisons.

As a baseline, I show the results of the molar yields obtained in low salt conditions in Figure 110a. The stacked bar plots show the average molar yields from 5 independent replicate samples. The colors show the percentage of the molar yields that comprise of GUVs from the size classifications that include small GUVs (with diameters, d , $1 \leq d < 10$), large GUVs ($10 \leq d < 50$), and very large GUVs ($d \geq 50$). The error bars show the standard deviation of the mean of the small GUVs (bottom) and large and very large GUVs (top). The molar yields produced from the agarose and dextran tracing paper samples in low salt solutions are both around 30% and are both not statistically different than the molar yields produced from tracing paper. Interestingly the PVA gels result in a slight decrease in yields compared to the glass method. Figure 110b shows the molar yields in $1\times$ PBS solutions. Direct addition of the salts without modulation of the ionic strength results in a decrease in the molar yields from all the substrates. Interestingly, the decrease in the yields from dextran tracing paper and agarose gels are similar at around $\sim 15\%$. These substrates result in the highest molar yields in physiological conditions for any method where modulation of salts is not performed. The electroformation molar yields also significantly decrease in physiological salts dropping to around 7%. However, compared to the glass and tracing paper samples the electric field does appear to have a positive effect on the yields in high salts producing slightly higher yields. The PVA, although reported to produce high yields of GUVs in salt solutions, decreases significantly to a similar yield as the glass and tracing paper surfaces around 1%.

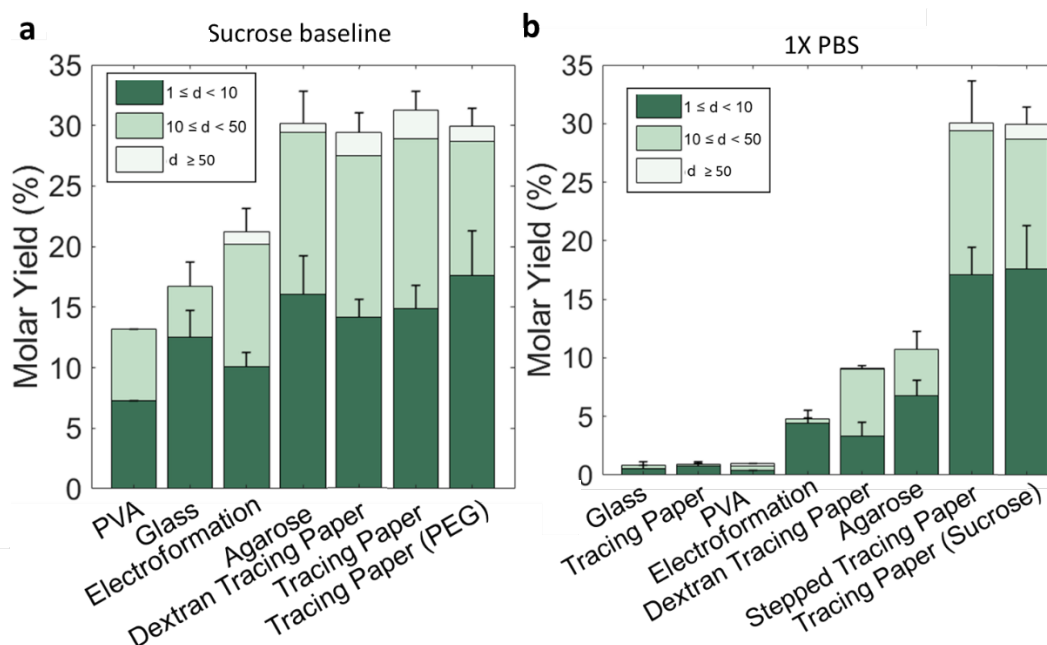


Figure 110: Molar yields of GUVs obtained from surface-assisted methods decrease in physiological salts. Stacked bar plots showing **a** a baseline of the molar yields of GUVs obtained in low salt, 100 mM sucrose solutions, and **b** the molar yields in 1× PBS solutions from various surfaces tested. The colors of the bars show the contributions to the total molar yield of the size ranges marked in the legend. Each point is from an average 5 independent repeats with error bars showing one standard deviation from the mean.

3.2 Effect of osmotic pressure gradients on the assembly of GUVs in physiological salts

Considering the budding and merging model from Chapter 3, since the only difference between the dextran-coated tracing paper and the tracing paper substrates is the presence of the dextran. The presence of osmolytes on the surface could result in an osmotic pressure difference that overcomes the adhesion between the membranes and results in the formation of the buds. To investigate, I first observe the difference in the buds on the surface of the dextran coated paper after hydration in 1× PBS buffer. Figure 111 shows the effect of decreasing the amount of dextran at the surface of the tracing paper on the formation of the buds. As a reference, in the molar yield experiments I used a 1 wt % (w/v) concentration of dextran solution to obtain the dextran coated paper. At the lowest concentration 0.01 wt % (Figure 111a), only very few and small buds can be observed on the surface. At the middle concentration 0.1 wt % (Figure 111b), significantly more buds can be observed on the surface however the membranes appear rigid and the buds do not appear to be fully formed. At the highest concentration 1 wt % (Figure 111c), the GUV buds appear more similar to how they appear in low salt

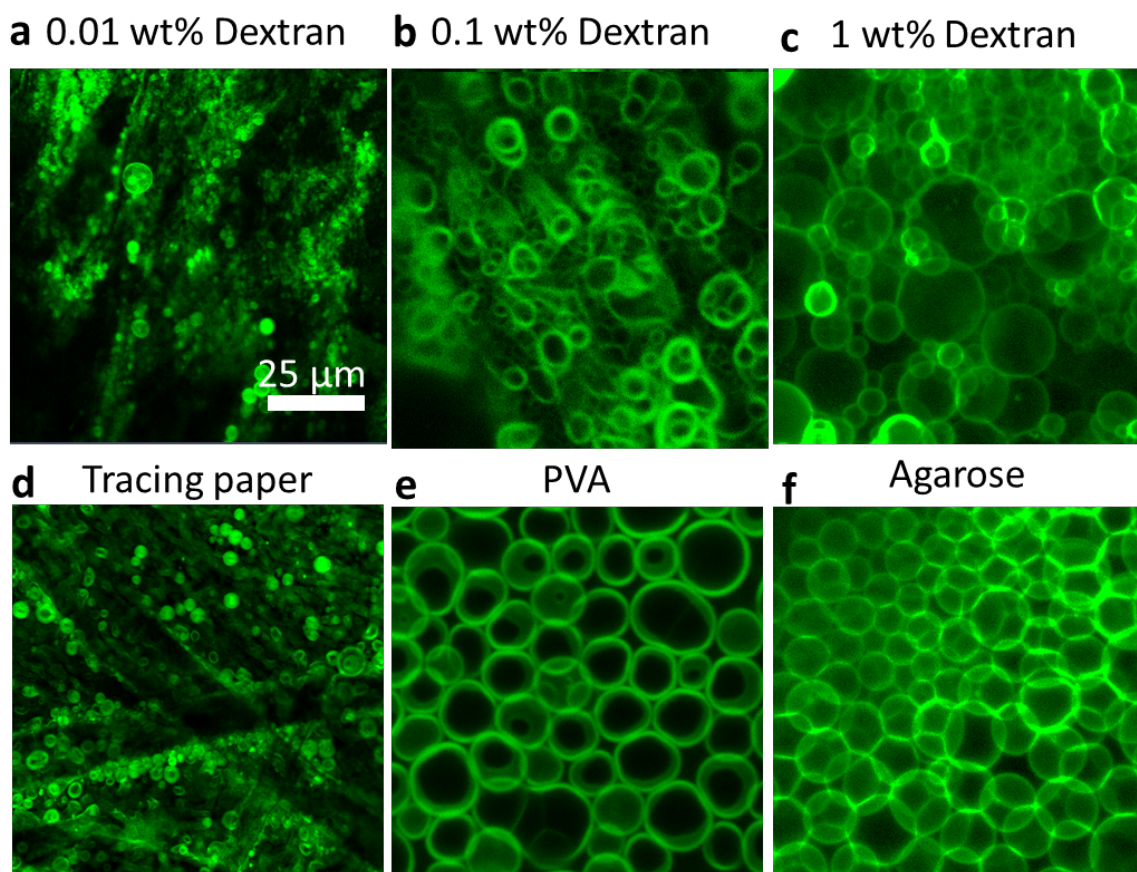


Figure 111: Confocal images of GUV buds forming from various surfaces during hydration in physiological salts. Representative confocal images during the assembly of GUVs in physiological salts from the **a** 0.01 wt % dextran-coated tracing paper, **b** 0.1 wt % dextran-coated tracing paper, **c** 1 wt % dextran-coated tracing paper, **d** tracing paper, **e** 5 wt % PVA-coated glass, and **f** 1 wt % agarose-coated glass surfaces. Scale bar: **a-f** 25 μm .

conditions where they are distributed axially above the surface of the tracing paper and appear much larger in number and size. Interestingly at each increasing surface concentration, the vesicles at the surface are similar in appearance to observations I have made in the past, where the lowest dextran concentration 0.01 wt %, results in images that appear similar to tracing paper, the middle dextran concentration 0.1 wt %, results in images that appear similar to PVA, and the highest dextran concentration 1 wt % results in images that appear similar to agarose.

Along with a qualitative analysis, I also show the results of performing confocal tilescan experiments to quantify the molar yields of the GUVs obtained at each concentration. I include a concentration of 10 wt % dextran. Figure 112a-d shows the previous images of the GUV buds on the different dextran-coated surfaces with the addition

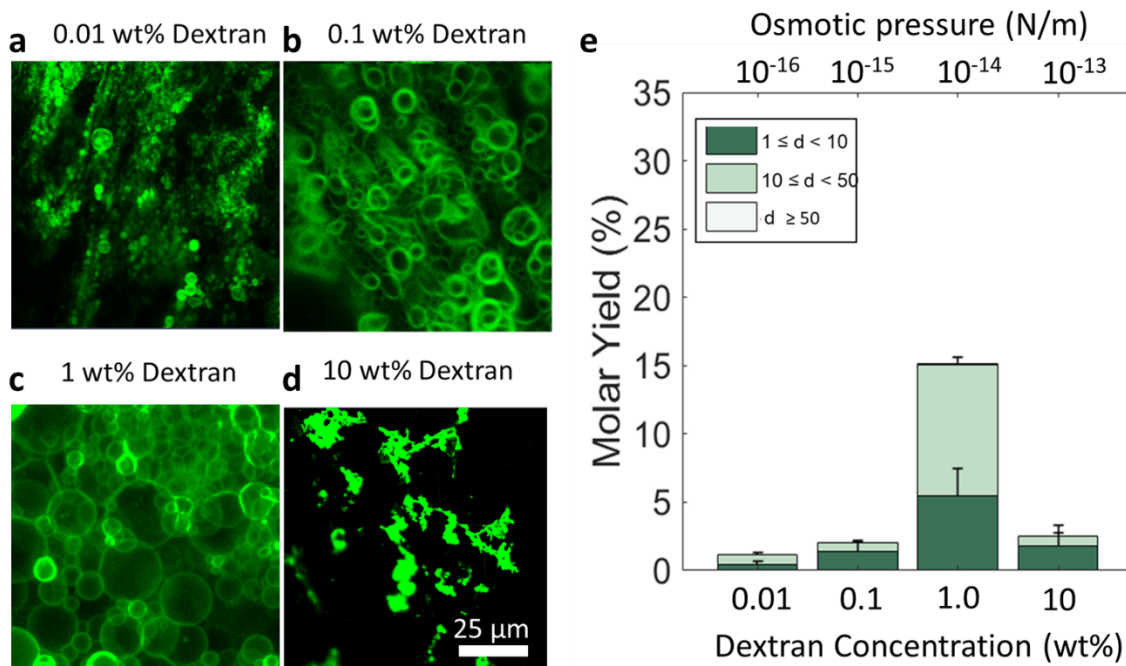


Figure 112: Effect of osmotic pressure on the molar yield of GUVs in physiological salt conditions. a-d Representative confocal images from the dextran samples in physiological salts in Figure 111, with the addition of d a 10 wt % dextran-coated tracing paper sample. e Stacked bar plot showing the average molar yield of the GUVs obtained from the different concentrations of dextran coated on the tracing paper surface. The error bars show the standard deviation from the mean from 3 replicate samples. The predicted values for the osmotic pressure associated to the membrane are shown above.

of the appearance of the 10 wt % dextran sample where most of the lipid has appeared to come off the surface. Figure 112e shows the stacked bar plots from an average of 3 replicate samples for each dextran concentrations. Since, the osmotic pressure that would be felt by the membranes coating the dextran-coated surface is directly correlated to the concentration of the dextran, I also show the expected osmotic pressure gradient that is expected to be felt by the membrane at each different dextran concentration at the top of the plot. These values were estimated assuming that at the initial hydration all of the osmolytes are between the surface of the tracing paper and the lipid membranes resting on the surface. Clearly, the concentration range where the molar yields increase significantly due to the presence of the dextran is extremely narrow. The molar yields at 0.01 wt %, 0.1 wt %, and 10 wt % dextran concentrations are all ~1–2 %, while only the molar yields at 1 wt % dextran concentration reach ~15 %.

3.3 Development of a pre-hydration method to assemble GUVs in physiological salts

Overall it appears that osmotic pressure gradients can drive the formation of GUVs in physiological salt environments. Figure 113 shows a schematic to conceptualize this mechanism. The left shows the a typical hydration in salts where the amount of osmolytes that are present is the same on both sides of the membrane and the membranes adhere to one another. On the right, the addition of water-soluble osmolytes at the surface results in an osmotic pressure gradient that drives the influx of water resulting in the lessening of the effects of adhesion and the budding of the membranes from the surface.

I hypothesize that this osmotic effect can be achieved through concentration gradients similar to the one-step modulation of salts. Figure 114 shows a schematic of a novel pre-hydration method I develop to produce high yields of GUVs in physiological salt solutions. On the left the lipid-coated surface is hydrated with a small 15 μL solution of a 10 \times concentrated amount of osmolytes in 1 \times PBS. During the initial hydration, the concentrated solution of osmolytes intercalate between the bilayers that self-assemble. Moving to the middle, after 3 minutes 135 μL of 1 \times PBS buffer is added to the solution to obtain a final concentration of 1 \times osmolytes and 1 \times PBS. The osmotic pressure gradient that is formed during the pre-hydration step results in the budding of GUVs in high salt solutions.

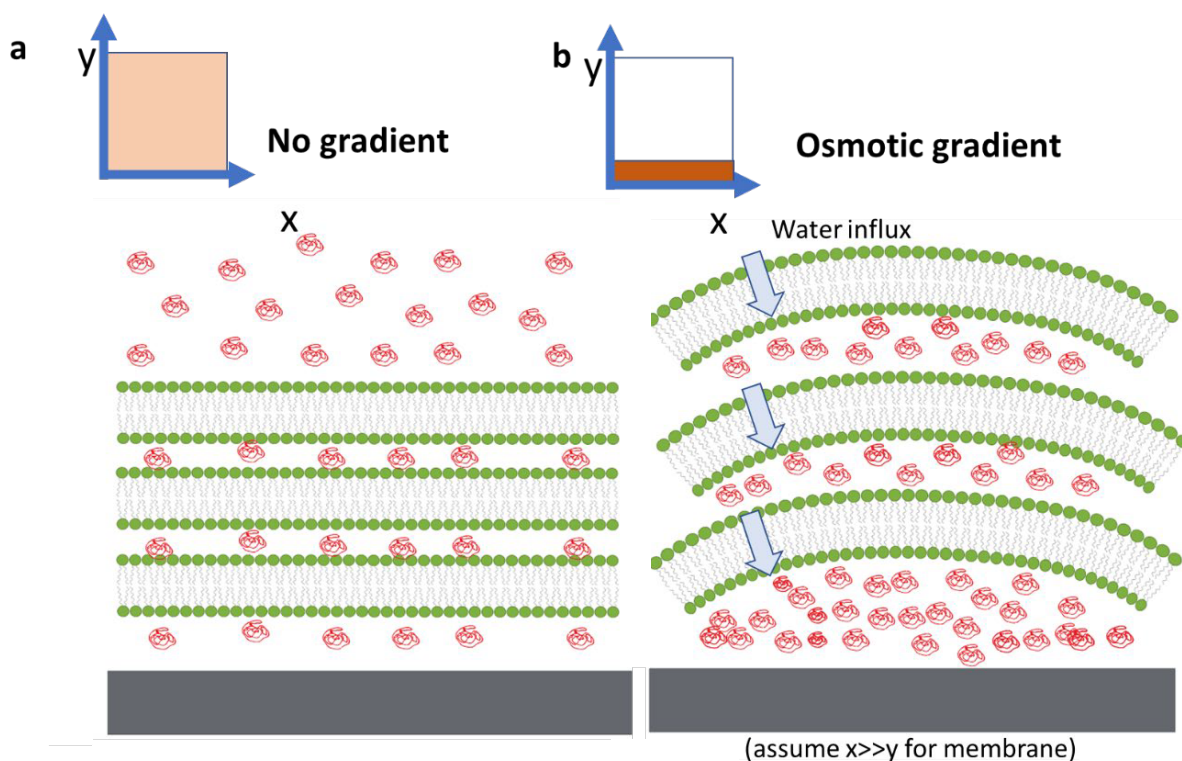


Figure 113: Schematic showing the effect of osmotic gradients . a,b Schematic showing the effect **a** no gradient and **b** a gradient in the concentration of osmolytes across the lipid

bilayer. In the example where no gradient is present in physiological conditions of salts the adhesion between the bilayers dominates and the bilayers remain attached to the surface. In the example where there is a gradient present, the additional osmotic pressure due to the influx of water overcome the adhesion between the bilayers and allow the bilayers to begin to bud.

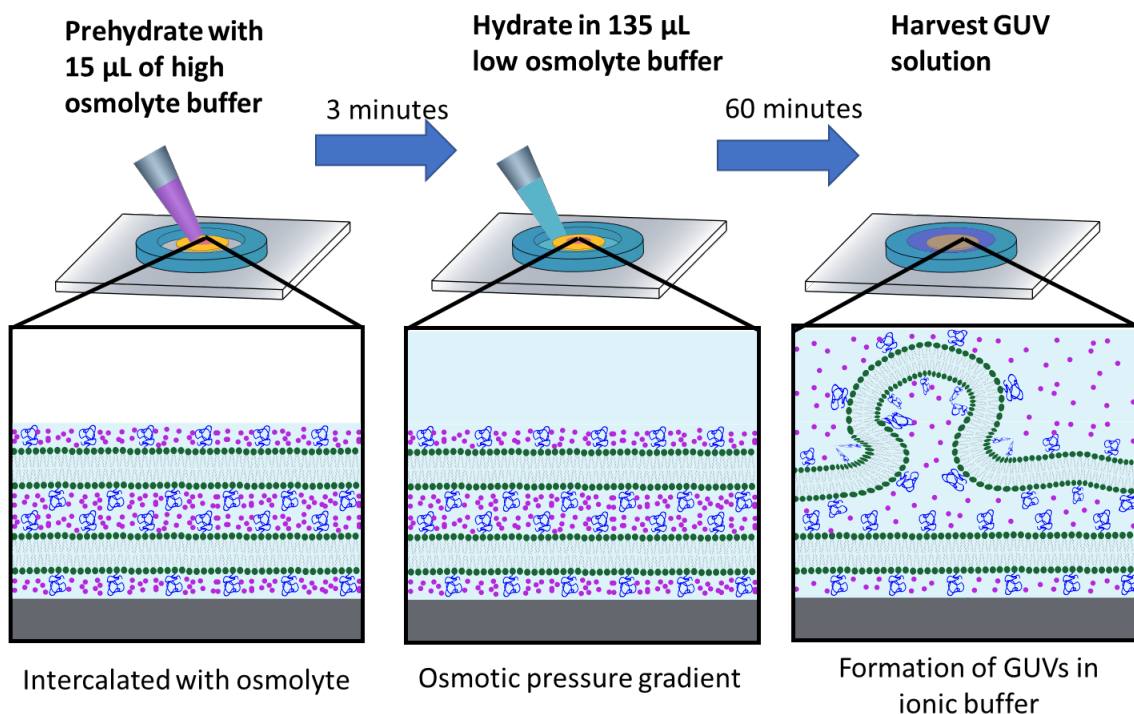


Figure 114: Schematic showing the pre-hydration methods used to obtain GUVs in physiological salts. The lipid-coated substrate is placed into a PDMS gasket (top left) and then pre-hydrated in 15 μL of a high osmolyte buffer in 1 \times PBS. A magnified view illustrates the expectation that as the lipid bilayers form, the osmolyte will intercalate evenly around the bilayers. In addition, since there is no osmotic gradient at this point and the adhesion energy is higher due to the 1 \times PBS, no budding is expected. After 3 minutes, the sample is hydrated in 135 μL of 1 \times PBS solution (middle). Since only the initial 15 μL contained osmolytes, a higher concentration of osmolytes is expected to be present between the bilayers and the surface compared to the solution in bulk. The osmotic pressure gradient drives the emergence of buds in the physiological salts and results in GUVs over the course of 60 minutes (right).

Figure 115 shows the qualitative results of the pre-hydration experiments from a variety of different substrates including 0.1 wt % dextran, 1M sucrose in ultrapure water, 1M sucrose in 1 \times PBS, and 20 \times PBS. The difference between the no pre-hydrate sample (Figure 115a) and the pre-hydrate samples is significant. Clearly many more buds form from the surface of the samples that are allowed a 3 minute period of pre-hydration with a concentrated osmolyte. Interestingly, even the 20 \times concentrated PBS buffer can be used

to promote the formation of the GUVs. This result is significant since encapsulation of desirable molecules inside the lumen of the GUVs could be performed without worry of contamination since the desired encapsulant molecules could be used themselves to promote the osmotic gradient that results in the formation of the GUVs. Current work to quantify the molar yields of the populations of GUVs obtained from these pre-hydration experiments in physiological conditions is currently ongoing.

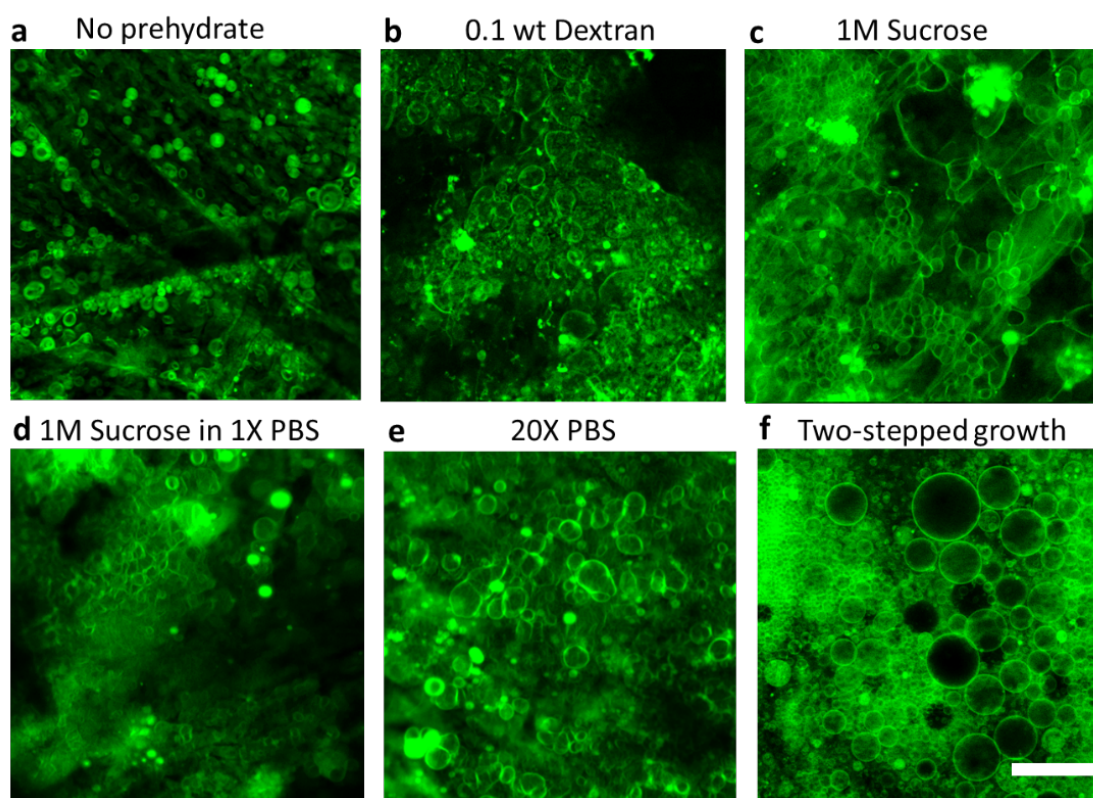


Figure 115: Appearance of buds assembled from pre-hydration in physiological salts. **a-f** Confocal images of the buds on the surface during pre-hydration experiments where **a** a control with no pre-hydration, **b** a 0.1 wt % dextran solution **c** a 1M sucrose solution, **d** a 1M sucrose in 1× PBS, **e** a 20× PBS solution, and **f** a modulated salt control were performed. Scale bar: **a-f** 100 μm .

4. Novel uses of cellulosic materials for biosensing applications

4.1 Development of a clogging-based immunoassay

Due to the large sizes of the particles that precipitate out of solution during a controlled reaction between a concentration of antibodies and equal concentration of antigens⁷, measurements of the change in turbidity of the solution can be made using a plate reader to determine the concentration of proteins from an unknown sample⁸. One common function of cellulose papers is to filter out larger particulates to purify sources of water⁹. Thus, through a clogging-based process, the quantification of the precipitation reaction between antibody proteins, immunoprecipitation, may be possible on cellulose paper. This has the advantage of being a more economical and scalable method of quantifying a biological reaction than previous methods such as a plate reader. A typical image of the papers I developed in the lab for this project is shown in Figure 116. Cellulose paper is composed of micrometer sized fibers and pores (Figure 116b), whereas nanocellulose paper is composed of nanometer sized fibers and pores (Figure 116e).

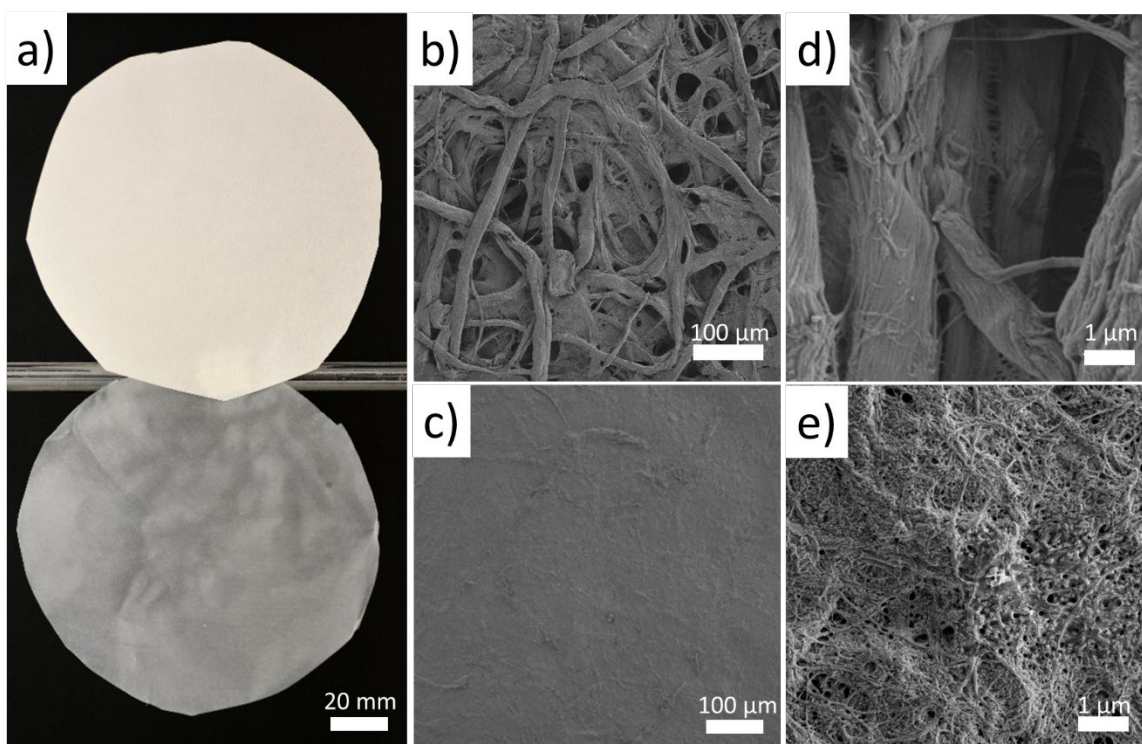


Figure 116: Cellulose and nanocellulose paper. a) Photograph of cellulose paper (top) and nanocellulose paper (bottom). At this scale the cellulose paper appears white and opaque while nanocellulose paper appears translucent. SEM image of cellulose paper at a low magnification (b) shows fibers and pores are visible at the micrometer range while the image of nanopaper at the same magnification (c) appears flatter and more continuous and the fibers and pores are not visible. At a higher magnification nanofibrils are visible on the

cellulose fibers (d) and the nanofibrils and pores are visible on the nanopaper (e). Scale bars: (a) 20 mm, (b,c) 100 μm , (d,e) 1 μm .

From preliminary experiments, I determine that ordinary cellulose papers have pore sizes that are too large. Thus, I conduct experiments using a new class of paper which I termed nanohybrid paper (Chapter 3). Nanohybrid paper is a combination of regular cellulose paper and nanocellulose paper. I prepare devices of nanohybrid papers by depositing a 40 μL droplet of aqueous nanocellulose fibrils on top of regular cellulose paper devices and allowing the water to evaporate (Figure 117a). After evaporation, a thin nanocellulose film (approximately 10 μm thick) adheres to the surface of the cellulose paper device (Figure 117b). I discovered that nanohybrid paper measures an immunoprecipitin reaction by monitoring the distance that the fluid front travels in the paper (Figure 117c). The development of nanohybrid paper was essential since regular cellulose paper had pore sizes that were too large, while paper composed purely of nanocellulose did not wick liquids (Figure 117d) because the pore sizes were too small. I developed a Matlab routine to quantify the distribution of pore sizes between cellulose and nanohybrid paper devices and demonstrate that the smaller pore sizes correlated with the ability to quantify. To confirm that the pore size decreased at the device entrance I collected SEM images at three different magnifications. In μPADs large pores were clearly visible at each of the different magnifications (Figure 118), whereas in nanoPADs pores became visible at the higher magnifications (Figure 118b). I used a custom code in Matlab to detect and quantify the pores from 10 representative images at each of the different magnifications. Examples of the pore segmentation in images are shown in Figure 118c,d. The pore size distribution was plotted and determined over the entire 5 mm² surface area of the device entrance. Compared to the μPADs (Figure 118e), the pore size distribution was significantly shifted towards the nanoscale for nanoPADs (Figure 118f), confirming that the pore size did decrease with the addition of nanocellulose.

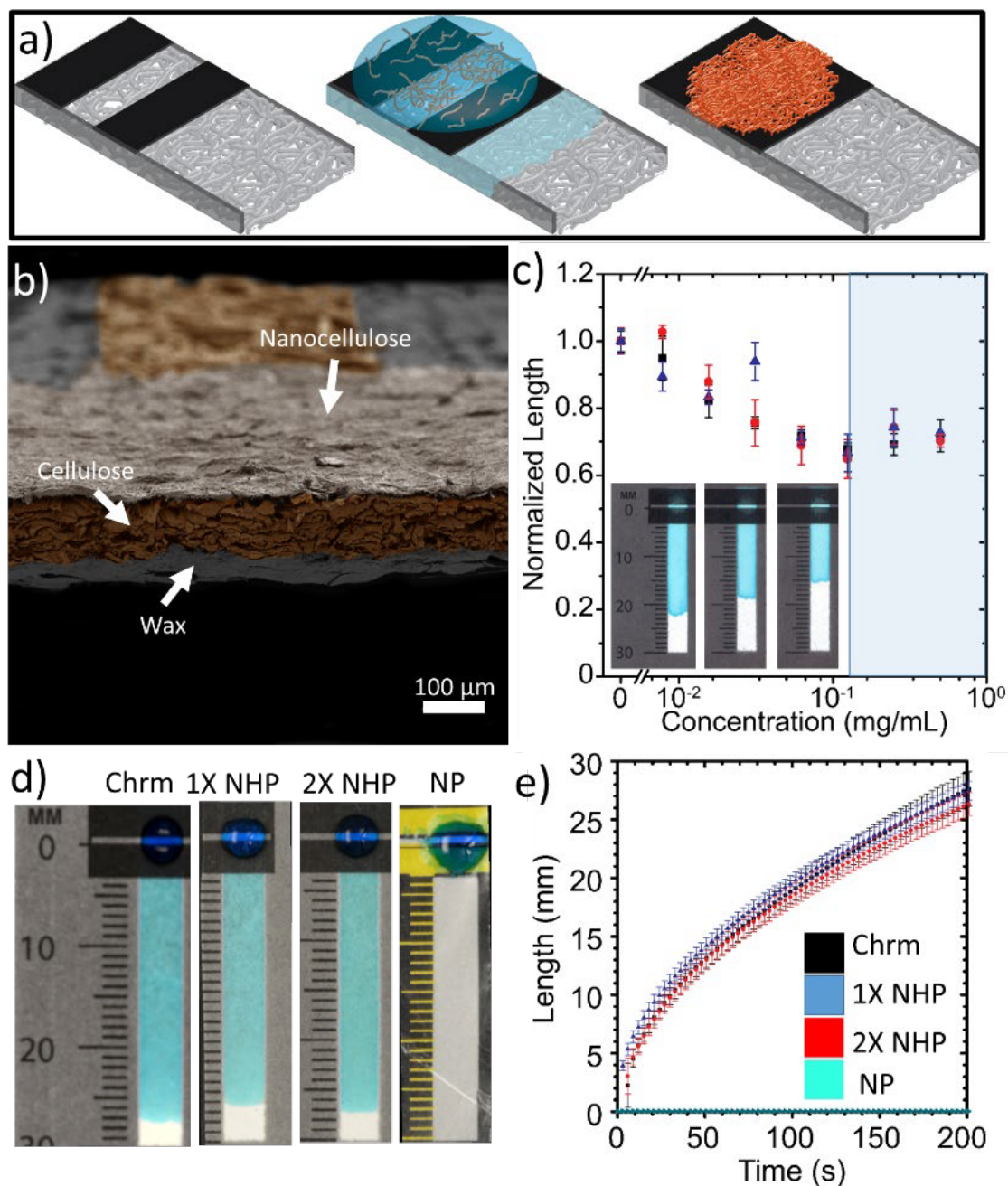


Figure 117: Development of nanohybrid paper. a) Schematic illustrating the method to develop nanohybrid paper. The cellulose paper based devices (left) are incubated with 40 μL droplets of nanocellulose suspension (center). The devices completely imbibe the liquid and after 1 hour of drying a nanocellulose film rests on the entrance of the device (right). b) False colored SEM image of the cross section of a nanohybrid paper device. The dry nanocellulose film (white) can be seen adhered to the entrance of the device and is roughly 10 μm thick. c) Plot of the imbibition length of precipitin solutions in nanoPADs with respect to the antigen concentrations (normalized to the zero). A correlation between the decreasing imbibition length and increasing antigen concentration can be seen until the

equivalence point at 0.125 mg/mL. Insets show nanoPADs stained with FD&C blue dye marking fluid front after 5 minutes. d) Stills after 3 minutes of infiltration of water droplets into the paper devices. The cellulose paper and nanohybrid paper devices show little difference in imbibition properties. The purely nanopaper devices however do not imbibe fluids over this time scale. e) The fluid front was tracked using a camera and images were analyzed and plotted using code in Matlab. The plot shows quantitatively that there was little difference between the imbibition of nanohybrid and cellulose paper devices. Scale bars: (b) 100 μm .

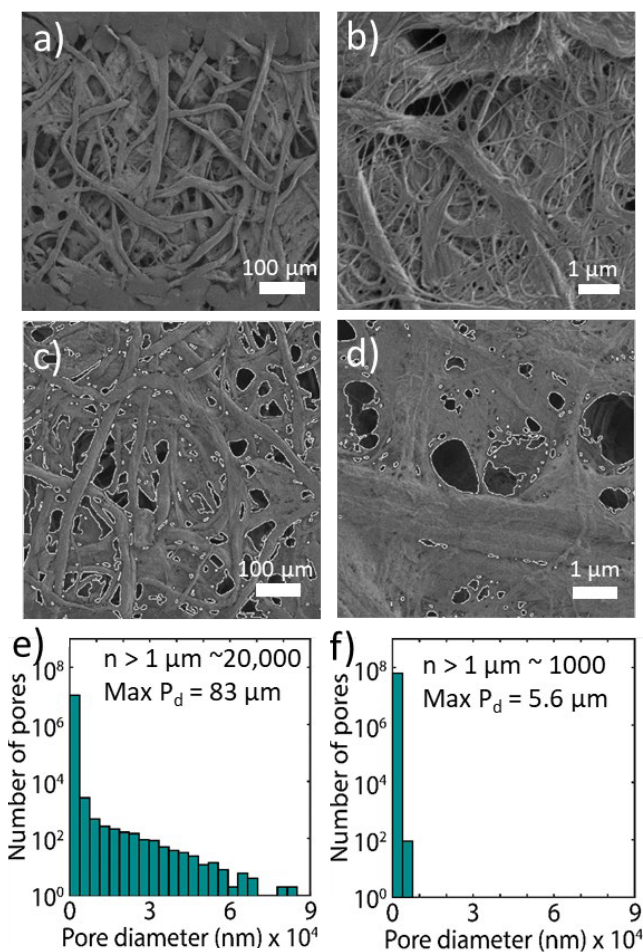


Figure 118: Characterization of nanohybrid paper using electron microscopy. SEM images of cellulose paper (a) and nanohybrid paper (b) devices at different magnifications. I analyzed the pore size distribution of each device at ten images at 3 different magnifications using a custom routine in Matlab. A representation of the segmentation of the pores in cellulose paper can be seen in (c) and of nanohybrid paper can be seen in (d). Extrapolation of our data was carried out over the 5 mm² area of the device entrance. The histograms of the pore sizes in cellulose paper (g) and nanohybrid paper (h) show that the pore size distribution is significantly shifted to the left towards the nanometer for the nanohybrid paper. Scale bars: (a, b, e) 100 μm , (c, d, f) 1 μm .

4.2 Semi-quantitative measurements of a model immunoprecipitation reaction

To test the quantification of the immunoprecipitation in practice, I develop procedures to test a model reaction where I conduct experiments on samples of artificial urine spiked with human albumin protein in the nanoPAD devices (5 minute infiltration of 40 μ L droplets), using two channels for each sample. I recorded the lengths the fluid front imbibed into the paper for each sample and correlated these lengths to an appropriate concentration using the calibration curve. I made sure to multiply the diluted samples by a factor of 5 to determine the correct calculated concentration. To determine a final calculated concentration, I simply took an average of the neat and diluted calculated concentrations.

The results from the four tests indicated that 22 out of 24 (92%) of the samples tested in nanoPADs provided the correct diagnosis of albuminuria and can be seen in Table 12. Correspondence plots showed a reasonable correlation between the actual and the measured concentrations in nanoPADs (Figure 119a) as compared to data on the same samples in a plate reader (Figure 119b). ROC curves indicated that at a cut off concentration of 0.03 mg/mL, the test showed good differentiation between normal and microalbuminuria levels (Figure 119c).

	Sample	Actual Concentration	Calculated Concentration*	Diagnosis*	Calculated Concentration**	Diagnosis**	Correct/Total Diagnosis
Normal Range	1	0.010	0.026	Norm	0.022	Norm	2/2
	2	0.028	0.029	Norm	0.037	Micro	1/2
Microalbuminuria	3	0.030	0.039	Micro	0.043	Micro	2/2
	4	0.050	0.054	Micro	0.038	Micro	2/2
	5	0.10	0.050	Micro	0.051	Micro	2/2
	6	0.15	0.103	Micro	0.128	Micro	2/2
	7	0.20	0.077	Micro	0.057	Micro	2/2
	8	0.25	0.092	Micro	0.056	Micro	2/2
	9	0.29	0.257	Micro	0.085	Micro	2/2
	10	0.30	0.214	Micro	0.215	Micro	2/2
Macroalbuminuria	11	0.31	0.363	Macro	0.194	Micro	1/2
	12	0.5	0.429	Macro	0.364	Macro	2/2

* Data from experiments run on paper 1

** Data from experiments run on paper 2

Table 12: Evaluation of albuminuria test in nanoPADs. The first two columns of the table show the samples and actual concentrations I prepared to evaluate the diagnostic ability of nanoPADs over the clinically relevant albuminuria ranges. The corresponding concentration readings I obtained from nanoPADs are in the calculated concentration columns. From the table I can see that nanoPADs does a relatively good job providing the correct diagnosis between the normal, micro, and macro levels of albumin in our samples

(22 out of 24 samples correctly diagnosed). However, nanoPADs appear to significantly underestimate the concentrations of samples in the higher microalbuminuria range (Samples 7-10), suggesting the test is currently limited to semi-quantitative.

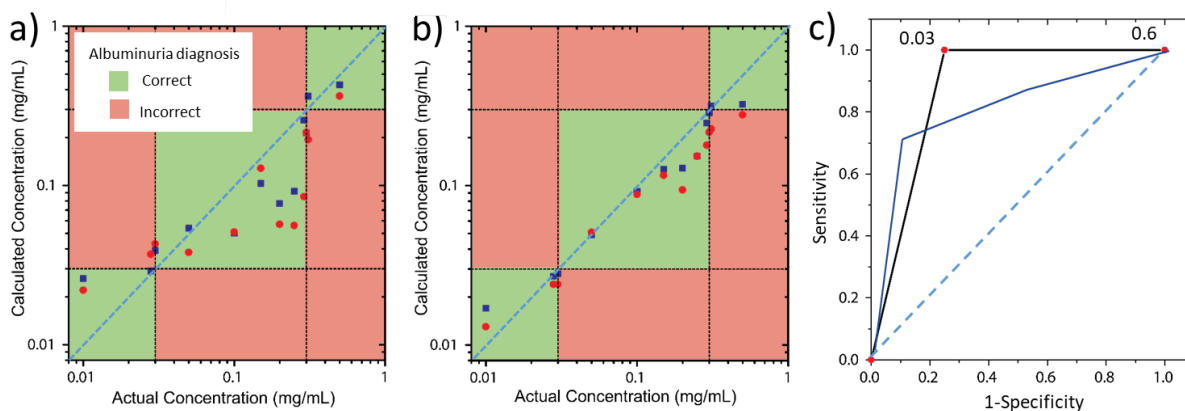


Figure 119: Correspondence and ROC plots for albuminuria test. Plots showing the correspondence of the actual concentrations to calculated concentrations in albuminuria samples tested using nanoPADs (a) and a plate reader (b). The dotted line signifies perfect correspondence. I can see that most measurements in the plate reader give the correct diagnosis and correspond well to the actual concentration. I can see that most measurements in nanoPADs also give the correct diagnosis, but do not correspond as well to the actual concentration, particularly for the higher microalbuminuria region (0.2 - 0.3 mg/mL). c) Receiver operating characteristic curve (ROC curve) used to visualize the ability of nanoPADs to discriminate microalbuminuria from normal albuminuria. The dotted line represents a test that has no discriminative ability (50-50 chance to provide correct diagnosis). I can see that nanoPADs (black line) show good discriminative ability for microalbuminuria at a cut-off concentration of 0.03 mg/mL. The area under the nanoPAD ROC curve (AROC) is 0.88. Although not directly comparable, the ROC curve for the Micral Test® (point of care test strip for albuminuria) from Incerti et al.¹⁰, is overlaid in blue with a reported AROC of 0.83. I can see that the nanoPAD and Micral Test® ROC curves are similar for the microalbuminuria test.

4.3 Templating dense networks of lipid nanotubes with complex compositions on cellulose string

I have also shown it is possible to grow ultra-dense arrays of lipid nanotubes exhibiting liquid-liquid phase coexistence from cellulose string (Figure 120a-c). To label the liquid ordered phase I used Topfluor-Cholesterol (TFC) a probe which is known to partition into the liquid ordered phase¹¹, and to label the liquid disordered phase I used a Rhodamine-DPPE probe which has been shown previously to partition into the liquid disordered phase¹¹⁻¹⁷. From the nanotube figures I can see that there are small green domains along the mostly red tubes suggesting phase coexistence. Vesicles grown on nanopaper from a mixture of

ESM:DOPC:Cholesterol:TFC:RhoPE with a composition of 54.8:20:25:0.1:0.1 mol % are shown in Figures 9d-f and from a mixture of ESM:DOPC:Cholesterol: TFC:RhoPE with a composition of 33:33:33:0.5:0.5 mol % are shown in Figures _g-i. Smaller green domains along the mostly red vesicles can be observed suggesting phase coexistence. Moving forward, I plan to quantify the phase behavior I observe from various lipid vesicle mixtures, so I can evaluate the homogeneity of the lipid composition between our vesicles.

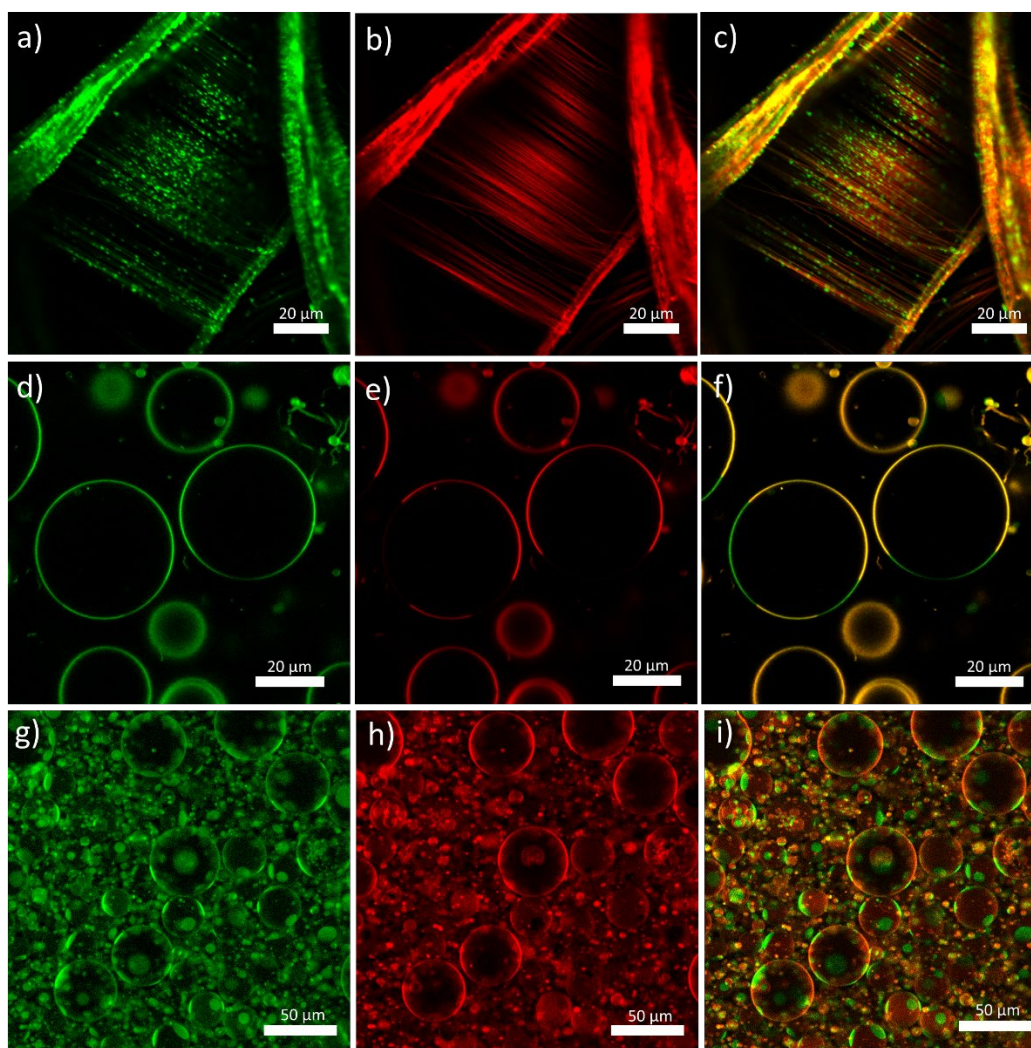


Figure 120: Phase separation in various lipid structures. Confocal fluorescence false colored images of phase separation in lipid structures with green (TFC) indicating the liquid ordered phase, red (RhoPE) indicating the liquid disordered phase and yellow indicating that both dyes cannot be resolved. (a-c) Lipid nanotubes prepared on cellulose string from a 33:33:33:0.5:0.5 mol % mixture of ESM:DOPC:Cholesterol:TFC:RhoPE. (d-f) Vesicles prepared on nanopaper from a 54.8:20:25:0.1:0.1 mol % mixture of ESM:DOPC:Cholesterol:TFC:RhoPE. (g-i) Vesicles prepared on nanopaper from a 33:33:33:0.5:0.5 mol % mixture of ESM:DOPC:Cholesterol:TFC:RhoPE. a) Nanotubes appear incomplete with bright and dark regions. b) Nanotubes appear complete with similar

intensities. c) Nanotubes appear red with green regions along the tubes. d) Vesicle membranes appear complete but with bright and less bright regions. e) Vesicle membranes appear incomplete with bright and dark regions suggesting phase separation. f) Vesicle membranes appear complete with green and yellow regions. g) Vesicle membranes appear complete with bright and less bright regions. Circular regions appearing within the membrane suggest domain formation. h) Vesicle membranes appear complete, and many of the circular regions are not visible. i) Vesicles appear mostly red with circular green domains within and along the edges of the membranes suggesting phase separation. Scale bars: (a-f) 20 μm , (g-i) 50 μm .

4.4 Inkjet printing lipids onto cellulose paper

Cellulose fibers and lipid membranes share a unique biological function as barriers to provide compartmental features in plants. Studies of the interactions between lipid membranes and cellulosic membranes may reveal more unique engineering functions than just the ability to assemble high yields of GUVs. One process that may allow for the rapid prototyping of many different lipid-coated cellulose surfaces with a high fidelity to obtain high resolution features of the lipids on the surface is to use an inkjet printer to print lipids onto cellulose paper. Typical ink formulations contain many additives to achieve specific viscosity and evaporation rate that is optimal for printing¹⁸. However, I am able to achieve reproducible and accurate printing onto nanopaper with lipid dissolved in pure isopropanol solvent. Using a Cannon inkjet printer (Figure 121a) and replacing the ink cartridges with a DOPC lipid ink (Figure 121b), I am able to print patterns of lipids onto nanopaper (Figure 121c). To determine if the lipids remained unaffected by the printing process I examined the lipids after hydration and observed that at regions with high enough concentrations of lipids, the lipids self-assemble into GUVs as expected (Figure 121d).

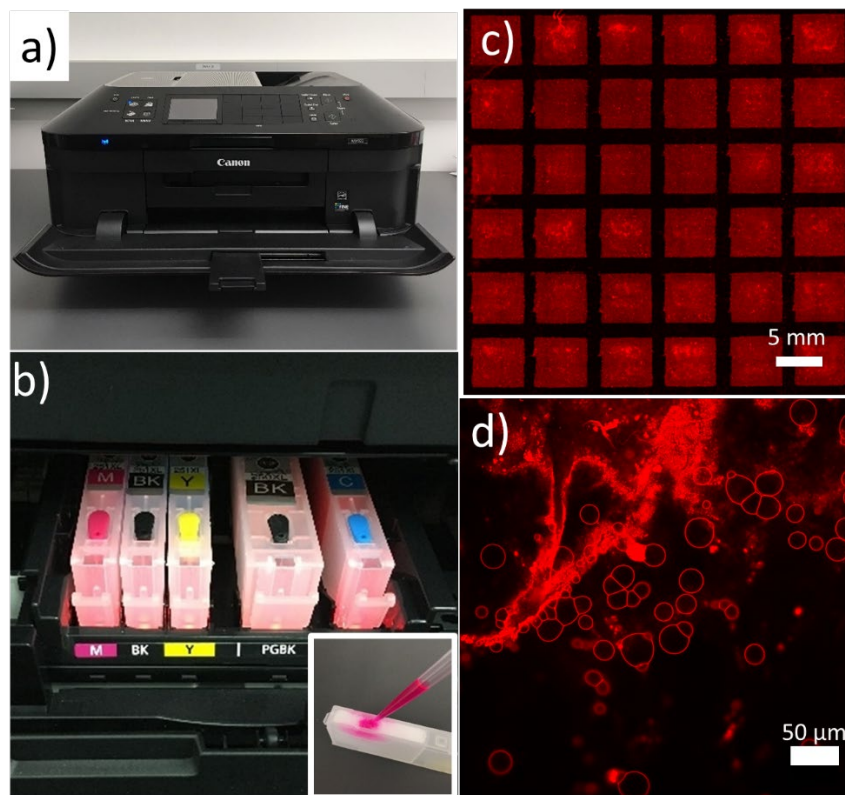


Figure 121: Inkjet printing lipids onto nanopaper. a) Photographs of (a) canon inkjet printer used for lipid printing experiments and (b) customizable magenta, black, yellow and cyan ink cartridges filled with lipids inks. Inset is an image demonstrating the direct filling of the ink cartridge with lipids using a pipette. Confocal fluorescence false colored images of (c) a tilescan of square lipid regions printed onto nanopaper and (d) a region just above the surface of the lipid-coated nanopaper where vesicles are growing. The tilescan (c) shows good fidelity of the lipid pattern printed onto the nanopaper. The higher magnification image (d) shows vesicles growing from the lipid-coated area suggesting a bilayer or multilayer rests on the surface of the nanopaper. Scale bars: (c) 5 mm, (d) 50 μm .

5. Raw code used to process confocal images and analyze GUVs

5.1 Running all of the scripts at once using Run_All.m

```
run SegmentObjects.m  
run SelectObjects.m  
run GenerateMontageSegmented.m  
run GenerateMontageSelected.m
```


5.2 Segmentation of the GUVs using SegmentObjects.m

```

1  % Input:      .czi images of z-stacks of extracted vesicles
2  with metadata
3  % Process:   Performs watershed segmentation on image files
4  % Update:   stores tiling positions and relabels images by
5  tiling
6
7  close all
8  clear all
9  files1 = dir('*.czi');
10 a=pwd;
11 mkdir('Segmented_mat')
12
13 for k=1:length(files1)
14     %Open czi file
15     filename = files1(k).name;
16     data= bfopen(filename);
17     omeMetal = data{1,4};
18     Xscale =
19 double(omeMetal.getPixelsPhysicalSizeX(0).value());
20     for z=1
21         zmax = data{1,1}{z,1};
22         I = zmax;
23         I2 = imclearborder(I);
24         I2 = imfill(I2,'holes');
25
26         %Otsu threshold
27         thresh = multithresh(I2,3);
28
29         %Convert grayscale image to binary image
30         BI_s = imbinarize(I2,double(thresh(1))/255);
31         BI_l =
32 imbinarize(I2,double((thresh(2)+thresh(1))/2)/255);
33
34         %Distance transform
35         DT_s = -bwdist(~BI_s);
36         DT_l = -bwdist(~BI_l);
37         DT_s(~DT_s) = -Inf;
38         DT_l(~DT_l) = -Inf;
39         L1_s = watershed(DT_s);
40         L1_l = watershed(DT_l);
41
42         %Obtain region properties
43         shapes_s = regionprops('table',L1_s,zmax,
44 'PixelIdxList','Eccentricity');
```

```

45         shapes_1 = regionprops('table',L1_1,zmax,
46 'PixelIdxList','Eccentricity');
47
48         %Correct oversegmentation
49
50 E_s=cell2mat(shapes_s.PixelIdxList(shapes_s.Eccentricity >
51 1));
52
53 E_l=cell2mat(shapes_1.PixelIdxList(shapes_1.Eccentricity >
54 1));
55         L2_s = zeros(size(L1_s));
56         L2_l = zeros(size(L1_l));
57         L2_s(E_s)=1;
58         L2_l(E_l)=1;
59         L2_s = imclose(L2_s,strel('disk',1));
60         L2_l = imclose(L2_l,strel('disk',1));
61         L3_s = max(L2_s,double(L1_s>1));
62         L3_l = max(L2_l,double(L1_l>1));
63         cc_s = bwconncomp(L3_s);
64         cc_l = bwconncomp(L3_l);
65         L3_s = labelmatrix(cc_s);
66         L3_l = labelmatrix(cc_l);
67
68         %Obtain region properties
69         shapes_s = regionprops('table',L3_s,zmax,
70 'PixelIdxList','EquivDiameter');
71         shapes_l = regionprops('table',L3_l,zmax,
72 'PixelIdxList','EquivDiameter');
73
74         D_s =
75 cell2mat(shapes_s.PixelIdxList(shapes_s.EquivDiameter <
76 10/Xscale));
77         D_l =
78 cell2mat(shapes_l.PixelIdxList(shapes_l.EquivDiameter >=
79 1/Xscale & shapes_l.EquivDiameter < 130/Xscale));
80
81         %Combine optimally thresholded images of small and
82 large vesicles
83         L2_s = zeros(size(L3_s));
84         L2_l = zeros(size(L3_l));
85         L2_s(D_s) = 1;
86         L2_l(D_l) = 1;
87         L1 = max(L2_s,L2_l);
88         cc = bwconncomp(L1);
89         L1 = labelmatrix(cc);
90

```

```

91         %Correct for oversegmentation
92         shapes1 = regionprops('table',L1,zmax,
93 'Eccentricity','PixelIdxList','EquivDiameter');
94         L2 = zeros(size(L1));
95
96 E=cell2mat(shapes1.PixelIdxList(shapes1.Eccentricity >
97 0.6));
98         L2(E)=1;
99         L2 = imclose(L2,strel('disk',1));
100        L3 = max(L2,double(L1>1));
101
102        %Numerically label the objects
103        cc2 = bwconncomp(L3);
104        L = labelmatrix(cc2);
105
106
107
108        %Obtain region properties of final combined image
109        shapes =
110 regionprops('table',L,zmax,'Area','EulerNumber','FilledArea
111 ','...
112
113 'Eccentricity','EquivDiameter','Centroid','BoundingBox',...
114         'MeanIntensity','PixelValues','PixelList',
115 'Image','Perimeter','PixelIdxList');
116
117        %Save data
118        outputFileNameMAT1 = strcat(filename(1:end-
119 4),'_z',num2str(z),'.mat');
120
121 save(outputFileNameMAT1,'cc2','shapes','zmax','Xscale','L')
122 ;
123
124 movefile(outputFileNameMAT1, strcat(a, '\Segmented_mat'));
125     end
126 end

```

5.3 Selection of the GUVs using SelectObjects.m

```

1  %Input:.mat files with regionprops information for vesicles
2  %Process: Identifies unilamellar vesicles and labels tif
3  files
4  %Output: .mat files with regionprops information on
5  vesicles classified as unilamellar
6
7  close all, clear all
8  mkdir('Selected_mat'),
9  mkdir('Selected_histogram')
10 a=pwd;
11 cd Segmented_mat
12 files2 = dir('*.mat');
13
14 %Compile segmented data
15 MIedges = 0:1:255;
16 NMIedges = MIedges/255;
17 CVedges = 0:1/255:1;
18
19 MICenters = MIedges(1:end-1)+0.5;
20 NMICenters = MICenters/255;
21 CVcenters = CVedges(1:end-1)+0.5/255;
22
23 NMI = [];
24 D = [];
25 CV = [];
26 ind = [];
27 zmax = {};
28 PID = {};
29 centers = [];
30 for k=1:length(files2)
31     samples = files2(k).name(1:end-4);
32     data = open(files2(k).name);
33     zmax{k} = data.zmax;
34     shapes = data.shapes;
35     Xscale = data.Xscale;
36     NMI = [NMI;data.shapes.MeanIntensity./255];
37     D = [D;data.shapes.EquivDiameter*Xscale];
38     CV_temp = [];
39     for i=1:height(shapes)
40
41 CV_temp(i)=std2(shapes.PixelValues{i,1})./mean2(shapes.Pixe
42 lValues{i,1});
43     end

```

```

44     PID = [PID;shapes.PixelIdxList];
45     CV = [CV;CV_temp'];
46     ind = [ind;ones(length(shapes.MeanIntensity),1)*k];
47     centers = [centers;shapes.Centroid];
48 end
49
50 %Analyze Intensity Histograms and Select GUVs
51 peakCV = [];
52 peakNMI = [];
53 D_GUV = [];
54 PID_GUV = {};
55 ind_GUV = [];
56 centers_GUV = [];
57
58 for i =1:1:20
59     b1 = i;
60     if i == 20
61         b2 = i+100;
62     else
63         b2 = i+1;
64     end
65     CV_temp = CV(D>=b1&D<b2);
66     HistCV = smooth(histcounts(CV_temp,CVedges));
67     Max_peak_CV = max(HistCV)*0.999999;
68
69     [pks,locs,w,p] =
70 findpeaks(HistCV,'MinPeakHeight',Max_peak_CV);
71     peakCV = locs(1)/255;
72
73     ub_CV = peakCV*1.5;
74     lb_CV = peakCV*0.5;
75
76     NMI_temp = NMI(D>=b1&D<b2&CV<ub_CV&CV>lb_CV);
77     HistNMI = smooth(histcounts(NMI_temp,NMIedges));
78     Max_peak_NMI = max(HistNMI)*0.999999;
79
80     [pks2,locs2,w2,p2] =
81 findpeaks(HistNMI,'MinPeakHeight',Max_peak_NMI);
82     peakNMI = locs2(1)/255;
83
84     ub_NMI = peakNMI*1.5;
85     lb_NMI = peakNMI*0.5;
86
87     D_GUV =
88 [D_GUV;D(CV<ub_CV&CV>lb_CV&NMI<ub_NMI&NMI>lb_NMI&D>=b1&D<b2
89 )];

```

```
90     ind_GUV = [ind_GUV;
91 ind(CV<ub_CV&CV>lb_CV&NMI<ub_NMI&NMI>lb_NMI&D>=b1&D<b2)];
92     PID_GUV =
93 [PID_GUV;PID(CV<ub_CV&CV>lb_CV&NMI<ub_NMI&NMI>lb_NMI&D>=b1&
94 D<b2)];
95     centers_GUV =
96 [centers_GUV;centers(CV<ub_CV&CV>lb_CV&NMI<ub_NMI&NMI>lb_NMI&
97 I&D>=b1&D<b2,:)];
98
99
100 end
101
102 save('Selected.mat','zmax','Xscale','ind','NMI','CV','D','P
103 ID','centers','D_GUV','ind_GUV','PID_GUV','centers_GUV');
104 movefile('Selected.mat',strcat(a,'\Selected_mat'));
105
106 cd ../
107
```

5.4 Visual checking of the segmentation using GenerateMontageSegmented.m

```

1  % Input:      .czi images of z-stacks of extracted vesicles
2  with metadata
3  % Process:   Performs watershed segmentation on image files
4  % Update:    stores tiling positions and relabels images by
5  tiling
6
7  %%RENAME THE FIRST FILE OF THE TILESCAN SERIES TO 1.CZI SO
8  THAT BFOPEN
9  %%DOES NOT TRY TO RELOAD ALL FILES AT EACH ITERATION
10 close all
11 clear all
12 mkdir('Segmented_montage');
13
14 b=pwd;
15 cd 'Segmented_mat'
16 files1 = dir('*.*mat');
17
18 for k=1:length(files1)
19     filename = files1(k).name;
20
21     samples = files1(k).name(1:end-4);
22     data = open(files1(k).name);
23     centers = data.shapes.Centroid;
24     diameters =
25 round(data.shapes.EquivDiameter*data.Xscale);
26 %     centers(diameters<4,:) = [];
27 %     diameters(diameters<4) = [];
28     mask = boundarymask(data.L); %Define mask to allow
29 checking
30     RGB = label2rgb(data.L, 'jet', [0 0 0],
31 'shuffle');
32     B = imoverlay(RGB,mask,'k');
33     C = imfuse(data.zmax,B,'blend');
34     D =
35 insertText(C,centers,diameters,'FontSize',16,...
36
37 'TextColor','white','BoxOpacity',0,'AnchorPoint','RightCent
38 er');
39     D1 = imfuse((data.zmax),D,'montage');
40     outputFileName2=(strcat(filename(1:end-
41 1),'_zaa',num2str(k),'_montage.tif'));
42     imwrite(D1,outputFileName2,'compression','lzw');
43
44 movefile(outputFileName2,strcat(b,'\Segmented_montage'));

```



```
45  
46 end  
47 cd ../
```

5.5 Visual checking of the selected GUVs using GenerateMontageSelected.m

```

1  close all, clear all
2  c=pwd;
3  cd 'Selected_mat'
4
5  files2 = dir('*.mat');
6  samples = files2(1).name(1:end-4);
7  data = open(files2(1).name);
8  L1 = zeros(3212,3212);
9  D = data.D;
10 centers = data.centers;
11 ind = data.ind;
12 PID = data.PID;
13 D(D<1) = []; centers(D<1,:) = []; ind(D<1) = []; PID(D<1) =
14 [];
15 centers_GUV = data.centers_GUV;
16 D_GUV = data.D_GUV;
17 ind_GUV = data.ind_GUV;
18 PID_GUV = data.PID_GUV;
19 D_GUV(D_GUV<1) = []; ind_GUV(D_GUV<1) = [];
20 centers(D_GUV<1,:) = []; PID_GUV(D<1) = [];
21
22 for k=1:1:20
23     zmax = data.zmax{k};
24     L2 = L1;
25
26     p = PID(ind==k);
27     p_GUV = PID_GUV(ind_GUV==k);
28     c_GUV = centers(ind_GUV==k,:);
29     dia_GUV = D(ind_GUV==k);
30     dia_GUV = round(dia_GUV);
31
32     All = cell2mat(p); GUV = cell2mat(p_GUV);
33
34     L2(All)=6;
35     L2(GUV)=2;
36
37     mask = label2rgb(L2,'hot',[0 0 0]);
38     M = imfuse(zmax,mask,'blend');
39     M1 = insertText(M,c_GUV,dia_GUV,'FontSize',16,...
40 %
41 'TextColor','white','BoxOpacity',0,'AnchorPoint','RightCent
42 er');
43     M2 = imfuse(zmax,M1,'montage');

```

```
44
45 imwrite(M2, strcat('Tile_', num2str(k), '.png'), 'compression',
46 'lzw');
47 end
```

6. Bibliography

- (1) Horger, K. S.; Estes, D. J.; Capone, R.; Mayer, M. Films of Agarose Enable Rapid Formation of Giant Liposomes in Solutions of Physiologic Ionic Strength. *J. Am. Chem. Soc.* **2009**, *131* (5), 1810–1819. <https://doi.org/10.1021/ja805625u>.
- (2) Greene, A. C.; Sasaki, D. Y.; Bachand, G. D. Forming Giant-Sized Polymersomes Using Gel-Assisted Rehydration. **2016**, No. May, 3–9. <https://doi.org/10.3791/54051>.
- (3) Dao, T. P. T.; Fauquignon, M.; Fernandes, F.; Ibarboure, E.; Vax, A.; Prieto, M.; Le Meins, J. F. Membrane Properties of Giant Polymer and Lipid Vesicles Obtained by Electroformation and Pva Gel-Assisted Hydration Methods. *Colloids Surfaces A Physicochem. Eng. Asp.* **2017**, *533* (July), 347–353. <https://doi.org/10.1016/j.colsurfa.2017.09.005>.
- (4) Scott, A.; Noga, M. J.; Graaf, P. De; Westerlaken, I.; Yildirim, E.; Danelon, C. Cell-Free Phospholipid Biosynthesis by Gene- Encoded Enzymes Reconstituted in Liposomes. **2016**, 1–23. <https://doi.org/10.1371/journal.pone.0163058>.
- (5) Pott, T.; Bouvrais, H.; Méléard, P. Giant Unilamellar Vesicle Formation under Physiologically Relevant Conditions. *Chem. Phys. Lipids* **2008**, *154* (2), 115–119. <https://doi.org/10.1016/j.chemphyslip.2008.03.008>.
- (6) Has, C.; Sunthar, P. A Comprehensive Review on Recent Preparation Techniques of Liposomes A Comprehensive Review on Recent Preparation Techniques of Liposomes. *J. Liposome Res.* **2019**, *0* (0), 1–30. <https://doi.org/10.1080/08982104.2019.1668010>.
- (7) Heidelberger, B. Y. M.; Kendall, F. E. The Precipitin Reaction Between Type III Pneumococcus Polysaccharide and Homologous Antibody. **1935**, No. I.
- (8) Otsuji, S. Turbidimetric Immunoassay of Serum C-Reactive Assay Reproducibilities. **1982**, *2124*, 2121–2124.
- (9) Voisin, H.; Bergström, L.; Liu, P.; Mathew, A. Nanocellulose-Based Materials for Water Purification. *Nanomaterials* **2017**, *7* (3), 57. <https://doi.org/10.3390/nano7030057>.
- (10) Incerti, J.; Zelmanovitz, T.; Camargo, J. L.; Gross, J. L. Evaluation of Tests for Microalbuminuria Screening in Patients with Diabetes. **2005**, No. August, 2402–2407. <https://doi.org/10.1093/ndt/gfi074>.
- (11) Klymchenko, A. S. Review Fluorescent Probes for Lipid Rafts : From Model Membranes to Living Cells. **2014**, 97–113. <https://doi.org/10.1016/j.chembiol.2013.11.009>.
- (12) Veatch, S. L.; Keller, S. L. Seeing Spots: Complex Phase Behavior in Simple Membranes. *Biochim. Biophys. Acta - Mol. Cell Res.* **2005**, *1746* (3), 172–185. <https://doi.org/10.1016/j.bbamcr.2005.06.010>.

- (13) Kresse, K. M.; Xu, M.; Pazzi, J.; García-ojeda, M.; Bala, A. Novel Application of Cellulose Paper as a Platform for the Macromolecular Self-Assembly of Biomimetic Giant Liposomes. 1–22.
- (14) Juhasz, J.; Davis, J. H.; Sharom, F. J. Fluorescent Probe Partitioning in Giant Unilamellar Vesicles of ‘Lipid Raft’ Mixtures. *Biochem. J.* **2010**, *430* (3), 415–423. <https://doi.org/10.1042/BJ20100516>.
- (15) Samsonov, a V; Mihalyov, I.; Cohen, F. S. Characterization of Cholesterol-Sphingomyelin Domains and Their Dynamics in Bilayer Membranes. *Biophys. J.* **2001**, *81* (3), 1486–1500. [https://doi.org/10.1016/S0006-3495\(01\)75803-1](https://doi.org/10.1016/S0006-3495(01)75803-1).
- (16) Ogl, K.; Rangamani, P.; Liedberg, B.; Kraut, R. S. Oscillatory Phase Separation in Giant Lipid Vesicles Induced by Transmembrane Osmotic Differentials. **2014**, 1–18. <https://doi.org/10.7554/eLife.03695>.
- (17) Bordovsky, S. S.; Wong, C. S.; Bachand, G. D.; Stachowiak, J. C.; Sasaki, D. Y. Engineering Lipid Structure for Recognition of the Liquid Ordered Membrane Phase. *Langmuir* **2016**, *32* (47), 12527–12533. <https://doi.org/10.1021/acs.langmuir.6b02636>.
- (18) Tekin, E.; Smith, P. J.; Schubert, U. S. Inkjet Printing as a Deposition and Patterning Tool for Polymers and Inorganic Particles. *Soft Matter* **2008**, *4* (4), 703. <https://doi.org/10.1039/b711984d>.